**Studies of the Dynamics of One-Photon Double-Photoionization of $D_2O$**

By

ZACHARY LOUIS STREETER

DISSERTATION

Submitted in partial satisfaction of the requirements for the degree of

DOCTOR OF PHILOSOPHY

in

CHEMICAL PHYSICS

in the

OFFICE OF GRADUATE STUDIES

of the

UNIVERSITY OF CALIFORNIA

DAVIS

Approved:

---

Professor C. William McCurdy (Chair)

---

Professor Lee-Ping Wang

---

Professor Frank Yip

Committee in Charge

2021

To the dreamer.

# Contents

# Acknowledgments

Before I share my research, I would like to express my gratidude to the individuals who deserve as much congratulations as I do for this work. Without them, I would not have had as much success during my academic career.

First and foremost I would like to thank my advisor, Prof. Bill McCurdy. Bill provided a research environment that allowed me to focus only on my work and growth as a scientist. I learned quickly that he would always take care of his group members, and the importance of this foundational support that he provided cannot be overstated. Along with this, he opened a world of collaboration with amazing scientists, and within those collaborations allowed me to dictate the theoretical story as a graduate student. He is a true leader in that he can guide but also lean on his group members when warranted.

I would like to thank Prof. Robert Lucchese for being generous with his time while working with me on numerous computational and conceptual problems. It's hard to articulate how enjoyable it was to work with Robert, with his oblique insight into scientific problems and his overall gentle nature. I must thank the third "McKoy Boy", Prof. Tom Rescigno. Tom's razor-sharp wit and scientific insight is only matched by his playful mind. I knew instantly why he was an amazing scientist and am grateful to have worked with him. In addition I must thank Roger Bello for his tireless work on the double photoionization project. Without his efforts, this project would be in a very different place.

A great deal of my work is enriched and validated by masterful experiments done at multiple labs and universities. Theory not grounded in experimental observation is said to be just mathematics. Therefore, I have to thank all the experimentalists who have worked tirelessly during my graduate career. Without their efforts, this work would not look as nearly as impressive.

I would also like to thank my undergrad mentor Prof. Gary Findley. Gary is the sole reason why I was able to go to graduate school. I will be forever grateful to him for giving me a chance to

become a scientist. Last but indeed not least, I would like to thank my family for their love and support during my long and arduous academic career. In particular, thanks must go to my mother. She has and will always be a pillar in my life.

# Abstract

One-photon double-photoionization (DPI) is an exquisitely sensitive experimental probe of electron correlation. For more than three decades, DPI theoretical and experimental efforts have produced a rich literature investigating simple atoms and diatomics like $H_2$, but remained stagnant in terms of complexity of the systems. No complete experiments (measuring body-frame double-ionization-differential-cross-sections) of polyatomic systems with more than two electrons were done prior to this work because the residual dications did not dissociate in their ground and low lying states required by the COLd Target Recoil Ion Momentum Spectroscopy (COLTRIMS) experimental technique. A COLTRIMS experiment performed at the Advanced Light Source (ALS) found that the water di-cation does dissociate completely in its ground and low lying excited electronic states, opening the door to such studies. This successful DPI experiment on water also allows an investigation into the differences between body-frame inter-shell (different orbitals) and intra-shell (same orbital) electron correlation for the first time. For example, the $1b_1$ orbital is the lone-pair orbital of water that is perpendicular to the plane of the molecule and, therefore is expected to produce a DPI intra-shell cross-section that resembles an atom's cross-section. The other lone-pair orbital of water, the $3a_1$ orbital, is in the plane of the molecule and, therefore is expected to produce a DPI intra-shell cross-section that has a structure more indicative of a molecule due to the correlated electrons' motion perturbed by the the nuclei. Moreover, a DPI example of inter-shell cross-section could be one electron from the $1b_1$ orbital and the other correlated electron from the $1a_1$ orbital, which has never been calculated before for the body-frame. Thus, an *ab initio* investigation of DPI of water provides a path to new physics not yet explored and will further our understanding of electron correlation that is fundamental in electron dynamics in atomic and molecular physics. However, the first crucial step in this theoretical pursuit is to clearly define the molecular frame at the moment of photoabsorption to investigate multi-orbital electron correlation with respect to this defined frame of reference and the work reported in this thesis provides this necessary first step.

This overarching theme of understanding electron correlation within the body-frame for more complex polyatomic and in the continuum after the two correlated electrons are ionized on an *ab inito* level is the new standard for DPI studies and this dissertation lays the foundation for that standard by investigating the dynamics of $D_2O^{++}$ breakup after double-photoionization while unambiguously defining the molecular frame. To begin, unraveling all the nuclear dynamics by classical trajectories propagated on the nine di-cation states of $D_2O^{++}$ that are energetically accessible for double ionization by a 61 eV photon, is presented. Excellent agreement between theory and experiment is obtained and a state-selective analysis of the electron correlation is provided by these theoretical simulations. Breakdown in the axial-recoil approximation for some states of $D_2O^{++}$ is discovered, and a blueprint is defined for guiding experimental observations that indicate this breakdown.

Agreement between theory and the single-photon double-ionization experiment encouraged a comparison between intense field multiphoton double ionization of $D_2O$ and these classical trajectory simulations. The dynamics of intense-field multiphoton ionization is at the heart of modern attosecond and femtosecond molecular physics. Here it is shown how difference between the dynamics of single-photon double ionization of water and those of intense field double ionization are revealed by the final momenta of the fragments. In this work a detailed picture of the combined nuclear and electronic dynamics of intense-field double ionization on the femtosecond time scale begins to emerge.

Finally, a look into propagation of classical trajectories with initial conditions sampled from a Wigner distribution built from a vibrationally excited wavefunction is presented. The vibrationally excited wavefunction will contain nodes that in-turn produce negative regions in the generated Wigner distribution. The volume of negativity in the Wigner distribution is a signature of quantum character and, therefore this study explores probing quantum character using a semi-classical technique. Interesting connections between classical and quantum behavior is reported and multiple theoretical predictions are stated for possible future experiments on the nuclear breakup of $D_2O^{++}$ from a vibrationally excited ensemble of neutral heavy water.

# List of Figures

# List of Tables

CHAPTER 1

# Introduction

One-photon double-photoionization of $H_2$ is followed promptly by the Coulomb explosion of the $H_2^{++}$ di-cation, and a coincidence measurement of the momenta of the two ejected electrons and one of the protons (together with momentum conservation) produces a kinematically complete description of the double ionization and breakup process. This technique permits reconstruction of the molecular geometry at the time of photoionization assuming a vertical electronic transition, and allows the observation of the triply differential cross section (TDCS) in the molecular frame. The TDCS is the cross section that is differential in the solid angles of both outgoing electrons and the energy of one of them and, therefore it is the most detailed mesurement possible. Both theory [**22**, **24**, **79**] and experiment [**39**, **108**, **110**] have provided a cohesive story for this simple diatomic molecule. Naturally, one would like to continue this research to many-electron molecules like $N_2$ and $O_2$. However the ground state and first few excited states of these molecules after double ionization, namely $N_2^{++}$ and $O_2^{++}$, have barriers to dissociation and therefore do not allow for four-fold coincidence (two ions and two electrons) measurement, which leaves a desire for more practical targets for particle coincidence studies of double-photoionization. The experimental four-fold coincidence technique described above is called Cold Target Recoil Ion Momentum Spectroscopy (COLTRIMS). COLTRIMS experiments require a breakup process resulting in two ions and two electrons from the investigated system for a four-fold coincidence measurement. In other words, for the systems considered here, for example, having the general form $AH_n$ must undergo, $AH_n + h\nu \rightarrow A^*H_{n-2} + 2H^+ + 2e^-$, where A is a placeholder for a multi-nuclei subsystem and the asterisk indicates that this multi-nuclei subsystem maybe in an excited state. From these kinematically complete experiments one can infer the momentum of the residual neutral subsystem, $A^*H_{n-2}$, but no other empirical information about the neutral subsystem can be extracted. For example, in complete four-fold breakup of ammonia, $NH_3 + h\nu \rightarrow N - H + 2H^+ + 2e^-$, the residual neutral subsystem, $N - H$, may be a diatom or separate atoms. This information is lost with direct measurements of the

$2H^+$ momentum vectors. Increasing the number of nuclei in the residual neutral subsystem leads to more potential breakup channels, and the experimentally inferred momentum of this subsystem may not be half the story. Furthermore, multi-electron systems require knowledge of these orbitals from which the two correlated electrons are ionized. Put in another way, a di-cation state-selective experimental measurement guided by theoretical simulations is required for the associated electron measurement. Previous experimental and theoretical studies of $H_2$ [**106**, **110**, **111**, **112**] allowed one to ignore these considerations, but with the push for studies on double-photoionization of more complex systems [**5**, **33**], unraveling all the nuclear dynamics using theoretical calculations is necessary to completely understand experimental observation.

Experimentalist took the first step towards a complete picture of the double-photoionization of a polyatomic molecule. Recent COLTRIMS experiments on heavy water provided highly resolved measurements that opened the door for a detailed theoretical analysis of the nuclear dynamics following the complete-breakup process, $D_2O + h\nu \rightarrow O^* + 2D^+ + 2e^-$. The initial experiment was performed on $H_2O$ using a 57 eV photon [**80**] but heavy water was chosen for a subsequent experiment for better statistics. In this experiment, a 61 eV photon was chosen after calculations revealed this was the highest energy photon that would only double ionize from the valence orbitals and safely not perturb the lower core orbitals ($2a_1$ and $1a_1$). Using the harmonic approximation, the dispersion in the postion and momenta for the ground vibrational state is given by

$$\begin{aligned} (\Delta q)^2 &= \frac{\hbar}{2m\omega} \\ (\Delta p)^2 &= \frac{\hbar m\omega}{2}, \end{aligned} \tag{1.1}$$

showing the distributions of position and momentum change by a factor of $1/2^{1/4}$ and $2^{1/4}$, respectively, when the masses change by a factor of 2. This difference is captured in the generated initial conditions and will manifest in the final distributions of the measured momentum vectors. Therefore, the classical trajectory simulations were performed both on water and heavy water for accurate comparisons between the two respected experiments. The theoretical simulations showed the dynamics of both water and heavy water followed the same overall pattern and, therefore these two investigations into water and heavy water will be used interchangeably. At the 61 eV photon

energy of the experiment, the DPI process could proceed via any of the nine energetically accessible valence-electronic states of $D_2O^{++}$. To discover which ionization channels contribute to the observed triple differential cross section (TDCS) for the electrons measured in coincidence with different kinetic energy releases, classical trajectory studies have been carried out for breakup of the water di-cation on all nine potential surfaces, sampling from a Wigner phase space distribution for the vibrational ground state of $D_2O^{++}$. The direct Coulomb breakup and sequential breakup, $D_2O^{++} + h\nu \rightarrow OD^+ + D^+$, channels are investigated in their entirety. Excellent agreement with experiment and a blueprint for interpretation of future COLTRIMS experiments on systems with three or more nuclei is provided by this semi-classical theoretical analysis.

This agreement between the single photon COLTRIMS experiment and the semi-classical theoretical method outlined above provides a bridge to compare a single-photon Franck Condon interpretation with strong-field ionization (SFI) experiments and interpretations. For many experiments, the ideal scenario is that SFI serves as a "sudden" transition where the nuclei do not move during the pulse that induces the ionization [**52**, **85**, **88**]. The extent to which SFI with short pulses can be considered vertical is explored by comparing SFI coincidence velocity map images of the fragment ion with the semi-classical trajectory simulations. As demonstrated here, even for short pulses ($<$ 10 fs) the ionization cannot be considered to be "vertical", but involves reshaping of the vibrational wave function during the ionization dynamics.

Finally, exploration of quantum behavior using the quasi-probabilistic Wigner distribution is presented. The Wigner function, which was formulated in 1932 by Eugene Paul Wigner [**118**], has seen a resurgence in popularity with its applications to quantum information [**113**, **114**]. The quantum signature is found in the negativity of the Wigner function [**15**], and this negativity can be produced from excited normal modes as these modes produce self-interference patterns that result in nodes that are quantum in nature. An algorithm for Metropolis sampling [**43**, **81**] for the case of these excited normal modes treated as initial conditions for classical trajectories of the Coulomb breakup of $D_2O^{++}$ is outlined. Resulting momentum images and branching ratios are presented and controlled dynamics on the $D_2O^{++}$ potential energy surfaces are proposed for future experimentation.

To present this scientific story, this thesis is organized as follows:

- Chapter 2 presents the COLTRIMS experiment for one-photon double-photoionization of $D_2O$. The full breakup of $D_2O^{++}$ is measured using momentum conservation and momentum images are then generated. If the photodissociation fragments separate with large enough kinetic energy, then an approximation can be made that the trajectories of the fragments proceed along the direction of the vibrational motion of the broken bond. This approximation is called *axial-recoil* and is assumed when generating the COLTRIMS coordinate system. Given this is the first triatomic molecule analyzed in a detailed COLTRIMS experiment, the axial-recoil assumption maybe too simplistic and the dynamics perhaps are more involved. Therefore, a challenge to theory is proposed in the final section of this chapter. This challenge involves investigating the validity of the axial-recoil approximation, identifying all the experimentally-observed states of $D_2O^{++}$, and in general unravel all the nuclear dynamics that in-turn give experimentalists a blueprint involving simulations and interpretations that are critical in this new era of COLTRIMS investigations of more complex polyatomic molecules.
- Chapter 3 presents the calculations of the nine electronic states of $D_2O^{++}$. A closed form fit is then used to produce a representation of each potential energy surface that can be differentiated, and thus propagate dynamics in time. Lastly because conical intersections exist for these dication states, an approximation to the diabat for the $3^1A_1$ state needed for classical dynamics is given.
- Chapter 4 gives an introduction to the Wigner phase space method for generating initial conditions, and for propagation of the dynamics via solving Hamilton's equations in phase space. The Monte Carlo sampling method [**61**, **90**] used to produce the phase space distribution is presented and, lastly, this method is applied to the ground vibrational state of neutral water.
- Chapter 5 provides a theoretical background for the time propagation of the Wigner distribution in phase space and its interpretation. A discussion of "vertical transition" is provided with a few notes on the trajectory analysis.
- Chapter 6 presents a full comparison of theory and experiment for the direct breakup channel, $D_2O^{++} \rightarrow O + D^+ + D^+$. A look into the axial-recoil approximation and its

limitations with respect to the resulting direct breakup channel is given. A conclusion section is provided for a summary of results and guidance for future experiments.

- Chapter 7 presents a full comparison of theory and experiment for the sequential breakup channel, $D_2O^{++} \rightarrow OD^+ + D^+ \rightarrow O + D^+ + D^+$. An introduction to the *native frames* analysis experimental technique is provided. To compare with experiment an *appearance window* interpretation and calculation is given. Finally, a concluding section summarizes all of the sequential breakup findings, and comparison between experiment and theory is tabulated.
- Chapter 8 presents a comparison between multi-photon and single-photon DPI of $D_2O^{++}$.
- Chapter 9 revisits the Wigner phase space method when the quasi-probability function is allowed to have negative values. The equations for how to sample from such a distribution is outlined and, finally, predictive results are given for future experimentation.
- Finally, in Appendix X, reprints and preprints of the papers that used this work are reporduced here.

CHAPTER 2

# COLTRIMS Experiment and Nuclei Measurement

## 2.1. $D_2O^{++}$ Complete Breakup

The single photon double-photoionization (DPI) COLTRIMS experiment was initially done on $H_2O$ using a 57 eV photon [**80**]. A second experiment using heavy water, $D_2O$, was performed using a 61 eV photon to improve the statistics in the measurement, while not ionizing from the 2a or 1a core orbitals [**93**]. In principle, the complete breakup of $D_2O$ after double-photoionization can lead to dissociation into the following nuclear two- and three-body breakup channels:

$$\begin{aligned} D_2O + h\nu &\rightarrow D_2^{+*} + O^{+*} + 2e^- \\ &\rightarrow D^+ + D^* + O^{+*} + 2e^- \\ &\rightarrow O^{+2} + 2D^* + 2e^- \\ &\rightarrow D^+ + OD^{+*} + 2e^- \\ &\rightarrow 2D^+ + O^* + 2e^- \end{aligned}$$

where a superscript asterisk (*) indicates the possibility of either a ground or an excited electronic state. Current COLTRIMS experiments can measure the momentum vectors of four or five charged bodies. Of these five channels only the last two were observed in the DPI COLTRIMS experiment using a 61 eV photon [**80**]. These channels are referred to as sequential and direct breakup, respectively. In the sequential breakup channel, the $OD^{+*}$ subsequently broke apart to produce a free deuterium ion, $D^+$, and a oxygen atom, resulting in a complete breakup process required by the COLTRIMS technique. In addition to these observations, a single ionization followed by autoionization of the residual excited $OD^*$ molecule, producing an identical signature as a DPI process

seen by Sann *et al.* [**86**], was observed,

$$D_2O + h\nu \rightarrow D^+ + OD^* + e^-$$

$$OD^* \rightarrow OD^+ + e^-.$$

A complete explanation of the COLTRIMS experimental details can be found in the literature(see Refs. [**32**, **57**, **104**]). Here we will focus on the comparison of our theoretical results with these experiments. A near-$4\pi$ solid angle collection efficiency is realized for all four charged particles. The detectors are position and time sensitive, allowing the full 3D momentum vectors for each charged particle to be calculated. For direct breakup, the neutral (perhaps excited) oxygen atom is directly observed. However, the large momentum difference between atomic and electronic fragments permits the application of conservation of linear momentum between the atomic fragments to calculate the momentum of the neutral, unmeasured oxygen atom. This enables the determination of the asymptotic angle $\beta$ between the two proton momenta.

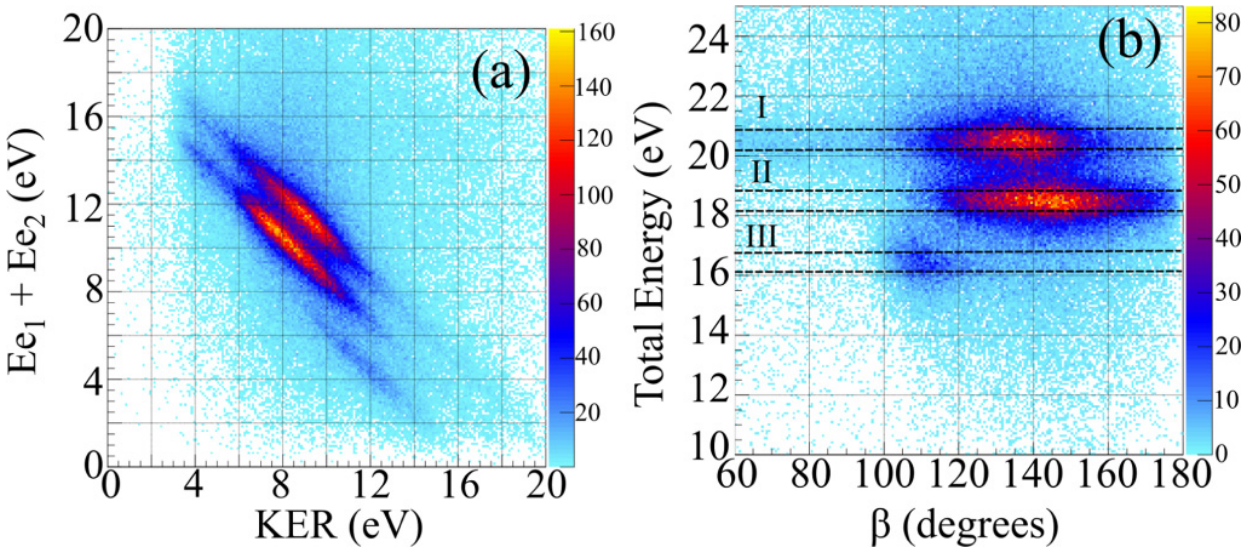


FIGURE 2.1. Energy correlation plots for the three-body breakup, including investigation of the angle between proton momenta. (a) $H^+ + H^+ + O$ yield as a function of the electron energy sum ($E_{esum}$) and KER (total kinetic energy release of the ions added to the inferred neutral fragments kinetic energy release). (b) Yield as a function of the total energy ($E_{esum}$ + KER) and $\beta$ (asymptotic angle between proton momenta). The three labeled features correspond to asymptotic oxygen terms: I, $^3$P; II, $^1$D; III, $^1$S.

TABLE 2.1. Oxygen term energy separation and comparison with NIST data.

| Term | NIST (eV) | Expt (eV) | Label |
|---|---|---|---|
| O($^3$P) | 0.0 | 0.0 | I |
| O($^1$D) | 1.967 | 1.94±0.51 | II |
| O($^1$S) | 4.190 | 4.02±0.63 | III |

Measurement of the complete breakup of $D_2O$ in the COLTRIMS experiment can be succinctly visualized by plotting the four-fold coincidence measurements of both position and time sensitive detectors; namely plot an observable for the ions on one axis and an observable for the electrons on the other axis. Since our experiment is kinematically complete and we measure the full 3D momentum vectors of the ionic fragments, a useful observable for the ions is the total kinetic energy release yield of all dissociating fragments (i.e. the sum of all the measured kinetic energy releases for the ions and the inferred neutral subsystem). This kinetic energy release is abbreviated KER and will be used throughout this thesis. This observable is plotted on the x-axis and the electron energy sum for both electrons is plotted on the y-axis of Fig. 2.1(a). This leaves three features of the distinct total continuum energy visible. These features correspond to the lowest three states of the neutral oxygen fragment, $^3$P, $^1$D, and $^1$S, which can can be verified from the asymptotic limits of the dissociation di-cation potential energy surfaces leading to $H^+ + H^+ + O$ discussed in great detail by Gervais *et al.* [**38**]. Experimental verification is done by comparison of the NIST data of Moore [**37**], which show consistent agreement of the neutral oxygen state assignment (see Table 2.1). Since the three-body breakup has an angular component among the ionic fragments, an additional spectrum is presented in Fig. 2.1(b), namely, the $H^+ + H^+ + O$ yield as a function of the total continuum energy (sum of KER and electron energies) and $\beta$. We note that it is clear from this figure that the asymptotic limits of the dissociating di-cations leading to O($^3$P), O($^1$D), and O($^1$S) have unique $\beta$ distributions.

It was found that plotting the KER of the measured momentum vectors with respect to the asymptotic angle $\beta$ showed interesting structure and hereafter, such figures are referred to as nuclear conformation maps. Inspection of Fig. 2.2 clearly shows two distinct features, with the first feature having high counts starting around 100 degrees and continuing to 180 degrees, on a KER interval of $3 - 15$ eV. The second feature is the low count uniform distribution (referred to as the "carpet") starting at low $\beta$ and continuing until the more dominant high statistics islands on a KER interval

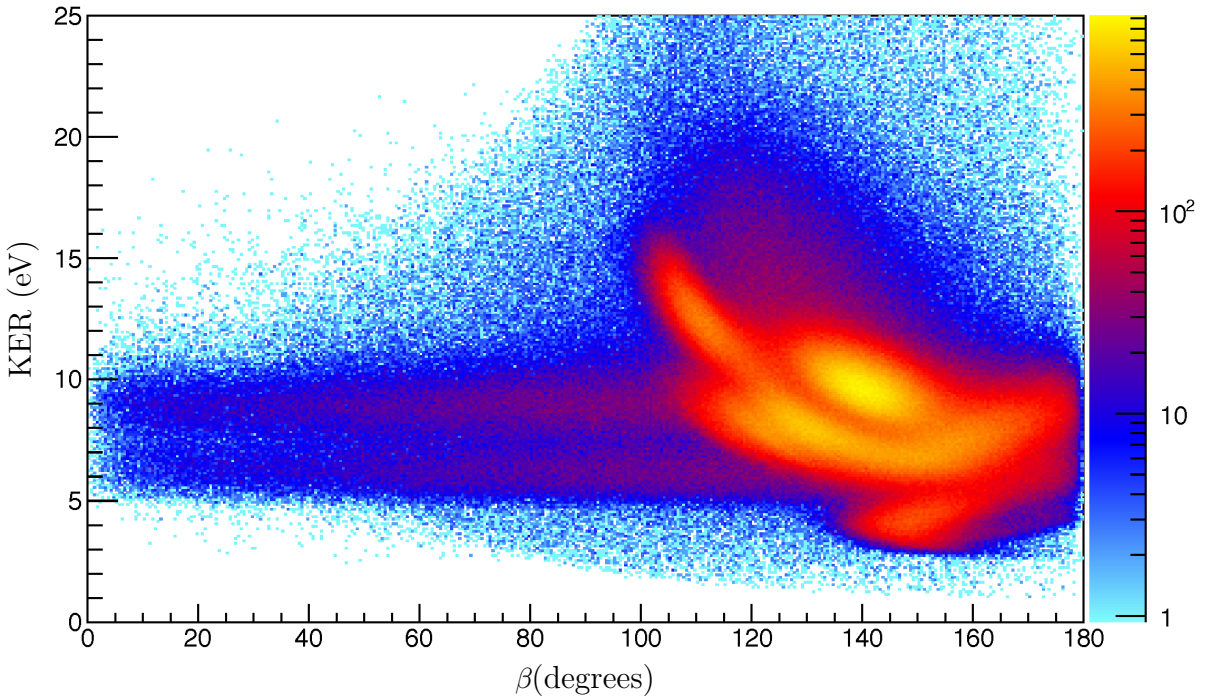


FIGURE 2.2. $D^+ + D^+ + O$ yield as a function of Kinetic Energy Release and the angle between the two proton momenta, $\beta$; dumped nuclear conformation map. Two distinct features are present: the islands of density on the interval around 100 to 180 $\beta$ angles, and another feature of a uniform $\beta$ angle carpet on the interval around 5.5 to 10 eV.

of $5 - 10$ eV. Yield plots contrasting various dissociation angles and energies have been used in the literature to, for example, distinguish between concerted and stepwise bond cleavage in molecular systems (see Ref. [**78**] as an example).

Many features in Fig. 2.2 overlap and require further separation of the data by observable cut-offs called *gates* to gain more insight. We can use our knowledge that the three total continuum energy streaks in Fig. 2.1 correspond with leaving the neutral oxygen atom in the $^3$P, $^1$D, or $^1$S state. By gating on each neutral oxygen state and then plotting the respected measurements as nuclear conformation maps, we see more refined separated islands of density appear (see Fig. 2.3). This separation is rooted in each total continuum energy streak having well separated $\beta$ distributions. These further separated islands are now limited to the respected di-cation states that dissociate to the corresponding oxygen asymptote. For example, the islands of density in Fig. 2.3 (b) are the

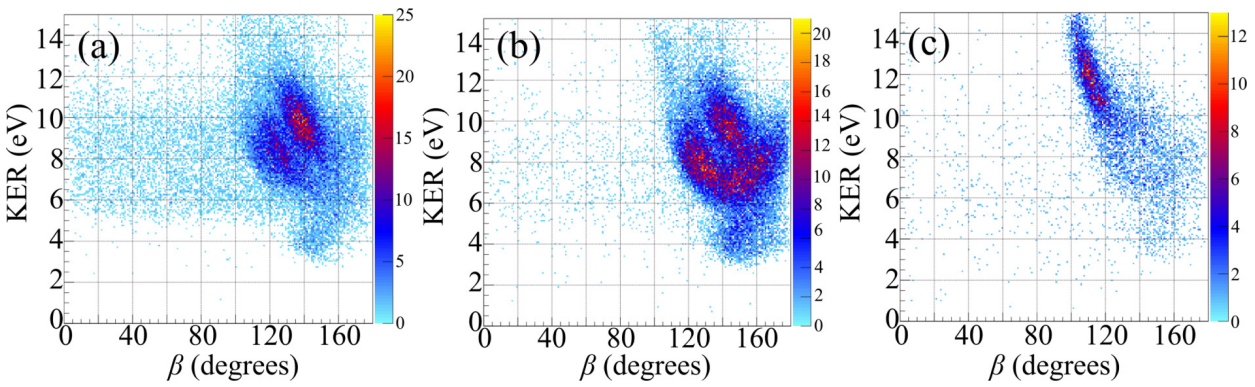


FIGURE 2.3. Nuclear conformation maps, restricted by the total continuum energy as shown in Fig. 2.1(b). (a) Gate I, corresponding to the $O(^3P)$ asymptote. (b) Gate II, corresponding to the $O(^1D)$ asymptote. (c) Gate III, corresponding to the $O(^1S)$ asymptote.

proton coincidence measurements that correspond to all five states of $H_2O^{++}$, which after complete breakup leaves the unmeasured neutral oxygen in the $O(^1D)$ state (namely, the breakup asymptote $O(^1D) + H^+ + H^+$). The crucial fact in this experimental analysis is that the COLTRIMS method is kinematically complete using a single photon. With more photons, or for an experiment that is not kinematically complete where an experimentalist cannot use momentum conservation, gating on the inferred neutral subsystem after Coulombic explosion to gain further insight into the measurement is not feasible. This procedure showcases one of the subtle strengths of the COLTRIMS technique and opens the door for experimental state-selective DPI investigation in a polyatomic molecule for the first time.

### 2.2. Axial-Recoil Approximation

In addition to the nuclear conformation maps, knowledge of the full 3D momentum vectors of each molecular fragment gives us access to another powerful analysis tool. In the COLTRIMS experiment, in the absence of knowledge of the dissociation dynamics, the assumption of the axial recoil approximation can be used to determine the apparent orientation of the molecule at the moment of photoabsorption and thus locate the directions of the ejected electrons in the body-frame. A detailed review of the axial-recoil approximation is given by Wood *et al.* [**119**], but the meaning of "axial recoil" approximation in interpreting momentum coincidence experiments in the case of diatomics is the assumption that the fragments are ejected along the direction of vibration

and that the axis of the molecule does not rotate appreciably before dissociation is complete. Here, for the dissociation of the triatomic water di-cation, strict "axial recoil" dynamics would mean that the two protons are ejected along the bond directions. However, for the purposes of determining the initial orientation of the symmetry axis of the molecule in this case, it suffices that the two protons be ejected symmetrically near the original bond directions.

This orientation for the water di-cation defined under the axial-recoil approximation can be visualized by creating a coordinate system from the measured momentum vectors. Specifically, we define the $z$ axis for the molecular plane as

$$\frac{\vec{P}_{H_1} + \vec{P}_{H_2}}{|\vec{P}_{H_1} + \vec{P}_{H_2}|^2} = \vec{Z}_{COLTRIMS}, \tag{2.1}$$

with $\vec{P}_{H_1}$ and $\vec{P}_{H_2}$ being the momentum vectors for each proton, and $\vec{Z}_{COLTRIMS}$ is the $z$ axis defined in the COLTRIMS experiment, implying the directions of the momenta of the protons are assigned equal angles above and below the $\vec{Z}_{COLTRIMS}$ axis. The $y$ axis is defined as the perpendicular coplanar axis relative to the $\vec{Z}_{COLTRIMS}$ axis. The momentum of the oxygen is deduced by momentum conservation under the assumption of a cold target with no center-of-mass momentum, and thus has the opposite sign for its $z$ component relative to the dissociating protons. To the degree that the dissociation is direct and symmetric, this procedure determines the plane of the molecule and its orientation in that plane for the purposes of coincidence measurements with the ejected electrons.

A plot of the fragment ions, while constraining the positive $z$ axis along a bond is referred to as a Newton plot. Such Newton plots are used to visualize the correlations between the fragment ion momenta in the molecular frame; an application of Newton plots can be found in the work of Ablikim *et al.* [**2**] and Neumann *et al.* [**72**]. In our case of the triatomic water di-cation, constraining the positive $z$ axis as the bisector of the two measured proton fragments, we create Newton-*like* plots. Under the axial-recoil approximation, such plots would reveal the dynamics of the dissociating water di-cation in the rest frame of the molecule. The Newton-like momentum plot, integrated over all water di-cation states, is presented in Fig. 2.4.

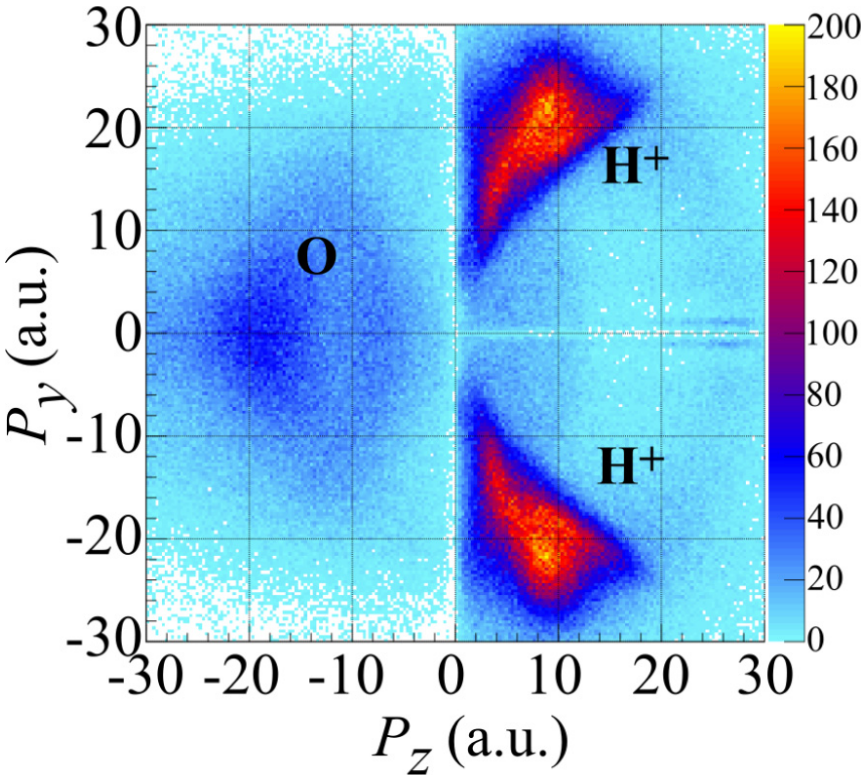


FIGURE 2.4. Newton-like plot of the dissociating water molecule, in the molecule dissociating frame, for the three-body breakup. The horizontal axis is along the sum of the proton unit momenta. Protons are in the first or second quadrants, by definition, while the inferred oxygen momentum is the third or fourth quadrant.

The Newton-like momentum plot shows an image of the original orientation of the water molecule that has smeared out, due to the dynamics of the dissociating fragments, before hitting the detector. This image suggests that the orientation of the water molecule is well defined at the moment of photoabsorption and the protons' dynamics proceed along the bonds defined at the equilibrium geometry. Therefore, the axial-recoil approximation seems valid for this particular set of measurements, and the investigation of electron correlation dynamics with respect to this molecular frame is justified. However, proton dynamics along the bonds where the symmetric and antisymmetric normal modes dictate the majority of the initial dynamics would only produce a Gaussian distribution in the inferred neutral oxygen measurements. In Fig. 2.4 on the interval $-15 < P_y < 15$ and $-10 < P_z < 0$ we see structures that suggest more involved dynamics, where the bending

normal mode could be at play. This non-Gaussian structure in the inferred neutral subsystem is the experimental evidence that calls into question the validity of the axial-recoil approximation.

### 2.3. Challenge to Theorists

Experimental observations of one-photon double-photoionization of heavy water using the COLTRIMS method provided a complete momentum plane picture of the final momenta of the protons after double-photoionization, yielding detailed structures in high fidelity. This picture naturally leads to questions that require theoretical effort. Do the islands of density in the $\beta$ versus KER plots represent particular states of $D_2O^{++}$ and if so can we identify them in order to provide a map of those ionization processes contributing to the observed TDCS? Can we explain the structure in Fig. 2.4 for the inferred neutral oxygen momentum hinted at in the last section, and is the axial-recoil approximation valid? Can we also explain the carpet features presented in the $D_2O^{++}$ nuclear conformation map, Fig. 2.2?

The theoretical approach used here is a semi-classical method reminiscent of the work by Goursaud *et al.* [**40**], where the potential energy surfaces were calculated in full quantum correlation and the dynamics that have initial conditions generated from a Wigner distribution are then propagated by solving Hamilton's equations of motion in phase space and therefore, are treated classical. Using this method for simulating quantum mechanics is not without its faults and a detailed study of the quantum corrections to this semi-classical method was done by Heller [**46**, **47**]. Specifically, this method is assuming the time derivative of a general phase space densities $\Gamma_w(p,q)$ can be expanded in $\hbar$ in the following form given by Heller:

$$\begin{aligned}\frac{\partial \Gamma_w}{\partial t} =& \frac{-\partial H}{\partial p}\frac{\partial \Gamma_w}{\partial q} + \frac{\partial H}{\partial q}\frac{\partial \Gamma_w}{\partial p} \\ & - \frac{\hbar^2}{24}\frac{\partial^3 H}{\partial q^3}\frac{\partial^3 \Gamma_w}{\partial p^3} + \frac{\hbar^4}{1920}\frac{\partial^5 H}{\partial q^5}\frac{\partial^5 \Gamma_w}{\partial p^5} + O(\hbar^6) + \cdots .\end{aligned} \tag{2.2}$$

Here, $H$ is the classical Hamiltonian $H(p,q)$ and we see the first two terms on the right-hand side are just the classical Liouville equation and therefore, as $\hbar \to 0$ the dynamics of $\Gamma_w$ would obey classical mechanics in the semi-classical limit. However, this expansion in $\hbar$ is only valid at high temperatures or for mixed-states. At low temperatures or when $\Gamma_w$ is derived from a highly coherent, pure state, a power series in $\hbar$ maybe invalid. Instead, in these situations the form of $\Gamma_w$ involves $\hbar$ as essential

singularities, and the classical limit applied to Eq. 2.2 is not as straightforward. Albeit our system is cold in the COLTRIMS experimental setup, the Coulombic explosion of a di-cation polyatomic is expected to be well simulated by this semi-classical approach, which leads to a final question for the theorist. Does a detailed theoretical nuclear dynamics analysis of the breakup of the water di-cation using this semi-classical approach agree, to some extent, with the experimental results provided in this chapter and does this theoretical technique provide a blueprint for experimentalist when measuring more complicated cold-target polyatomic molecules in a single-photon COLTRIMS experiment in the future?

CHAPTER 3

# Electronic States of $D_2O^{++}$

## 3.1. Theoretical Background

To begin our explanation of the semi-classical approach used in simulating the nuclear breakup of $D_2O^{++}$, we first review potential energy surfaces, and the approximations assumed here. One important approximation to note is how we addressed the issue of dynamics near a conical intersection. The water di-cation system does have conical intersection but they were found to only play a minor role in the dynamics. Specifically, these conical intersections connect to the $O^+ + H^+ + H$ channel and this channel was measured to be 0.6% of the total COLTRIMS yield. For that reason we construct approximate diabatic states for the electronic states that correlate with neutral oxygen atom (i.e the $O + H^+ + H^+$ channel). Neglecting of these conical intersections by propagation on the diabatic surfaces could potentially give drastically different results than experimental observed. Indeed most photochemistry, like photosynthesis (see Ref. [**74**] as an example) or DNA repair from UV-radiation due to the rapid radiationless population transfer from excited states to the ground state (see Ref. [**91**] as an example), arises from nuclear dynamics through conical intersections on excited molecular hypersurfaces. (See [**89**] for a review of the role of conical intersections in molecular spectroscopy and photoinduced chemical dynamics.) However, our analysis superseded an experiment that showed nuclear dynamics propagated on diabatic surfaces would capture the majority of the observed physics and hence, our motivation for using a diabatic framework.

Next, to further expand on that framework the MOLPRO [**115**, **116**] calculation of the nine potential energy surfaces of water di-cation are presented. The calculations of the first eight states of $D_2O^{++}$ were checked with the calculations performed by Gervais *et al.* [**38**]. Good agreement between the two icMRCI [**16**, **117**] calculations motivated the use of the same level of calculation in generating the $3^1A_1$ potential energy surface not investigated in [**38**]. This led to the discovery of multiple crossings around 8.5 bohr by three high lying excited states that connect to the $O^+ +$

$H^+ + H$ asymptote. A subsequent larger MOLPRO calculation, that will be detailed shortly, was utilized to adequately represent the $O^+ + H^+ + H$ asymptote and allow for calculation of potential energy points that do not correlate with the $O^+ + H^+ + H$ asymptote.

With all nine potential energy surfaces calculated at a high level of correlation, a parameterization in a simple mathematical formula used in [**38**] is presented. The simplicity of this representation of the high dimensional potential energy surfaces allows for fast derivative calculations and, thus large batch jobs of dynamic simulations performed in a reasonable time. This section maybe skipped if the reader prefers to reference Gervais' *et al.* work [**38**], specifically the "APPENDIX: PES FIT" section.

Finally, the $3^1A_1$ state that has a calculated grid of energy points excluding the geometries where the multiple crossing occur is shown to be an approximate diabat once cast onto the representation presented in the last section. Again this decision to obtain at least an approximation of the diabatic surface was motivated by a clean signal in the experiment correlating with leaving the neutral oxygen atom in its $^1S$ state (see Fig. 2.3(c)) and, therefore connecting to the $O + H^+ + H^+$ asymptote.

**3.1.1. The Born-Oppenheimer Approximation.** The molecular Hamiltonian can be written as

$$H = -\sum_i \frac{\nabla^2_{e,i}}{2m} + \sum_{j>i} \frac{e^2}{|r_j - r_i|} - \sum_i \frac{\nabla^2_{N,i}}{2M_i} + \sum_{j>i} \frac{Z_j Z_i e^2}{|R_j - R_i|} - \sum_{ij} \frac{Z_j e^2}{|r_i - R_j|} \tag{3.1}$$

$$H \equiv T_e + V_e + T_N + V_N + V_{eN} \tag{3.2}$$

where we have separated the electronic coordinates $\{r\}$ ($r$-space) from the nuclear coordinates $\{R\}$ ($R$-space). From left to right the terms in Eq. 3.1 are the electron kinetic energy, the electron-electron repulsion, the nuclear kinetic energy, the nuclear-nuclear repulsion, and finally the electron nuclear attraction. The mass of the proton is approximately $2,000$ times heavier than the mass of the electron. This mass difference implies that the correlated ionized electrons will be far removed from the nuclei before the breakup of the deuterium ions occur. Moreover, the nuclear motion of the neutral oxygen atom will be far slower than the electrons' motions. Therefore, this separable

Hamiltonian in Eq. 3.1 is appropriate for modeling the nuclear breakup of heavy water di-cation, $D_2O^{++} \rightarrow O + D^+ + D^+$.

The Schrödinger equation describing the dynamics of our molecule then reads

$$H\Psi(r,R) = (T_N(R) + V_N(R) + H^{el}(r;R))\Psi(r,R) = E\Psi(r,R), \tag{3.3}$$

where we defined the electronic Hamiltonian $H^{el}(r;R) = T_e(r) + V_e(r) + V_{eN}(r;R)$. Within the Born-Oppenheimer approximation $\Psi(r,R)$ is set to be proportional to a single "adiabatic state" that is a solution of the electronic Schrödinger equation for fixed values of the nuclear coordinates

$$H^{el}(r;R)\varphi_n(r;R) = E_n(R)\varphi_n(r;R), \tag{3.4}$$

the semicolon indicates that the electronic Hamiltonian is parametrically dependent on the nuclear coordinates. Then the total wave function in the Born-Oppenheimer approximation is

$$\Psi(r,R) \approx \varphi_n(r;R)\zeta(R). \tag{3.5}$$

where $\zeta(R)$ is the wave function for nuclear motion (vibration and/or reaction) satisfying (for stationary state)

$$H(r,R)\zeta(R) = (T_R + V_N(R) + E_n^{el}(R))\zeta(R) = E\zeta(R) \tag{3.6}$$

in which we recognize the Born-Oppenheimer Hamiltonian for nuclear motion. To arrive at Eq. 3.6 we neglected any derivatives of the Born-Oppenheimer electronic states with respect to R, i.e., we neglected the result of the nuclear Laplacian operating on the electronic wave function, $\nabla_R^2\varphi_n(r;R)$ (called the *scalar coupling term*), and the gradient of the electronic wave function with respect to the nuclear coordinates, $\nabla_R\varphi_n(r;R)$ (called the *derivative coupling term*). Utilizing only one adiabatic state is a good approximation if the other adiabatic states that are within the manifold of solutions to Eq. 3.4 are sufficiently remote in energy to this particular adiabatic state for all nuclear configurations $R$. In summary, the Born-Oppenheimer approximation is the assumption that electrons adjust instantaneously to the slower motion of the nuclei so that the motion of the latter is governed by a single adiabatic potential energy surface.

**3.1.2. Experimentally Motivated Basis.** When two or more adiabatic potential energy surfaces intersect, or pass close to one another, or when nuclear speeds are very high, however, the Born-Oppenheimer approximation breaks down and it becomes necessary to consider more than one surface in the calculation. We can take a finite set of adiabatic states in our sum as follows (for exact equivalence we would take a *complete* adiabatic basis [**11**] and our sum would be $n$ to $\infty$)

$$\Psi(r,R) = \sum_n \varphi_n(r;R)\zeta_n(R) \tag{3.7}$$

and those states will be coupled to each other, so the Schrödinger equation describes nuclear motion occurring on more than one potential surface simultaneously. In Eq. 3.7 the adiabatic electronic state, $\varphi_n(r;R)$, are normalized as functions of the electronic coordinates, r, but the nuclear wave functions are not normalized. They represent the probability amplitude that the system is found in a particular adiabatic electronic state (at a geometry given by $R$), and that probability can be small or zero. Including more than one state in this sum allows the flow of energy between electronic and nuclear motion via the derivative and scalar coupling terms.

Albeit, including more states requires more unknowns (i.e. parameters) to solve the system of linear equations. For example, consider two one-dimensional adiabatic potential energy curves at their crossing (e.g two adiabatic states for a diatomic molecule crossing at a point $R_c$). For this to occur, we must have a diagonalizable Hamiltonian at each point in $R$, and the two diagonal elements must be the same at some nuclear configuration $R_c$ for there to be a crossing. Put in a mathematically way, this means

$$\mathbf{V}^\dagger\mathbf{H}\mathbf{V} = \tilde{\mathbf{H}} = \begin{pmatrix} \tilde{H}_{11}(R) & \tilde{H}_{12}(R) \\ \tilde{H}_{21}(R) & \tilde{H}_{22}(R) \end{pmatrix} = \begin{pmatrix} E_c & 0 \\ 0 & E_c \end{pmatrix},$$

where $E_c$ is the eigenvalue at the crossing point. Since the matrix is Hermitian, that means that two conditions must be simultaneously satisfied

$$\begin{aligned} \tilde{H}_{12}(R) &= \tilde{H}_{21}(R) = 0 \\ \tilde{H}_{11}(R) &= \tilde{H}_{22}(R). \end{aligned} \tag{3.8}$$

Therefore, we have two equations and one unknown degree of freedom, $R$, to determine the crossing-point energy of two adiabatic states. Except for a degeneracy that arises from symmetry conditions where $H_{12}$ vanishes due to orthogonality for all $R$ because the states have different symmetry (e.g. $\Sigma$ and $\Pi$), we cannot in general find a solution where both equations are satisfied by using a single variable $R$. Thus, for this one-dimensional case the two curves will avoid each other. This phenomenon is called an *avoided crossing* [**107**] and it only occurs for diatomic molecules.

If the molecule has two or more degrees of freedom, then the crossing conditions in Eq. 3.8 can be simultaneously satisfied. For example, consider two two-dimensional adiabatic curves, meaning there are two nuclear degrees of freedom, say $X$ and $Y$. Then for a crossing to occur we must satisfy the following:

$$\begin{aligned} \tilde{H}_{12}(X,Y) &= \tilde{H}_{21}(X,Y) = 0 \\ \tilde{H}_{11}(X,Y) &= \tilde{H}_{22}(X,Y). \end{aligned} \tag{3.9}$$

Now we have two equations in two unknowns provided by the molecule's degrees of freedom, which allows for the two curves to cross at a point in the $X$, $Y$ plane. This higher-dimensional point of crossing is called a *conical intersection* (see Refs. [**66**, **96**, **121**] for excellant sources on the subject of conical intersections). In 3D, we use up two degrees of freedom to enforce the conditions in Eq. 3.8, and we find intersections along a line. In general the intersection will be along a "surface" of dimension $N_{vib} - 2$, where $N_{vib}$ is the number of vibrational degrees of freedom. If there are $N$ nuclei, there are $3N - 6$ internal degrees of freedom for our water di-cation molecule after we remove the center of mass and overall rotational degrees of freedom, so the intersection will be on a hypersurface of dimension $3N - 8$ once we account for our crossing constraints in Eq. 3.8.

Nuclear dynamics passing through conical intersections are governed by nonadiabatic matrix elements that are notoriously difficult to calculate (see Refs. [**20**, **102**] as examples). However, the COLTRIMS experiment observed the majority of the physics of the nuclear breakup of $D_2O^{++}$ was performed on the states that were diabatically connected to the O + $H^+$ + $H^+$ channel. Therefore, we chose to run our classical trajectories on the excited electronic states of $D_2O^{++}$ in the *diabatic* basis [**10**] that preserves the symmetry of the electronic wave function in the course of dynamical evolution. Within this representation we assume that the electronic states have no

dependence on the nuclear coordinate $R$ and thus have no nonadiabatic matrix elements that couple the different electronic states. The chose of the diabatic basis that results in ignoring much of the difficulty arising from nonadiabatic transitions was entirely dictated by experimental observations and shouldn't be considered a decision that was made *a priori*.

### 3.2. MOLPRO Calculations

TABLE 3.1. Presented here for reference are the symmetries for the respected point groups and electronic configuration. The diatomic state that correlates with pulling one proton off of the respected triatomic state is also presented. "Config." here means the dominant configuration of $H_2O^{++}$ at the equilibrium geometry of neutral $H_2O$

| $C_s$ sym. | $C_{2v}$ sym. | $C_{2v}$ config. | $OH^+$ |
|---|---|---|---|
| $X^3A''$ | $^3B_1$ | $(3a_1 1b_1)^{-1}$ | $X^3\Sigma^-$ |
| $2^3A''$ | $^3A_2$ | $(1b_2 1b_1)^{-1}$ | $A^3\Pi$ |
| $1^3A'$ | $^3B_2$ | $(1b_2 3a_1)^{-1}$ | $A^3\Pi$ |
| $1^1A'$ | $^1A_1$ | $(1b_1)^{-2}$ | $a^1\Delta$ |
| $1^1A''$ | $^1B_1$ | $(3a_1 1b_1)^{-1}$ | $a^1\Delta$ |
| $2^1A'$ | $^1A_1$ | $(3a_1)^{-2}$ | $b^1\Sigma^+$ |
| $2^1A''$ | $^1A_2$ | $(1b_2 1b_1)^{-1}$ | $^1\Pi$ |
| $3^1A'$ | $^1B_2$ | $(1b_2 3a_1)^{-1}$ | $^1\Pi$ |

There are nine states of $D_2O^{++}$ accessible to a 61 eV photon used in the COLTRIMS experiment. At the equilibrium geometry of $D_2O$, these nine states can be described qualitatively as the states that arise from the removal of two electrons from the highest three molecular orbitals of the Hartree-Fock ground-state electronic configuration, $1a_1^2 2a_1^2 1b_2^2 3a_1^2 1b_1^2$ (see Table. 3.1). In a previous isotope effect study of the breakup channel of the water di-cation into the $H^+ + OH^+$ channel, Gervais *et al.* [**38**] computed potential energy surfaces of the first eight states dissociating to the $^3P$ and $^1D$ states. Those surfaces were calculated on a sophisticated level using internally contracted multireference configuration interaction (icMRCI) methods [**16**, **117**] at the configuration interaction singles and

doubles (CISD) level including Davidson correction to quadruple excitations in order to have better size consistency behavior.

Since our interest is in the three-body breakup of the di-cation, and since the experiment observed all three states of neutral oxygen including the $^1S$ state, we calculated the remaining potential surface for the $3^1A_1$. This calculation was initially similar to that of Gervais, namely it was performed with the MOLPRO [**115**, **116**] suite of quantum chemistry programs using the same icMRCI methods at the configuration interaction singles and doubles (CISD) level including the Davidson correction for quadruple excitations. The Gaussian basis was the cc-pVTZ Dunning correlation consistent basis [**58**], and the MRCI calculations were based on orbitals from complete active-space self-consistent field (CASSCF) calculations on the lowest $^3B_1$ state in $C_s$ symmetry, with one a$'$ orbital frozen and six electrons in the five a$'$ and two a$''$ orbitals. The grid of 4722 geometries consisted of 11 angles from $80^o$ to $180^o$ and values of $R_{OH}$ from 1 to 50 bohr with fine spacings at short distances, which was similar to the energy grid calculation of Gervais for the lower eight states. These two calculations, which gave the nine potential energy surfaces of the water di-cation accessible to the experimental photon energy going to the neutral oxygen asymptotes (O[$^3$P,$^1$D,$^1$S],$H^+$,$H^+$), are shown in Fig. 3.1.

The energies of the three-body asymptotes of the $H_2O^{++}$ ion are given in Fig. 3.2. The lowest three electronic energy terms of the oxygen atom in its ground-state electronic configuration of $1s^22s^22p^4$ are the $^3P$, $^1D$, and $^1S$ levels, whose degenerate components of which (neglecting spin-orbit coupling) comprise three triplet and six singlet states. When combined with two protons, these atomic states correlate with the nine lowest states of the $H_2O^{++}$ di-cation at the equilibrium geometry, as shown in Fig. 3.1. There are thus three energetic asymptotes for the process $D_2O^{++} \rightarrow D^+ + D^+ + O$ for the nine lowest states of the di-cation and are indicated in Fig. 3.1. Additionally, there are low-energy asymptotes of the form $D + D^+ + O^+$ which have the oxygen ion in either its ground state $O^+$ ($^4S$) or in its first excited state $O^+(^2D)$. To calculate these states using MOLPRO, a different CASSCF reference wave function was required. In $C_{2v}$ symmetry, a state averaged CASSCF reference wave function was calculated including the $2^3B_1$ state, the $2^3A_2$ state, and the lowest $^3B_2$ state. In these calculations the orbital basis set included $4a_1$, $2b_1$, and $2b_2$ orbitals with the $1a_1$ orbital always being doubly occupied. The one-electron basis was the aug-cc-pVTZ

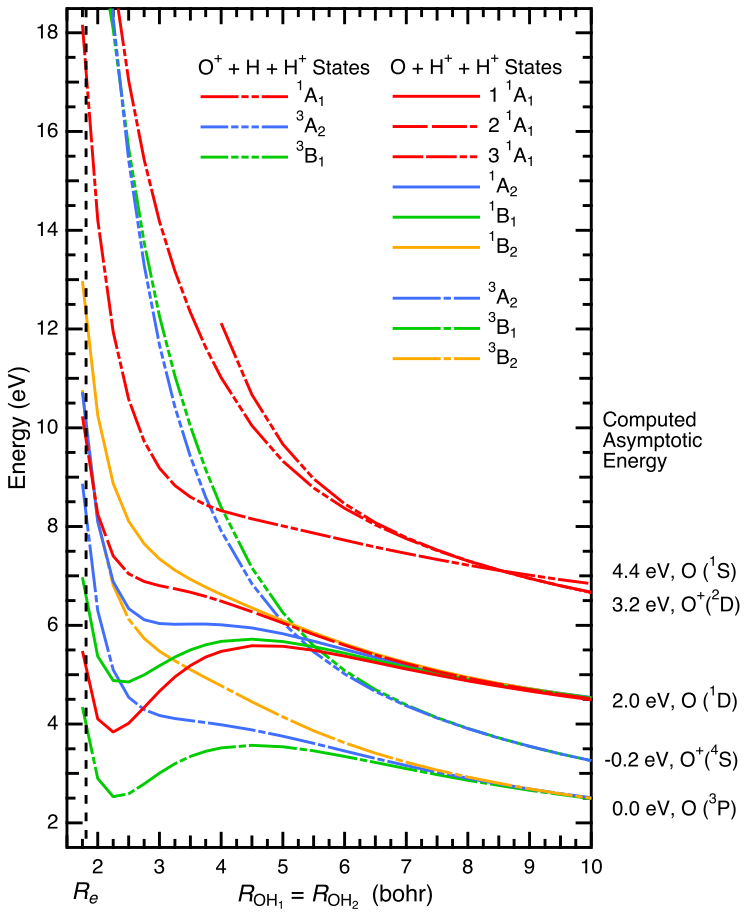


FIGURE 3.1. Potential curves for the symmetric breakup ($\theta_{HOH} = 104.5^o$), $H_2O^{++}$ $\rightarrow$ O + $H^+$ + $H^+$ and $O^+$ + $H^+$ + H from internally contracted multireference configuration interaction (icMRCI) calculations, showing the nine states of the water di-cation that correlate with the valence states of oxygen atom and four of the valence states that correlate with the oxygen atomic ion. The energies given on the right-hand side of the figure indicate the computed asymptotic energies for the three particle breakup with the indicated atomic O state and the H atom, if present, in its ground state. The energies on the vertical on the left and the asymptotic energies on the right are relative to the O($^3P$) + $H^+$ + $H^+$ asymptotic energy.

basis set. This multiconfigurational SCF can represent all of the states going to the (O[$^3$P],$H^+$,$H^+$) and ($O^+$[$^4$S],H,$H^+$) asymptotes, including both neutral and ionized H atom states asymptotically. Using that orbital basis, we did the same icMRCI calculation described before to obtain all the states in Fig. 3.1. Note that at the equilibrium geometry these states $2^3B_1$, $2^3A_2$, and $4^1A_1$ are above the nine states that connect with the $D^+$ + $D^+$ + O asymptotic states. However, as seen

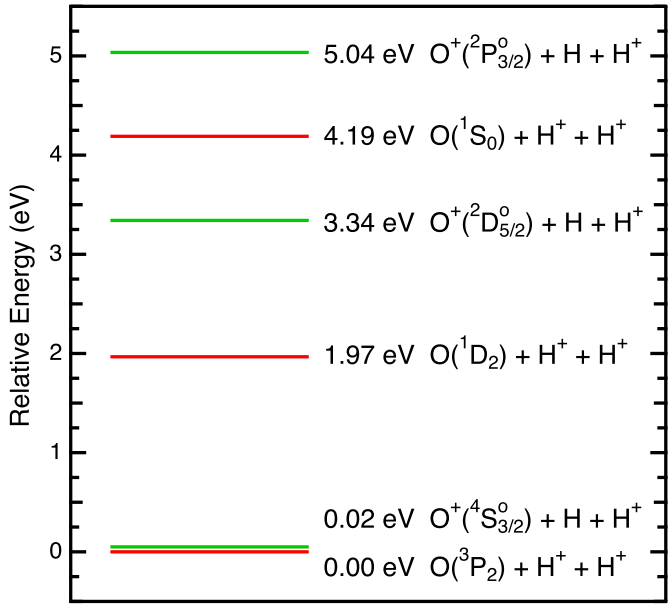


FIGURE 3.2. Experimental energies of the low-energy asymptotes of the three-body breakup of $H_2O^{++}$ relative to the lowest state $O(^3P) + H^+ + H^+$.

in Fig. 3.1, the states leading to $D^+ + D^+ + O(^2D)$ crosses the $3^1A_1$ state of the same symmetry leading to the $D^+ + D^+ + O(^1S)$ asymptote which generates a conical intersection around 8.5 bohr in symmetric stretch at the equilibrium bond angle of $104.5^o$. This conical intersection is in fact part of a full conical intersection *seam* (see Ref. [**69**] for an example), mapped out as the geometry $R$ is explored. These crossings occur at fairly large separations and so the experimental dynamics are believed to propagate on the diabatic energy curve.

Fig. 3.1 suggests that the nuclear dynamics for breakup of the di-cation might be direct, with the two protons dissociating roughly along the OH bonds for some channels, and perhaps surmounting barriers to do so for the others. However these interpretations are only based on *slices* of the potential hypersurfaces and one cannot deduce the full dynamics by this lower dimensional view. To showcase this lack of information in a hypersurface slice we plot the bending curves on the nine surfaces with the OH distances fixed at the equilibrium distance of the neutral (see Fig. 3.3). We can make the simple observation that at the equilibrium geometry the potential surfaces of three of the states, the $^3B_1$, $^1B_1$, and $2^1A_1$, have a strong or significant component of the gradient in

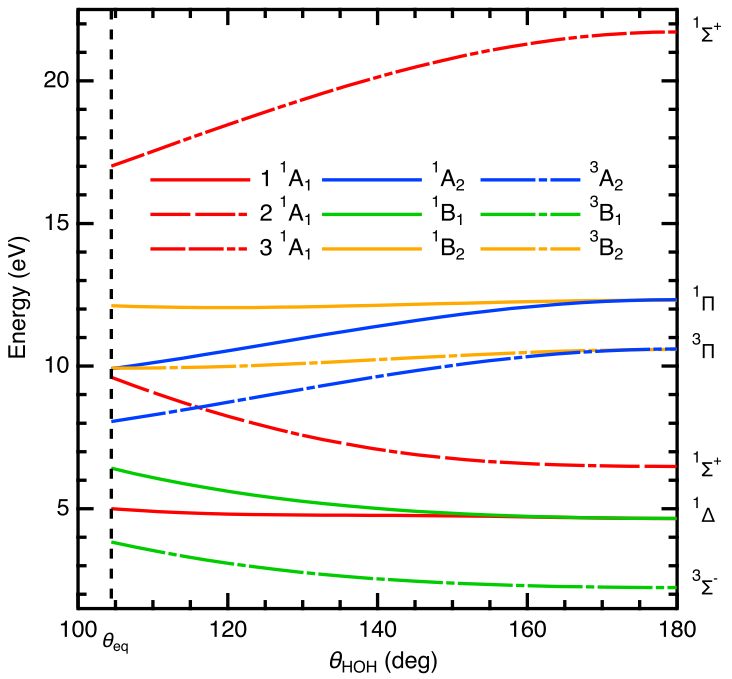


FIGURE 3.3. Potential curves for bending with $R_{OH=1.81}$ bohr from multireference CISD calculations for the nine states of the water di-cation that correlate with the valence states of the oxygen atom (see Fig. 3.1).

the direction of larger bond angles. These large gradients to opening the HOH angle coupled with the gradients to symmetric and antisymmetric stretch will lead to classical trajectories that do not follow the simple argument of direct dissociation gathered from Fig. 3.1, and thus a full dimensional trajectory analysis is the only way to unravel all of the nuclear dynamics. We also note in Fig 3.3 the $1^1A_1$ has virtually no gradient to opening from the equilibrium bond angle of $104.5^o$ to $180^o$. This lack of opening angle gradient coupled with the symmetric stretch barrier leads one to believe that the dynamics of the $1^1A_1$ state will not follow a three-body breakup.

### 3.3. Analytic Fit of $D_2O^{++}$ Potential Energy Surfaces

In order to run classical trajectories on these nine excited states of the water di-cation we need the gradient of these potential energy surfaces, and therefore we need an analytical fit of the triatomic $D_2O^{++}$ as $2D^+ \rightarrow \infty$. An analytical representation of the potential for the full breakup process of $D_2O^{++}$ into the O + $D^+$ + $D^+$ and $OD^+$ + $D^+$ channels was developed by Gervais *et al.* [**38**]; we give a brief summary of the fit here.

The analytical fit of the potential energy surfaces of $D_2O^{++}$ has the form

$$V(R_1, R_2, cos\theta) = \frac{1}{R_1} + \omega_1 + \sum_{n=2}^{5} \omega_n a_n(\alpha_n, R_3) + \sum_{n\geq 6} \omega_n g_n(R_1, R_2) P_{m(n)}(cos\theta), \tag{3.10}$$

where $R_1$ and $R_2$ are the oxygen-protons bond lengths; $R_3 = (R_1^2 + R_2^2 cos\theta)^{1/2}$ is the proton-proton bond length; and $\theta$ is the bending angle of the molecule. The $\omega_1$ offset is the energy of the three states of neutral oxygen, $^3$P, $^1$D, and $^1$S. The functions $P_{m(n)}$ are the Legendre polynomials of degree $m$ associated with $g_n$. The $g_n$ functions change form depending on where on the grid they are evaluated. For example, for the asymptotic part of the grid, these functions are defined as $b_n$ to distinguish them from other parts of the grid and have the form

$$b_1(n, \alpha, R_1, R_2) = y_{\alpha 1}^n + y_{\alpha 2}^n, \tag{3.11}$$

$$b_2(n, \alpha, R_1, R_2) = y_{\alpha 1}^n y_{\alpha 2}^n, \tag{3.12}$$

$$b_3(n, \alpha, R_1, R_2) = y_{\alpha 1}^n y_{\alpha 2}^n + y_{\alpha 1}^n y_{\alpha 2}^n, \tag{3.13}$$

with

$$y_{\alpha i} = \frac{1 - e^{\alpha R_i^2}}{R_i}. \tag{3.14}$$

These radial functions $b_{1,2,3}$ account for long-range behavior. Similar radial functions for middle-range and short-range behavior are presented in Ref. [**38**]. The complete fitting formula contains 100 basis functions and a full list of the functions $g_n$ can be found in "APPENDIX: PES FIT" of Ref. [**38**].

The functions $a_n$ are exponentially screened Coulomb functions with the form

$$a(\alpha, R) = \frac{e^{-\alpha R}}{R}, \tag{3.15}$$

with screening length $\alpha^{-1}$, that gives the correct asymptotic behavior as $OD^+ \rightarrow \infty$. The $\omega_n$ coefficients were adjusted by a standard least-squares fit procedure. With an analytical form of the potential, we can find the force via the gradient and solve Hamilton's equations for new positions and momenta in a time propagation method. The fits are valid for any geometry when $R_{OH} > 1.0$ a.u. and $\theta > 80^o$. The typical deviation of the fit from the *ab initio* calculation is of the order of

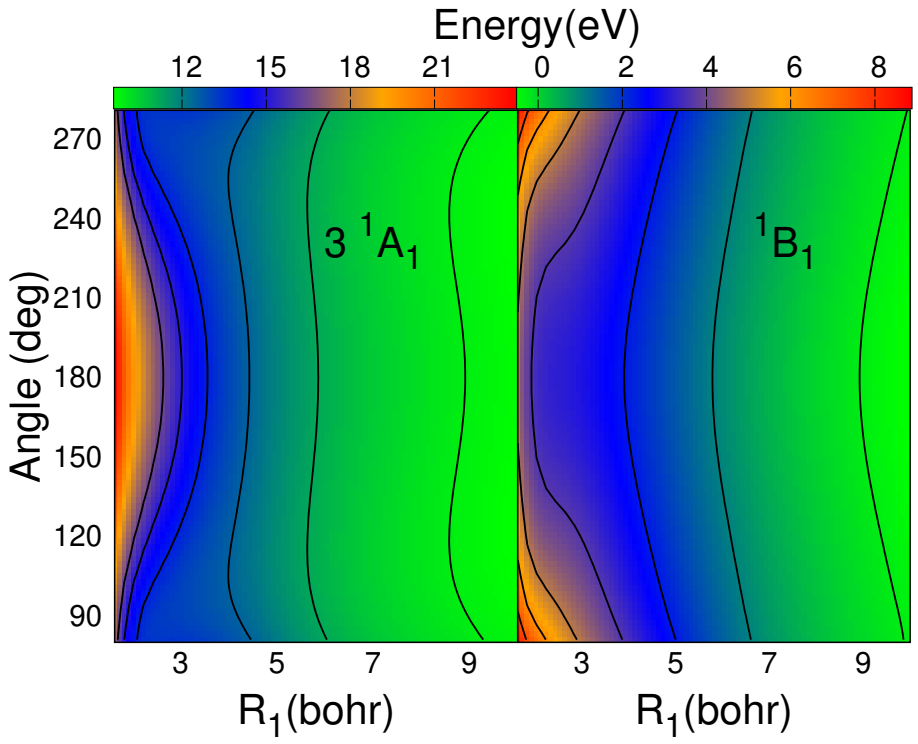


FIGURE 3.4. Analytic fits of the $3^1A_1$ and $^1B_1$ potential surfaces as a function of $R_{OH}$ distance and HOH angle with the other internuclear distance fixed at $R_{OH} =$ 1.81 bohrs

$10^{-3}$ Hartrees, which is less than 1% of the KER values. This simple form for the fitting potential allows one to evaluate analytically the forces, making the computations fast and precise.

### 3.4. Approximate Diabatic Surface for the 3 $^1\mathbf{A}_1$

At the energy scale of the 61 eV photon used in the experiment, which corresponds to 24.3 eV on the energy scale used in Fig. 3.1, the states that are diabatically connected to the $O^+ + H^+ + H$ asymptotes are not energetically accessible. However, we know from the asymptotes, illustrated in Fig. 3.2, that the diabatic states of $^1A'$ symmetry leading the $O^+(^2D^o_{5/2}) + H^+ + H$ must cross the $^1A'$ state (which has $^1A_1$ symmetry in $C_{2v}$ geometries) that is connected to $O(^1S_0) + H^+ + H^+$. Additionally, we can see in Fig. 3.1 that the PESs that correlate to the $O^+(^4S)$ asymptote do not cross any of the lower triplet states correlating to the $^3P$ of neutral oxygen atom. However, the PESs that correlate to the $O^+(^2D)$ asymptote cross the $3^1A_1$ PES at 8.5 bohr in the symmetric stretch dimension. Additional insight into these different PESs is given by considering cuts of the

eight lowest $^1A'$ PESs with fixed $\theta = 100^o$ and constant $R_{OH_1} + R_{OH_2} = 14.75$ a.u. shown in Fig. 3.5. The diabats shown there were constructed by sorting the fixed-nuclei energies into sets that gave the smoothest connected curves. We note that there is an exceedingly small energy splitting found where the states connected to the different asymptotes crossed. The very weak interactions between the diabats is presumablly due to the fact that any such splitting would be caused by the tunneling of an electron from an O atom to a proton at a distance of over 7 bohr.

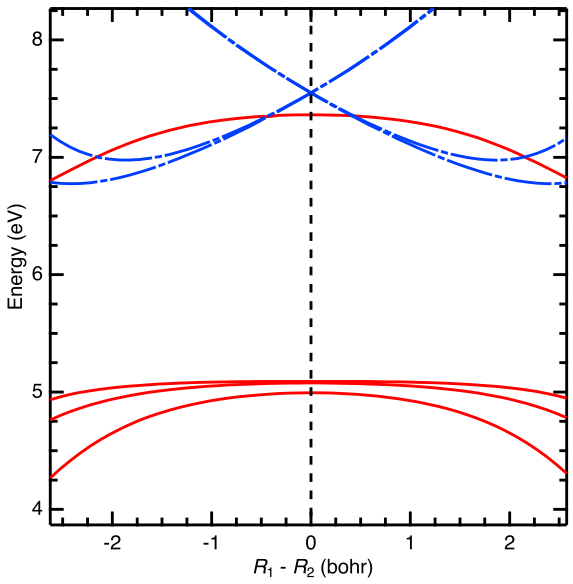


FIGURE 3.5. Cuts through the icMRCI diabatic PESs for the lowest eight A′ states of $H_2O^{++}$ for $\theta = 110^o$ with $R_{OH_1} + R_{OH_2} = 14.74$ bohrs. The solid red lines are for the PESs that diabatically connect to the O + $H^+$ + $H^+$ asymptotes and the dashed blue lines are for the PESs that diabatically connect to the $O^+$ + $H^+$ + H asymptotes.

The choice of a CASSCF reference wave function in the computation of the potential surface for the $3^1A_1$ state used to study the breakup dynamics included only one state, the $^3B_1$ ground state of the di-cation. This reference space could adequately represent states that connect to the O + $H^+$ + $H^+$ asymptote but was insufficient for converging the icMRCI calculations using MOLPRO for states dominated by configurations describing the $O^+$ + $H^+$ + H asymptote. Thus there was a subset of geometries where the icMRCI did not converge to a $3^1A_1$ state with a strong overlap with the reference space. These energy points were left out and a subsequent calculation was performed on the $3^1A_1$ with the same $^3B_1$ reference state, starting with both protons at 20

bohr and stepping towards the equilibrium geometry until the conical intersection was encountered. Müliken analysis [**70**] was used during the calculation to check that indeed all electrons were on the O atom while both protons were at these larger distances. This *stitched grid* potential was then fit using the analytical form of Gervais *et al.* [**38**] and is shown in Fig. 3.6 in contour form.

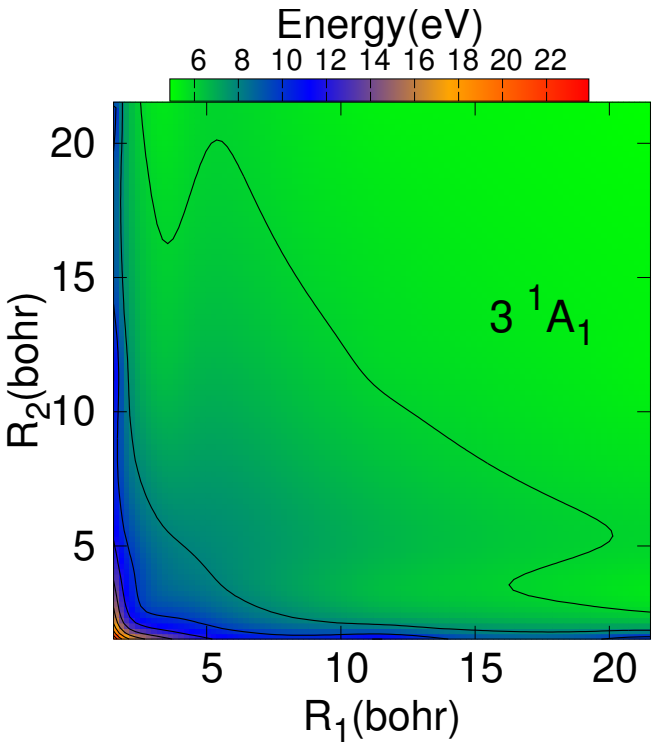


FIGURE 3.6. Stitched grid fit of the $3^1A_1$ surface as a function of $R_{OH}$ distances with $\theta = 104.45^o$ showing the shallow $OH^+$ well.

As seen in Figure. 3.7, the choice of the $^3B_1$ state as the reference wave function coupled with the assumptions made in the fitting procedure of the stitched grid provided an approximate diabat for the $3^1A_1$state. This approximate diabatic surface allowed the calculation of classical trajectories leading to the O + $H^+$ + $H^+$ asymptote, neglecting the effects of small coupling to other states leading to the other arrangements. We observe that the $OH^+$ + $H^+$ asymptote of the potential surface for the $3^1A_1$ ($4^1A'$) state is the $^1\Sigma^+$ state with a dominant configuration $1\sigma^2 1\pi^4 2\sigma^2$ which is not bound but has a barrier to symmetric dissociation, apparent in Fig. 3.6, of about 0.56 eV. None of the simulated classical trajectories in the ensemble were observed to remain trapped behind the barrier.

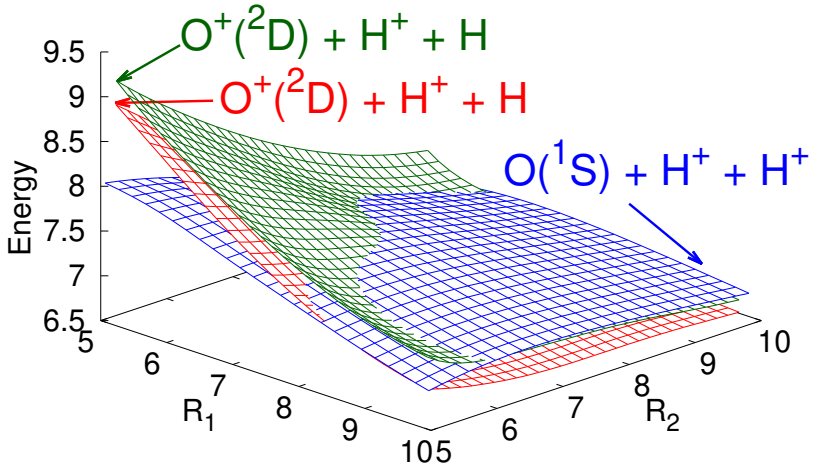


FIGURE 3.7. Calculated PESs in eV as a function of $R_1$(bohr) and $R_2$(bohr) distances with $\theta = 110^o$. The red and green surfaces are the fifth and sixth adiabatic states of $^1A'$ symmetry in the icMRCI calculation based on five states in the SA-CASSCF calculation. The blue surface is the potential that was fit to the converged icMRCI points where the fourth $^1A'$ could be well described as being connected to the O($^1S$) + $H^+$ + $H^+$ asymptote. This approximate diabat for the $3^1A_1$ state passes through the two surfaces that correlate to $O^+(^2D)$ state.

In this chapter, we presented our calculations of the nine states of water di-cation that are energy accessible to a 61 eV photon and generated a fit in full degrees of freedom. This fit gives a differentiable form that allows for fast and accurate simulations of the nuclear breakup process of $D_2O^{++}$ in a time-dicretization scheme. However, the crucial step in solving for this discreet dynamical system is defining the initial conditions that are an accurate representation of the COLTRIMS experiment. Generating initial conditions that represent an accurate mapping to the COLTRIMS experimental target's initial conditions is the topic in the next chapter.

CHAPTER 4

# Wigner Phase Space Method

## 4.1. Theoretical Background

In the COLTRIMS experiment, single molecules of the sample are provided via a gaseous free molecular jet created by supersonic expansion. This expansion produces space for less collisions within the sample, cooling individual molecules. As such, in the COLTRIMS experiment the individual molecule is assumed to be in its ground vibrational state at the moment of photoabsorption. This assumption opens the door for a harmonic approximation treatment of the initial conditions in simulating the nuclear breakup of $D_2O^{++}$ and allows for a semi-classical formulation of the nuclear breakup problem called the Wigner phase space method to be implemented.

Much insight can be gained from attempting to derive the phase space description of quantum mechanics. In 1932, Eugene Wigner sought to find such a derivation by investigating the classical probability of a configuration of quantum particles via the Boltzmann formula $exp[-\beta V]$, where $V$ is the potential at a particular configuration and $\beta$ is the reciprocal temperature $T$ multiplied by the Boltzmann constant [**118**]. At high temperatures $T$, this classical probability is the same in quantum mechanics due to much of the quantum interference structure and quantum coherence effects being quenched by the averaging imposed by high temperatures. This behavior is destroyed at low temperature and a correction term provided from a Taylor series expansion in powers of Plank's constant, $h$, had to be introduced. That approach is the essence of most semi-classical approximations. This work led to an equivalent formulation of quantum mechanics by proposing an anzatz for phase space densities that is a function of both position and momentum. This is called the Wigner distribution, $W(Q, P)$, instead of the traditional view of quantum mechanics where probability amplitudes of either position, $\varphi(x)$, or momentum, $\varphi(p)$, are used. However, due to the uncertainty principle for conjugate variables, one cannot define a probability for a particle that simultaneously has both a well defined position and momentum like the Wigner distribution

$W(Q,P)$ seems to suggest. Put another way, one cannot define a true phase space distribution for a quantum mechanical particle [**50**]. Therefore, the Wigner function is sometimes referred to as a *quasi-distribution*, which will be shown to potentially have negative values, and the quantum mechanical results within the Wigner space method must be interpreted with care.

In this deviation from the Copenhagen interpretation, formulation of quantum mechanics is motivated by an interesting connection between classical and quantum mechanics reminiscent of the correspondence principle. The classical average of an arbitrary function of position and momentum, $A(q,p)$ can be expressed as

$$\langle A\rangle = \int dq \int dp A(q,p)P(q,p), \tag{4.1}$$

where $P(q,p)$ is some phase space distribution function. Now lets say we want the phase space representation of an arbitrary quantum mechanical operator $\hat{A}$. This is given by the Weyl transform (see Case [**15**])

$$A_W(q,p) = \int e^{-\frac{i}{\hbar}pr}\langle q+r/2|\hat{A}|q-r/2\rangle dr. \tag{4.2}$$

The overlap of two such distributions $A_W(q,p)$ and $B_W(q,p)$ is then defined by

$$\begin{aligned}\int\int A_W(q,p)B_W(q,p)dqdp = \\ \int\int\int\int e^{-\frac{i}{\hbar}p(r+r')}\langle q+r/2|\hat{A}|q-r/2\rangle \\ \times\langle q+r'/2|\hat{B}|q-r'/2\rangle dqdpdrdr'.\end{aligned} \tag{4.3}$$

Performing the $p$ integration results in a $\delta$-function that is used in the $r'$ integration resulting in

$$\begin{aligned}\int\int A_W(q,p)B_W(q,p)dqdp &= 2\pi\hbar\int\int\langle q+r/2|\hat{A}|q-r/2\rangle \\ &\quad\times\langle q-r/2|\hat{B}|q+r/2\rangle dqdr.\end{aligned} \tag{4.4}$$

Now we perform a change of variables $u = q - r/2$, $v = q + r/2$, and $dudv = dqdr$, giving

$$\begin{aligned}\int\int A_W(q,p)B_W(q,p)dqdp &= 2\pi\hbar\int\int\langle v|\hat{A}|u\rangle\langle u|\hat{B}|v\rangle dudv \\ &= 2\pi\hbar\mathrm{Tr}[\hat{A}\hat{B}],\end{aligned} \tag{4.5}$$

which shows that the integral over phase space of the product of two Weyl representations of two quantum mechanical operators is given by their trace. Eq. 4.5 is the key relation for showing the form of the equation for a classical average, Eq. 4.1, can resemble the form of an equation for the average of a quantum mechanical observable.

In quantum mechanics the particle is described by a density operator $\hat{\rho}$ and the Wigner anzatz is defined as proportional to the Weyl representation of this particular operator

$$W(q,p) \coloneqq \frac{\rho_W(q,p)}{2\pi\hbar} = \frac{1}{2\pi\hbar}\int dr e^{-ipr/\hbar}\hat{\rho}(q-r,q+r). \tag{4.6}$$

Using Eq. 4.5 with the definition of the Wigner anzatz we have the following relation for the product of an arbitrary quantum mechanical operator with the Wigner function

$$\begin{aligned}\int\int W(q,p)A_W(q,p)dqdp &= \frac{1}{2\pi\hbar}\int\int \rho_W(q,p)A_W(q,p)dqdp \\ &= \mathrm{Tr}(\hat{\rho}\hat{A}) \\ &= \langle A\rangle\end{aligned} \tag{4.7}$$

where the last equality comes from the expectation value of an observable, $A$, corresponding to an operator $\hat{A}$ is the trace of the product of that operator with the density operator $\hat{\rho}$. Eq. **??** expresses quantum mechanical expectation values as phase space integrals via the Wigner function. What we have just shown is that one may cast quantum mechanical results into a form in which they resemble classical ones and this fundamental connection motivated us to cast our investigation of the Coulomb explosion of $D_2O^{++}$ into the Wigner formalism.

The resemblance of Eq. 4.1 with Eq. 4.7 should be interpreted with care. Indeed, if we project this phase space distribution onto one of the conjugate variables, then we obtain the probability distribution for that variable. For example, integration over the momentum distribution gives the position distribution

$$|\varphi(q)|^2 = \int W(q,p)dp, \tag{4.8}$$

and, conversely, integration over the position distribution gives the momentum distributions

$$|\varphi(p)|^2 = \int W(q,p)dq. \tag{4.9}$$

These results would lead one to believe we could interpret the Wigner distribution $W(q,p)$ as a probability distribution on the same footing as the probability amplitudes $\varphi(q)$ and $\varphi(p)$ within a phase space constructed from conjugate variables, but this interpretation is wrong.

To explicitly show why we cannot interpret the Wigner distribution as a probability distribution, consider two density operators, $\hat{\rho_a}$ and $\hat{\rho_b}$ from the respected states $\varphi_a$ and $\varphi_b$. Using Eq. 4.6 for both densities and integrated out both conjugate variables gives

$$\int\int dqdpW_a(q,p)W_b(q,p) = h^{-1}|\langle\varphi_a|\varphi_b\rangle|^2. \tag{4.10}$$

We see the inner product of two Wigner distributions is the square inner product of the respected wave functions with a resolution of Plank's constant, $h$. Requiring that both wave functions be orthogonal makes the right hand side of Eq. 4.10 equal to zero. The only way for the product of two distributions to result in zero is if they destructively interfere with one another. In other words, the Wigner distributions must be allowed to have negative values if we require orthogonality in the wave functions. Therefore, the Wigner function can not be a true probability distribution.

### 4.2. General Formulation of Normal Modes of Vibration for a Polyatomic Molecule

The idea is to cast the ground vibrational state wave function into phase space via the Wigner function, creating a full distribution of position and momentum. However, to reduce the dimensionality of our phase space, we shall not work in Cartesian coordinates of the atoms, but rather in normal coordinates. To describe normal coordinates we start from the definition of the Lagrangian

$$\mathfrak{L} = T - V, \tag{4.11}$$

where $T$ is the kinetic energy term and $V$ is some arbitrary potential. Assuming the potential is approximately harmonic allows us to expand the potential in a Taylor series expansion. This expansion can be further simplified by noting that our molecule is in its equilibrium geometry so the gradient with respect to all the Cartesian coordinates will be zero. Furthermore, we can define $V(x^0) = 0$ and assume any terms higher in order than quadratic are vanishingly small. Therefore

we can write the Lagrangian in a more explicit form

$$\mathfrak{L} = \sum_{i=1}^{3N} \frac{m_i \dot{x}_i^2}{2} - \frac{1}{2} \sum_{i,j=1}^{3N} \frac{\partial^2 V}{\partial x_i \partial x_j} \Delta x_i \Delta x_j. \tag{4.12}$$

where $N$ is the number of atoms in our system; $x_i$ denotes the Cartesian coordinates of the atoms; and $\Delta x_i = (x_i - x_i^0)$, or the Cartesian displacement from equilibrium. If we define the mass weighted coordinates as

$$\eta_i = \sqrt{m_i} \Delta x_i, \tag{4.13}$$

then the Lagrangian takes the form

$$\mathfrak{L} = \frac{1}{2} \dot{\vec{\eta}}^T \cdot \dot{\vec{\eta}} - \frac{1}{2} \vec{\eta}^T \cdot \mathbf{B} \cdot \vec{\eta} \tag{4.14}$$

with the mass weighted Hessian matrix $\mathbf{B}$ denoted by

$$B_{i,j} = \frac{\partial^2 V}{\partial \eta_i \partial \eta_j} = \frac{1}{\sqrt{m_i}\sqrt{m_j}} \frac{\partial^2 V}{\partial x_i \partial x_j}. \tag{4.15}$$

We can diagonalize the Hessian matrix by constructing the orthonormal matrix $\mathbf{L}$ of eigenvectors of $\mathbf{B}$,

$$\mathbf{L}^T \mathbf{B} \mathbf{L} = \mathbf{\Lambda}. \tag{4.16}$$

There will be either $3N - 6$ or $3N - 5$ nonzero eigenvalues $\mathbf{\Lambda_j}$ corresponding to 3 translations and either 3 or 2 rotational degrees of freedom respectively (the latter corresponds to linear molecules that have no rotation about their principal axis). These eigenvalues are in fact the harmonic frequencies defined by $\Lambda_j = \omega_j^2$. We define the normal coordinates $Q_j$ in terms of our mass weighted coordinates as

$$\mathbf{Q} = \mathbf{L}^T \boldsymbol{\eta}, \tag{4.17}$$

and we see each normal mode is a linear combination of Cartesian coordinates of the atoms. With the definition of normal coordinates, we can use our mass weighted coordinates to get the displacements from equilibrium. Multiplying Eq. 4.17 by $\mathbf{L}$, then using Eq. 4.13 and scaling out

the mass gives

$$\begin{aligned} \Delta x_i(t) &= \frac{1}{\sqrt{m_i}} \sum_{j=1}^{3N-6} L_{i,j} Q_j(t) \\ x_i(t) &= x_i^0 + \Delta x_i(t) \end{aligned} \tag{4.18}$$

where $x^0$ is the Cartesian equilibrium geometry and the sum only goes over non-zero eigenvalues. Eq. 4.18 shows how the matrix of orthogonal eigenvectors that diagonalize the Hessian in Eq. 4.16 is the transformation matrix needed to give the displaced Cartesian coordinates in terms of the normal coordinates.

Now we can write Eq. 4.14 in terms of our normal coordinates by using the orthogonality of $\mathbf{L}$ as

$$\begin{aligned} \mathfrak{L} &= \frac{1}{2}\dot{\mathbf{Q}}^T \cdot \dot{\mathbf{Q}} - \frac{1}{2}\mathbf{Q}^T \cdot \boldsymbol{\omega}^2 \cdot \mathbf{Q} \\ &= \frac{1}{2}\sum_{i=1}^{3N} \left( \dot{Q}_i^2 - \omega_i^2 Q_i^2 \right) \end{aligned} \tag{4.19}$$

The Lagrangian equation of motion is now defined by,

$$\frac{d}{dt}\frac{\partial \mathfrak{L}}{\partial \dot{Q}_i} - \frac{\partial \mathfrak{L}}{\partial Q_i} = 0, \tag{4.20}$$

where we note the normal coordinates dictate motion to all the atoms in the system. Eq. 4.20 immediately gives the harmonic equation of motion for each mode,

$$\begin{aligned} &\ddot{Q}_i + \omega_i^2 Q_i = 0 \\ &Q_i(t) = Q_i^{TP} cos(\sqrt{\omega_i^2} t + \delta_i) \end{aligned} \tag{4.21}$$

where $Q_j^{TP}$ denotes the turning point value of the normal coordinate. The classical turning points occur where the kinetic energy is zero and the total potential energy is equal to $(n_i + 1/2)\hbar\omega_i$:

$$\frac{1}{2}\omega_i^2 (Q_i^{TP})^2 = (n_i + 1/2)\hbar\omega_i. \tag{4.22}$$

Solving for the turning point, we have

$$Q_i^{TP} = \sqrt{(2n_i + 1)\hbar/\omega_i}, \tag{4.23}$$

which has units of $\sqrt{\text{mass}} \times$ length.

### 4.3. Wigner Distribution in Normal Coordinates for the Ground State Wavefunction

The crux of our analysis in the last section is in the harmonic approximation for the Taylor series expansion of the potential that led to the form of the Lagrangian in Eq. 4.12. The quantum Hamiltonian analog of this Lagrangian in normal coordinates is

$$\hat{H} = \frac{1}{2}\hat{P}^2 + \frac{\omega^2}{2}Q^2 \tag{4.24}$$

for each normal mode, with $\omega = \sqrt{\Lambda}$, $\hat{P} = -i\hbar\partial/\partial Q$, and $[Q, \hat{P}] = i\hbar$. The eigenvalues are $E_n = (n + 1/2)\hbar\omega$, where $n$ is the quantum number in each normal mode.

In the COLTRIMS experiment, we assume the molecule under investigation is in its ground vibrational state, and therefore the normal modes are sufficiently harmonic in nature and would evolve in time via the harmonic Hamiltonian in Eq. 4.24, absent of any perturbation. The ground vibrational wave functions can be written as,

$$\begin{aligned} \varphi_o(Q) &= \frac{1}{\sqrt{2\pi\hbar}} \int_{-\infty}^{+\infty} e^{iPQ/\hbar} \tilde{\varphi}_o(P) dP = \left(\frac{\omega}{\pi\hbar}\right)^{1/4} e^{-\frac{\omega}{\hbar}Q^2/2}, \\ \varphi_o(P) &= \frac{1}{\sqrt{2\pi\hbar}} \int_{-\infty}^{+\infty} e^{iPQ/\hbar} \tilde{\varphi}_o(Q) dQ = \left(\frac{1}{\omega\pi\hbar}\right)^{1/4} e^{-\frac{1}{\omega\hbar}P^2/2}, \end{aligned} \tag{4.25}$$

where $Q$ and $P$ are the normal mode coordinates for position and momentum, respectively, in one mode and $\tilde{\varphi}$ is the Fourier-transform of $\varphi$. Instructed by Eq. 4.6, we write the Wigner distribution function corresponding to this wave function for a single mode as

$$W(Q, P) = \frac{1}{h} \int_{-\infty}^{+\infty} e^{-PR/\hbar} \varphi_0(Q + R/2) \varphi_0^*(Q - R/2) dR, \tag{4.26}$$

which works out to be

$$W(Q, P) = \frac{1}{\pi\hbar} e^{\frac{\omega}{\hbar}Q^2 - \frac{1}{\hbar\omega}P^2}. \tag{4.27}$$

We can check this form of our Wigner function in normal coordinates by projecting onto either conjugate variable and seeing if Eq. 4.8 and Eq. 4.9 hold:

$$\begin{aligned}\int_{-\infty}^{+\infty} W(Q,P)dP &= \sqrt{\frac{\omega}{\pi\hbar}}e^{-\omega Q^2/\hbar} = |\varphi_0(Q)|^2 \\ \int_{-\infty}^{+\infty} W(Q,P)dQ &= \frac{1}{\sqrt{\pi\hbar\omega}}e^{-P^2/\hbar\omega} = |\tilde{\varphi}_0(P)|^2 \ .\end{aligned} \tag{4.28}$$

Generalizing Eq. 4.27 for all degrees of freedom that a nonlinear polyatomic molecule with $N$ atoms will possess gives the Wigner distribution for the ground vibrational state in all modes corresponding to the classical Lagrangian in Eq. 4.12

$$\boxed{W(\mathbf{Q},\mathbf{P}) = \frac{1}{(\pi\hbar)^{3N-6}}\prod_{j=1}^{3N-6} e^{-\frac{\omega_j}{\hbar}Q_j^2 - \frac{1}{\hbar\omega_j}P_j^2}.} \tag{4.29}$$

This Wigner function is positive-definite for the ground states of all the harmonic modes. For excited-vibration states, the form of the Wigner function will not be positive-definite and will be explored in a later chapter. For each value of $\mathbf{Q}$, $\mathbf{P}$ from sampling this distribution, the corresponding initial values for classical trajectories are provided by the transformation matrix of eigenvectors $\mathbf{L}$ as seen in the previous Section:

$$\begin{aligned}x_i &= x_i^{(0)} + \frac{1}{\sqrt{m_i}}\sum_{j=1}^{3N-6} L_{i,j}Q_j \\ p_i &= \sqrt{m_i}\sum_{j=1}^{3N-6} L_{i,j}P_j.\end{aligned} \tag{4.30}$$

### 4.4. Monte Carlo Metropolis Sampling

We will model the dissociation dynamics from a particular initial vibrational state with classical trajectories instead of propagating the wave packet. To do so we need to sample initial conditions from a distribution corresponding to the initial vibrational state in 3D, which means a 6D phase space average. Given the high-dimensionality of our problem we would like to use a method that builds up an approximation to this high-dimensional object in phase space. We chose a Monte Carlo [**61**, **90**] approach because a random sampling scheme need not increase exponentially with the number of degrees of freedom, $n$, which may lead to a lower computational cost.

The Metropolis algorithm [**68**] is one of the most popular and efficient Markov Chain Monte Carlo sampling schemes. The algorithm pseudocode applied to approximating the ground vibrational state of water in normal coordinates is as follows:

**Algorithm 1** Pseudo code Metropolis Monte Carlo sampling for ground vibrational state of water

**procedure** METROPOLIS($\mathrm{Q}_{old}, \mathrm{P}_{old}, \omega$) ▷ $\omega$ is the ground state frequency for each normal mode
  $count = 0$
  $nsamp = 1000$ ▷ Sample size the user chooses
  $\mathrm{W}_{old} = \mathrm{W}(\mathrm{Q}_{old},\mathrm{P}_{old})$
  **while** $count < nsamp$ **do**
    $stepscale\_Q = 1/\sqrt{\omega}$
    $stepscale\_P = \sqrt{\omega}$
    $Q_{test} = Q_{old} + random(-stepscale\_Q, stepscale\_Q)$
    $P_{test} = P_{old} + random(-stepscale\_P, stepscale\_P)$
    $W_{new} = W(Q_{test}, P_{test})$
    **if** $random(0,1) \leq W_{new}/W_{old}$ **then** ▷ Stepped to a higher probability configuration
      $(Q_{old}, P_{old}) = (Q_{test}, P_{test})$
      $W_{old} = W_{new}$
      $approx\_function = (Q_{old}, P_{old})$
      $++count$
    **else** ▷ Stay at original point
      $approx\_function = (Q_{old}, P_{old})$
      $++count$
  **return** $approx\_function$ ▷ $approx\_function$ is a full list of configurations

This algorithm essentially samples all the configurations of water geometries in phase space as the water molecule jiggles in each normal mode at a frequency $\omega$, and thus approximates our Wigner function from Eq. 4.29. The caller of this subroutine passes in an initial position and momentum of all the atoms for the molecule one would like to build up the phase space distribution, and also the frequencies $\omega$ of the molecule's normal modes. The number of sample points in this pseudo

code example is $nsamp = 1000$, but of course this can be changed for higher accuracy. The initial Wigner function, $W_{old}$, is evaluated at the configuration passed in. Then the **while** loop continues until the number of sample points the user defines is reached via the *count* variable. Next, an interval in position, $stepscale\_Q$, and momentum, $stepscale\_P$, is chosen based on the normal mode frequencies. A random number on this interval is chosen by the pseudo code function *random* thus providing a random walk which is added to the previous position $Q_{old}$ and momentum $P_{old}$ giving a new testing position $Q_{test}$ and momentum $P_{test}$. We then calculate the Wigner function at this new random location in phase space, $W_{new}$. If we step to a higher probability in phase space, we redefine our position in phase space as *old* and save this new configuration into our return array $approx\_function$. If we don't step to a higher probability location in phase space, then we save our configuration into the returning array again and try another random walk step.

### 4.5. Practical Considerations and Interpretations

Using classical trajectories to simulate the nuclear breakup of three bodies can be done in a multitude of ways. The two factors that must be considered with care are the accuracy of the representation of the full potential energy surfaces and how well do the initial conditions mimic the initial vibrational state of the experiment. In the previous chapter, we dealt with the accuracy of the potential from the equilibrium geometry towards asymptotic configurations, and in this chapter we provide a gold standard approach to generating initial conditions (if one can afford some approximations). Under the harmonic approximation, the Hamiltonian is separable into functions of momenta and positions, $H(Q,P) = T(P)+U(Q)$ (see Eq. 4.24). This is fundamentally because the ground vibrational state used to generate the Wigner distribution does not contain nodes – that is this particular Wigner distribution $W_0(\mathbf{Q},\mathbf{P})$ is positive definite everywhere. To be more explicit, for $N$ Metropolis sample points our statistical energy observable can be written in a general form as

(4.31)
$$\langle H\rangle = \frac{\int H(\mathbf{Q},\mathbf{P})W_0(\mathbf{Q},\mathbf{P})d^3Q\,d^3P}{\int W_0(\mathbf{Q},\mathbf{P})d^3Q\,d^3P} = \frac{1}{N}\sum_i H(\mathbf{Q}_i,\mathbf{P}_i) \text{ with } \mathbf{Q}_i,\mathbf{P}_i \in \text{ Metropolis sample.}$$

For Eq. 4.31 to have the same form as Eq. **??**, the Wigner distribution must be normalized to 1 like a true probability distribution, and for the special case of a Wigner distribution constructed

from a ground vibrational state this normalization is indeed the case:

$$\int W_0(\mathbf{Q},\mathbf{P}) d^3Q\, d^3P = 1, \tag{4.32}$$

which gives

$$\begin{aligned} \langle H \rangle &= \int H(\mathbf{Q},\mathbf{P}) W_0(\mathbf{Q},\mathbf{P}) d^3Q\, d^3P \\ &= \frac{1}{N} \sum_i H(\mathbf{Q}_i,\mathbf{P}_i) W_0(\mathbf{Q},\mathbf{P}) \text{ with } \mathbf{Q}_i,\mathbf{P}_i \in \text{ Metropolis sample.} \end{aligned} \tag{4.33}$$

Thus, our analysis of the Wigner phase space method within the harmonic approximation, only using the ground vibrational state, allows for complete classical analysis and interpretation. In other words, we are afforded propagation of this particular Wigner distribution as though it were a classical phase space distribution where Liouville's theorem would apply.

Also, a computational benefit of using the harmonic approximation that leads to a Hamiltonian of the form in Eq. 4.24 is that the analytical form of the eigenvalues allows for checking the average of the Hamiltonian via

(4.34)

$$\langle H \rangle = \frac{1}{N_{sample}} \sum_i H(\mathbf{Q}_i,\mathbf{P}_i) W_0(\mathbf{Q},\mathbf{P}) \approx \sum_{i=1}^{3N_{atoms}-6} \frac{\hbar\omega_i}{2}, \text{ with } \mathbf{Q}_i,\mathbf{P}_i \in \text{ Metropolis sample.}$$

Following Von Neumann's mean ergodic theorem for unitary operators [**71**], if the Markov chain is uniformly ergodic, for which the central limit theorem holds, convergence to equality is provided by increasing sample size $N_{sample}$ of the Wigner distribution, $W(\mathbf{Q},\mathbf{P})$. (Note: Eq 4.34 is looking at the ground vibrational state energy observable, so $n = 0$ in the analytic energy formula.) This is of practical interest because fewer sample points in the Wigner distribution can save on computational cost and still may agree with experiment within graphical accuracy.

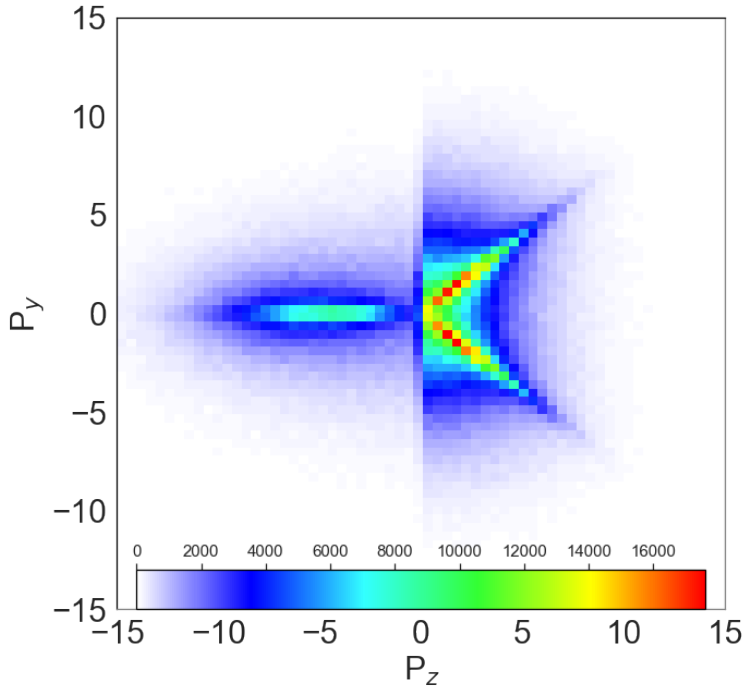


FIGURE 4.1. Wigner distribution of the 3 normal modes of neutral water projected onto the momentum space plotted using the axial-recoil approximation. This distribution was generated from sampling Eq. 4.29 in a Metropolis Monte Carlo scheme laid out in the previous section. The higher density along the O-D bonds is from 2 out of the 3 normal modes motion is along this bond, the symmetric and antisymmetric modes. The fanning distribution off the bonds is from the bending mode.

This statistically constructed, ground state Wigner distribution $W_0(\mathbf{Q}, \mathbf{P})$ projected onto the momentum axis is presented in Fig. 4.1. This distribution was constructed with a million sample points in phase space and resulted in an accuracy of $10^{-6}$ Hartrees using Eq. 4.34. Here we used the normal modes from a CASSCF calculation of neutral $D_2O$ using the same CAS choice and basis as in the calculation on the excited state ions. The calculated normal-mode frequencies were $1238.75cm^{-1}$ (bend), $2712.82cm^{-1}$ (symmetric stretch) and $2839.92cm^{-1}$ (antisymmetric stretch). National Institute of StaStandards and Technology (NIST) listed $D_2O$ normal mode frequencies as $1178.33cm^{-1}$ (bend), $2671.46cm^{-1}$ (symmetric stretch) and $2788.05cm^{-1}$ (antisymmetric stretch) [**95**]. Also the product of the three normal modes in the ground vibrational wave function is seen in the density profile, Fig. 4.1. The product of the two symmetric and antisymmetric stretch modes produces high counts along the O-H bond but multiplying by the bending mode

gives lower counts fanning out from these high count regions. Conventionally, the principle axis of symmetry would be along the $P_y$ axis, which implies the symmetries of the bend and symmetric stretch modes are $A_1$ and the symmetry of the antisymmetric stretch mode is $B_2$.

This chapter generated initial conditions that represent an accurate mapping to the initial conditions assumed the target water molecule in the COLTRIMS apparatus obtains after supersonic expansion. With our initial conditions rigoursly defined in such a way and all nine potential energy surfaces calculated and fitted (see Chapter 2), we are ready to propagate our nuclei on the nine states of water di-cation.

CHAPTER 5

# Classical Trajectories

## 5.1. Theoretical Background

There are multiple semi-classical and *ab initio* approaches that calculate nuclear dynamics of an electronically excited molecule. Most of these methods are either mathematically or conceptually built from Eric Heller's foundational work [**44**, **45**, **48**, **49**]. In Ehrenfest dynamics, the classical nuclei propagator is built from a mean-field potential energy (see Refs. [**28**, **65**] as examples of this technique). Another popular approach is *trajectory surface hopping* (TSH), which represents the dynamics of a nuclear wavepacket by a swarm of independent classical trajectories that are able to "hop" between electronic surfaces in regions of high nonadiabaticity dictated by some hopping criteria (see Ref. [**103**] as an example of this technique). A method that must be mentioned is the *Ab Initio* Multiple Spawning (AIMS) methods developed by Todd Martínez *et al.* [**7**, **8**] that utilize a basis of frozen multidimensional Gaussian functions which evolve according to Hamilton's equations of motion.

The method described in this dissertation is not as elegant as these tools but does allow for massive parallel batch jobs, providing higher statistics that are crucial for comparing with experiments that have $\approx 10^7$ measurements that esatblish a distribution of final momenta of the fragments. The method used for simulating the nuclear breakup of $D_2O^{++}$ measured in the COLTRIMS experiment is as follows:

- Step 1: Generate a representation that is differentiable for all the potential energy surfaces that will be energetically accessible in the experiment. This step was described in Chapter 3.
- Step 2: Generate a distribution of initial position and momenta that simulate the assumed initial conditions in the experiment. This step was described in Chapter 4.

- Step 3: Run many trajectories where each trajectory is produced by solving Hamilton's classical equations of motion to propagate the Wigner distribution in phase space with respect to the potential defined in step 1, using any time discretization method (like fourth order Runge-Kutta [**63**, **82**]). This step is the topic of this chapter.

Understanding how the Wigner distribution evolves in time naturally begins with the Wigner function, Eq. 4.26, time derivative

$$\frac{\partial W}{\partial t} = \frac{1}{h}\int e^{-ipr/\hbar}\Big[\frac{\partial \varphi^*(q-r/2)}{\partial t}\varphi(q+r/2) + \varphi^*(q-r/2)\frac{\partial \varphi(q+r/2)}{\partial t}\Big]dr, \tag{5.1}$$

where $q$ and $p$ are general position and momentum coordinates. The partial derivatives of the wave function with respect to time is given by the time-dependent Schrödinger equation

$$\frac{\partial \varphi(q,t)}{\partial t} = -\frac{\hbar}{2im}\frac{\partial^2 \varphi(q,t)}{\partial q^2} + \frac{1}{i\hbar}U(q)\varphi(q,t). \tag{5.2}$$

Plugging Eq. 5.2 into Eq. 5.1 we have

$$\begin{aligned}\frac{\partial W}{\partial t} = \frac{1}{4\pi i m}\int e^{-ipr/\hbar}\Big[\frac{\partial^2 \varphi^*(q-r/2)}{\partial q^2}\varphi(q+r/2) - \varphi^*(q-r/2)\frac{\partial^2 \varphi(q+r/2)}{\partial q^2}\Big]dr \\ + \frac{2\pi}{ih^2}\int e^{-ipr/\hbar}\Big[U(q+r/2) - U(q-r/2)\Big]\varphi^*(q-r/2)\varphi(q+r/2)dr.\end{aligned} \tag{5.3}$$

We can write this equation in a more suggestive way following Case [**15**]

$$\begin{aligned}\frac{\partial W}{\partial t} &= \frac{\partial W_T}{\partial t} + \frac{\partial W_U}{\partial t} \\ &= -\frac{p}{m}\frac{\partial W(q,p)}{\partial q} + \sum_{s=0}(-\hbar^2)^s \frac{1}{(2s+1)!}\big(\frac{1}{2}\big)^{2s}\frac{\partial^{2s+1}U(q)}{\partial q^{2s+1}} \times \big(\frac{\partial}{\partial p}\big)^{2s+1}W(q,p),\end{aligned} \tag{5.4}$$

where the $\frac{\partial W_T}{\partial t}$ term is derived by integration by parts; and the $\frac{\partial W_U}{\partial t}$ term is derived under the assumption that the potential $U(q)$ can be expanded in a Taylor series (modified to be expanded in terms of angular momentum $s$). Eq. 5.4 is the phase space analog to the time-dependent Schrödinger equation, Eq. 5.2. The term arising from the kinetic energy has no $\hbar$ dependence and is therefore purely classical. The $\hbar$ dependence – and therefore the quantum behavior in phase space – arises solely from the higher spatial derivatives of the potential $U(q)$ beyound its gradient. For our vibrational analysis, using the harmonic approximation, spatial derivatives of $U(q)$ higher than

second order are zero and the second term in Eq. 5.4 becomes

$$\frac{\partial W_U}{\partial t} = \frac{\partial U}{\partial q}\frac{\partial W(q,p)}{\partial p}. \tag{5.5}$$

Thus by generating our Wigner distribution using normal coordinates of the ground-vibration state within the harmonic approximation, we also produced a distribution that evolves according to the classical Liouville equation

$$\frac{\partial W}{\partial t} = -\frac{p}{m}\frac{\partial W(q,p)}{\partial q} + \frac{\partial U}{\partial q}\frac{\partial W(q,p)}{\partial p}. \tag{5.6}$$

In other words, our Wigner distribution will evolve in time exactly like a classical physical system and the individual particles' motion is governed by Hamilton's equations

$$\dot{q} = \frac{\partial H}{\partial p}, \qquad \dot{p} = -\frac{\partial H}{\partial q}, \tag{5.7}$$

with $\dot{q}$ and $\dot{p}$ are the time derivative of position and momentum respectively. These equations are solved by a stable time discretized scheme, namely the fourth order Runge-Kutta scheme.

**5.1.1. Vertical-Transition.** The probability that a ground state wave function is connected to an excited state via the electric dipole operator $\boldsymbol{\mu_e}$ can be expressed as

$$\langle \psi' | \boldsymbol{\mu_e} | \psi \rangle = \langle \varphi_e' \varphi_v' \varphi_s' | \boldsymbol{\mu_e} | \varphi_e \varphi_v \varphi_s \rangle = \int \varphi_e^{*\prime} \varphi_v^{*\prime} \varphi_s^{*\prime} \boldsymbol{\mu_e} \varphi_e \varphi_v \varphi_s \boldsymbol{d\tau} \tag{5.8}$$

where the wave function $\psi$ is decomposed into a product of electronic, vibrational, and spin eigenfunctions. As reviewed in Chapter 3, the electronic wave function is parametrically dependent on the nuclear coordinates. If the transition dipole moment for the coupling of two electronic states by a weak external field is roughly independent of nuclear coordinates over the extent of the initial wave function, then we may factor off the vibrational integral and write

$$\int \varphi_e^{*\prime} \varphi_v^{*\prime} \varphi_s^{*\prime} \boldsymbol{\mu_e} \varphi_e \varphi_v \varphi_s \boldsymbol{d\tau_v} \boldsymbol{d\tau_e} \boldsymbol{d\tau_s} \approx \int \varphi_v^{*\prime} \varphi_v \boldsymbol{d\tau_v} \int \varphi_e^{*\prime} \boldsymbol{\mu_e} \varphi_e \boldsymbol{d\tau_e} \int \varphi_s^{*\prime} \varphi_s \boldsymbol{d\tau_s}. \tag{5.9}$$

The first integral is called the *Franck-Condon factor* which is interpreted as that the initial vibrational wave function is simply "vertically lifted" onto the excited state potential energy surface (for a review, see [**25**]). The electronic integral connected by the electronic dipole operator is non-zero

based on dipole selection rules, and the spin overlap integral is also non-zero if the spin states are the same.

### 5.2. Propagation of Trajectories

The initial conditions of each trajectory for the nuclear breakup of $D_2O^{++}$ is provided by the Wigner distribution constructed from the ground vibrational state of neutral water. Put another way, we assume a vertical transition of the initial configurations of the neutral ground state of water onto each of the nine electronic states of $D_2O^{++}$. This assumption is depicted in Fig 5.1 by the vertical shaded grey section, indicating the extent of the Franck-Condon region. Therefore, the entire Wigner distribution built from the neutral water ground state is the set of initial conditions for the classical trajectories on each excited state. As such, this ensemble of initial conditions provides a classical approximation to the quantum dissociation dynamics initiated by an electronic transition to the double continuum governed by the Franck-Condon approximation, and no modulation of the population on the excited state arising from the cross-section magnitude is considered. This lack of consideration of each excited state's photoionization cross-section leads to theoretical results of the nuclear dynamics that are entirely dictated by the initial conditions within the harmonic approximation for the initial state and the topology of the nine excited states of $D_2O^{++}$. The initial classical trajectory simulation was for $1,000$ trajectories, implemented in a serial code. As mentioned earlier, this method for simulating the nuclear breakup of $D_2O^{++}$ is ideal for massive parallel calculations and later versions of the code were implemented to run in parallel using MPI [**21**]. This version of the code decomposed the domain of initial conditions in the Winger ensemble to multiple processors. Once a subset of trajectories defined by their unique initial conditions were mapped to multiple processors, the trajectories were all run locally on each processor, and therefore the problem was *embarrassingly parallel*, submitting batch jobs up to $1,000,000$ trajectories while finishing in a comparable time to the initial serial batch size of $1,000$.

The two channels considered in this classical trajectory analysis were

$$\begin{aligned} &D_2O^{++} + h\nu \rightarrow OD^+ + D^+ \qquad \text{2-body channel} \\ &D_2O^{++} + h\nu \rightarrow O + D^+ + D^+ \qquad \text{3-body channel.} \end{aligned} \tag{5.10}$$

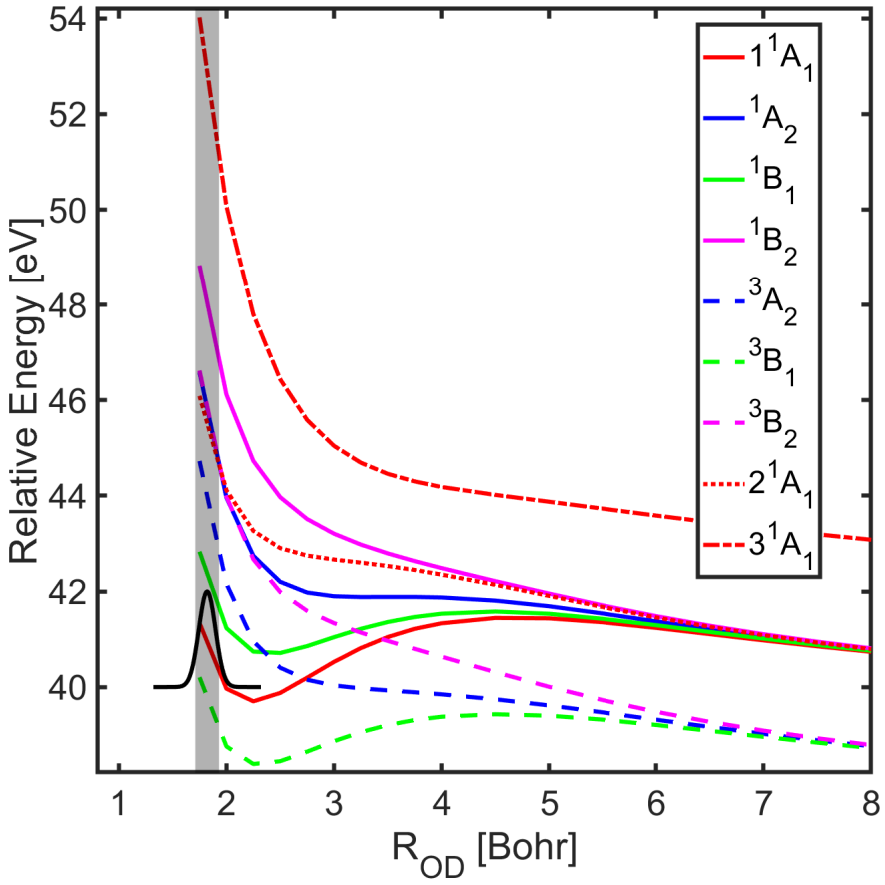


FIGURE 5.1. Potential energy curves for the first nine states of $D_2O^{++}$ as a function of the symmetric-stretch coordinate, together with the neutral ground state wave function (solid black line). The vertical shaded grey line illustrates the extent of the ground state wave function or in other words, the extent of the Franck-Condon region. The zero of energy is the minimum of the ground state potential at the equilibrium geometry.

Initial investigation into the dynamics showed a clear separation between these two channels for all states. If a deuterium ions' trajectory on any state reached 10 bohr away from the oxygen atom, then that deuterium ion would not return to the oxygen atom as the dynamics of the 2-body diatom $OD^+$ would follow. This cut off of $R_{OH} = 10$ bohr was initially used in the post selection of three- and two-body trajectories with later analyses having much larger criteria for categorizing a trajectory as three-body, and with the $R_{OH}$ distance of one proton being 200 bohrs or greater than that of the other reaching at least 50 bohrs. The longer distances used for the criterion to separate

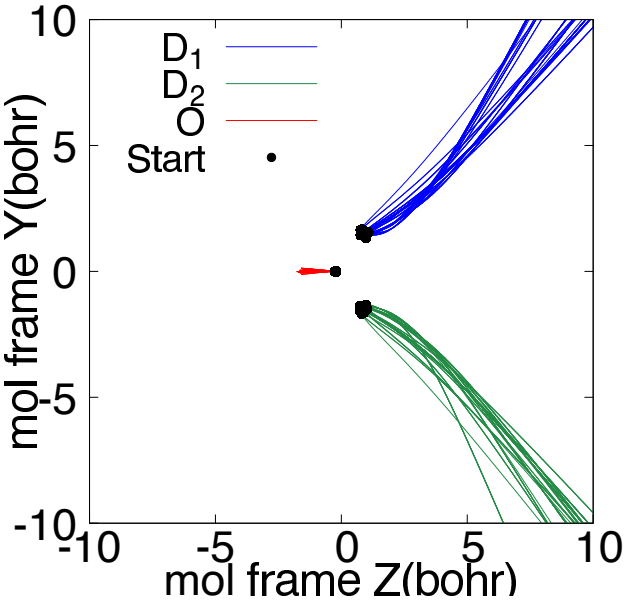


FIGURE 5.2. 60 classical trajectories of direct breakup of $D_2O^{++}$ plotted with respect to the *molecular frame*. These trajectories are referred to as direct because the $D^+$ ions trajectory path is approximately along the original bond of the water molecule.

two-body from three-body dissociation channels are chosen because the diatomic fragments can be produced with vibrational excitation near their dissociation limits. High vibrational and rotational excitation in the products produced by dynamics on several of the potential surfaces is discussed by Gervais *et al.* [**38**] who compute the internal energy distributions of the diatomic fragments in the two-body channels. Resulting three-body branching ratios for $1,000$ trajectories are tabulated in Table 5.1. These branching ratios clearly reflect the slopes in the Walsh diagram, Fig. 3.3, with the two-body trajectories following the states that are downhill to opening and the three-body channels follow the states that are uphill to opening. This pattern illustrates the pitfalls in PES slice interpretation, and the need for full dimensionality trajectory analysis. Looking at the symmetric stretch of $R_{\mathrm{OH}^+}$ in Fig. 3.1, one would be lead to think the $2^1A_2$ state, for example, breaks up following the symmetric stretch mode and this would be incorrect. Only when utilizing the full dimensional hypersurface does one see that this state has a larger gradient to opening relative to symmetric-stretch gradient and, thus proceeding along a more elaborate trajectory.

The purpose of this chapter was to inform the reader of the general procedure used in this thesis for simulating the nuclear dynamics of the water di-cation breakup process. For example, this work

TABLE 5.1. Branching ratios for three-body breakup channel from ensembles of 1000 classical trajectories with initial conditions sampled from the Wigner distribution of the initial neutral state.

| $D_2O^{++}$ Electronic state | % Three-body $O + 2\ D^+$ |
|---|---|
| $^3B_1$ | 7.6 |
| $1^1A_1$ | 1.6 |
| $^1B_1$ | 15.4 |
| $2^1A_1$ | 67.5 |
| $^3A_2$ | 100 |
| $^3B_2$ | 99.8 |
| $^1A_2$ | 99.6 |
| $^1B_2$ | 99.1 |
| $3^1A_1$ | 100 |

used the fourth-order Runge-Kutta time-discretization scheme for solving Hamilton's equations of motion. As noted before, this semi-classical technique of generating all the potential energy surfaces in full degrees-of-freedom and then classically propagating on a fit of each hypersurface using initial conditions that are justified by the experiemental setup, allowes for embarrassingly parallel jobs to be run that are necessary when comparing with experiments that have tens of millions of mesurements and therefore produce a complete distribution of final momenta. We only present the resulting branching ratios in Table 5.1 and other qualitative observations of the simulations in this chapter. In the next chapters, these simulations are compared with the COLTIMS results.

CHAPTER 6

# Direct Breakup

## 6.1. State Selective Measurement

We start our classical trajectory analysis with the three-body channel, $D_2O^{++} + h\nu \rightarrow O + D^+ + D^+$. The theoretical results of kinetic energy release (KER, the sum of kinetic energies of the atomic fragments) versus the angle $\beta$ between the two momenta vectors of the deuterium ions for all 8 states of $D_2O^{++}$experimentally observed, are presented in Fig. 6.1. Comparing this theoretical figure with its experimental counterpart, in Fig. 2.2, a glaring difference is immediately clear. The carpet of uniform angles on the interval of about $5.5 - 10$ eV KER in Fig. 2.2 is absent from Fig. 6.1. These experimental measurements are from an indirect three-body breakup process that will be explored in the following chapter. Therefore, the islands of high density here and in the experimental observation followed a *direct* three-body breakup channel where the $\beta$ angle is defined. In other words, no intermediate steps where involved in the production of the observed fragments that produced these islands of higher density in Fig. 6.1.

As explained in Chapter 2 (see Ref. [**80**]), the experimental data can be separated by the final electronic state of the oxygen atom, since the two proton are observed in coincidence with the two electrons, and since the sum of these kinetic energies distinguishes the electronic state of the oxygen fragment. The experimental results analyzed in that way are shown in the lower row of Fig. 6.2 as a density plot that represents a histogram of coincidence counts. In the upper panel, the asymptotic values for the kinetic energy release and angle between the proton momenta for the classical trajectories surviving into the three-body breakup channel are plotted as individual points.

The classical trajectory results in Fig. 6.2 show that the correlation between KER and $H^+$– $H^+(D^+ – D^+)$ angles can be used to identify initial states of the $H_2O^{++}$ ($D_2O^{++}$) ions that dominate in various regions of the plot. The agreement between the experimental and theoretical distributions

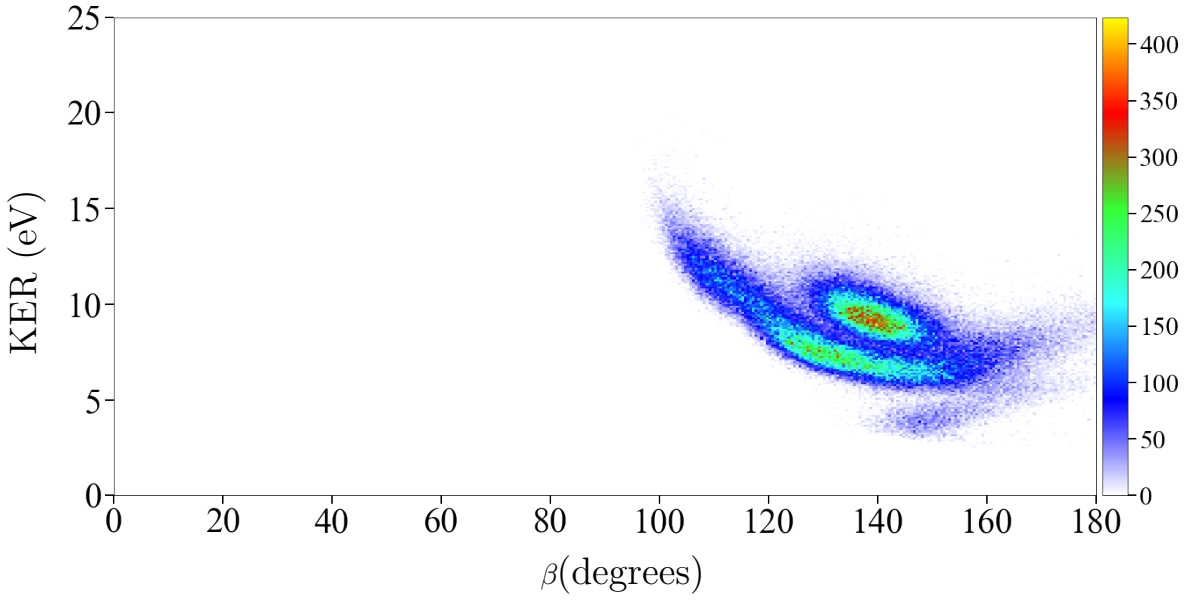


FIGURE 6.1. Theoretical $\beta$ Vs. KER density plot of $100,000$ trajectories for all states for the three-body breakup channel. Comparing this figure with the experimental $\beta$ Vs. KER, Fig. 2.2, the carpet of uniform angles is completely absent indicating the islands of higher density in Fig. 2.2 are the direct three-body breakup channel, $D_2O^{++} \rightarrow O^* + D^+ + D^+$

in that figure demonstrates that this correlation can be used to perform the same identification in other experiments in which the photoelectrons are observed in coincidence with the protons. For the purposes of measuring the TDCS for double-photoionization, this analysis is key to the determination of which electronic state of the di-cation produced the two electrons measured in coincidence with the protons. In particular, an accounting of where all of the energy deposited by the photon ends up (in electron kinetic energy, fragment kinetic energy, or internal energy like excited states of the oxygen atom). There appears to be considerable correlation between the intensities of the features in the experimental observation and the density of classical trajectories in the upper panels of Fig. 6.2. However, the relative numbers of classical trajectories in each of the features is determined by the branching ratios to produce the three-body channel on each di-cation potential surface. Only if the total double-photoionization cross-sections were approximately the same in magnitude for all of the states would one expect the classical trajectories alone to predict the relative intensities of the experimental features. Otherwise, it would be necessary to weight the classical trajectory intensities by the relative cross-sections for double ionization to produce their

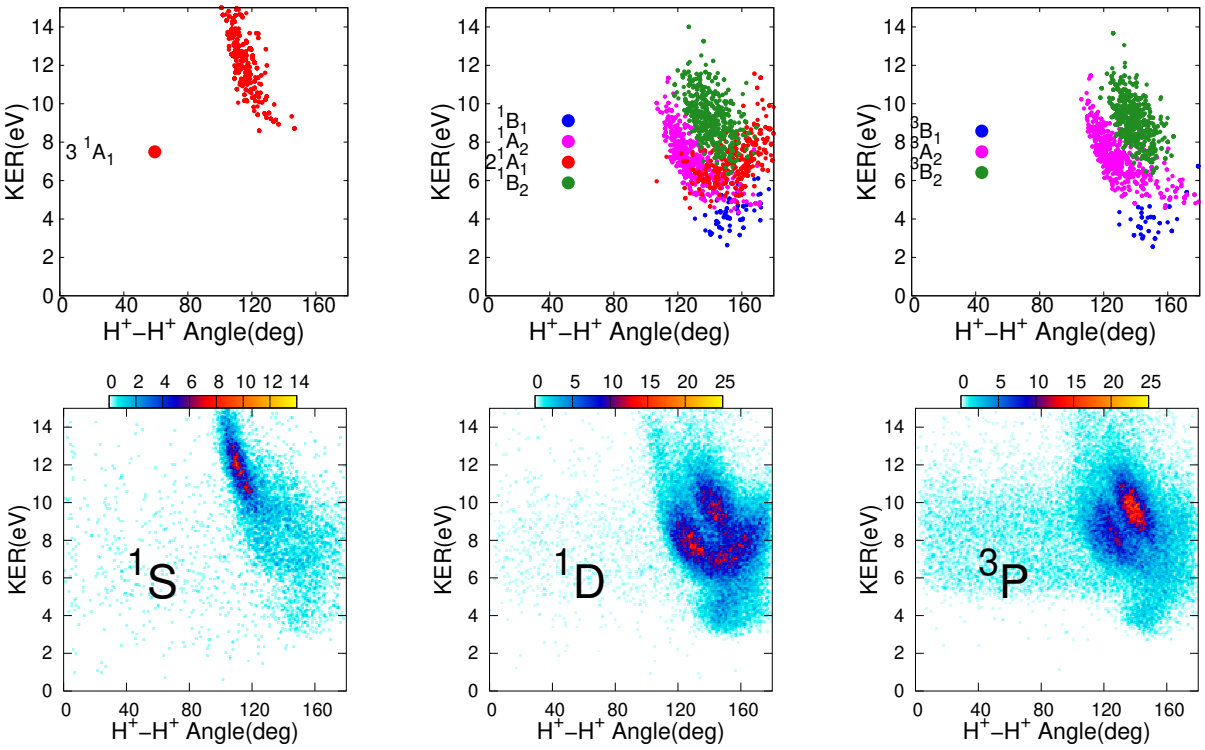


FIGURE 6.2. Plots of the total kinetic energy release of the atomic fragments versus the angle between the momenta of the ejected protons (or $D^+$) shown separately for the three states of the oxygen atom that can be distinguished in the experiment. Top row: classical trajectories, bottom row: histogram plot of experimental measurements.

respective di-cation states. This is an important finding that shows the core assumption that having the initial conditions for the classical trajectories as a Wigner distribution without different weights for the different electronic states of the dication captures most of the experimental observation.

We note that the $1^1A_1$ state produces too few trajectories in the three-body breakup channel to appear in the plot that predicts the KER versus the angle between the ejected protons for states that correlate to the $^1$D state of the oxygen atom. The fact that there are only four features in the experimental observation in the corresponding panel (bottom middle) of Fig. 6.2 is consistent with the theoretical prediction based solely on the branching ratio of the classical trajectories. This is ultimately due to the $1^1A_1$ state having no gradient to opening (see Figure. 3.3) and therefore not able to overcome any stretch (symmetric or antisymmetric) barriers to three-body dissociation.

The comparison in the rightmost panels of Fig. 6.2 of classical trajectory and experimental distributions for the $^3$P asymptote shows two strong feature in close agreement but the experiment also displays one weak feature between KER values of about 5.5 eV to 10 eV and extending over all $H^+$– $H^+$ ($D^+$– $D^+$) angles. This shows that the broad distribution noted in Fig. 2.2 is somehow connected to the $^3$P state. We mention that the Franck-Condon region for double-photoionization to produce the $2^1A_1$ state corresponds to at least the upper part of that range of KER, and correlates in the two-body channel, which it produces about 33% of the time (Table 5.1), to the $b^1\Sigma^+$ state of $OH^+$. That state is known to be predissociated by an intersystem crossing with the $A^3\Pi$ of $OH^+$ [**27**, **38**] to produce $O(^3P)$ + $H^+$ with a lifetime on the order of 2 picoseconds. It is reasonable therefore to speculate that this two-body dissociation channel could produce events in this fourth feature of the experimental distribution for the $O(^3P)$ three-body channel. Fig. 3.1 suggests that a similar mechanism might connect both the $1^1A_1$ and $^1B_1$ states of $H_2O^{++}$ ($D_2O^{++}$) with the triplet three-body asymptote, producing other events in this range of KER for which the axial recoil approximation would also break down. These speculations will be resolved in detail in the following chapter.

It is now apparent that the combination of asymptotic continuum energy (corresponding to the neutral oxygen term), KER and $\beta$ might be used as a signature to select individual di-cation states in the data as they dissociate into the three-body channel $D^+ + D^+ + O^*$. The theoretical results from Fig. 6.2 show that there is some significant overlap in these states, particularly those leading to the $O(^1D)$ asymptote. The nearness of the $^1B_2$, $2^1A_1$ and $^1A_2$ potential surface slices, shown in Fig. 3.1, helps visualize this overlap. We use the prescribed combination of asymptotic continuum energy, KER and $\beta$ from Fig. 6.2 to create state-selection gates for each of the eight di-cation states of the dissociating water molecule. The gates are polygons surrounding each di-cation state in the conformation map. The polygon gates are summarized in Table 6.1 and visualized in Fig. 6.3, with Table 6.2 giving the state's fraction using these state-selection gates. In this table the left column lists the selected state's $C_{2v}$ symbol, the right column lists the state fractions and the central columns indicate the prevalence of each state. For the given data set, we chose gates both to minimize cross-state contamination and to maximize total events. The application of these gates excludes some valid data from each state, while admitting some contamination from nearby

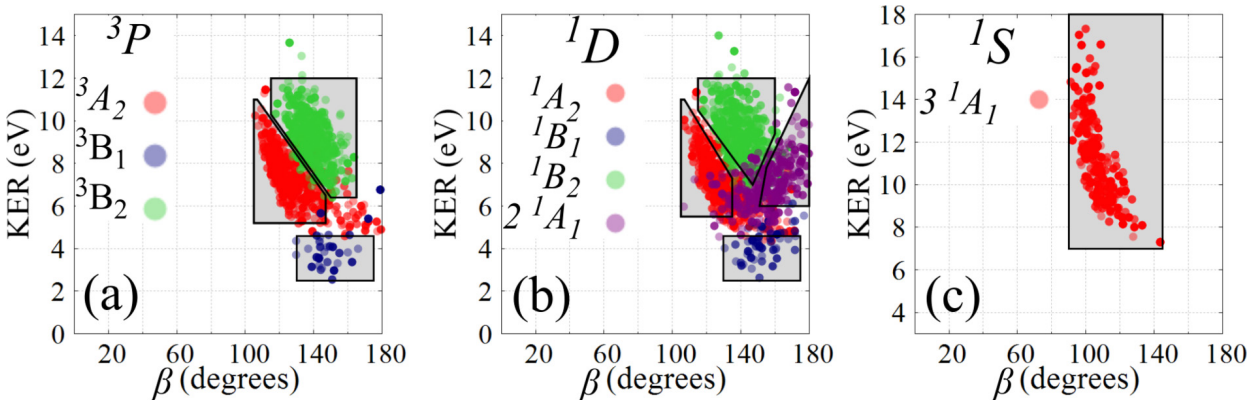


FIGURE 6.3. Gates are constructed as polygons of connected points surrounding each di-cation state in conformation map space. Table 6.1 lists the points used to construct each polygon.

TABLE 6.1. Gates used to state-select three-body breakup on conformation maps (KER vs $\beta$).

| $C_{2v}$ | Points ($\beta$, KER) |
|---|---|
| $^3B_1$ | (130,2.5),(130,4.6),(175,4.6),(175,2.5) |
| $^3A_2$ | (105,11),(107,11),(147,6.5),(147.5.2),(105,5.2) |
| $^3B_2$ | (115,12),(165,12),(165,6.4),(150,6.4),(115,10.3) |
| $^1B_1$ | (130,4.6),(175,4.6),(175,2.5),(130,2.5) |
| $^1A_2$ | (105,11),(107,11),(135,7.3),(135,5.5),(105,5.5) |
| $2^1A_1$ | (150,6),(151,7.8),(180,12),(180,6) |
| $^1B_2$ | (115,12),(160,12),(160,9.4),(147,7),(115,10.5) |
| $3^1A_1$ | (90,7),(90,18),(145,18),(145,7) |

states in the conformation map space. We apply the gates to classical trajectory calculations to characterize the quality of the state selection in two ways. First, we observe the distribution of the different states present in the gated data, i.e., the state prevalence. Second, we observe the amount of the selected state present in the gate as a fraction of the total number of simulated events for that state, i.e., the state fraction.

With the gates from Table 6.1, the states are selected with better than 91% targeted state prevalence for all states except $2^1A_1$ (see Table 6.2). We anticipate that with a more robust data set and more refined gates, many of these values can be improved. It is clear from Fig. 6.2 that we lose a significant number of events from all dication states leading to the O($^1D$) asymptote due to their overlap in the conformation map around KER = 6 eV and $\beta = 140^o$. However,

TABLE 6.2. Dication prevalence and fraction by state-selection gate (%)

| Selected | State prevalence (%) | | | | | | | | Fraction |
|---|---|---|---|---|---|---|---|---|---|
| state | $^3B_1$ | $^3A_2$ | $^3B_2$ | $^1B_1$ | $^1A_2$ | $2^1A_1$ | $^1B_2$ | $3^1A_1$ | (%) |
| $^3B_1$ | 96.7 | 3.3 | 0 | — | — | — | — | — | 67.8 |
| $^3A_2$ | 0.4 | 98.3 | 1.3 | — | — | — | — | — | 84.8 |
| $^3B_2$ | 0 | 4.7 | 95.3 | — | — | — | — | — | 93.6 |
| $^1B_1$ | — | — | — | 94.0 | 6.0 | 0 | 0 | — | 59.5 |
| $^1A_2$ | — | — | — | 0 | 91.2 | 8.0 | 0.8 | — | 77.5 |
| $2^1A_1$ | — | — | — | 2.5 | 3.9 | 83.8 | 9.8 | — | 53.1 |
| $^1B_2$ | — | — | — | 0 | 2.4 | 3.9 | 93.7 | — | 81.9 |
| $3^1A_1$ | — | — | — | — | — | — | — | 100 | 100 |

utilizing these gates provided by theory, reasonable state-selected experimental Newton-like plots are generated and are presented in Fig. 6.4. Comparing with the analogous theoretical Newton-like images presented in Fig. 6.5, we see the $3^1A_1$ state is captured by a 100% state-prevalence gate in Fig. 6.4, for example. And as Table 6.2 would suggest, the $2^1A_1$ state's contaminated gate produces a Newton-like image in Fig. 6.4 that lacks many counts in regions seen in the Fig. 6.5 for this state.

This is crucial analysis because Fig. 6.4 shows the apparent orientation of the water molecule at the moment of photoabsorption and, thus provides experimentalist the body-frame for each state of $D_2O^{++}$ opening the door to analyze the intra-shell and inter-shell TDCS of the ejected electrons. However, as alluded to in Chapter 2, these plots contain more information that calls into question the orientation of $D_2O^{++}$ implied by Fig. 6.4. For example, the states $^1A_2$, $3^1A_1$, $^1B_2$, $^3B_2$ and $^3A_2$ oxygen's momentum-vector measurement produced approximately Gaussian distributions which implies that the measured two protons did dissociate approximately along the bonds and the axial-recoil approximation is valid. In contrast, the $2^1A_1$, $^1B_1$ and the $^3B_1$ states all have markedly different Newton-like images. For these states, the oxygen atom's momentum vector has only counts between $P_z = -10$ to $P_z = 0$ in the $z$ direction. Moreover, there seems to be a line of counts for the oxygen atom's momentum vector starting at $P_z = -10$ for these particular states. (Note the $2^1A_1$ state has a slight curved cut in the oxygen atom's momentum vector but this is only an artifact from performing a poor gate on the $\beta$ vs. KER data for this state. Table 6.2 shows this states' prevalence is the worst at 83.8% with more contamination from other states and, therefore

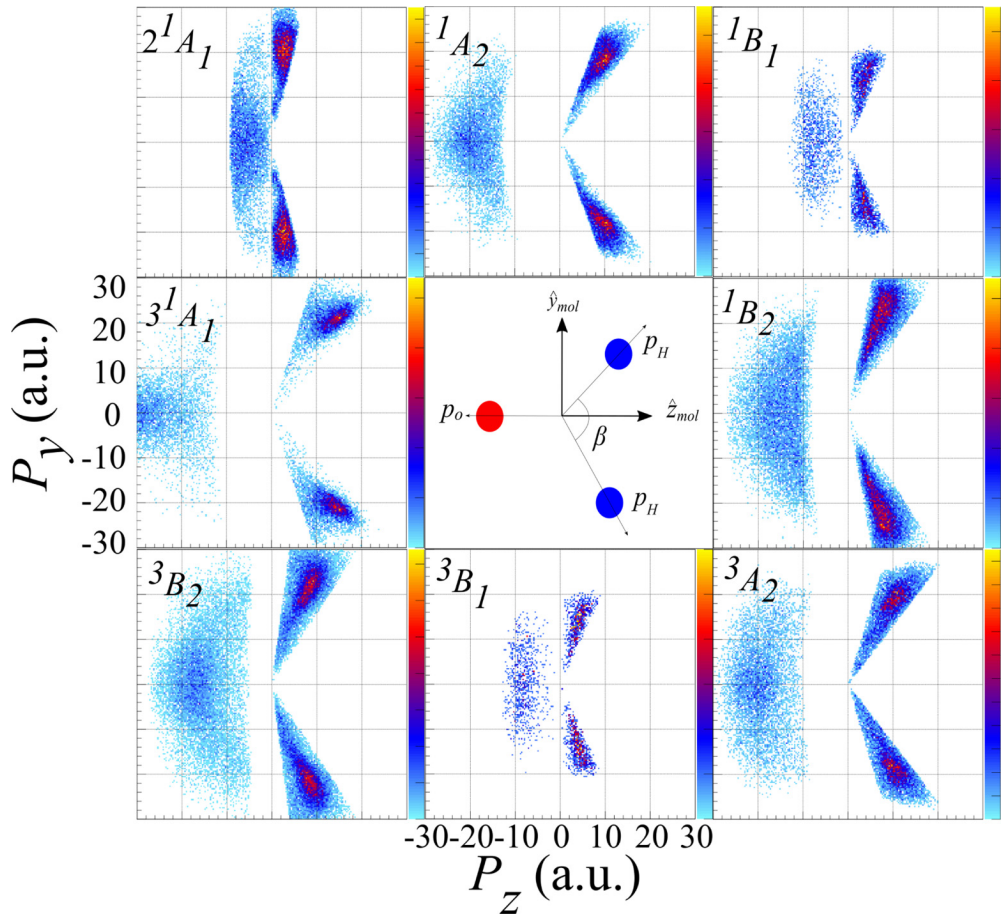


FIGURE 6.4. Experimental plots as in Fig. 2.4, with the gates of the total energy [Fig. 2.1(b)] and the KER and $\beta$ gates in Fig. 6.3 applied to separate the individual di-cation states. The selected state of each panel is noted in the upper left corner. The schematic in the center panel reminds the reader about the dissociation frame axes and the positions of the oxygen (red circle) and protons (blue circles) creating Newton-like images. Axis scales are identical in each panel but are provided only once to improve the visual clarity. This plots are to be compared with their theoretical analog in Fig. 6.5.

required a more restrictive gate to produce the Newton-like plot). These apparent differences in the Newton-like plots necessitate a discussion into the breakdown of the axial-recoil approximation.

### 6.2. Axial-Recoil Breakdown

Guided by Fig. 6.4, we begin our analysis of axial-recoil breakdown by specifically looking at the $3^1A_1$ and the $^1B_1$ states. Fig. 6.6 shows the final momenta of the protons from the classical trajectories for these two states are plotted. In a COLTRIMS experiment, in the absence of knowledge of

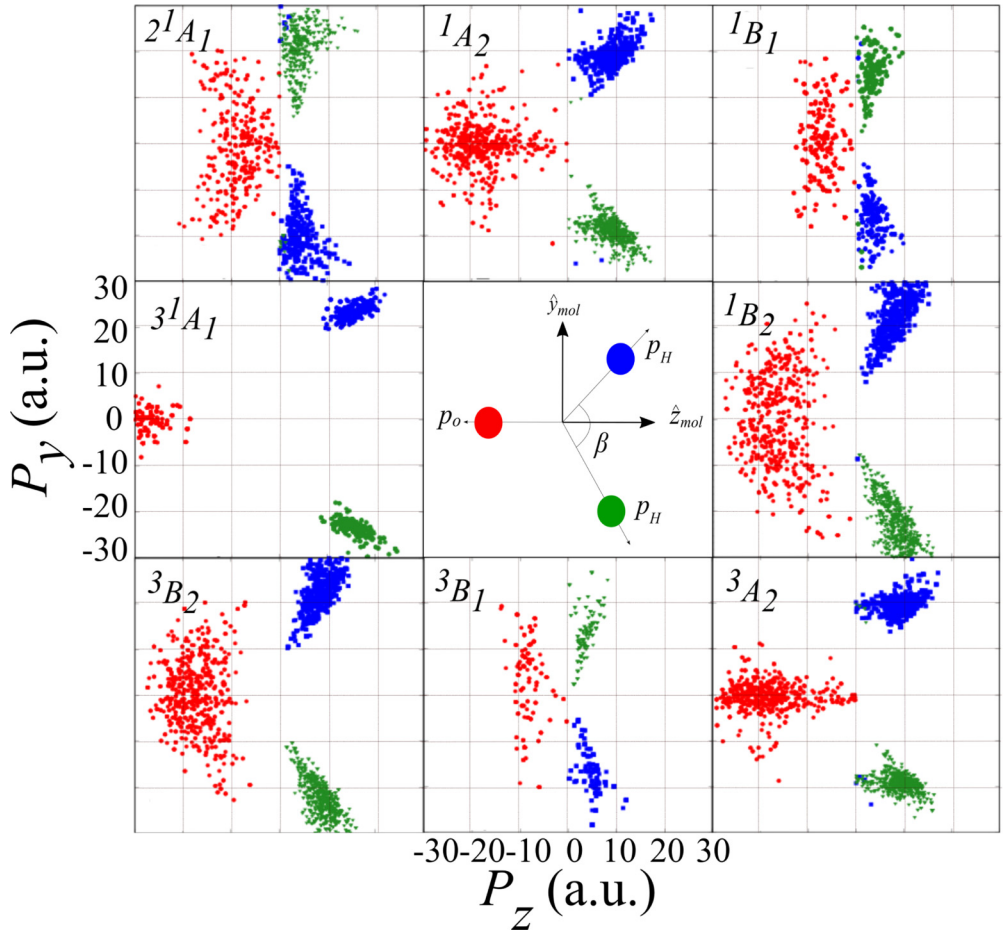


FIGURE 6.5. Theoretical plots as in Fig. 2.4 for all eight di-cation states using classical trajectory simulation results for the three-body breakup and in the experimental dissociation frame to compare with Fig. 6.4 above. The state of each panel is noted in the upper left corner. The schematic in the center panel reminds the reader about the experimental dissociation frame axes and the positions of the oxygen (red circle) and protons (blue and green circles) creating Newton-like images. Axis scales are identical in each panel but are provided only once to improve the visual clarity.

the dissociation dynamics, the assumption of the axial recoil approximation can be used to determine the apparent orientation of the molecule, and thus used to locate the directions of the ejected electrons in the body frame. The meaning of "axial recoil" approximation [**126**] (see Chapter 2) in interpreting momentum coincidence experiments in the case of diatomics is the assumption that the fragments are ejected along the bond and that the axis of the molecule does not rotate appreciably before dissociation is complete. Here, for the dissociation of the triatomic water di-cation, strict "axial recoil" dynamics would mean that the two protons are ejected along the bond directions as

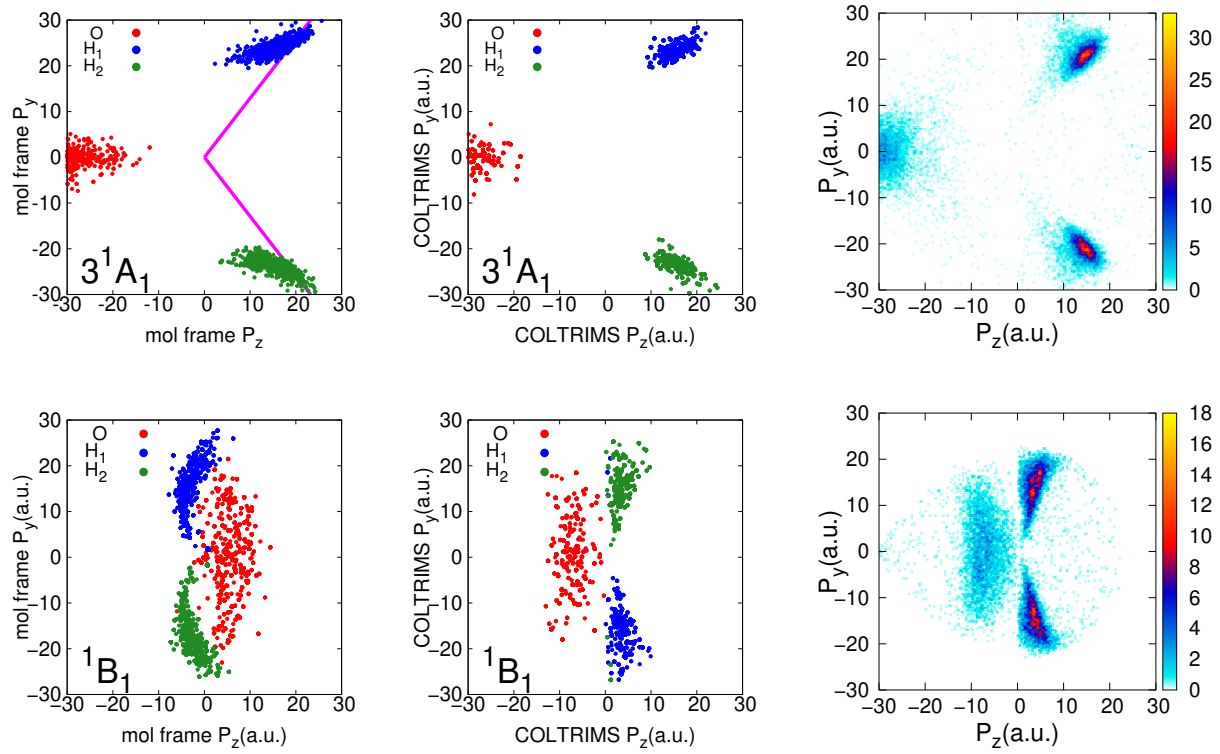


FIGURE 6.6. Fragment momentum distributions for $3^1A_1$ and $^1B_1$. Left panels: computed final momenta of the classical trajectories plotted in the molecular frame indicated by labeling the axis with "mol frame", solid lines indicate directions of strict axial recoil dynamics. Middle panels: momenta from the classical trajectories analyzed and plotted to determine the apparent molecular plane and orientation under the assumption of axial recoil as explained in the text, with the distinction made by labeling the axis with "COLTRIMS". Right panels: COLTRIMS experimental data analyzed and plotted as in the middle panels.

indicated in the top left panel of Fig. 6.6. However, for the purposes of determining the initial orientation of the symmetry axis of the molecule in this case, it suffices that the two protons be ejected symmetrically near the original bond directions.

Thus, in the analysis of the experimental data shown in Fig. 6.6, the bisector of the angle between the momenta of the two protons determines the $z$ axis of the momentum plane, and the directions of the momenta of the protons are assigned equal angles above and below those axes. The momentum of the oxygen is deduced by momentum conservation under the assumption of a cold target with no center of mass momentum, and thus has the opposite sign for its $z$ component. To the degree that the dissociation is direct and symmetric, this procedure determines the plane

of the molecule and its orientation in that plane for the purposes of coincidence measurements with the ejected electrons. The final momenta of computed classical trajectories can be plotted in exactly the same way to allow a direct comparison with the experiment, and this is what is also shown in the middle. To make this distinction in the theoretical figures clear, the left panel in Fig. 6.6 is the theoretical results plotted in the molecular frame and has axis labeled with "mol frame". The middle panel in Fig. 6.6 is the theoretical results after transforming into the COLTRIMS coordinate frame and is indicated by labeling the axis with "COLTRIMS". For the $3^1A_1$ state the comparison in Fig. 6.6 of classical trajectory results with experiment shows that the axial recoil approximation captures the majority of the physics of dissociation. Importantly, when the computed final momenta are plotted in the same way as the COLTRIMS experimental data they are little changed by the assumption of axial recoil. With both plotted in this way the agreement of theory with the experimental data is excellent. However, for the $1^1B_1$ state the majority of the protons in the three-body channel emerge traveling towards the *opposite* side of the molecule from the one in which they originated, signaling the complete breakdown of the axial recoil approximation (note the changing order of the colors in comparing left and middle panels of the bottom row). The origin of this distinctive difference between the dissociation dynamics of the $1^1B_1$ and that of the $3^1A_1$ state is the strong gradient of the potential surface toward bond angle opening in the former case, and the gradient toward bond angle closure in the latter. The contrast between these aspects of the two potential surfaces can be seen in Figs. 6.7, 3.4 and 3.3, and was described in Chapter 3.

To illustrate how the gradient in the potential surface affects the dissociation dynamics, a random selection of a subset of the trajectories on the $3^1A_1$ and on the $1^1B_1$ potential surface is plotted in Fig. 6.8a and Fig. 6.8b respectively. Trajectories on the $3^1A_1$ state demonstrate dynamics along the bonds defining the original orientation of the molecule, and thus the axial recoil approximation is valid, while dynamics on the $1^1B_1$ state show how they invert the sense of the original bond angle, producing a breakdown in the axial recoil approximation. Apart from small clues provided by Newton-like plots, COLTRIMS experiments can't reveal the exact mechanism for how this breakdown occurs. This insight is only provided by the theoretical calculations performed here.

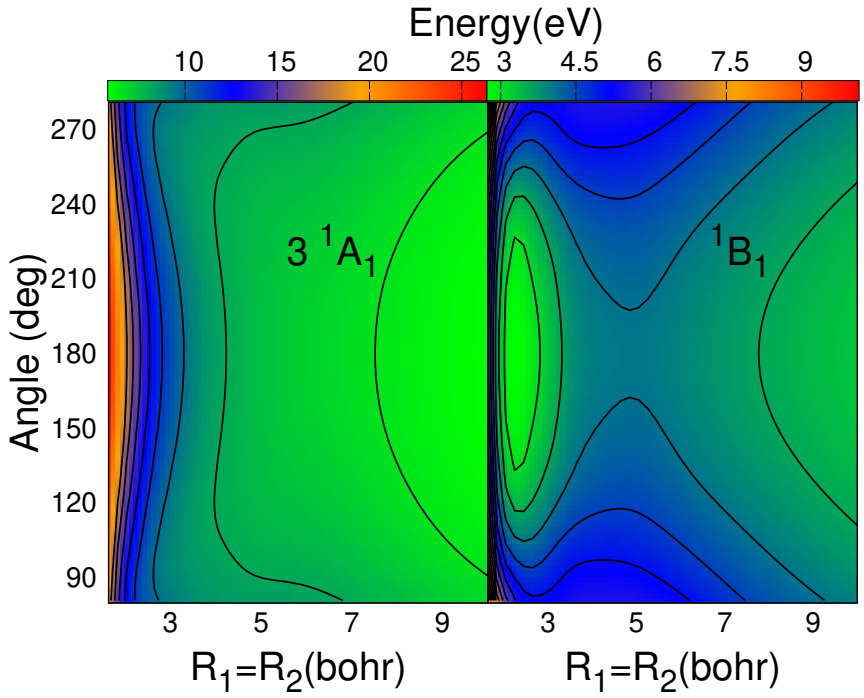


FIGURE 6.7. Comparison of $3^1A_1$ and $^1B_1$ potential surfaces as a function of symmetric stretch and DOD angle. The strong gradient to opening or the lack there of completely explains the trajectories in Figs. 6.8.

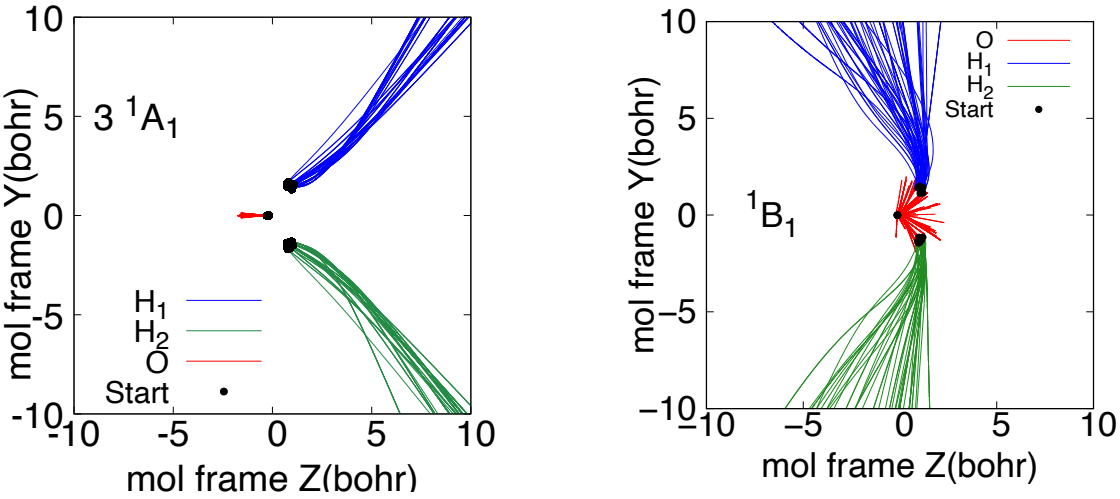


(a) Valid Axial-Recoil

(b) Axial-Recoil Breakdown

FIGURE 6.8. Following the paths of 60 classical trajectories showcasing the differences in the dynamics when axial-recoil is valid and when the approximation breakdown; namely valid axial-recoil trajectories for the 3 $^1A_1$ state (a) and axial-recoil breakdown trajectories for the $^1B_1$ state (b). (See Fig. 6.7 for the associated potential energy surfaces.)

TABLE 6.3. Axial Recoil categorization for three-body breakup channel from ensembles of 1000 classical trajectories. Note that the states that are downhill to opening (see Fig. 3.3) breakdown axial recoil.

| $D_2O^{++}$ Electronic state | Axial Recoil Breakdown |
|---|---|
| $^3B_1$ | Yes |
| $1^1A_1$ | – |
| $^1B_1$ | Yes |
| $2^1A_1$ | Yes |
| $^3A_2$ | No |
| $^3B_2$ | No |
| $^1A_2$ | No |
| $^1B_2$ | No |
| $3^1A_1$ | No |

Nonetheless, when the classical trajectories are plotted in the same way as the experimental data, under the assumption of axial recoil as described above (center panels of Fig. 6.6), they reproduce the experimental momentum plane image (right panels of Fig. 6.6), verifying that the trajectories on this potential surface accurately represent the observed dissociation dynamics. Similar results are found for all three states ($^3B_1$, $^1B_1$ and $2^1A_1$) whose potential surfaces have a strong gradient towards bond opening, as shown in Fig. 3.3 and as tabulated in Table 6.3. We note in passing that similar scissoring dynamics that invert the sense of the bond angle have been observed in dissociative attachment of electrons to water to produce oxygen anions [**4**].

Thus for the eight states that are evidently observed in the experiment, the three-body dissociation dynamics of five of these satisfy the axial recoil approximation, while for the other three, the axial recoil approximation breaks down completely, but does so in a particularly simple and potentially nonetheless describable way. The lower panels of Fig. 6.6 illustrate a mapping of the experimental results analyzed under the assumption of axial recoil onto the correct momentum plane. The classical trajectory results allow the isolation of parts of the experimental observations that are dominated by trajectories that unambiguously invert the original plane of the molecule.

The signature of the breakdown of axial recoil in the experiment can be seen in inferred neutral oxygen atom in the Newton-like images, Fig. 6.4. Defining the *positive* $z$ axis as the bisector of the two deuterium ions will lead to different trajectories, showcased in Fig. 6.8a and Fig. 6.8b, producing similar orientations of the water molecule in the COLTRIMS measurements, as is the

case in the right most panels in Fig. 6.6. However, the treatment of the inferred neutral oxygen atom within the axial recoil approximation will still retain memory of the different dynamics by manifestation of a "structure" seen in the Newton-like momentum image. For example, in the upper right most panel of Fig. 6.6, the inferred oxygen atom for the $3^1A_1$ state has a uniform Gaussian distribution. For direct breakup of the two deuterium ions along the bond, the inferred oxygen atom must go directly backwards for momentum conservation and will have a spread off the $P_y = 0$ line dictated by the magnitude of the asymmetry in the momentum of the two deuterium ions. Therefore, anything other than a uniform Gaussian distribution (i.e. structure) seen in the neutral inferred fragment must indicate a breakdown in the axial recoil approximation. Hence, the breakdown in axial recoil for the $^1B_1$ state can be inferred experimentally by investigating the neutral inferred oxygen in the lower right most panel Fig. 6.6. The distinct line starting at around $-10$ $P_z$ (a.u.) in this figure is due to the oxygen atom having positive momentum (see lower left most panel in Fig. 6.2), but this momentum has a distinct maximum limit to conserve momentum between the three fragments forming a line in the inferred neutral oxygen distribution. This structure can be seen in each Newton-like plot in Fig. 6.4 for the states that break axial-recoil. This discovery demonstrates how an experimentalist may assign skepticism to the validity of axial recoil even if the COLTRIMS ion measurements produce an image that seems to indicate the orientation of the molecule.

### 6.3. Conclusions

We have verified that the three-body dissociation dynamics of the water dication for the states that dissociate to the oxygen atom in its $^3$P, $^1$D and $^1$S states and two protons, are well described by classical trajectories on the computed potential energy surfaces. The theoretical calculations predict the momentum-plane distributions of the final states in good agreement with experimental data, and open the way for a full experimental determination of the TDCS in the body frame for one-photon double-photoionization of the water molecule. A complete comparison of theory and experiment for the remaining six states, is given in Fig. 6.4 and Fig. 6.1 for the experiment and theory simulations respectively. Also, Table 6.4 gives numerical comparison between the peak

TABLE 6.4. Peak KERs and $\beta$s from experimental data (expt.) and simulations for the three-body breakup.

| $C_{2v}$ | Expt. KER ($\sigma$) | KER | Expt. $\beta(\sigma)$ | $\beta$ |
|---|---|---|---|---|
| $^3B_1$ | 4.29(0.42) | 4.2 | 145.9(8.7) | 152.2 |
| $^3A_2$ | 7.99(1.14) | 7.3 | 121.4(9.8) | 129.0 |
| $^3B_2$ | 9.66(1.22) | 9.2 | 138.6(10.7) | 138.5 |
| $^1B_1$ | 4.26(0.41) | 4.2 | 148.3(10.1) | 154.9 |
| $^1A_2$ | 7.58(0.98) | 7.2 | 125.5(8.0) | 130.0 |
| $2^1A_1$ | 7.65(1.03) | 7.1 | 163.6(6.7) | 155.8 |
| $^1B_2$ | 9.81(1.11) | 9.3 | 142.9(9.3) | 140.5 |
| $3^1A_1$ | 11.4(1.83) | 11.4 | 110.8(11.4) | 106.0 |

KERs and $\beta$s in the experimental distributions and the theoretical simulations. These peaks were evaluated after each state was separated via the gates in Fig. 6.3 and defined in Ref. [**80**].

We have found that for three of those dication electronic states, the axial recoil approximation, which has been the basis for the interpretation of most COLTRIMS experiments, and which previously seemed essential to the construction of body frame information from coincidence measurement of ions and photoelectrons, breaks down radically. Nonetheless, the analysis in Sec. 6.2 will potentially allow the measurement of the TDCS in the body frame for those states as well. Those experiments have the potential to reveal for the first time the details of double-photoionization in the body frame of a polyatomic molecule.

Experiments such as these will pose a profound challenge to theory to predict the body-frame TDCS for double-photoionization of water. The current state of the art for *ab initio* calculation of double-photoionization amplitudes is to treat the dynamics of two active electrons completely while freezing the others in target atomic or molecular orbitals. Such calculations have only been carried out on atoms [**1**, **23**, **41**, **98**, **122**, **123**, **124**, **125**] to our knowledge, but in those cases surprisingly good agreement with experimental angular distributions of the ejected electrons was obtained. To calculate the TDCS for one-photon double ionization of water, we can make the same two-active-electron approximation, and use the computational methods involving a single center expansion and numerical grids that we have used previously in double-photoionization calculations on $H_2$ [**53**, **54**, **100**, **106**]. This approach promises to accurately describe correlation between the two outgoing electrons. A critical open question is whether the approximation of treating only two active electrons

will be sufficient to describe the effects of initial state correlation on the removal of two electrons from the same orbital as well as from different orbitals of the neutral molecule to produce different states of the dication.

CHAPTER 7

# Sequential Breakup

## 7.1. Analysis

As mentioned in previous chapters, the experimental measurement of the nuclear breakup presented in Fig. 2.2 hints at more involved dynamics than the direct breakup mechanism explored in Chapter 6. In addition to the discrete features, the initial experiment showed one broad distribution in angle as seen in the $^3$P experimental figure, Fig. 6.2 (bottom-right). However, the more refined experiment performed on $D_2O^{++}$ (Fig. 2.2) illuminated two broad distributions in KER vs. $\beta$ implying two electronic states are involved. This "carpet" feature, having a broad angular spread between the protons' ejection direction, indicates a sequential breakup mechanism via an $OD^+$ intermediate following the steps listed below (color is used to mark the deuterium, distinguished by being bound to the oxygen atom in a first step):

$$D_2O^{++} \rightarrow D^+ + OD^+ \text{ (Step 1)}$$

$$OD^+ \rightarrow D^+ + O(^3P) \text{ (Step 2)}\,. \tag{7.1}$$

This mechanism would lead to a loss in angle correlation, producing the "carpet" feature seen in Fig. 2.2, because as the $D^+$ dissociates in Step 1, the diatom $OD^+$ will begin to rotate in the plane of the water molecule. This rotation loses any memory of the initial angle between the two protons, and thus produces a broad distribution in angle once Step 2 proceeds.

To assess the proposed sequential dynamics, an experimental analysis using the same COLTRIMS data from Chapter 2, bolstered by theoretical simulations, was conducted. It was demonstrated recently that momentum imaging coincidence experiments, without time-resolved X-ray or laser pulses, can in fact be used to detect the steps in a sequential reaction [**3**, **30**, **42**, **51**, **72**, **77**, **87**, **109**,

**120**]. Recently, the "native-frames analysis" was introduced [**77**,**92**], and it was shown that photo-induced momentum imaging observations can resolve the sequence of events in the dissociation of a molecule involving vibrational and rotational dynamics following single-photon multiple ionization events.

Following Gervais *et al.* [**38**] and de Vivie *et al.* [**27**], the two states suggested to proceed along this sequential breakup channel were the $2^1A_1$ and $^1B_1$ states through $OD^+(b\ ^1\Sigma^+)$ and $OD^+(a\ ^1\Delta^+)$ intermediate states, respectively. They found that these intermediate states nonadiabatically transition to the $OD^+(A^3\Pi)$ state via spin-orbit coupling and with enough internal energy, the diatoms would subsequently break apart producing the second-measured deuterium ions. Gervais also noted the other $\Delta$ component will nonadiabatically transition to the $OD^+(A^3\Pi)$ state that may then breakup apart. The di-cation state that connects to this other $\Delta$ component is the $1^1A_1$. However, this channel was shown to have negligible $OD^+(A^3\Pi)$ population with enough internal energy to break apart and, therefore is not a dominant channel that is favorable to COLTRIMS measurement. This is validated by observing only two broad distributions in the COLTRIMS results in Fig. 2.2. Hence, our proposed sequential reaction channels producing the two broad distributions in Fig. 2.2 are then as follows:

$$\begin{aligned} &D_2O^{2+}(2\,^1A_1) \rightarrow D^+ + OD^+(b\,^1\Sigma^+) \\ &\text{followed by } OD^+(b\,^1\Sigma^+) \rightarrow D^+ + O(^3P)\,, \end{aligned} \tag{7.2}$$

and

$$\begin{aligned} &D_2O^{2+}(1\,^1B_1) \rightarrow D^+ + OD^+(a\,^1\Delta) \\ &\text{followed by } OD^+(a\,^1\Delta) \rightarrow D^+ + O(^3P)\,. \end{aligned} \tag{7.3}$$

The first step in sequential breakup requires one O–D bond to break, while the $OD^+$ fragment left behind remains bound. In Fig. 7.1(a) we show the asymmetric stretch of $D_2O^{++}$ leading to $D^+ + OD^+$ breakup, with cuts in a few potential energy surfaces (PES) computed for a bond angle of 104.45° while holding the other O–D internuclear distance at 1.812 a.u. (both are equilibrium values of $D_2O$). (We also show the $1^1A_1$ state in Fig. 7.1(a) for completeness, as this was the other

state potentially proceeding along the sequential breakup channel.) Figure 7.1(b) displays cuts in a few PES of $D_2O^{++}$ for the same bond angle, but when one $D^+$ is at 1000 a.u. (and therefore its interaction with the remaining $OD^+$ is negligible). This is effectively a plot of the $OD^+$ states correlating with the $D^+ + O(^3P)$ and $D^+ + O(^1D)$ dissociation limits, which are involved in the predissociation of the intermediate $OD^+$ molecule.

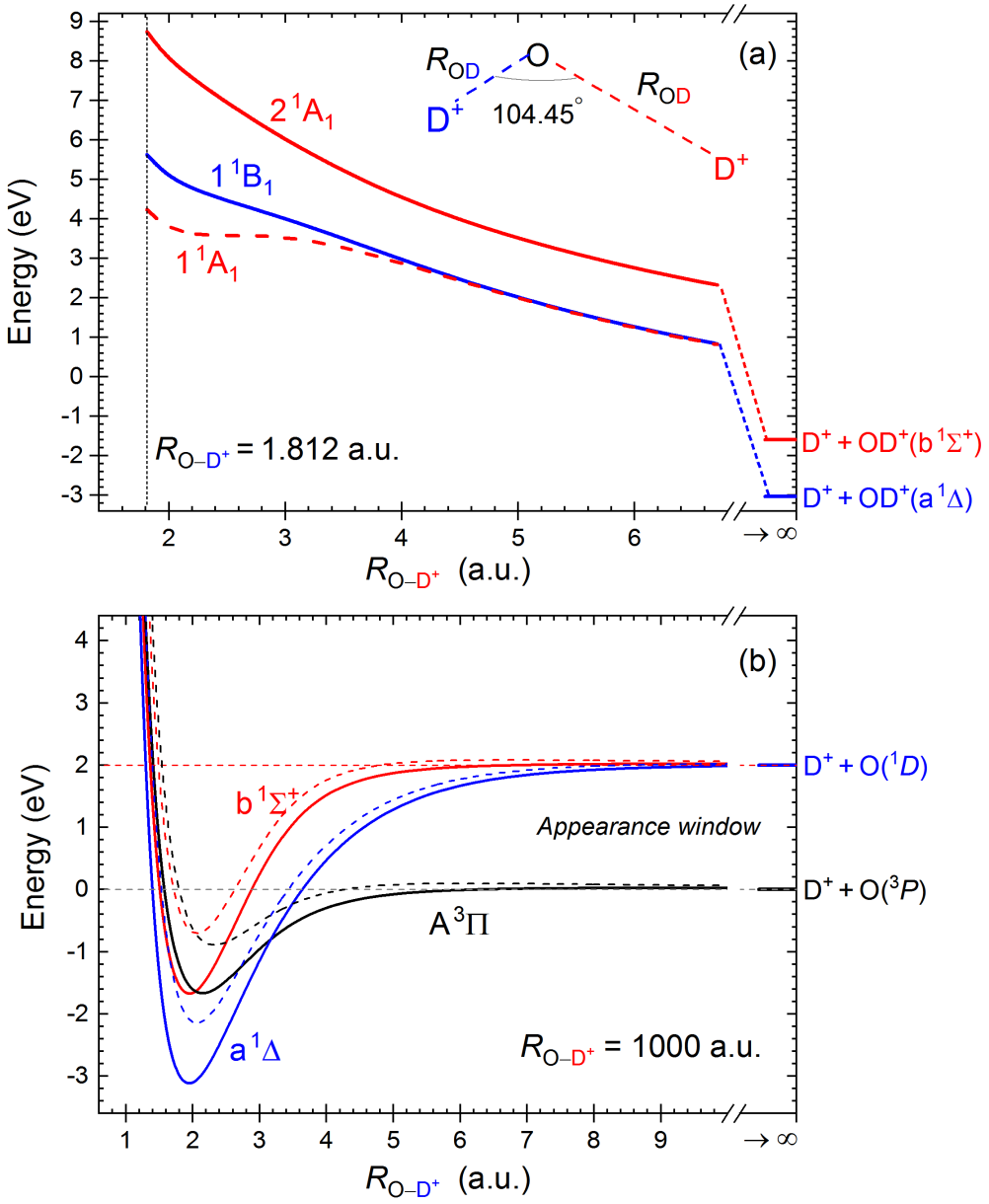


FIGURE 7.1. The relevant potential energy surface for sequential fragmentation of water di-cations via $OD^+$ intermediate explored by Gervais *et al.* [**38**]: Cut through the potential energy surfaces showing (a) the asymmetric stretch of $D_2O^{2+}$ for a fixed bond angle (104.45°) and internuclear distance (1.812 bohr) of the other O–D bond for the three states of $D_2O^{2+}$ that produce the diatomic intermediate which further dissociates (see text), and (b) the $OD^+$ potentials when the interaction with the other $D^+$ is negligible (solid and dashed lines are for $J = 0$ and $J = 30$, respectively). The states in (a) plotted as solid blue and solid red curves produce the diatomic ion with enough internal energy to predissociate via the $A\,^3\Pi$ state. The energy scale is relative to the $D^+ + D^+ + O(^3P)$ dissociation limit. Note that on this energy scale the asymmetric stretch limits for the $1\,^1B_1$ and $2\,^1A_1$ states in panel (a) are $-3.021$ and $-1.619$ eV, respectively.

Using the PES information detailed above, we modeled the reaction dynamics by the propagation of ensembles of classical trajectories on the relevant potential surface for a few picoseconds, at which time the $OD^+$ internal energy was evaluated. The computational approach used is the same as that of discussed in Chapter 6. The molecule is initially in its ground vibrational state and undergoes a Franck-Condon transition to the doubly ionized excited state. The initial conditions for the one-million computed classical trajectories, for each $D_2O^{2+}$ state we consider, were sampled from the corresponding Wigner distribution, assuming that the ground vibrational state can be represented by direct product wave function of the normal modes. At the end of the propagation, the internal energy, and the rotational angular momentum $J$ of the $OD^+$ fragment were computed from the Cartesian momenta and coordinates of the atoms, together with the value of the potential energy. The $OD^+$ is considered to be bound if the total energy of an O–$D^+$ pair is less than the $J$-dependent barrier to dissociation associated with the relevant final states of $OD^+$, specifically the $D^+ + O(^1D)$ limit shown in Fig. 7.1(b).

As noted before, The second step of the sequential fragmentation is the dissociation of the $OD^+$ ion produced in the first step in its $b\,^1\Sigma^+$ and $a\,^1\Delta$ states, by a nonadiabatic transition to the $A\,^3\Pi$ state mediated by spin-orbit coupling. If the $OD^+$ ion is produced vibrationally (and rotationally) excited to energies above the dissociation limit of the $A\,^3\Pi$ state shown in Fig. 7.1(b), it can be predissociated by this nonadiabatic transition. The central dynamical assumption of our treatment takes advantage of the relatively short lifetimes for this predissociation via a nonadiabatic transition to the $A\,^3\Pi$ state, as compared to the fragments' flight time in the experimental setup. We therefore assume in our classical trajectory calculations that all $OD^+$ ions, with internal energy above the $D^+ + O(^3P)$ dissociation limit, predissociate within a few picoseconds due to spin-orbit coupling with the $A\ ^3\Pi$ state (see Refs. [**27**, **38**]).

Thus, for example, all trajectories with vibrational energy in the $b\,^1\Sigma^+$ state having zero rotational angular momentum, and with vibrational energies between the two horizontal dashed lines in Fig. 7.1(b) labeled "appearance window", are assumed to lead to $D^+ + O$ fragments. (This name was chosen to suggest any trajectories that lead to a diatom $OD^+$ with internal energy within this window will *appear* in the COLTRIMS experiement.) Such an "appearance window" was recently found to play an important role in another polyatomic molecule, namely in the valence

double-photoionization of ammonia [**64**]. Nonzero rotational angular momentum adds a centrifugal barrier to this picture for all three states of $OD^+$ in Fig. 7.1(b), modifying the "appearance window" and leaving a clear signature of rotational excitation in the kinetic energy of the atomic fragments produced by this mechanism, as we discuss below. An angular momentum value of $J = 30$ a.u. was chosen for this plot because the majority of the sequential trajectories were found to have, on average, an angular momentum of $J = 30$ a.u., which will be presented below. Tunneling through the centrifugal barrier for $J \neq 0$ is neglected in this treatment. Three states of $D_2O^{++}$, the $1\,^1A_1$, $2\,^1A_1$, and $1\,^1B_1$ states shown in Fig. 7.1(a), produce the $b\,^1\Sigma^+$ state (which correlates with the $2\,^1A_1$ state) and the two components of the degenerate $a\,^1\Delta$ state of $OD^+$ [**27**, **38**]. However only two of those, the $2\,^1A_1$ and $1\,^1B_1$ states, produce the diatomic ion with enough internal energy to dissociate appreciably by this mechanism to be seen in one-photon double-photoionization, as is suggested by Figure 5 in Ref. [**38**].

### 7.2. Native Frames

Three-body breakup can be analysed using the conjugate momenta of the Jacobi coordinates, where the coordinates describe the relative positions of the three fragments. This is the key ingredient of the "native frames" method [**77**, **92**]. Instead of using the Newton-like diagram from before, this technique takes advantage of the two-step nature of the process and analyzes the data in the two *native frames* of reference associated with each breakup step by transforming to Jacobi coordinates and, hence the name. In our present case, shown schematically in Fig. 7.2(b), the relative momentum associated with the first fragmentation step is given by

$$\mathbf{p}_{\mathrm{OD,D}} = \frac{m_{\mathrm{OD}}}{M}\mathbf{P}_{\mathrm{D}} - \frac{m_{\mathrm{D}}}{M}\left[\mathbf{P}_{\mathrm{D}} + \mathbf{P}_{\mathrm{O}}\right] , \tag{7.4}$$

where $\mathbf{P}_{\mathrm{D}}$ and $\mathbf{P}_{\mathrm{O}}$ are the measured momenta of the $D^+$ and O fragments, respectively; $m_{\mathrm{D}}$ is the mass of $D^+$; $m_{\mathrm{OD}}$ is the mass of $OD^+$; and $M$ is the mass of the $D_2O^{++}$.

Similarly, the relative momentum associated with the second step is

$$\mathbf{p}_{\mathrm{OD}} = \mu_{\mathrm{OD}}\left[\frac{\mathbf{P}_{\mathrm{O}}}{m_O} - \frac{\mathbf{P}_{\mathrm{D}}}{m_{\mathrm{D}}}\right] , \tag{7.5}$$

where $\mu_{\mathrm{OD}}$ is the reduced mass of $\mathrm{OD}^+$. Finally, the angle between the two relative momenta, $\theta_{\mathrm{OD,D}}$, is computed from the dot product of these vectors. Equations (7.4) and (7.5) are the conjugate momenta of the Jacobi coordinates for the $\mathrm{D} + \mathrm{OD}$ arrangement.

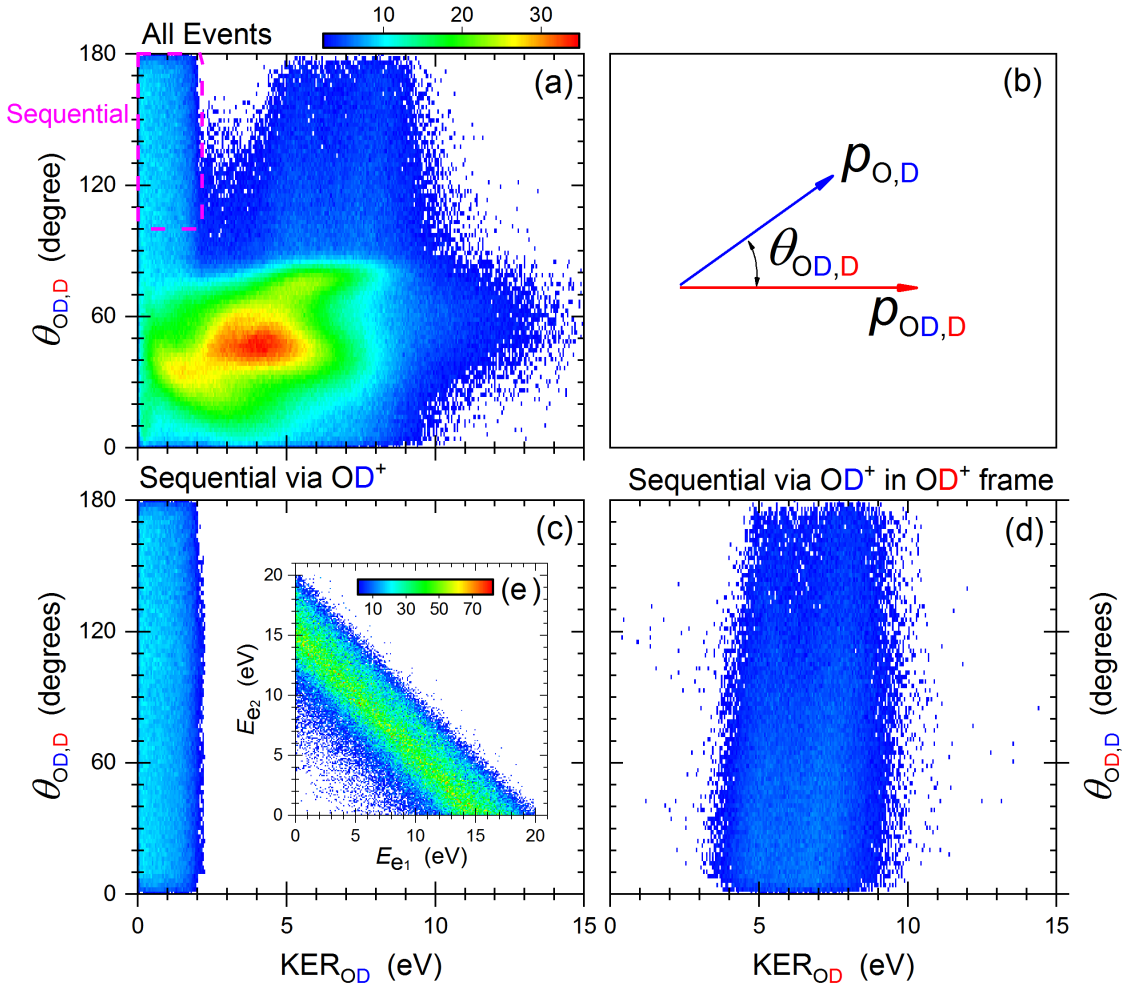


FIGURE 7.2. Experimental data and native frames analysis of the $D^+ + D^+ + O$ breakup (see text). (a) All the measured $D^+ + D^+ + O$ events as a function of the kinetic energy released upon $OD^+$ dissociation, $KER_{OD}$, and the angle between the relative momenta, $\theta_{OD,D}$. Sequential fragmentation events via $D^+ + OD^+$ are identified (see text) by the uniform angular distribution within the red-dashed rectangle (i.e., $KER_{OD} < 2.3\,eV$ and $100° < \theta_{OD,D} < 180°$). (b) Schematic diagram of the relative momenta and the angle between them. Sequential breakup via $OD^+$ analyzed in the (c) $OD^+$ and (d) $OD^+$ frames, i.e., the correct and wrong fragmentation-step order of the $D^+$ fragments, respectively (see text). Note that analysis of the events in the wrong reference frames, as is the case shown in panel (d) and indicated by the different axis labels ($KER_{OD}$ and $\theta_{OD,D}$), yields a distribution significantly different than the one expected for sequential fragmentation [**77**], specifically, a non-uniform angular distribution, a $KER_{OD}$ that depends on the angle $\theta_{OD,D}$, and a much higher than expected $KER_{OD}$. Panel (e) is the energy-correlation map of the ionized electrons associated with this sequential fragmentation.

The second ingredient needed to separate sequential fragmentation is a clear signature distinguishing it from other fragmentation processes. Rotation of the intermediate diatomic ion in the fragmentation plane provides such a signature(see Refs. [**42**,**72**,**77**,**92**,**94**,**109**,**120**] for examples). In the native frames analysis this rotation manifests itself as a nearly uniform $N(\theta_{\mathrm{OD,D}})$ angular distribution, if the predissociation lifetime is long enough so that the rotation of $OD^+$ wipes out any initial angular preference. The kinetic energy release (KER) in the second fragmentation step combined with molecular structure of the intermediate molecule provides an additional constraint for identifying sequential breakup. To that end, we plot in Fig. 7.2(a) all the measured $D^+ + D^+ + O$ events (specifically including the lowest $^3P$, $^1D$, and $^1S$ states of oxygen) as a function of $\mathrm{KER_{OD}} = \mathbf{p}^2_{\mathrm{OD}} \,/\, 2\,\mu_{\mathrm{OD}}$ and $\theta_{\mathrm{OD,D}}$, where we arbitrarily designate one of the two $D^+$ fragments "red" (ejected first) as a correct "coin flip" assignment for half of the sequential events. Then, we identify the (properly assigned) sequential breakup as the uniform angular stripe marked by the dashed-red rectangular boundary in the figure. Note that the KER distribution of this stripe matches the predicted 0–2.25 eV range [**27**,**38**], indicated by the appearance window in Fig. 7.1(b) and Fig. 7.3.

Three observations are appropriate at this point: First, in Fig. 7.2(c) we show the complete angular distribution of this sequential-fragmentation channel of $D_2O^{++}$, which was reconstructed taking advantage of the fact that $N(\theta_{\mathrm{OD,D}})$ is nearly uniform [**77**]. (In Figure. 7.2(e) we plot the energy of the two ionized electrons that are associated with the measured sequential fragmentation in Fig. 7.2(c).) In short, identified sequential events within the red boundary in Fig. 7.2(a) are used to create equivalent events by randomly rotating them to smaller angles until the whole range has a uniform yield within the uncertainty of the data. It is important to note that any other information for each event, like $\mathrm{KER_{OD}}$, is preserved by this reconstruction algorithm [**77**] (see Ref. [**92**] for further details).

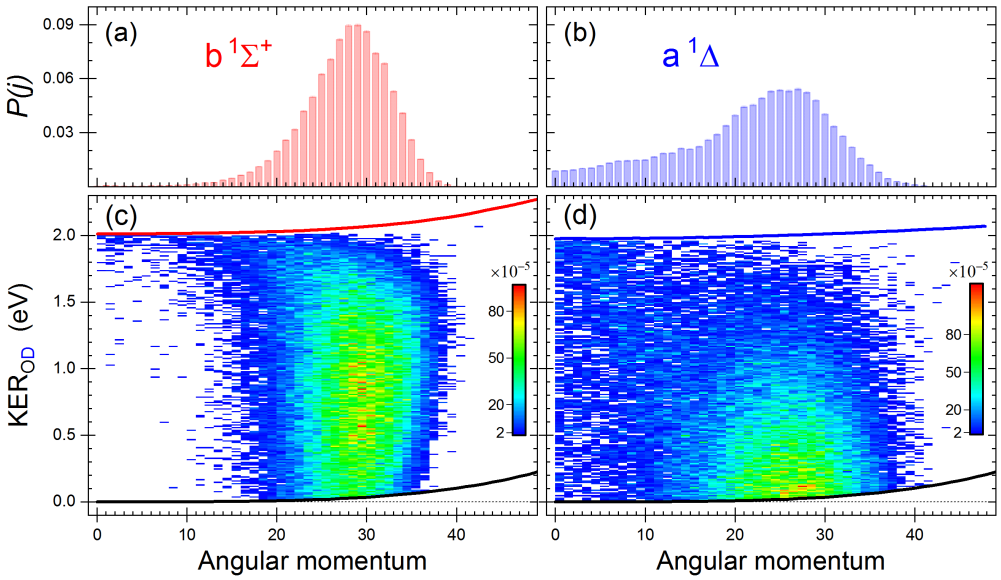


FIGURE 7.3. Normalized angular momentum distribution, $\Sigma_j P(j) = 1$, of the (a) $b\,^1\Sigma^+$ and (b) $a\,^1\Delta$ states of $OD^+$ populated during $D_2O^{2+}$ fragmentation (see text), as well as the, respective, angular momentum – $KER_{OD}$ correlation maps in panels (c) and (d). The lines in panels (c) and (d) represent the modification of the "appearance window" in Fig. 7.1(b) for nonzero rotational angular momentum by the addition of a centrifugal potential to both the singlet and triplet potential curves (specifically, $A\,^3\Pi$ – black, $b\,^1\Sigma^+$ – red, and $a\,^1\Delta$ – blue). In the absence of tunneling no dissociating trajectories can appear outside these lines.

Second, in Fig. 7.2(d) we present the $N(\mathrm{KER}_{\mathrm{OD}}, \theta_{\mathrm{OD,D}})$ distribution, which is a similar distribution to that shown in panel (c) but with the "wrong" fragmentation-step order. In other words, we are plotting sequential breakup occurring via the $OD^+$ intermediate in the frame assuming a $OD^+$ intermediate. To generate such a distribution with certainty, we use the events identified as sequential fragmentation via $D^+ + OD^+$ shown in Fig. 7.2(c), but analyze them as if the $D^+$ was ejected first (i.e. using the reference frames that are not associated with the relevant center-of-mass of each breakup step). In other words, their momenta are calculated in the other Jacobi coordinate arrangement, namely $\mathbf{p}_{\mathrm{OD,D}}$ and $\mathbf{p}_{\mathrm{OD}}$. One can clearly see that the two distributions, shown separately in panels (c) and (d) of Fig. 7.2 are significantly different from each other. Both these distributions are also visible in the "raw" data shown in panel (a). Hence, one can associate each $D^+$ with the relevant fragmentation step. After correctly assigning which $D^+$ comes from the $OD^+$

intermediate, we combine the data for all plots presented below (i.e. we use all sequential events via $OD^+$).

Finally, we note that the high degree of rotational excitation in the intermediate $OD^+$ $b^1\Sigma^+$ and $a^1\Delta$ states, which leads to the sequential breakup signature, has its origin in the strong force towards bond opening on the corresponding $2^1A_1$ and $^1B_1$ potential surfaces upon the loss of two electrons. In the simplest picture of the electronic structure of water, these states are created by the loss of two lone-pair electrons. From simple molecular orbital considerations, losing one or two electrons out of the in-plane $3a_1$ lone pair orbital should lead to an opening of the bond. It was found in the direct analysis of Chapter 3 that this torque is strong enough to cause the two $D^+$ fragments, ejected initially near the 104° equilibrium bond angle in a concerted three-body fragmentation on these surfaces, to invert this angle to greater than 180° while they are still close to the oxygen atom. Similar trajectories that lead to the two-body breakup into $D^+ + OD^+$ impart a strong torque on the $OD^+$ fragment leading to high rotational excitation. Gervais *et al.* [**38**] also found high rotational excitation in diatomic ion fragments from HOD having insufficient internal energy to predissociate, with the highest being from these two di-cation states. For the trajectories here that produce the $OD^+$ ion with enough internal energy to predissociate via the $A^3\Pi$ state, this leads to even higher levels of rotational excitation, peaking near $J = 30$, as shown in Fig. 7.3. This rotational distribution leaves its signature in the kinetic energies of the atomic fragments after dissociation, as discussed below.

**7.2.1. Results.** As we have established above, we can identify and select the events undergoing sequential fragmentation via a $D^+ + OD^+$ intermediate (via $OD^+$ for short, hereafter) out of all measured $D^+ + D^+ + O$ three-body breakup events. Here, we focus on what one can learn about the sequential process by employing the methodology described in the preceding section.

First, we determine which three-body dissociation limit is associated with sequential fragmentation via $OD^+$. To that end, in Fig. 7.4 we present all the measured $D^+ + D^+ + O + 2e^-$ events (red-solid line), resulting from the absorption of a single 61-eV photon, as a function of the total energy release, i.e. $E_{\text{release}} = \text{KER} + E_{e_1} + E_{e_2}$, where $E_{e_1}$ or $E_{e_2}$ is the kinetic energy of an electron in the continuum. The expected value of $E_{\text{release}}$ for each dissociation limit is evaluated from the known photon energy, the complete dissociation energy of water, and the initial state (i.e. ground

state) of the heavy water molecule (those locations are marked by vertical lines and labeled by the oxygen final state in Fig. 7.4) though with a small shift down, ∼0.4 eV, due to experimental uncertainties. [1] It is evident from the figure that the likelihood of fragmentation to the lowest two dissociation limits, i.e. $O(^3P)$ and $O(^1D)$, is approximately equal, and each of them is more likely than a breakup to the $O(^1S)$ limit. In the same figure we also plot (blue line) the sequential events via $OD^+$, selected by $KER_{OD} < 2.3$ eV (see Sec. 7.2). Figure 7.4 clearly shows that the sequential fragmentation via $OD^+$ leads solely to the $D^+ + D^+ + O(^3P)$ dissociation limit [2]. We also note that the electrons associated with this sequential breakup exhibit an energy sharing that is typical for direct double-photoionization involving no auto-ionization, as shown in Fig. 7.2(e). Here we see a diagonal stripe in $E_{e_1}$ vs $E_{e_2}$ indicating equal energy sharing between the two ionized electrons associated with the nuclei that breakup sequentially via the $OD^+$ intermediate.

[1] The expected total energy release, $E_{\text{release}}$, is computed by subtracting the complete dissociation energy of the heavy water di-cation into $D^+ + D^+ + O(^3P)$ from the measured photon energy used in our experiment. The accumulated error in the measured $E_{\text{release}}$ and photon energy, as well as uncertainties in the complete dissociation energy of water recommended by NIST, add up to an estimated uncertainty of the order of the energy shift needed to match the measured spectrum shown in Fig. 7.4.

[2] The broad energy distribution (clearly visible in the sequential breakup) is mainly due to the extended target along the light-propagation direction, energy resolution, and the spread in center-of-mass momentum that cannot be corrected for because the neutral oxygen fragment is not detected, but evaluated from momentum conservation.

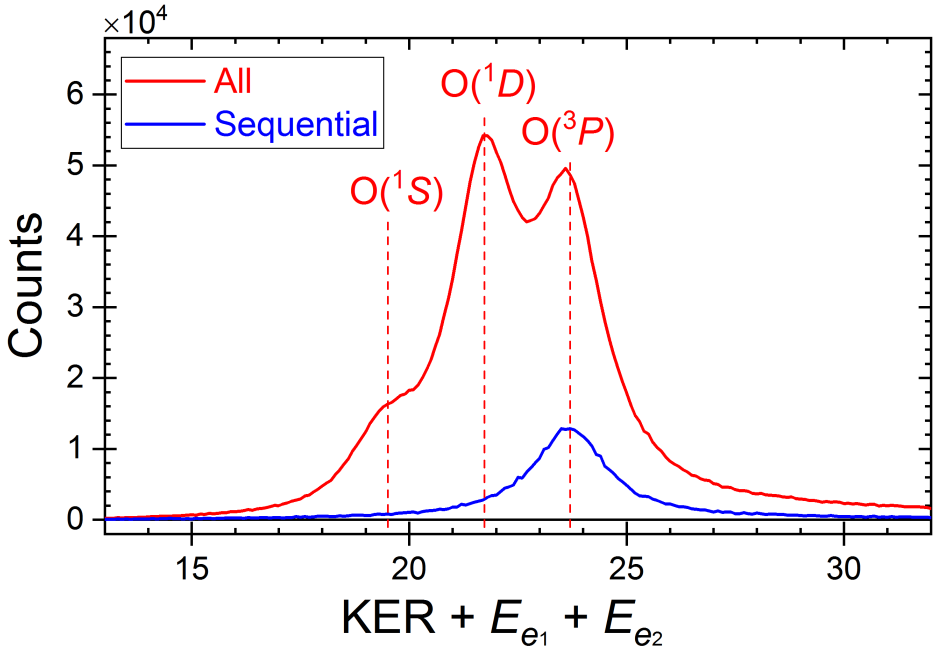


FIGURE 7.4. Total energy release distribution following double-photoionization of water, i.e. $N(\mathrm{KER} + E_{e_1} + E_{e_2})$. The vertical lines indicate the expected energy of each $D^+ + D^+ + O$ dissociation limit, which are labeled by the final state of the oxygen and shifted down by 0.4 eV (see text). Note that sequential fragmentation via $OD^+$ correlates only with the $D^+ + D^+ + O(^3P)$ dissociation limit.

Inspection of Fig. 7.1(a) indicates that the $b\,^1\Sigma^+$ state of $OD^+$ correlates to the $2\,^1A_1$ state of $D_2O^{++}$. If the latter state is populated by a vertical transition from the $D_2O$ ground state (i.e. by removing two electrons without changing the internuclear distances or bond angle, which is a reasonable approximation for ionization by a single photon), then a kinetic energy release of about 7 eV is expected in the first fragmentation step, $D^+ + OD^+(b\,^1\Sigma^+)$, on route to $D^+ + D^+ + O(^3P)$.

To verify this suggested pathway we plot in Fig. 7.5(a) the measured sequential fragmentation events [3] leading to $D^+ + D^+ + O(^3P)$ as a function of $\mathrm{KER}_{\mathrm{OD,D}}$ and $\mathrm{KER}_{\mathrm{OD}}$ (i.e. the KER in the first and second fragmentation step, respectively). One can clearly see the feature centered about the expected $\mathrm{KER}_{\mathrm{OD,D}}$ with a broad, relatively flat, $\mathrm{KER}_{\mathrm{OD}}$ distribution extending to about 2.1 eV. This affirms the predicted sequential fragmentation path $D_2O^{++}(2\,^1A_1) \rightarrow D^+ + OD^+(b\,^1\Sigma^+)$, followed by $OD^+(b\,^1\Sigma^+) \rightarrow D^+ + O(^3P)$.

[3] We use the same conditions to select the $D_2O^{2+}$ sequential fragmentation events, specifically $\mathrm{KER}_{\mathrm{OD}} < 2.3$ eV (see Section 7.2).

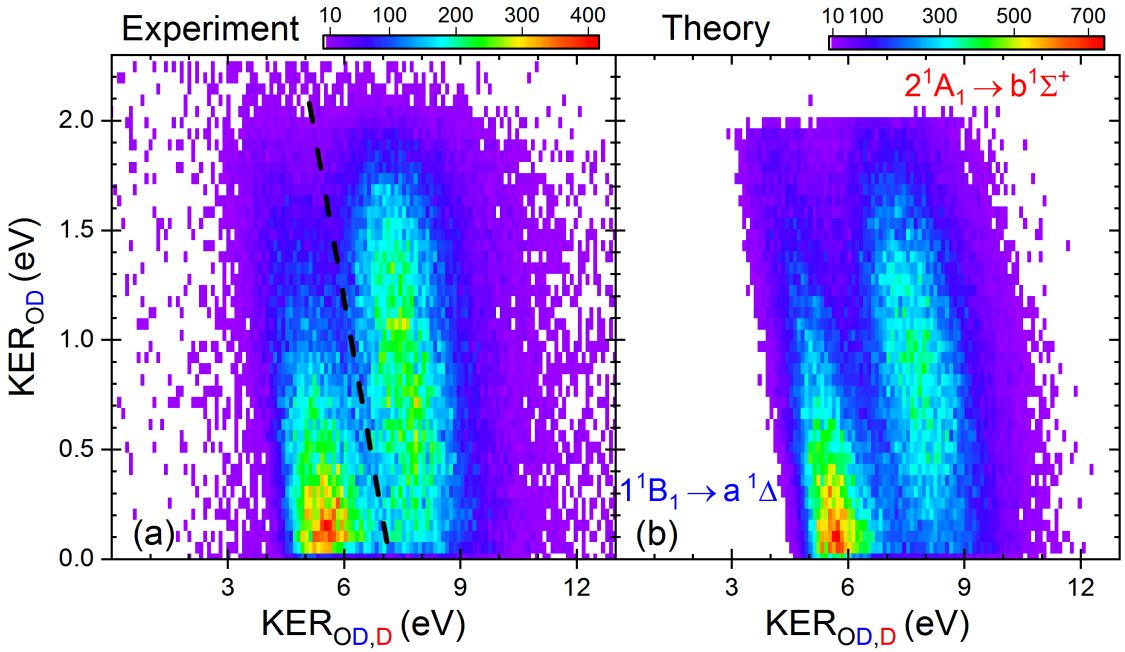


FIGURE 7.5. Sequential fragmentation of $D_2O^{2+}$ into $D^+ + D^+ + O(^3P)$ as a function of $KER_{OD,D}$ and $KER_{OD}$: (a) Experiment and (b) Theory. The two panels nicely match each other, aided by the choice of similar statistics in the theory to match the experimental data quality. The black-dashed line in panel (a) is used to separate the two sequential fragmentation paths (see text), specifically $2\,^1A_1 \rightarrow b\,^1\Sigma^+$ (right) from $1\,^1B_1 \rightarrow a\,^1\Delta$ (left).

As noted in Fig. 2.2, there is a prominent second feature in Fig. 7.5(a), which is centered about a lower $KER_{OD,D}$ of about 5.5 eV. Moreover, the $KER_{OD}$ distribution of this feature peaks near zero and tails off rapidly. The significant differences between the two features suggests another fragmentation pathway.

Examination of the potential energy along the asymmetric stretch coordinate, shown in Fig. 7.1(a), indicates that the $1\,^1B_1$ state of the di-cation, at the equilibrium $R_{OD}$ of water (1.812 a.u.), is about 5.5 eV above the $D^+ + D^+ + O(^3P)$ dissociation limit associated with the first fragmentation step, $D^+ + OD^+(a\,^1\Delta)$. Therefore, we attribute this lower $KER_{OD,D}$ feature to sequential fragmentation initiated by double-photoionization to the $1\,^1B_1$ state, which is consistent with the results of our classical trajectories on the $1\,^1B_1$ potential surface. This state, then, dissociates into $D^+ + OD^+(a\,^1\Delta)$. Later, the $a\,^1\Delta$ state predissociates into $D^+ + O(^3P)$ due to its spin-orbit coupling with the $A\,^3\Pi$ state of $OD^+$. We are not aware of a reported lifetime for the $a\,^1\Delta$ state. However, we expect it to

be similar to that of the $b\,^1\Sigma^+$ state given that both are coupled to the $A\,^3\Pi$ state, and that their spin-orbit matrix elements have similar magnitudes according to calculations by de Vivie *et al.* [**27**]. In summary, we have discovered another sequential fragmentation path, namely $D_2O^{2+}(1\,^1B_1) \rightarrow D^+ + OD^+(a\,^1\Delta)$ followed by $OD^+(a\,^1\Delta) \rightarrow D^+ + O(^3P)$.

In Fig. 7.5, we also compare the measured and simulated KER-correlation maps to each other. In this simulation, we assumed that the cross-sections for double-photoionization are the same for the $2\,^1A_1$ and $1\,^1B_1$ states. Both features in the figure match very well, suggesting that our classical trajectory approach, though it approximates the nonadiabatic dynamics, captures the essence of the physical process. Moreover, the measured KER-correlation map enables separation between the two sequential-fragmentation pathways, thus allowing their direct comparison without recourse to theory. This separation [4] is accomplished by selecting events to the right ($2\,^1A_1 \rightarrow b\,^1\Sigma^+$) or left ($1\,^1B_1 \rightarrow a\,^1\Delta$) of the black-dashed line shown in Fig. 7.5(a). Note that this line has a slight tilt that reflects a constant total KER (specifically, we used 7.18 eV in the analysis).

[4]This visualization of our pathway separation method, though correct, is simplified in practice by plotting the same data as a function of $KER_{OD,D} + KER_{OD}$ and $KER_{OD,D} - KER_{OD}$ (i.e., a 45° rotation of the spectrum in Fig. 7.5). Then, we project it onto the $KER_{total} = KER_{OD,D} + KER_{OD}$ axis, and separate events larger than $KER_{total} = 7.18$ eV to one channel ($b\,^1\Sigma^+$), while events with smaller $KER_{total}$ are associated with the other channel ($a\,^1\Delta$).

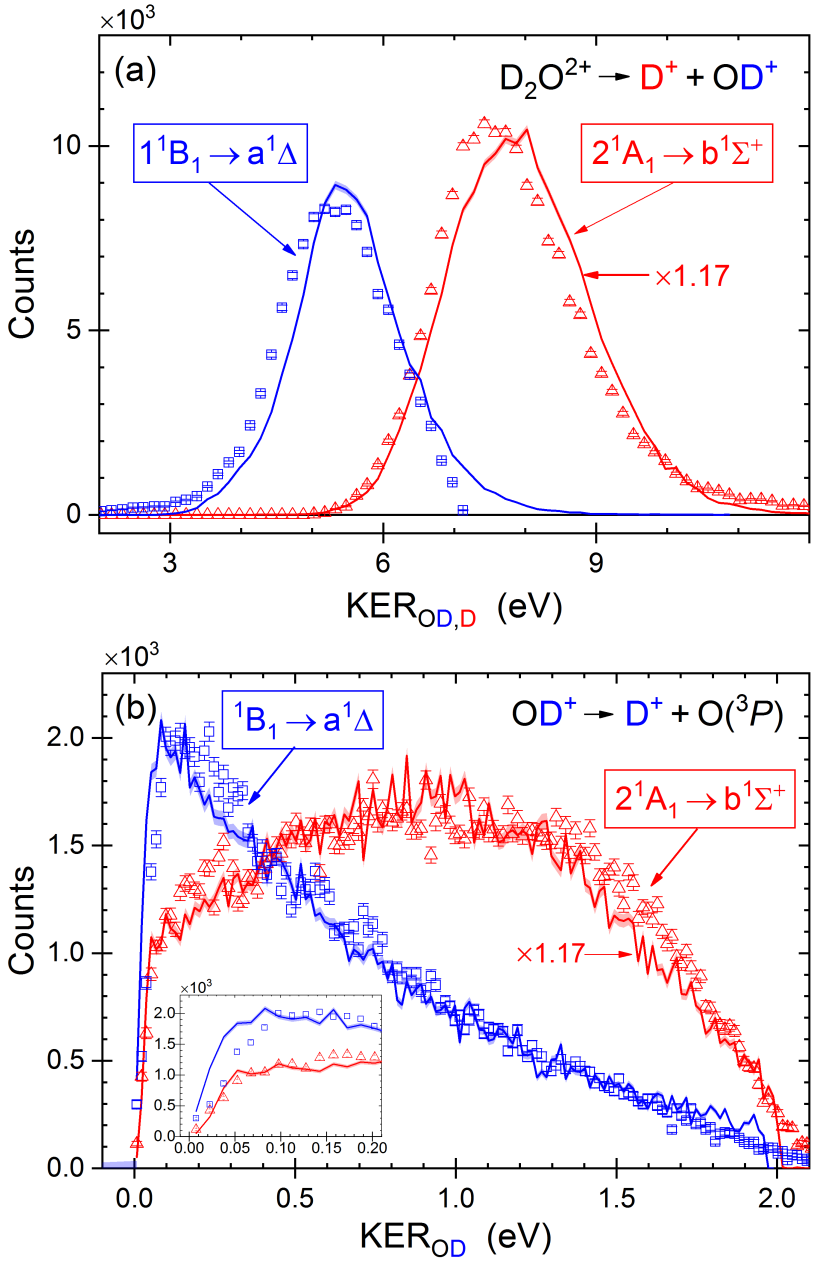


FIGURE 7.6. Sequential fragmentation of $D_2O^{2+}$ into $D^+ + D^+ + O(^3P)$ as a function of (a) $KER_{OD,D}$ and (b) $KER_{OD}$ (Inset: Zoom-in of low energy range). Comparison of experiment (symbols) and normalized theory (solid lines) for the two fragmentation pathways (and associated states) identified and separated using Fig. 7.5(a) (see text). As indicated on the figure, the theory scaling of one path is a factor of 1.17 larger than the other one (see text). The high energy cutoff in the measured $1\,^1B_1$ to $a\,^1\Delta$ data in the upper panel is likely due to the imperfect separation of the two channels by the black-dashed line in Fig. 7.5.

In Fig. 7.6, we compare the measured KER distributions to the calculated ones for both steps of each sequential fragmentation path. As neither our theory nor experiment are absolute, we scale them to match using a least square fit. Specifically, we scale the theory to preserve the measured information on the relative likelihood of the two sequential fragmentation paths. Note that the calculated KER distribution associated with the $2\,^1A_1 \rightarrow b\,^1\Sigma^+$ path is scaled by an additional factor of 1.17 relative to the scaling of the $1\,^1B_1 \rightarrow a\,^1\Delta$ path, as indicated in Fig. 7.6. This difference is mainly due to the relative magnitude of the cross-sections for double-photoionization by a single 61-eV photon landing on the $2\,^1A_1$ and $1\,^1B_1$ states of $D_2O^{2+}$.

Our classical trajectory calculations propagate the same number of trajectories ($10^6$) on each di-cation surface, with no regard to the cross-section for producing that di-cation state in double-photoionization. As a result, those calculations can accurately reflect the branching ratios between two- and three-body breakup channels on each electronic state, but provide no information about the photoionization cross-sections. In contrast, the experiment does determine the ratio between the two, thus providing a test of the magnitudes of the cross-sections to be determined by future double-photoionization calculations.

At a glance, the calculated and measured KER distributions associated with the $D_2O^{2+} \rightarrow D^+ + OD^+$ breakup, shown in Fig. 7.6(a), match each other nicely. However, a careful inspection shows that the calculated distributions are shifted up by about 0.15 eV. We suspect that this difference stems from approximating the initial wave function of $D_2O$, which is projected to the $D_2O^{++}$ states, by a product of normal mode harmonic oscillators instead of a more accurate representation including the effects of the anharmonicity in the ground state potential energy surface. Similar discrepancies have been observed in $H_2$ and were corrected by using a Morse potential to represent the initial state [**111**].

The calculated and measured KER distribution associated with the second fragmentation step, namely $OD^+ \rightarrow D^+ + O$ shown in Fig. 7.6(b), match very well for both sequential fragmentation paths. The differences between the KER distributions associated with these two fragmentation paths, noticeable in Fig. 7.5, become more apparent however. The sequential fragmentation via the $b\,^1\Sigma^+$ state yields a broad, relatively flat KER distribution peaked around 0.9 eV, while the

fragmentation via the $a\,^1\Delta$ state peaks at a much lower KER, ~0.15 eV, and falls off rapidly with increasing KER.

It is important to note that the KER in the predissociation of the $OD^+$ images the internal energy of this diatomic ion above the $O(^3P)$ dissociation limit (i.e. the internal energy is stored in highly excited vibrational and rotational states). This assertion is correct if the assumption, used in our modeling, that all rovibrational states above the $D^+ + O(^3P)$ dissociation limit predissociate is valid. The comparison of experiment and theory in Fig. 7.6(b) validates that assumption. The remaining population, in the lower rovibrational states of the $a\,^1\Delta$ and $b\,^1\Sigma^+$ states of $OD^+$, is measured as the dominant two-body breakup, $D^+ + OD^+$ [see previous reports on $H_2O$ [**80**, **99**]].

In addition to the internal energy of the $OD^+$ ion, our classical trajectory simulations provide the angular momentum distribution $P(J)$ of each state of $OD^+$, shown in Fig. 7.3. Similar to the KER distributions, here too, the $P(J)$ distributions of the $a\,^1\Delta$ and $b\,^1\Sigma^+$ states are different. The former peaks at a lower $J$ (~26) and has a long tail extending all the way to $J = 0$, while the latter peaks around $J = 30$ and is much narrower.

There are two observable consequences of these predicted $J$ distributions. First, the higher rotational angular momentum implies that the orientation of the long-lived $OD^+$ fragment will not be correlated with the direction of emission of the first $D^+$ fragment. This is in agreement with the nearly uniform $\theta_{OD,D}$ angular distribution seen in the experiment in Fig. 7.2. Second, the high rotational angular momentum of the $OD^+$ fragment results in a barrier with respect to the dissociation limit (i.e., a centrifugal barrier), as indicated in Fig. 7.3(c,d). The internal energy of the of the $OD^+$ fragment is reflected in the distribution of $KER_{OD}$ to which all angular momenta contribute. The threshold behavior in Fig. 7.6(b) in which the KER distribution vanishes as $KER_{OD}$ goes to zero has its origin in the fact that only a small fraction of the $OD^+$ ions is produced with zero rotational angular momentum, and only this contribution can yield zero KER. The steady rise in counts from zero follows the deformation of the $^3\Pi$ state as the centrifugal barrier increases with increasing angular momentum seen in Fig. 7.3(c-d). This threshold behavior of the $KER_{OD}$ distribution in the trajectory calculations is also seen in the experimental data, in close agreement with the theoretical prediction.

Due to the usefulness of the Newton-like plots in interpreting the final COLTRIMS measurements presented in Chapter 3, it is instructive to plot only the final-momentum vectors that proceeded through the sequential breakup channel outlined in this chapter as a Newton-like plots. To that end, we plot the two distributions in Fig. 7.5 as Newton-like plots, utilizing the dashed-line in Fig. 7.5(a) to separate the two distributions in the experimental data (the theoretical data is already separated). In Fig. 7.7 we have the resulting plot for the $2^1A_1$ state, followed by the resulting plot for the $^1B_1$ state in Fig. 7.8. These plots are rather perplexing and require explanation so we will examine the experimental Newton-like plot for the $2^1A_1$ state, Fig. 7.7(a), for example. For one COLTRIMS measurement producing this figure, one proton can be in the upper right ring of counts on the approximate $P_z$ interval of $[0, 45]$ a.u. with a $P_y$ interval of $[0, 45]$ a.u.. The other proton will be on the approximate $P_z$ interval of $[0, 20]$ a.u. with a $P_y$ interval of $[-25, 0]$ a.u., which will then produce an inferred neutral on the lower distribution in the negative $P_z$ region (i.e. on the approximate $P_z$ interval of $[-60, 0]$ a.u. with a $P_y$ interval of $[-45, 0]$ a.u.). However, since the two deuterium ions are indistinguishable the resulting Newton-like plot produces a mirror image of the prescribed measurement and is ultimately from the unequal energy sharing between the two deuterium ions. Fig. 7.5 shows the resulting two protons will have drastically unequal energy sharing, and with the center-of-mass constrained to zero, this will cause the neutral fragment to be displaced off of the line bisecting the two protons, namely $P_z = 0$. Moreover, in Fig. 7.7 and Fig. 7.8, the full ring of counts is indicative of the loss of angle correlation originally discovered in the $\beta$ vs. KER plot (Fig. 2.2). Thus, COLTRIMS future measurements producing Newton-like figures such as Fig. 7.7 and Fig. 7.8 now have evidence to suggest non-sequential dynamics.

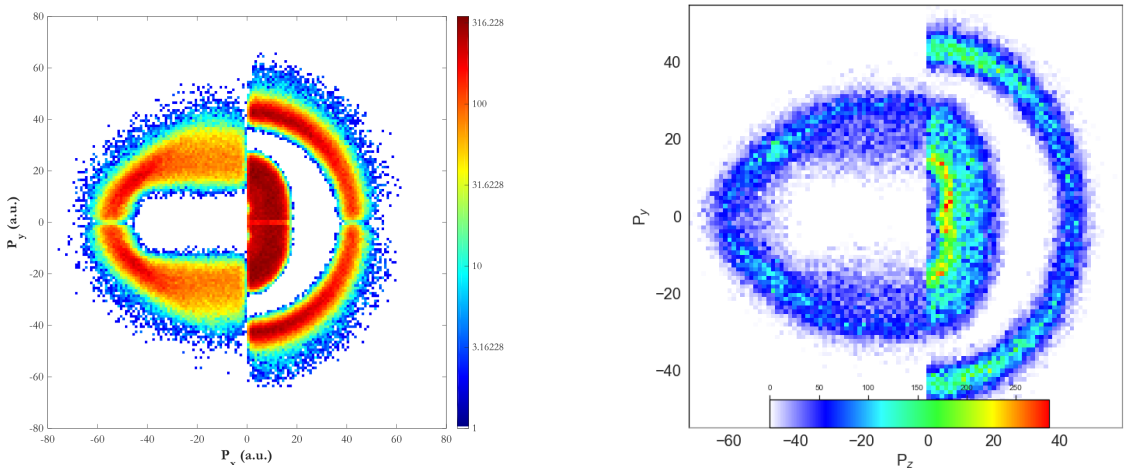


(a) Experiment (b) Theory

FIGURE 7.7. Newton-like plots for the sequential breakup channel of $2^1A_1$ state of $D_2O^{++}$.

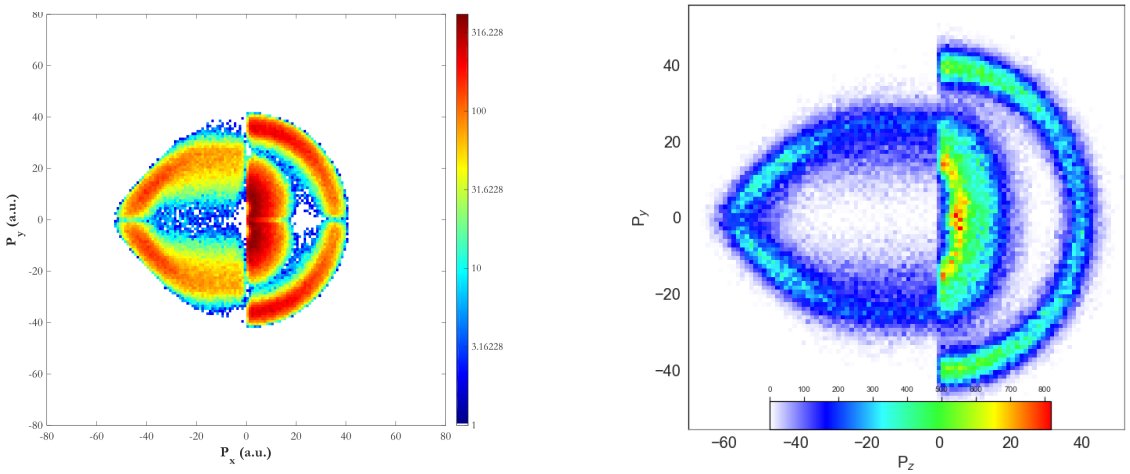


(a) Experiment (b) Theory

FIGURE 7.8. Newton-like plots for the sequential breakup channel of $^1B_1$ state of $D_2O^{++}$.

Indeed, Larsen *et al.* [**64**] initially found similar plots for one of the breakup channels of ammonia (see Fig. 7.9). The puzzling results were later resolved by proposing a sequential mechanism and invoking the "appearance window" argument (see Fig. 9 of [**64**]) outlined in this chapter. The sequential breakup pathway in that work was via a four-body fragmentation channel

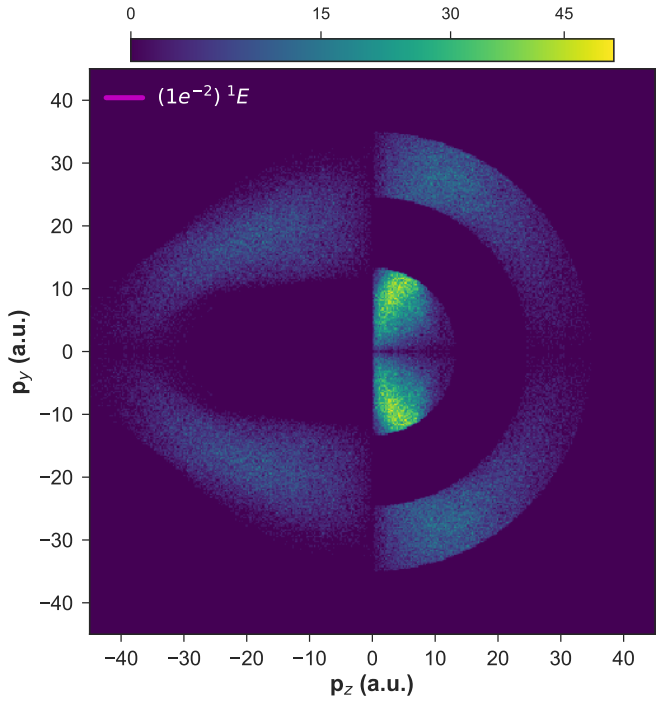


FIGURE 7.9. Momenta image plot for the complete breakup of $NH_3^{2+}(^1E) \rightarrow N + 2H^+ + H$ (see text). The full analysis of the COLTRIMS measurement of ammonia after one photon double-photoionization can be found in [**64**].

$$\begin{aligned} &NH_3^{++}(\,^1E) \rightarrow H + H^+ + NH^+(X\,^2\Pi) \\ &\text{followed by } NH^+(X\,^2\Pi) \rightarrow H^+ + N(^4S)\,, \end{aligned} \tag{7.6}$$

where the second fragmentation step involves predissociation of the $NH^+$ due to spin-orbit coupling between the X $^2\Pi$ state and the $^4\Sigma^-$ state, as described in Larsen *et al.* [**64**]. The associated momentum image from such a breakup channel is shown in Fig. 7.9. Note that because this channel has all four bodies dissociate, the inferred neutral in this image is a sum of the two separate nitrogen and hydrogen atoms. This novel momentum image requiring theoretical simulations to explain, highlights the necessity of nuclear simulations to guide experimental interpretations of future COLTRIMS experiments that explore more complex molecules.

### 7.3. Conclusion

We studied the sequential fragmentation of water following double ionization by a single photon in unprecedented detail. The events associated with this process were separated experimentally from other fragmentation processes leading to the same final three-body channel, namely $D^+ + D^+ + O(^3P)$, using the native frames method and taking advantage of the rotation of the metastable $OD^+$ intermediate in the fragmentation plane. We identified two sequential-fragmentation pathways involving different electronic states and followed them step by step, namely Eqs. 7.2 and 7.3. In both pathways, the second fragmentation step involves predissociation of the $OD^+$ due to spin-orbit coupling of the populated $b\,^1\Sigma^+$ and $a\,^1\Delta$ states with the $A\,^3\Pi$ state.

The results of our classical trajectory propagation on the $D_2O^{++}$ potential surfaces are overall in excellent agreement with the experimental data associated with both sequential fragmentation paths and the steps each one undergoes. We draw particular attention to our ability to calculate the internal energy of the intermediate $OD^+$ molecule, and probe it experimentally above the $D^+ + O(^3P)$ dissociation limit. Likewise, the angular momentum distribution of the intermediate $OD^+$ molecule has been computed and the predicted impact on the low KER distribution has been measured. Moreover, this work has provided novel interpretations to nuclear measurements that are required for future COLTRIMS experimentation on polyatomic molecules, as is evident in the immediate application in the nuclear breakup of $NH_3^{++}$ done by Larsen *et al* [**64**].

Though our methodology has been demonstrated for sequential fragmentation of water following double ionization by a single photon, it is not limited to this specific case. The combination of kinematically complete momentum imaging measurements, classical trajectory simulations on the relevant potential energy surface, and the native frames method should be applicable to a wide range of polyatomic molecules as long as the energy deposited in the system is known and there is a clear signature enabling identification of sequential fragmentation from other processes, like the rotation of the intermediate molecular fragment in our test case. This methodology enhances our capabilities for exploring molecular reaction dynamics on the potential energy surface around asymmetric stretch that is commonly the path for forming an intermediate molecular fragment in route to sequential fragmentation. The observation of sequential steps in a molecular dissociation

reaction via their unambiguous signature in the momenta of the fragments has added the dimension of time to an essentially time-independent measurement.

For completeness, Fig. 7.10 and Fig. 7.11 presents the initial and final configurations for the $2^1A_1$ and $^1B_1$ state, respectively, as momentum plots. The top row of Fig. 7.10 is the initial and final momenta configuration for the three-body breakup channel of the $2^1A_1$ state. The bottom row of the same figure is the initial and final momenta configuration for the two-body breakup channel of the $2^1A_1$ state. Fig. 7.11 is the same layout as Fig. 7.10, but for the $^1B_1$ state. We note how the two-body path selects particularly different segments of the initial Wigner distribution for the $2^1A_1$ state, but the initial conditions for both two and three-body paths for the $^1B_1$ state are identical. This indicates the $^1B_1$ state's dynamics are not selected by specific regions of phase space. However, the $2^1A_1$ state's dynamics are more *tunable*, in that specific two or three-body dynamics maybe selected for by starting with markedly different initial conditions. Put in another way, the initial conditions generated by normal modes of neutral water are in a region near the $2^1A_1$ state's *separatrix* [**26**] in phase space, while the same initial conditions are not in the region near $^1B_1$ state's separatrix once the vertical transition is applied. For the nuclear breakup of $D_2O^{++}$, the separatrix is a surface in phase space that separates initial conditions that only evolve with two or three-body dynamics. For a classical example of this phenomenon, consider the separatrix in phase space that separates the distinct dynamics of a swinging pendulum. Thus, the $2^1A_1$ state allows one to follow the final trajectory back in time to a particular region in phase space. This hint that probing the initial conditions and therefore moving over the separatrix, may produce different results for the $2^1A_1$ but not for the $^1B_1$ state will be explored in a later chapter.

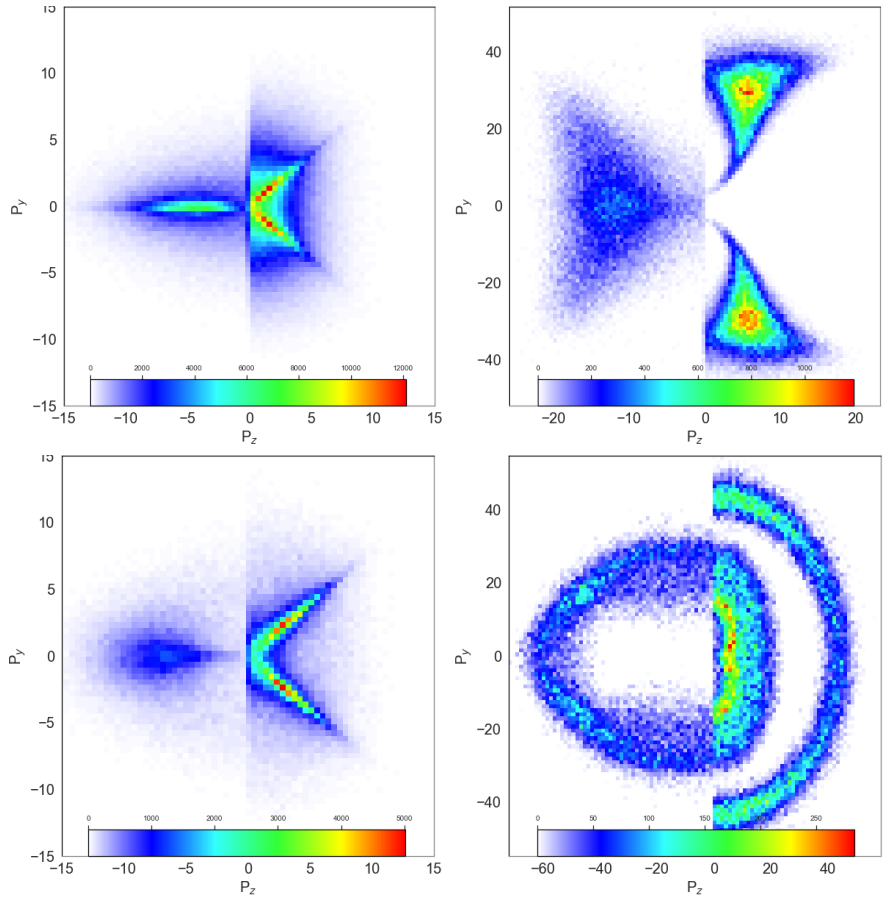


FIGURE 7.10. $2^1A_1$ Top row: Density plots of the initial(left) and final(right) momenta configuration for the three-body breakup channel. Bottom row: Density plots of the initial(left) and final(right) momenta configuration for the two-body breakup channel. The left column is markedly different, implying tunable dynamics (see text).

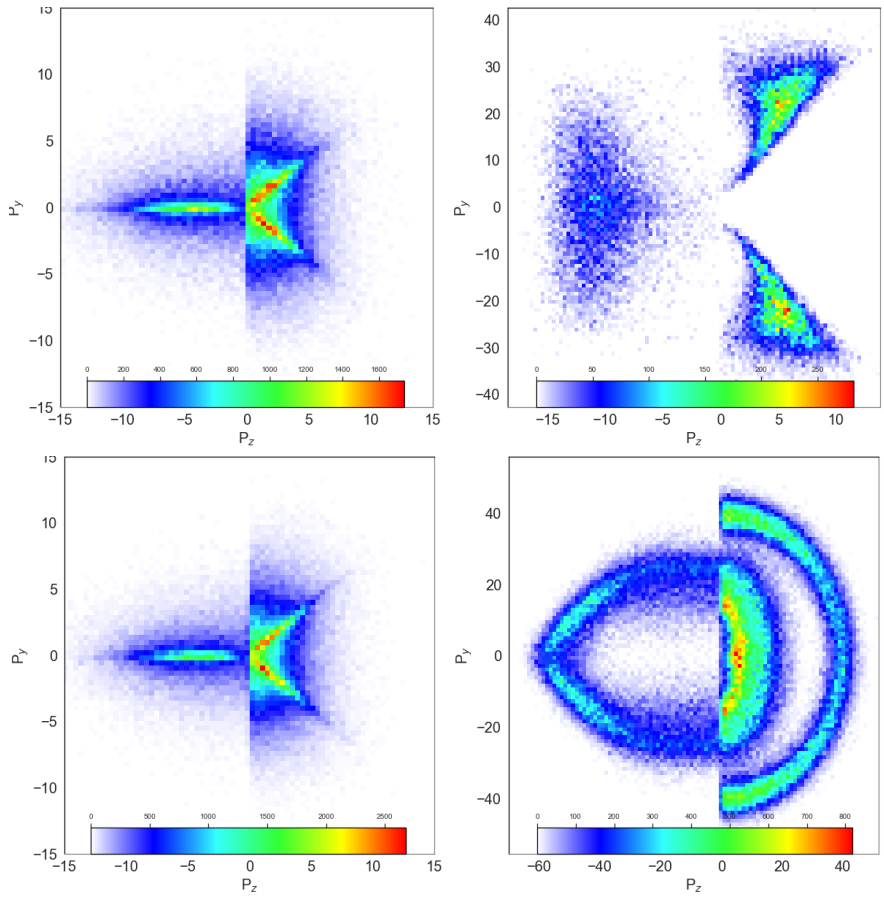


FIGURE 7.11. $^1B_1$ Top row: Density plots of the initial(left) and final(right) momenta configuration for the three-body breakup channel. Bottom row: Density plots of the initial(left) and final(right) momenta configuration for the two-body breakup channel. The left column is identical, implying non-tunable dynamics (see text).

CHAPTER 8

# Strong Field Ionization of $D_2O$

## 8.1. Multiphoton vs. Single photon

The previous chapters showed excellent agreement between the single-photon four-fold coincidence (i.e. two electrons in coincidence with two nuclear fragments) measurements in the COLTRIMS experiment and the classical trajectory analysis that assumed a vertical transition (see Sec. 5.1.1) of the initial ground state wavefunction onto each excited state of $D_2O^{++}$. Given this agreement with previous single-photon experiments, a recent strong-field double-photoionization of $D_2O^{++}$ experiment [**18**] sought to address a question of whether strong-field double-photoionization prepares a similar superposition of electronic states of the di-cation, and whether the wave packet launched on each state via strong-field ionization (SFI) is similar to the one launched by single-photon ionization – i.e. can the SFI process be thought of as *vertical*? These measurements, calculations and our analysis may help interpret previous work that made use of SFI as probe of excited state dynamics [**29**, **35**, **55**] and for vibrational wave packet holography [**76**].

This SFI experiment is different than the COLTRIMS experiment in a few notable ways so we briefly mention them here. The apparatus used to carry out the weak-field, 10 fs, pulse measurements is described in detail in Refs. [**19**, **127**]. The same procedure outlined in Ref. [**13**] was followed for the 40 fs measurements. The estimated intensities for the 10 fs and 40 fs measurements are 400 TW/cm$^2$ and 600 TW/cm$^2$, respectively. The key difference between the COLTRIMS experiment and the SFI experiment was in the COLTRIMS experiment two separate position and time-sensitive detectors are used for measuring the electrons and the nuclei in a four-fold coincidence measurement. However, in the SFI experiment the extracted ions and electrons are recorded using one microchannel plate (MCP), phosphor screen, and Timepix3 camera with 1.5 ns time resolution (see Ref. [**18**] for more details).

As noted in the previous chapters, the yields as a function of $\beta$ and KER produces separate islands of density counts representing different electronic states of $D_2O^{++}$ which provided a state-selective measurement. We therefore compare the same calculated double-photoionization yield as a function of $\beta$ and KER with the new SFI measurements as a gauge of how well the SFI measurement is state-selective. Fig. 8.1 shows the measured and calculated $D^+/D^+/O$ yield. Panel (a) shows the measured yield as a function of $\beta$ and KER. Panel (b) shows the calculated yield vs $\beta$ and KER assuming vertical ionization with equal population of the di-cation states and, therefore is the exact same calculation that produced Fig. 6.1. Panel (c) shows the same results as panel (b) with coefficients for the first 8 states of the di-cation fitted to achieve the best agreement with the measurements. Panel (d) shows the calculated results accounting for experimental broadening of the features due to the limited resolution of our velocity-map imaging (VMI) apparatus.

One benefit from single-photon COLTRIMS experiment is being kinematically complete allows for state information on the neutral fragment to provide a way to further refine the data. For example, in the water measurement presented in Chapter 2 the data could be analyzed by gating on each separate streak of counts that represent the three electronic states of the inferred oxygen fragment (see Fig. 2.1(a)). The multiphoton SFI experiment losses this neutral fragment information due to the use of only one detector and, therefore cannot gate on the specific states of the oxygen atom. This deficiency in the data-refinement process manifest in the fitting procedure. Thus, states of the same $C_{2\nu}$ symmetry (e.g. $^1B_1$ and $^3B_1$) have been incoherently summed together. From now on we just use the word "state" to represent different $C_{2\nu}$ symmetries. Based on the islands of high density seen from Fig. 8.5, a simple principle component analysis (PCA) [**36**] procedure that minimizes the residual was used to reproduce the $\beta$-KER plot. Different states population have been fitted and the reconstructed $\beta$-KER plot is shown as Fig. 8.1(c). The fitted-relative-state population has been listed as the table in the figure as well. The coefficients from the fit are decreasing with increasing ionization potential, roughly in agreement with expectations from a simple quasi-static tunnel ionization model of Ammosov-Delone-Krainov (ADK theory [**101**]). An interesting observation is that while the relative weights for states that involve removing electrons from different orbitals are in reasonable agreement with predictions from ADK theory, the relative weights for singlet states that involve removing two electrons from the same orbital with opposite spins are significantly higher

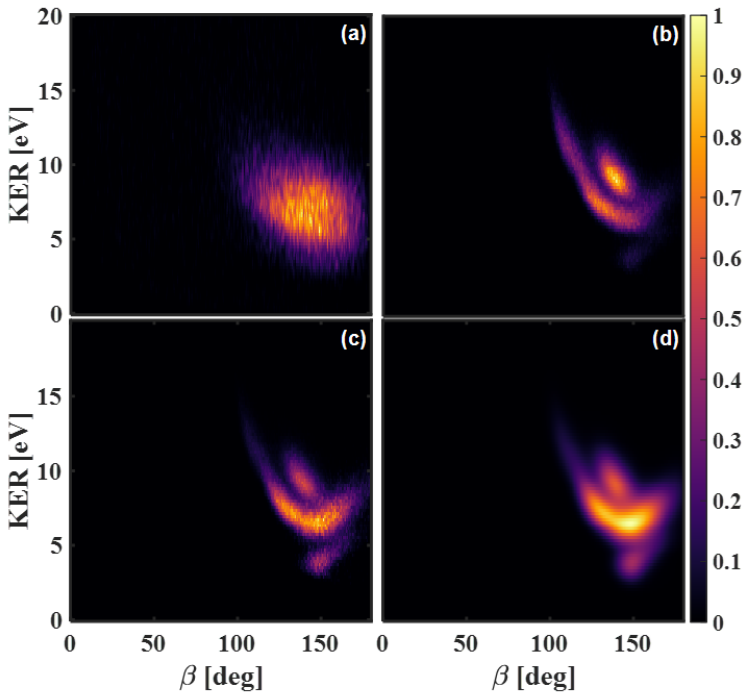


| State | $^*B_1$ | $2^1A_1$ | $^*A_2$ | $^*B_2$ | $3^1A_1$ |
|---|---|---|---|---|---|
| Weight | 1 | 0.804 | 0.287 | 0.163 | 0.092 |

FIGURE 8.1. Measured and calculated $D^+/D^+/O$ yield as a function of angle between the two $D^+$ ions' momentum, $\beta$, and the kinetic energy release (KER). Panel (a) Measured coincidence $D^+/D^+/O$ yield as a function of $\beta$ and KER for laser parameters described in the text; (b) Simulated $D^+/D^+/O$ yield as a function of $\beta$ and KER for equal population of each of the first nine states of the di-cation; (c) simulation $\beta$-KER with fit; (d) simulation $\beta$-KER with experimental resolution included. The table at the bottom lists the relative fitting populations for each states where the states are labeled with their $C_{2\nu}$ symmetry due to lack of the spin information in the observable. Details are outlined in the text.

than predictions based on ADK theory. This observation may indicate cooperative behavior, or non-sequential double-photoionization to states of the di-cation that involve removing two electrons from the same orbital.

The fitting in Fig. 8.1(c) only coarsely matches the measurements shown in Fig. 8.1(a). Although the experimental yield shows a center of mass similar to the calculations, the distinct state resolved features in the $\beta$-KER plot are not captured in the SFI results. An important first check

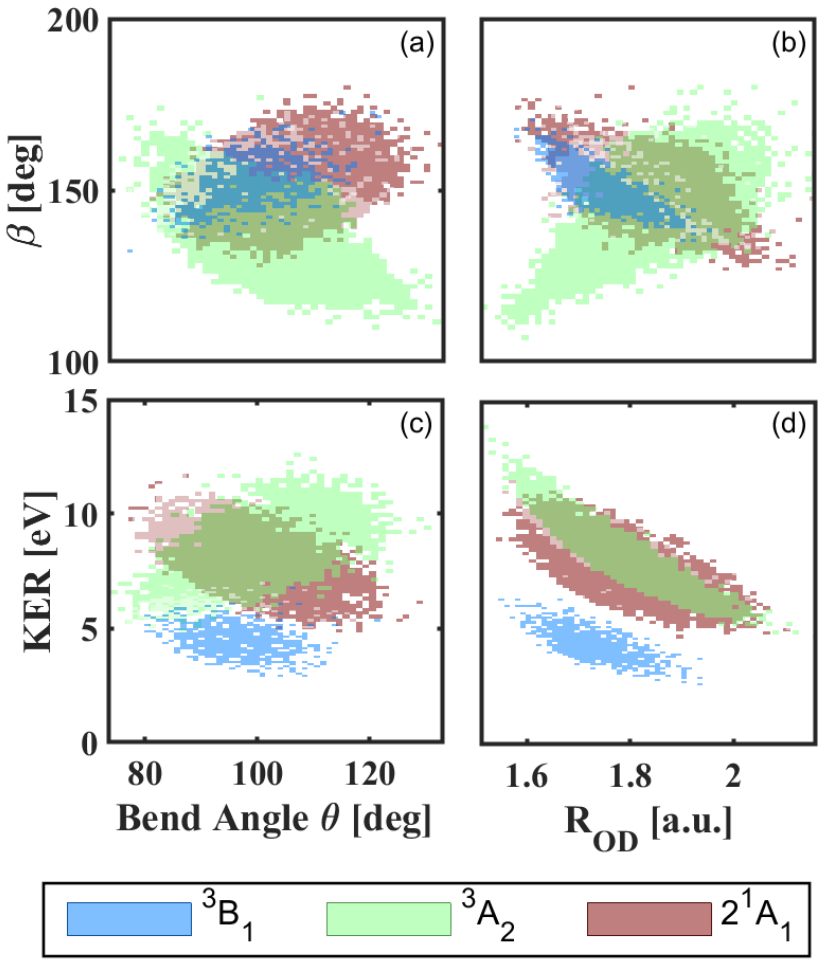


FIGURE 8.2. Calculated $D^+/D^+/O$ yield as a function of KER, $\beta$ and initial O-D separation or D-O-D bend angle $\theta$ for three states. The top left panel (a) shows the $D^+/D^+/O$ yield as a function of initial D-O-D angle and final $\beta$. Panel (b) shows the $D^+/D^+/O$ yield as a function of initial O-D distance and final $\beta$. Panel (c) shows the $D^+/D^+/O$ yield as a function of initial D-O-D angle and final KER. Panel (d) shows the $D^+/D^+/O$ yield as a function of initial O-D distance and final KER. The color coding here is consistent with Fig. 8.5.

that we carried out in addressing this discrepancy is to determine whether our experimental resolution broadens the features such that they are no longer resolved. Using the coincidence events from 2 body dissociation channel ($D^+/D^+/O$), we obtained an uncertainty for the measured $D^+$ momentum of 2.7 a.u by checking their nature of momentum conservation in all three dimensions ($p_x$, $p_y$ and $p_z$). The energy of each $D^+$ ion in the 3 body channel is about 4.5 eV. Thus the

uncertainty of KER is calculated to be $\delta\text{KER} = \sqrt{2}p\delta p/m = 0.99$ eV. Similarly one can obtain the uncertainty of angle between the two $D^+$ momentum to be $\delta\beta = \sqrt{2}\delta p/p = 6.24°$.

Applying the PCA, together with the experimental resolution correction, yields Fig. 8.1(d). The agreement between theory and experiment is still relatively poor: Notably, the islands corresponding to the $^1B_1$ and $^3B_1$ states are absent in the measurements. In the panel Fig. 8.1(d), where the states are blurred according to our instrument response function, the state islands feature are still present. This is completely at odds with the experimental yield shown in Fig. 8.1(a), where no discrete features are present. Thus, we conclude that there has to be some mechanism that drives the difference between simulation and the experiment. We note that this disagreement between experiment and theory is independent of exactly what representation one chooses (i.e. which observables to look at), and a number of different data representations are shown in the Fig. 8.3 and Fig. 8.4.

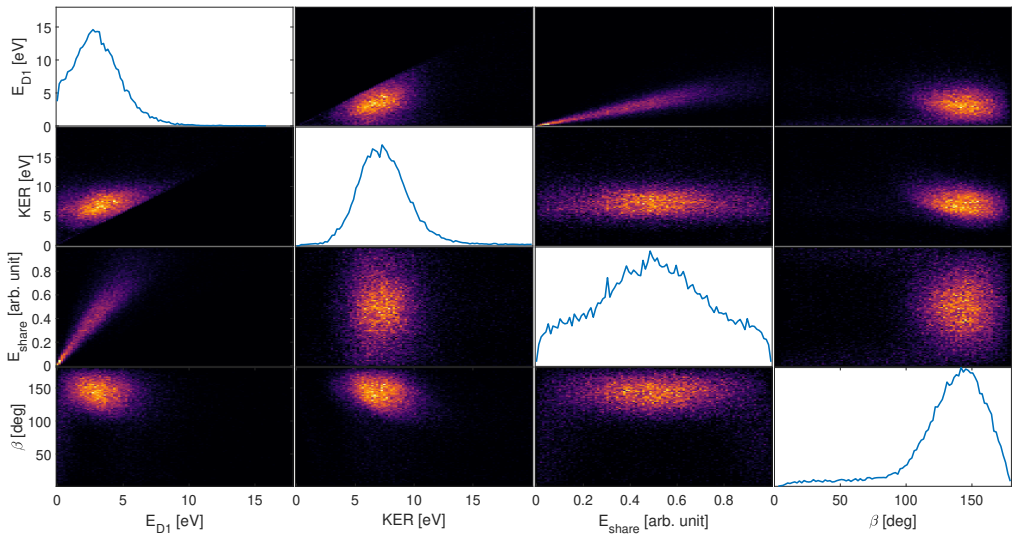


FIGURE 8.3. Representations of the multi-dimensional $D^+/D^+/O$ coincidence data along various coordinates. Shown are KER, $\beta$, $E_{D1}$ and $E_{share}$ cuts of the data along each of these coordinates in a matrix style plot. Here the diagonal represents the one-dimensional normalized line-out along each of the aforementioned axes.

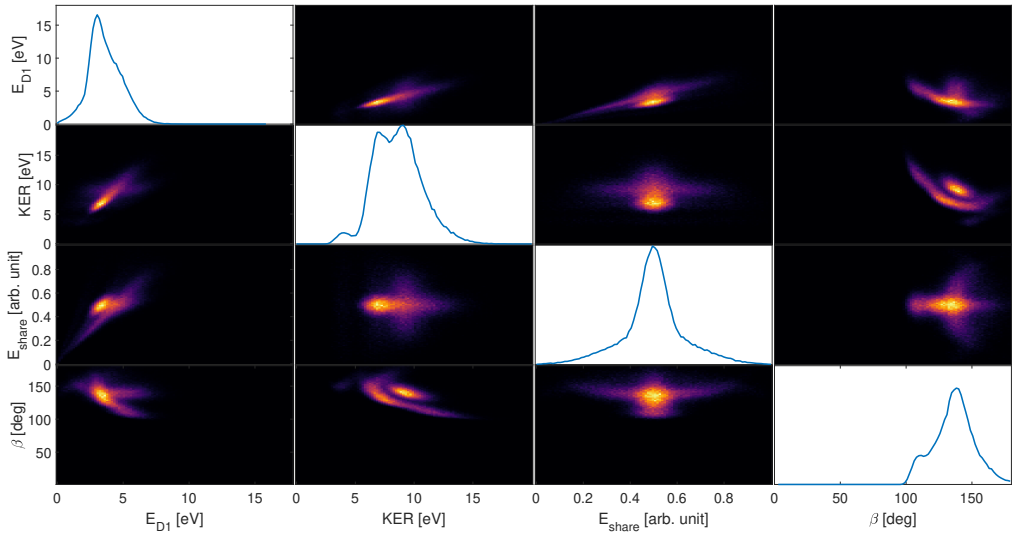


FIGURE 8.4. Cuts of theoretical results along the same coordinates outlined in Fig. 8.3 for the $D^+/D^+/O$ fragmentation channel in the classical trajectory simulations.

## 8.2. Failure of the Franck-Condon Approximation

The calculated and measured $\beta$-KER plots show some rough agreement, but disagree on many details, so it is natural to ask whether the discrepancies can be due to dynamics occurring during the SFI process. In particular, we consider the role of wave-packet reshaping (due to coordinate-dependent ionization rates for example) and nuclear dynamics (such as bending or rotation). As a first test of how much displacement the wave packet would need to alter the $\beta$-KER plot, we mapped the correlation between initial and final values for the distribution of sample points used in the classical trajectory calculations. As the dynamics calculations include an ensemble of initial and final coordinate values, we can plot the final values as a function of the initial ones, allowing us to see if there are correlations between them that lead the strong field reshaping of the ground state wave function to smear out the features in the measured $\beta$-KER plot.

Based on the simulation we constructed the correlation maps shown in Fig. 8.2. Presented are correlation maps for three different electronic states, illustrating the correlation between initial opening angle and symmetric stretch coordinate with respect to the final $\beta$ and KER. The correlation between initial symmetric stretch coordinate $R_{OD}$ and final $\beta$ and KER, or initial DOD angle and final $\beta$ and KER are a result of the finite width of the initial wave function and the nonzero

slope of the di-cationic PES at the Franck Condon location. The upper row in Fig. 8.2, which shows how the final $\beta$ values depend on the initial coordinates, exhibits a strong state dependence. The $^3B_1$ and $2^1A_1$ states show a positive correlation between the final $\beta$ value and the initial opening angle, while the $^3A_2$ state shows a negative correlation. The behavior with respect to the initial O-D distance is the opposite. This illustrates how reshaping or motion of the initial ground state wavefunction can result in different $\beta$ distributions than those predicted for single photon ionization. The bottom row in Fig. 8.2 shows the KER dependence on the initial coordinates. Again, there is a significant dependence of the KER on initial bend angle and O-D distance, illustrating how reshaping or motion of the initial ground state wavefunction can distort the KER distributions predicted for single photon ionization. These plots motivate an examination of the different strong-field mechanisms that can result in non-vertical ionization and the measured $\beta$-KER plots. The sensitivity of the correlation between initial and final coordinates to electronic state is related to the breakdown of the axial recoil approximation and "slingshot" motion of the $D^+$ ions for the $^3B_1$ and $2^1A_1$ states, as discussed in more detail in Chapter 6 and in Ref. [**99**].

The calculated $\beta$-KER plot shown in Fig. 8.1 (b) and Fig. 8.5 are results of applying one-photon perturbation theory to describe the transition from the initial neutral directly into the di-cation states, which is then followed by classical propagation to compute the final fragment energies and angles. In this treatment, the initial Wigner function launched on the di-cation states is then simply the Wigner function corresponding to the normal-mode ground state of the neutral species, that is, the Franck-Condon wave packet. While this treatment is applicable to weak-field ionization where one-photon perturbation theory is applicable, additional effects are present during SFI that modifies the initial neutral ground-state wavepacket before it arrives on the di-cation surfaces. First, the SFI rate can depend strongly on the nuclear coordinates, an effect which can reshape the initial ground state nuclear wavepacket during ionization. Second, multiple ionization via SFI is typically a sequential process where there is a time delay between the ejection of each liberated electron, thereby giving the nuclei a chance to relax and rearrange in between different ionization events. Finally, since there is still a strong-field present during this time delay, near-resonant laser-driven

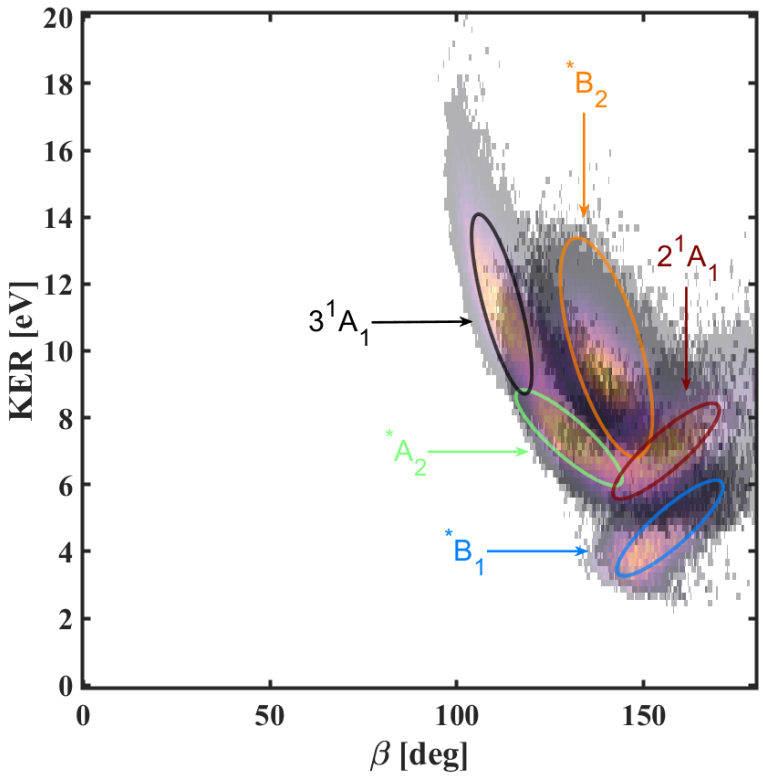


FIGURE 8.5. Transparent theoretical $\beta$-KER plot analogous to Fig. 6.1, which were generated from the simulations outlined in Chapter 4 for comparing with the SFI experiment. Annotations of the specific states associated with each distinct spectral feature are shown (ovals). A state dependent color coding consistent with Fig. 8.2 is adopted for clarity in the discussion within this chapter.

electronic transitions can occur, causing additional non-ionizing electronic transitions that reshape the nuclear wave packets while the molecule is in an intermediate ionic state.

We now outline each of these effects in more detail. We do not attempt a complete treatment of $D_2O$ double-photoionization in strong-fields with all degrees of freedom active, which although desirable, represents a massive theoretical and computational task. Rather, we limit ourselves to outlining each effect using simplified reduced-dimensionality models. Since ionization to both the X and A cation states is expected to occur [**17**], modifications and dynamics arising from ionization to both X and A are used to exemplify these effects.

*Coordinate-dependence of the SFI rate*: SFI with low-frequency fields can be envisioned as a quasistatic tunnel ionization process where the ionization rate depends exponentially on the

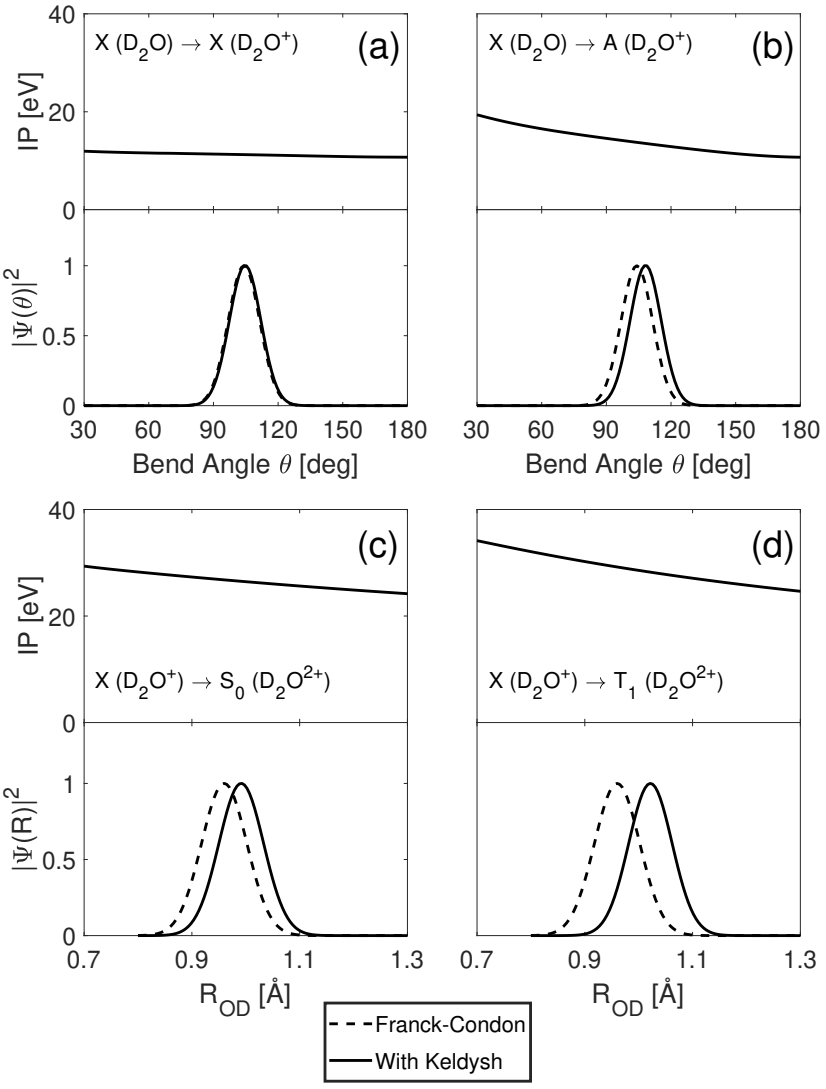


FIGURE 8.6. Modification of the nuclear wave packet due to the coordinate-dependent Keldysh ionization rate. Panels (a) and (b) show the effect of the Keldysh weighing on the bending coordinate during the single ionization event to both the X and A cation states. The panels plot both the ionization potentials (IP) for the transitions in question, the unmodified initial neutral (i.e. Franck-Condon) wave packet, and the nuclear wave packet after applying the Keldysh weighting. Panels (c) and (d) show the effects of the Keldysh weighting for two examples of single to double-photoionization transitions (indicated in the figures) as a function of $R_{OH}$ bond length of the symmetric stretch mode. All probability densities $|\Psi|^2$ have been normalized to have a maximum of 1.

ionization potential (IP) through the Keldysh tunneling rate $\Gamma(\mathbf{R}, t)$ [**59**, **75**, **83**, **105**]. In this description, ionization occurs in short sub-cycle bursts near the peaks of the laser oscillations. With the assumption that the nuclei remain stationary during a single ionization burst, the ionized wave packet after the burst can be written as

$$\Psi_K(\mathbf{R}) = \Gamma(\mathbf{R}, t)\Psi_0(\mathbf{R}). \tag{8.1}$$

where $\Psi_0(\mathbf{R})$ is the initial nuclear wave packet before ionization and $\mathbf{R}$ stands for all nuclear coordinates. If ionized from the neutral at equilibrium, $\Psi_0(\mathbf{R})$ is often called the Franck-Condon wavepacket. The Keldysh rate is given by

$$\Gamma(\mathbf{R}, t) = \mathcal{P} \exp\left[-\frac{2}{3}\frac{(2\ \mathrm{IP}(\mathbf{R}))^{3/2}}{|F(t)|}\right] \tag{8.2}$$

where $\mathcal{P}$ is a slowly-varying (i.e. non-exponential) prefactor that depends weakly on IP, $F$, and $\mathbf{R}$. Here $F$ denotes the amplitude of the electric field. In molecular systems, the $\mathcal{P}$ prefactor would also encode the molecular orientation dependence of SFI as well as other molecular effect such as enhanced ionization, and accurate computation of $\mathcal{P}$ would require some form of *ab initio* numerical simulation of the ionization process. In the following we set $\mathcal{P} = 1$ for simplicity and consider only the effects of the Keldysh exponent. Eq.(8.1) shows that the Keldysh rate can modify the spatial structure of Franck-Condon wave packet through the coordinate-dependence of the IP.

Fig. 8.6 shows examples of the Keldysh rate modifying the initial Franck-Condon wave packet in $D_2O$. Fig. 8.6a shows the IPs for the first ionization step from the neutral to the X state of the ion along the bend coordinate $\theta$ together with cuts through the nuclear wave function both with and without applying the Keldysh weighting applied. Fig. 8.6b plots the same but for the neutral to A state. While very little change in the wave function occurs for X ionization along this coordinate, it can be seen that the Keldysh weighting has the effect of shifting the Franck-Condon wave packet along the bend coordinate. Panels c and d plot similar cuts for two transitions of the second ionization steps, $X(D_2O^+) \rightarrow\ ^1A_1$ ($S_0(D_2O^{++})$) and $X(D_2O^+) \rightarrow\ ^3A_2$ ($T_1(D_2O^{++})$), but now taken along the symmetric stretch coordinate. Due to the increased magnitude and steep coordinate dependence of the IPs for these transitions, the Keldysh-induced shifts of the

wave function are more pronounced compared to the previous single-ionization examples from the neutral.

*Few-cycle nuclear motion in the ion*: Following the first ionization event, the nuclear wave packet can begin to move on the cationic surfaces before the second ionization occurs. This intermediate motion can change the nuclear wave packets before being projected onto the di-cationic states. From our investigations of the cationic surfaces, the dominant motion is expected to be along the bend coordinate. In reality the motion in the cation occurs in the presence of the laser field, but we first consider the effects of field-free motion, which alone can already cause pronounced reshaping of the wave packets. Laser-driven motion in the cation is considered below.

The bending wavepacket dynamics on the $X^2B_1$ and $A^2A_1$ cationic surfaces is simulated using the following simplified model of $D_2O^+$. First, the bond lengths are fixed at the neutral equilibrium values, $R_{eq}$, throughout the dynamics. Second, the bending is restricted to a single plane of motion, where the overall rotational motion about the center-of-mass is not considered during these wavepacket simulation. Finally, the mass of the oxygen atom is assumed to be infinite, which significantly simplifies the corresponding kinetic energy operator. With these restrictions, the Hamiltonian of the model system is written (in atomic units) as

$$\widehat{H}(\theta,t) = \begin{bmatrix} -\frac{1}{2\mu R_{eq}^2}\frac{\partial^2}{\partial\theta^2} + V_X(\theta) & 0 \\ 0 & -\frac{1}{2\mu R_{eq}^2}\frac{\partial^2}{\partial\theta^2} + V_A(\theta) \end{bmatrix}, \tag{8.3}$$

where $\mu = m_D/2$ is the reduced mass of the bend coordinate, $m_D$ is the mass of atomic deuterium, while $V_X(\theta)$ and $V_A(\theta)$ are the potential energy surfaces of the $X^2B_1$ and $A^2A_1$ states. This Hamiltonian is used to solve the time-dependent Schrödinger equation (TDSE) $i\partial_t\Psi(\theta,t) = \widehat{H}(\theta,t)\Psi(\theta,t)$. In order to investigate the effect of wave-packet motion as separate from the Keldysh effects discussed above, we populate both the X and A surfaces during the ionization event starting from the unchanged Franck-Condon wave packet, and hence the initial condition for $\Psi(\theta,t)$ at the moment of ionization is taken to be the bending ground state, $\psi_0(\theta)$, on the neutral surface. The TDSE is solved using the Fourier-split-operator technique [**34**].

The first three panels of Fig. 8.7 show the effects of intermediate field-free few-cycle motion on the X and A cation surfaces. Fig. 8.7(a) shows the Wigner function of the initial Franck-Condon

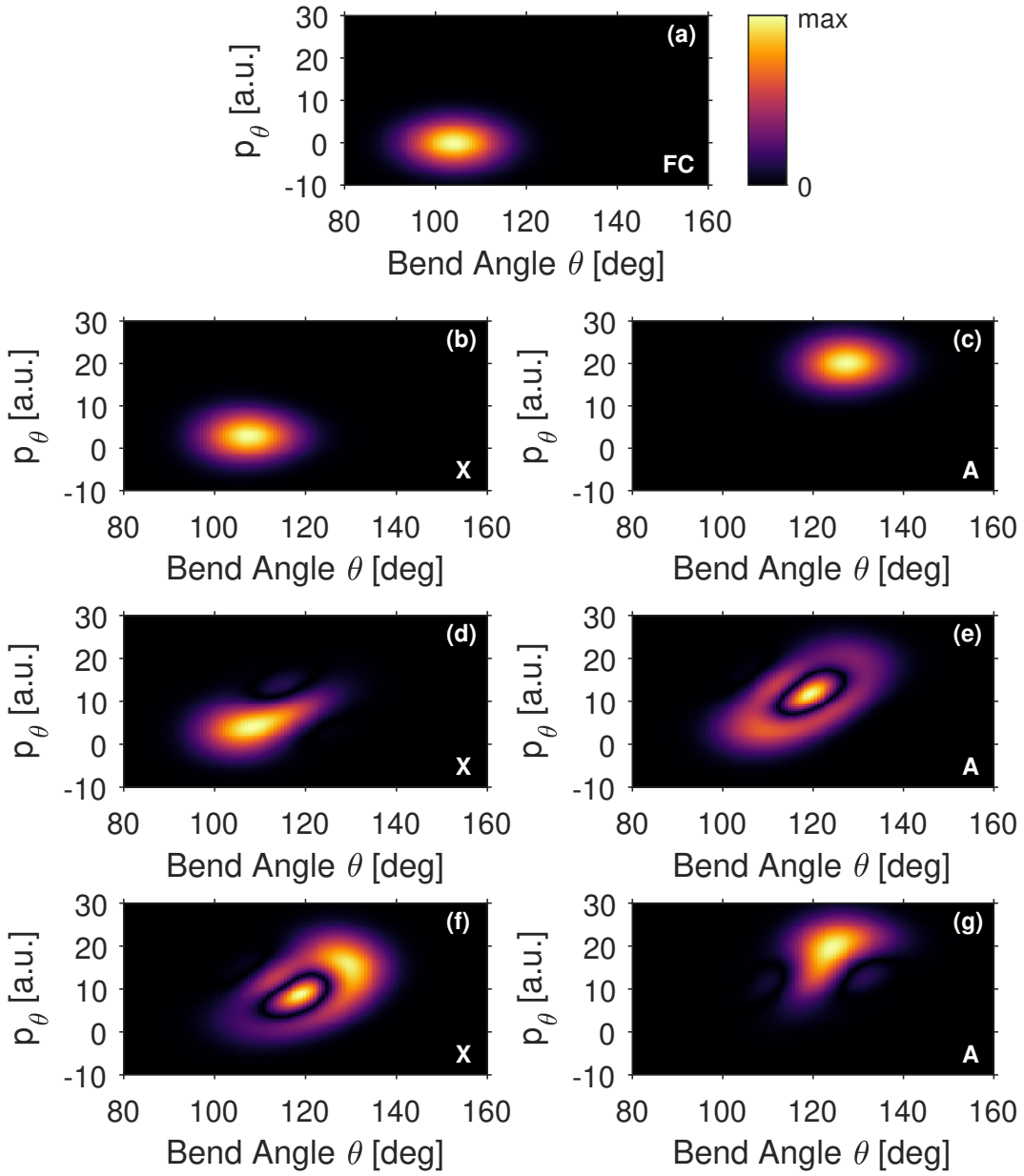


FIGURE 8.7. Wigner functions demonstrating the effects of nuclear dynamics in the cation. (a) Wigner function of the Franck-Condon wave packet. (b) & (c) Wigner functions after field-free propagation on the X and A states respectively for a time equal to 2 cycles of the laser. (d) & (e) Wigner functions on the X and A states after laser-driven propagation for a time of 2 laser cycles with the initial population starting on the X state. The simulation was started at the peak of the pulse ($t = 0$) with the laser parameter $\lambda_0$=780 nm, $I_0$ = 400 TW/cm$^2$, and $\tau$=10 fs. (f) & (g) Same as previous two panels but now with initial population on the A state. Note that in all cases the magnitude of the Wigner function is shown.

wave packet. This is the initial state of the bending coordinate that is used in the $\beta$-KER trajectory simulations. Figs. 8.7b and c plot Wigner functions after this initial state has propagated field-free for a time corresponding to 2 laser cycles of the 780 nm field (2×2.6 fs) on the X and A states, respectively. The X-state Wigner has undergone a little acceleration and motion as can be seen by the small shift of the center of the Wigner function, but there is still significant overlap between the propagated and initial Wigner functions in this case. However, the 2-cycle field-free propagation on the A-state substantially modifies the initial Wigner function, which now has effectively zero overlap with the initial state. The remaining panels of Fig. 8.7 pertain to laser-driven motion in the ion, which is outlined in the following:

*Near-resonant dipole coupling in the ion*: At 780 nm, the laser induces a near-resonance one-photon coupling between the X and A states. This coupling is included in the wave packet simulation by adding off-diagonal dipole terms to the Hamiltonian, which then becomes

$$\widehat{H}(\theta,t) = \begin{bmatrix} -\frac{1}{2\mu R_{eq}^2}\frac{\partial^2}{\partial\theta^2} + V_X(\theta) & -F(t)\cdot d_{XA}(\theta) \\ -F(t)\cdot d_{XA}(\theta) & -\frac{1}{2\mu R_{eq}^2}\frac{\partial^2}{\partial\theta^2} + V_A(\theta) \end{bmatrix}, \tag{8.4}$$

where $d_{XA}(\theta)$ is the transition dipole between these states, and $F(t)$ is the electric field of the laser which is chosen to be parallel to $d_{XA}(\theta)$, i.e perpendicular to the molecular plane. The electric field of the laser is taken to have a Gaussian envelope

$$F(t) = \mathcal{F}_0 \exp\left[-4\ln 2\left(\frac{t}{\tau\sqrt{2}}\right)^2\right]\cos(\omega_0 t) \tag{8.5}$$

where $\omega_0$ is the carrier frequency, $\mathcal{F}_0$ is the peak electric field magnitude, and $\tau$ is the full width at half maximum of the corresponding intensity envelope $|F(t)|^2$.

The effects of the dipole coupling on the Wigner functions can be seen in Figs. 8.7(d)-(g), while a more complete picture of the laser-driven dynamics is shown in Fig. 8.8. We first consider the Wigner functions. Figs. 8.7(d) and (e) plot the Wigner functions on the X and A states respectively after the system was initialized with the Franck-Condon wave packet on the X state at the peak ($t$=0) of a laser pulse with $\tau$ = 10 fs and intensity of 400 TW/cm$^2$, and allowed to propagate for 2 cycles of the laser. Initially only the X state is populated, but due to the near-resonant dipole coupling some population is transferred to the A state, which is discussed further below. In

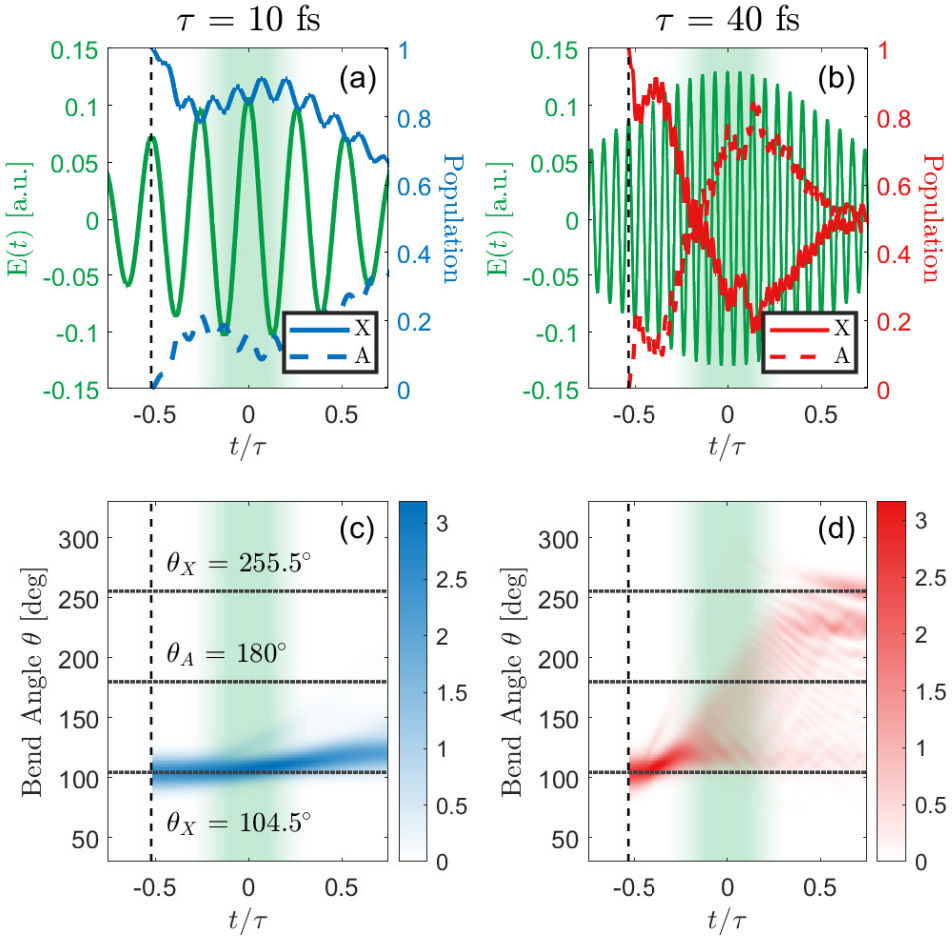


FIGURE 8.8. Time-resolved simulations of the strong-field coupling between the X state of the water cation and the A state in the presence of (a) the 10 fs pulse with $\lambda_0 = 780$ nm and $I_0 = 400$ TW/cm$^2$ and (b) the 40 fs pulse with central wavelength $\lambda_0 = 800$ nm and peak intensity $I_0 = 600$ TW/cm$^2$ (parameters chosen to match the experiments). In each case, the cation is initiated in the X state (red/blue solid line) at a local peak in electric field (solid green line) that roughly corresponds to the point at which the pulse intensity is half it's maximum value: $t/\tau \approx$ -0.5. Due to the presence of the field, the X population couples to the A state (red/blue dashed line). Plotted below each of these figures is the probability distribution over bend angle, $\theta$, for the mixture of states displayed above, shown separately for (c) the case of a 10 fs pulse (blue) and (d) the case of a 40 fs pulse (red). In each case, dotted gray lines denote the equilibrium bend-angles for the X and A states. In all four panels, green shading roughly indicates the window in time over which the second ionization event in sequential double-photoionization is expected to occur.

addition to the modifications due to field-free propagation, seen in Figs.8.7(b) and (c), both of the Wigner functions on the X and A states have acquired additional structures after the laser-driven propagation. These structures arise due to light-induced potentials created by the strong near-resonant laser field that modify the field-free potential energy surfaces, an effect known as bond softening [**14**, **84**]. Additionally, the transfer of population from one state back to the other, which occurs through cascaded one-photon transitions between the X and A states induced by the strong near-resonant laser, also contributes to these structures. Figs.8.7(f) and (g) plot Wigner functions for the same scenario but now with the initial population starting on the A state. Again, it is seen that new structure not present in the Franck-Condon wave packet have developed.

For the dipole moment effect on the nuclear dynamics simulation, a simple simulation was carried out and negligible change on the simulated dynamics has been seen. Other nonadiabatic or non-Born-Oppenheimer couplings, like the non-laser-induced nonadiabatic couplings are also considered. The assumption in our calculations is that these couplings are negligible so they are not included. These nonadiabatic couplings were also neglected in the classical trajectory simulations, so the two simulation sections in the thesis are consistent in this regard. More specifically in the classical trajectories, they were performed field free and sampled from the Wigner distribution of the initial ground state. No nonadiabatic coupling between the nine potential surfaces was included, nor coupling to other states that have conical intersections with some of these states which occur at geometries that are not probed by the classical trajectories. These points are discussed in Refs. [**38**, **99**]. Both works also neglected nonadiabatic transitions for the states considered here in the dissociation dynamics of the water di-cation. Comparison with experiment for one photon double-photoionization verify that nondiabatic effects do not appreciably change the final momentum distributions in the channels producing $O/D^+/D^+$ or $OD^+/D^+$. However, those effects can be important for the production of the products $O^+/D^+/D$, which are minor channels.

In order to put things into perspective, we compare the amount of X to A coupling that occurs in a 10 fs pulse to a significantly longer pulse with a duration of 40 fs. Fig 8.8 shows a broader picture of the laser-driven dynamics. The top panels show the population of ground and first excited states of the monocation together with the laser field as a function of time for 10 fs (top left) and 40 fs (top right) laser pulses. The bottom two panels show the corresponding probability

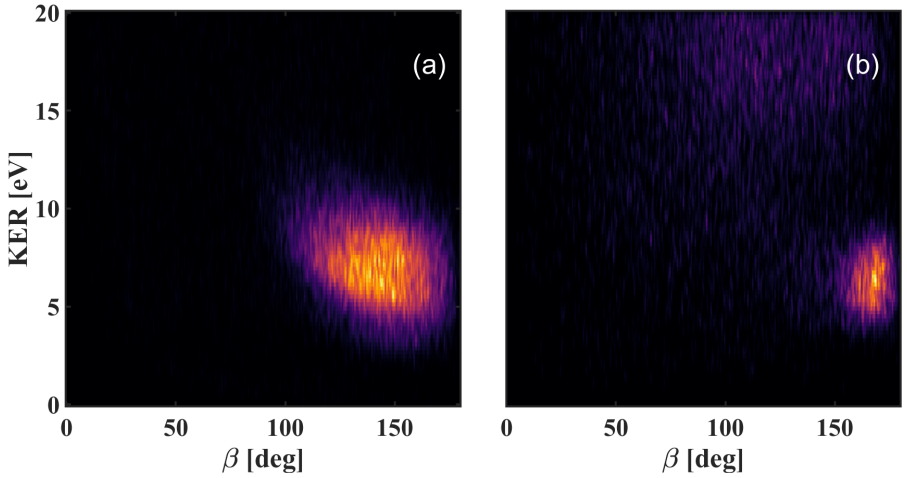


FIGURE 8.9. $\beta$-KER plot for SFI with (a) 10 fs and (b) 40 fs pulse durations. A higher kinetic energy feature is observed for the longer pulses in panel (b). This feature can be assigned to tri-cation formation and fragmentation via the $D^+/D^+/O$ channel.

density as a function of D-O-D angle and time. The figures illustrate the fact that while population transfer and nuclear dynamics can take place during a 10 fs pulse, they have a much more dramatic effect for a 40 fs pulse.

The calculations described above suggest that in a longer pulse, dynamics in the monocation en route to the di-cation during a longer pulse also leads to significant unbending and a $\beta$-KER plot that is shifted to larger angles. We therefore compare the $\beta$-KER plot for 10 and 40 fs pulses as a test of the conclusions of the theoretical results. Fig. 8.9 shows this comparison, which bears out the predictions based on the calculations above. We note that the comparison shows that 40 fs tend to have larger $\beta$ angles and also the lower KER. The former is what we expected from the simulation while the latter is not easy to explain. Nevertheless, this comparison provides strong evidence that while there is rough agreement between the measured and calculated momentum resolved fragment ion yields for sub 10-fs pulses assuming vertical ionization, reshaping of the wave packet and nuclear dynamics during ionization can lead to significant differences between strong- and weak-field ionization. And one needs to understand the strong-field dynamics in order to predict the reaction products in an SFI measurement. Finally, a weak diffuse feature at higher KER ($\sim$20 eV) and smaller $\beta$ values is observed for 40-fs pulses, which is notably absent for the short pulse case. This feature can readily be assigned to tri-cation Coulomb explosion.

### 8.3. Conclusion

This Chapter presented work and results provided by a large theoretical and experimental endeavor, which resulted in Ref. [**18**]. That extensive collaboration also included multiple theoretical efforts and should be credited accordingly. In particular, the author contributed the nuclear simulations and analysis for dynamics that start in the Franck-Condon region. The simulation of the non-vertical dynamics presented in Sec. 8.2 were performed by a theoretical collaborator, Michael Spanner, in order to investigate possible sources of discrepancies seen in the intense-field and COLTRIMS experiment. Overall, while we find rough agreement between measurements of the $D^+/D^+/O$ yield as a function of $\beta$ and KER for double-photoionization of $D_2O$ with 10 fs laser pulses and calculations of the same yield assuming weak-field/vertical ionization, there are significant differences in the details. Even after careful analysis on the state population in the strong field ionization and taking into account our experimental resolution, the experimental results still show discrepancies compared with theoretical expectations. These differences may be ascribed to different physical processes leading to wave packet reshaping. The R-dependent single and double-photoionization induced by strong-field ionization and nuclear dynamics induced by resonance coupling during the pulse are believed to drive the wave packet away from the initial form. Such modifications to the wave form have a great influence on the initial conditions of the trajectory calculations on di-cationic states. Thus the final experimental $\beta$-KER yield is different from the theoretical predictions from the simple single photon double-photoionization. These result in SFI being a non-vertical transition, with an understanding of the strong-field dynamics being important for the calculation of the fragment ion yield momentum distributions.

Our simple calculations indicate that the coordinate dependence of the tunnel ionization rate plays an important role in reshaping the initial wave packet, particularly for the second ionization step in a sequential double-photoionization process. Meanwhile, the monocation dynamics in the presence of the strong laser field indicate that field dressed nuclear dynamics can also reshape the vibrational wave packet. These observations are supported by measurements of the double-photoionization yield as a function of $\beta$ and KER for 10 fs and 40 fs pulses. This comparison has significant bearing on the use of SFI as a probe of molecular structure and dynamics, and indicates that while very short pulses ($< 10$ fs) can minimize nuclear dynamics during the pulse,

wave packet reshaping by the strong field of the laser can still result in significant distortion of the initial wave function of the molecule. We believe this work will have important consequences for pump-probe techniques, such as time-resolved Coulomb explosion imaging (CEI), that aim to track nuclear dynamics during excited state photochemical processes.

These results showcase the need for a more comprehensive theoretical description of SFI processes, which include the role of nuclear motion occurring during the ionizing laser pulse duration. As outlined in the introduction, such nuclear dynamics could have implications for computations of SFI from multi-cycle pulses when invoking the frozen-nuclei approximation, such as recent state-of-the-art time-dependent R-matrix ionization computations for $H_2O$ [**9**] that highlighted modifications to the angular dependence of ionization when significant laser coupling in the ion is present for the frozen-nuclei case. Further experimental investigations into the pulse shape and intensity dependence of SFI processes in water may help to target future modelling of these dynamics.

CHAPTER 9

# Excited Wigner Distribution: Propagating Quantum Features in Phase Space

## 9.1. Excited Normal Mode Initial Conditions

In Chapter 2, it was mentioned that one key feature of the COLTRIMS experiment is the target is always "cold", meaning the molecule is not rotating and is in its ground-vibrational state due to the super-sonic expansion. This assumption was the foundation for the theoretical analysis presented in this thesis, in that assuming the water molecule was in its ground-vibrational state allowed for the use of the harmonic approximation and the semi-classical Wigner approach had a simple classical interpretation. As Hudson discovered [**56**], this classical interpretation of the pseudo-probability distribution occurs for a squeezed vacuum or coherent states only. In fact, there has been much experimental work done for measuring the Wigner function (see [**6**,**31**,**97**]). Even more interesting, there has been experimental work at measuring the negative values of a Wigner function if the system is not a coherent state [**62**,**67**,**73**] like our ground-vibrational wave function of $H_2O$ or $D_2O$ analyzed thus far. The negativity of the Wigner function has been linked to non-locality, which depends on the *volume* of the negative part of the Wigner function, and has been investigated by Kenfack and Życzkowski [**60**].

Motivated by this body of work, we extend our classical trajectory analysis to include initial conditions constructed from excited-harmonic-normal modes to investigate potential quantum signature in the final momenta of the nuclei. Of course in this system with only three internal coordinates, it would be possible to propagate 3D quantum wave packets. However, one would be analyzing the results of those wave packet propagations in the three-body breakup final continuum state. That analysis is complicated by a set of formal and practical difficulties. For this reason, having a classical trajectory approach that might reproduce the principal features of a full quantum treatment is very valuable. That's the approach we investigate here, following ideas of

Heller and coworkers used in photodissociation calculations in the 1980s [**12**]. In particular, these excited-normal modes will have nodes that will generate Wigner functions that contain negative values which require a new Metropolis sampling routine than the one presented previously. With these excited-initial conditions, the classical trajectories on all nine surfaces of $D_2O^{++}$ is the same as before. It's worth noting that such an experiment is possible but not easily performed, to the author's knowledge, and may require more experimental effort. However, simulating the nuclear breakup of $D_2O^{++}$ using these excited-initial conditions leads to interesting results and we present them here as motivations for future experiments.

We start with the first excited-state wave function, with $n = 1$. The wave function and its momentum space representation, are

$$\begin{aligned} \varphi_1(Q) &= \frac{1}{\sqrt{2\pi\hbar}} \int_{-\infty}^{+\infty} e^{+iPQ/\hbar}\ \tilde{\varphi}_1(P)\ dP = \left(\frac{\omega}{\pi\hbar}\right)^{1/4} 2^{1/2} \left(\frac{\omega}{\hbar}\right)^{1/2} Q e^{-\frac{\omega}{\hbar}Q^2/2} \\ \tilde{\varphi}_1(P) &= \frac{1}{\sqrt{2\pi\hbar}} \int_{-\infty}^{+\infty} e^{-iPQ/\hbar}\ \varphi_1(Q)\ dQ = \frac{-i\sqrt{2}}{(\pi\hbar\omega)^{1/4}} \frac{P}{\sqrt{\hbar\omega}} e^{-P^2/2\hbar\omega} \end{aligned} \tag{9.1}$$

Note the difference in the form of these wave functions and the ground-vibrational state Eq. 4.25; the ground-vibrational state cannot take on negative values as the normal modes in position and momentum are positive-definite. However, the higher $n \neq 0$ wave functions all have a prefactor that contains a polynomial that change sign ultimately from the form of the orthogonal Hermite polynomials. The Wigner distribution function corresponding to this wave function for a single mode is

$$\boxed{W_1(Q,P) = \frac{1}{\pi\hbar}\left(2\frac{\omega}{\hbar}Q^2 + 2\frac{P^2}{\hbar\omega} - 1\right) e^{-\frac{\omega}{\hbar}Q^2} e^{-\frac{P^2}{\hbar\omega}}} \tag{9.2}$$

This is the same as Eq.(32) in the pedagogical paper by Case [**15**] in 2008, which contains other useful results. So the integrals of the Wigner distribution over momentum and coordinates give the position and momentum distributions respectively,

$$\begin{aligned} \int_{-\infty}^{+\infty} W_1(Q,P)dP &= \left(\frac{\omega}{\hbar}\right)^{3/2} \frac{2Q^2}{\sqrt{\pi}} e^{-\omega Q^2/\hbar} = |\psi_1(Q)|^2 \\ \int_{-\infty}^{+\infty} W_1(Q,P)dQ &= \frac{2P^2}{\sqrt{\pi}(\hbar\omega)^{3/2}} e^{-P^2/\hbar\omega} = |\tilde{\psi}_1(P)|^2\ . \end{aligned} \tag{9.3}$$

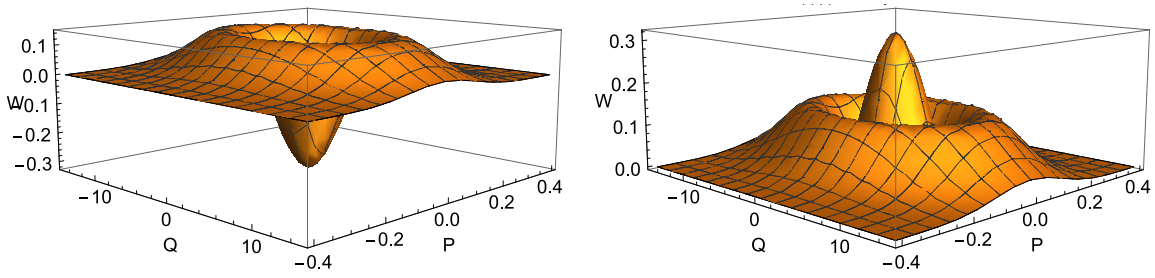


FIGURE 9.1. Left: Wigner distribution for the asymmetric-stretch mode of $H_2O$. Right: Absolute value of the Wigner distribution used in Metropolis sampling.

These results are evidently special cases of the general result

$$W_n(x,p) = W_n(u) = \frac{(-1)^n}{\pi\hbar} L_n(4\frac{u}{\hbar\omega}) e^{-2u/\hbar\omega} \qquad (9.4)$$
$$u = \frac{1}{2}m\omega^2 x^2 + \frac{p^2}{2m}$$

where $L_n$ denotes the $n$-th Laguerre polynomial, as we can see by defining mass weighted coordinates, $Q = \sqrt{m}x$ and $P = p/\sqrt{m}$.

We would like to simulate the wave packet corresponding to the (0,0,1) initial vibrational state of water, with one quantum of asymmetric-stretch excitation for example, propagating on the di-cation surfaces as we did for the ground (0,0,0) state in Chapter 5. In that case we simply used Metropolis sampling from the Wigner distribution in Eq.(4.29) to determine the initial conditions for an ensemble of trajectories running on the di-cation potential surfaces because $W(\mathbf{Q},\mathbf{P})$ was everywhere positive definite. But that is not the case for the excited states of the harmonic oscillator due to the introduction of the quantum interference structure, as shown in Fig. 9.1.

To decide how to proceed to make a similar approximation in the case of excited-vibrational states, it's worthwhile to be explicit about what quasiclassical approximation we are making. Using the definition of the Wigner function in Eq. 4.6 for the time dependent wave function, $\varphi(\mathbf{x},t)$, we are approximating the Wigner distribution corresponding to the time-dependent wave function by

$$W(\mathbf{x},\mathbf{p},t) \approx W(\mathbf{x}_0(\mathbf{x},\mathbf{p},t),\mathbf{p}_0(\mathbf{x},\mathbf{p},t),0) \qquad (9.5)$$

where $\mathbf{x}_0(\mathbf{x},\mathbf{p},t)$ and $\mathbf{p}_0(\mathbf{x},\mathbf{p},t)$ are the initial conditions that produce the trajectory ending at time at the phase space point $\{\mathbf{x},\mathbf{p}\} = \{\mathbf{x}(t),\mathbf{p}(t)\}$. In other words we propagate the Wigner

distribution as though it where a classical phase space distribution. If $W(\mathbf{x}_0, \mathbf{p}_0, 0)$ were a classical phase space distribution it would be positive everywhere and Liouville's theorem would apply.

Here we use classical trajectories to propagate the Wigner distribution, but retain the sign of the distribution function associated with the initial values of $Q$ and $P$. We do this by sampling the absolute value of the distribution, but using its sign in the phase space average. In essence we multiply and divide the integrand of the phase space average by the absolute value of the Wigner distribution. This idea appears in work in the 1980s by Heller and coworkers who used this general approach successfully in calculations on photodissociation from excited vibration states [**12**]. In the approximation we make in these calculations, we are propagating the Wigner phase space distribution with Liouville's equation (Eq. 5.6), but the correct propagator for $W(q,p)$ in general will have higher order terms in the expansion of the potential found in Eq. 5.4 and noted by Case [**15**] and Heller [**46**, **47**].

In Chapter 4 we used the fact that the Wigner function is normalized to one (see Eq. 4.32) to obtain Eq. 4.33. However, with one mode excited in our Wigner distribution this assumption is not valid and we must revisit how to sample from this quasiclassical distribution containing negative values. As Fig. 9.1 suggests, we can sample from the absolute value of the distribution, $|W(\mathbf{Q},\mathbf{P})|$, by multiplying and dividing by it

$$\begin{aligned}\langle H\rangle &= \frac{\int H(\mathbf{Q},\mathbf{P})\frac{W(\mathbf{Q},\mathbf{P})}{|W(\mathbf{Q},\mathbf{P})|}|W(\mathbf{Q},\mathbf{P})|d^3Q\,d^3P}{\int |W(\mathbf{Q},\mathbf{P})|d^3Q\,d^3P} \\ &= \frac{1}{N}\sum_j H(\mathbf{Q}_j,\mathbf{P}_j)\frac{W(\mathbf{Q}_j,\mathbf{P}_j)}{|W(\mathbf{Q}_j,\mathbf{P}_j)|} \text{ with } \mathbf{Q}_j,\mathbf{P}_j \in \text{ Metropolis sample}\end{aligned} \tag{9.6}$$

noting that $\frac{W(\mathbf{Q},\mathbf{P})}{|W(\mathbf{Q},\mathbf{P})|} = \text{sign}[W(\mathbf{Q},\mathbf{P})]$. But to get $\langle H\rangle$, we need the denominator, $\int |W(\mathbf{Q},\mathbf{P})|d^3Q\,d^3P$ of the ensemble average that Metropolis sampling is doing. We can use the fact that

$$\frac{\int \frac{W(\mathbf{Q},\mathbf{P})}{|W(\mathbf{Q},\mathbf{P})|}|W(\mathbf{Q},\mathbf{P})|d^3Q\,d^3P}{\int |W(\mathbf{Q},\mathbf{P})|d^3Q\,d^3P} = \frac{1}{N}\sum_j \frac{W(\mathbf{Q}_j,\mathbf{P}_j)}{|W(\mathbf{Q}_j,\mathbf{P}_j)|} \text{ with } \mathbf{Q}_j,\mathbf{P}_j \in \text{ Metropolis sample} \tag{9.7}$$

together with the fact that Wigner distribution is normalized, whether it's everywhere positive or not, $\int W(\mathbf{Q},\mathbf{P})d^3Q\,d^3P = 1$, to deduce that

$$\int |W(\mathbf{Q},\mathbf{P})|d^3Q\,d^3P = \frac{1}{\frac{1}{N}\sum_j \frac{W(\mathbf{Q}_j,\mathbf{P}_j)}{|W(\mathbf{Q}_j,\mathbf{P}_j)|}} \text{ with } \mathbf{Q}_j,\mathbf{P}_j \in \text{ Metropolis sample,} \tag{9.8}$$

which is just the renormalization to the positive-definite metric of our Wigner distribution. That gives us the working relation

$$\boxed{\langle H\rangle = \frac{\frac{1}{N}\sum_j H(\mathbf{Q}_j,\mathbf{P}_j)\frac{W(\mathbf{Q}_j,\mathbf{P}_j)}{|W(\mathbf{Q}_j,\mathbf{P}_j)|}}{\frac{1}{N}\sum_j \frac{W(\mathbf{Q}_j,\mathbf{P}_j)}{|W(\mathbf{Q_j},\mathbf{P}_j)|}} \text{ with } \mathbf{Q}_j,\mathbf{P}_j \in \text{ Metropolis sample from } |W(\mathbf{Q},\mathbf{P})|} \tag{9.9}$$

which is true for any Wigner distribution, so we can apply it in the normal mode problem no matter how many modes are excited to any level. This procedure of calculating phase space average $\langle H\rangle$ by keeping track of the sign of the Wigner function reproduces the excited state energies of the harmonic normal modes of the initial state vibrational Hamiltonian.

Importantly we can construct the distributions in P and Q in each normal mode by Metropolis sampling. To do so we make use of the basic relations in Eq. 4.8 and Eq. 4.9. In 1D we could construct the momentum distribution, for example, from a Metropolis sample using

(9.10)

$$|\tilde{\psi}(P_b)|^2 \approx \frac{1}{\Delta P_b}\frac{\frac{1}{N}\sum_j B_b(P_j)\frac{W(Q_j,P_j)}{|W(Q_j,P_j)|}}{\frac{1}{N}\sum_j \frac{W(Q_j,P_j)}{|W(Q_j,P_j)|}} \text{ with } \{Q_j,P_j|\} \in \text{ Metropolis sample from } |W(Q_j,P_j)|$$

$$B_b(P) \equiv \begin{cases} 1 & P_{b<} < P_j < P_{b>} \\ 0 & \text{otherwise} \end{cases}$$

$$\text{and } \Delta P_b = P_{b>} - P_{b<} \qquad P_b = (P_{b>} + P_{b<})/2.$$

The binning function, $B_b(P)$, for bin $b$, bins $P$ between the limits of our bin's size noted as $P_{b<}$ and $P_{b>}$. This expression is effectively the same as Eq.(9.9) with the Hamiltonian replaced by the binning function as the operator being averaged over the distribution. It's easy to see that the resulting square of the wave function is normalized according to $\sum_b |\tilde{\psi}(P_b)|^2\Delta P_b = \frac{1}{N}\sum_j \frac{W(Q_j,P_j)}{|W(Q_j,P_j)|}/\frac{1}{N}\sum_j \frac{W(Q_j,P_j)}{|W(Q_j,P_j)|} = 1$.

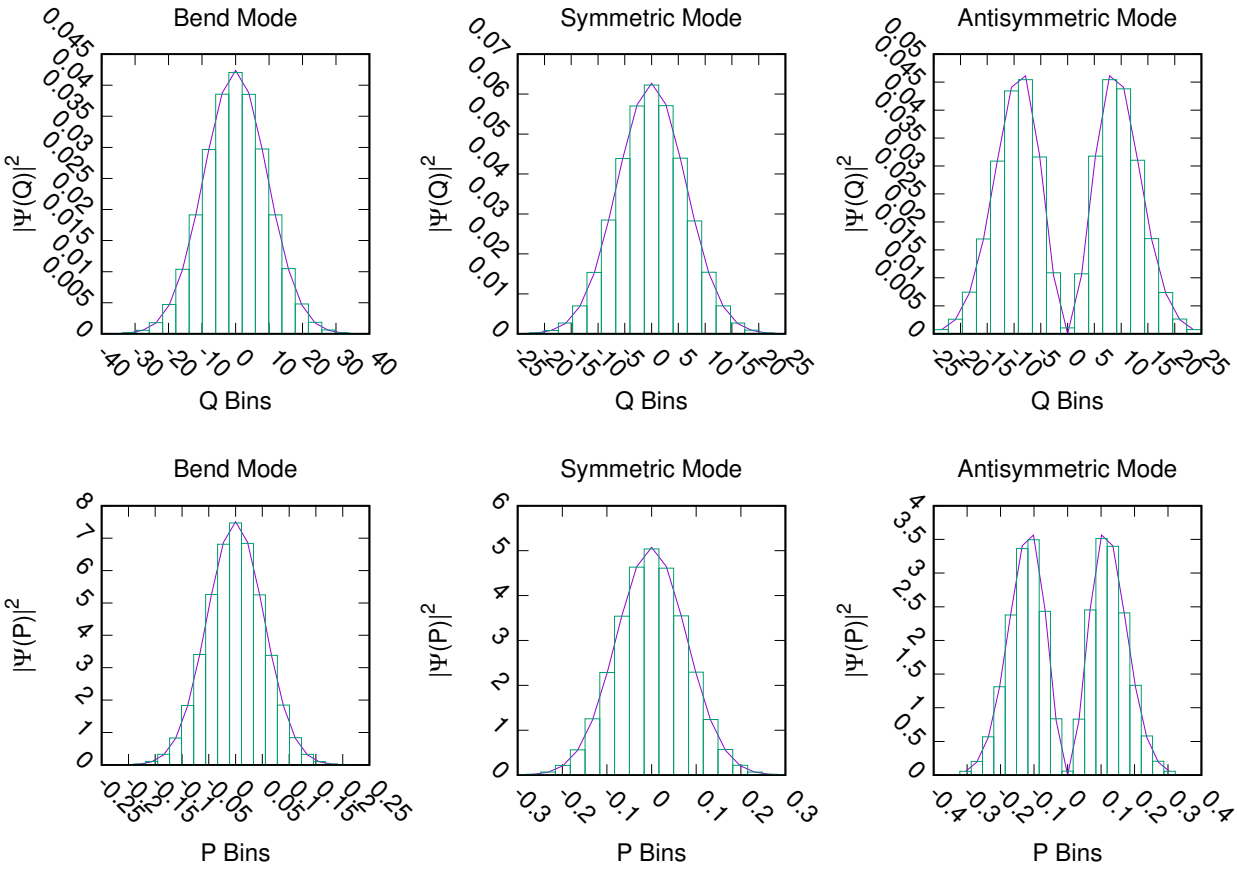


FIGURE 9.2. $|\Psi|^2$ of $Q$ and $P$ for each degree of freedom in the water example from integrating Wigner distribution using Eq(9.11) and 10,000 Metropolis steps. The line is the analytic solution to the general Wigner formula Eq. 9.2. Note that near the node in the distribution for the asymmetric-stretch excitation the Metropolis sample can give negative results for $|\Psi^2|$ because it is converging only as 1/N.

The multidimensional version of this Eq.(9.10) is, for the third momentum for example,

(9.11)

$$|\tilde{\psi}(P_3 = P_b)|^2 = \int W(Q_1, Q_2, Q_3, P_1, P_2, P_b)\, dQ_1 dQ_2 dQ_3 dP_1 dP_2$$

$$\approx \frac{1}{\Delta P_b} \frac{\frac{1}{N}\sum_j B_b(P_{3j}) \frac{W(\mathbf{Q}_j,\mathbf{P}_j)}{|W(\mathbf{Q}_j,\mathbf{P}_j)|}}{\frac{1}{N}\sum_j \frac{W(\mathbf{Q}_j,\mathbf{P}_j)}{|W(\mathbf{Q}_j,\mathbf{P}_j)|}} \text{ with } \{\mathbf{Q}_j, \mathbf{P}_j|\} \in \text{ Metropolis sample from } |W(\mathbf{Q}_j, \mathbf{P}_j)|$$

The results of such a calculation of the probability distribution for one coordinate is shown in Fig. 9.2.

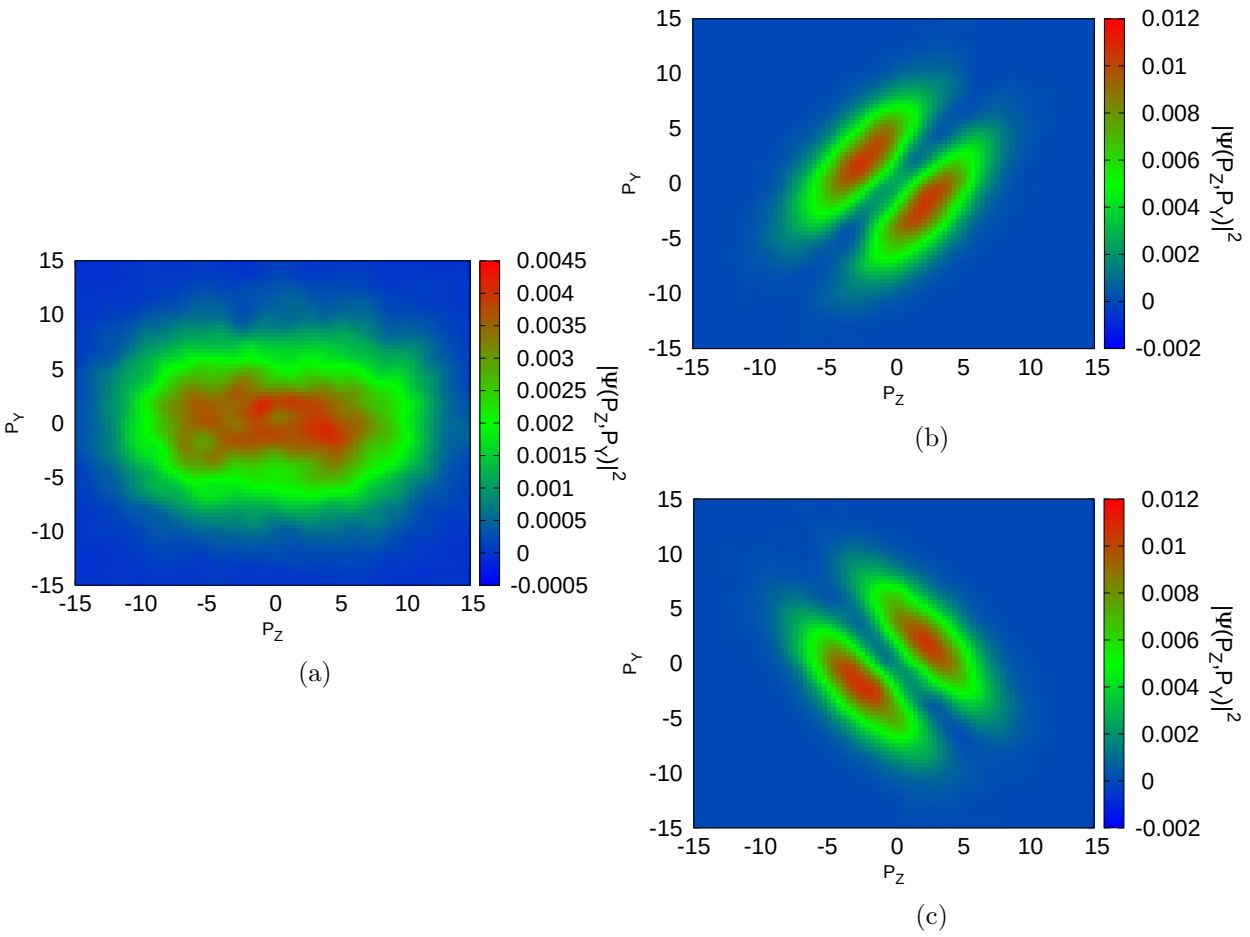


FIGURE 9.3. One quanta of excitation in the bending-mode-momentum distributions in Cartesian coordinates shown as contour plots. Metropolis sample has 100,000 points in the normal mode phase space, results are converted to Cartesian coordinates with the normal mode transformation. (a) Oxygen atom bend excitation, (b) and (c) are bend excitation for each hydrogen atom.

We can also apply Eq.(9.11) for the 9 pairs of Cartesian positions and momenta for the three nuclei. In that case our bins are two dimensional, not one dimensional, since the motion is in the yz plane containing the molecule. The only change is that now $\Delta P_b$ for example becomes the area of the b$^{th}$ two dimensional bin. The resulting two-dimensional, Cartesian momenta distributions for one quanta excitation of the bend mode are shown in Figs. 9.3, for symmetric-mode excitation are shown in Figs. 9.4, and asymmetric-mode excitation are shown in Figs. 9.5. We see these excited distributions have introduced nodes just like the interference nodes found in the excited-Wigner function, Fig. 9.1, but have a subtly different interpretation in the Cartesian coordinate system. For

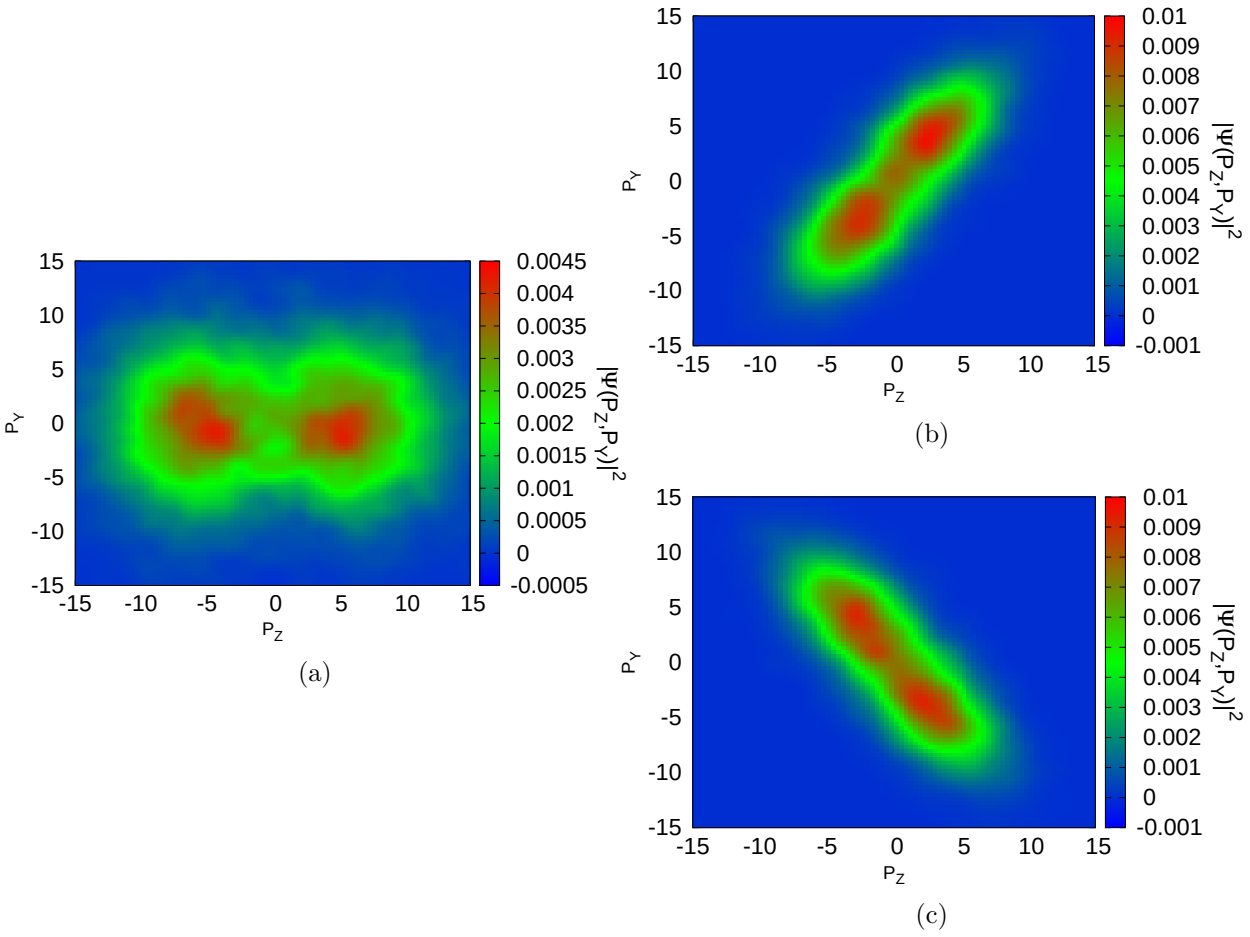


FIGURE 9.4. One quanta of excitation in the symmetric-stretch mode momentum distributions in Cartesian coordinates shown as contour plots. Metropolis sample has 100,000 points in the normal mode phase space, results are converted to Cartesian coordinates with the normal mode transformation. (a) Oxygen atom symmetric-stretch excitation, (b) and (c) are symmetric-stretch excitation for each hydrogen atom.

example, Fig. 9.5(a) shows a node for the oxygen atom. This node is from the excited-asymmetric-stretch motion of the two hydrogens dominating the other two modes, forcing the oxygen off the $P_y = 0$ a.u. line to conserve the center of mass equal to zero. Similarly, the conservation of center of mass in the Cartesian coordinate system produces nodes in the protons' motion with one quanta in the bending mode (see Fig. 9.3(bend)).

These distributions show that we now have a way to sample our excited-Wigner distribution, in any mode and for many quanta of excitation, in a Metropolis fashion. What we seek to answer is

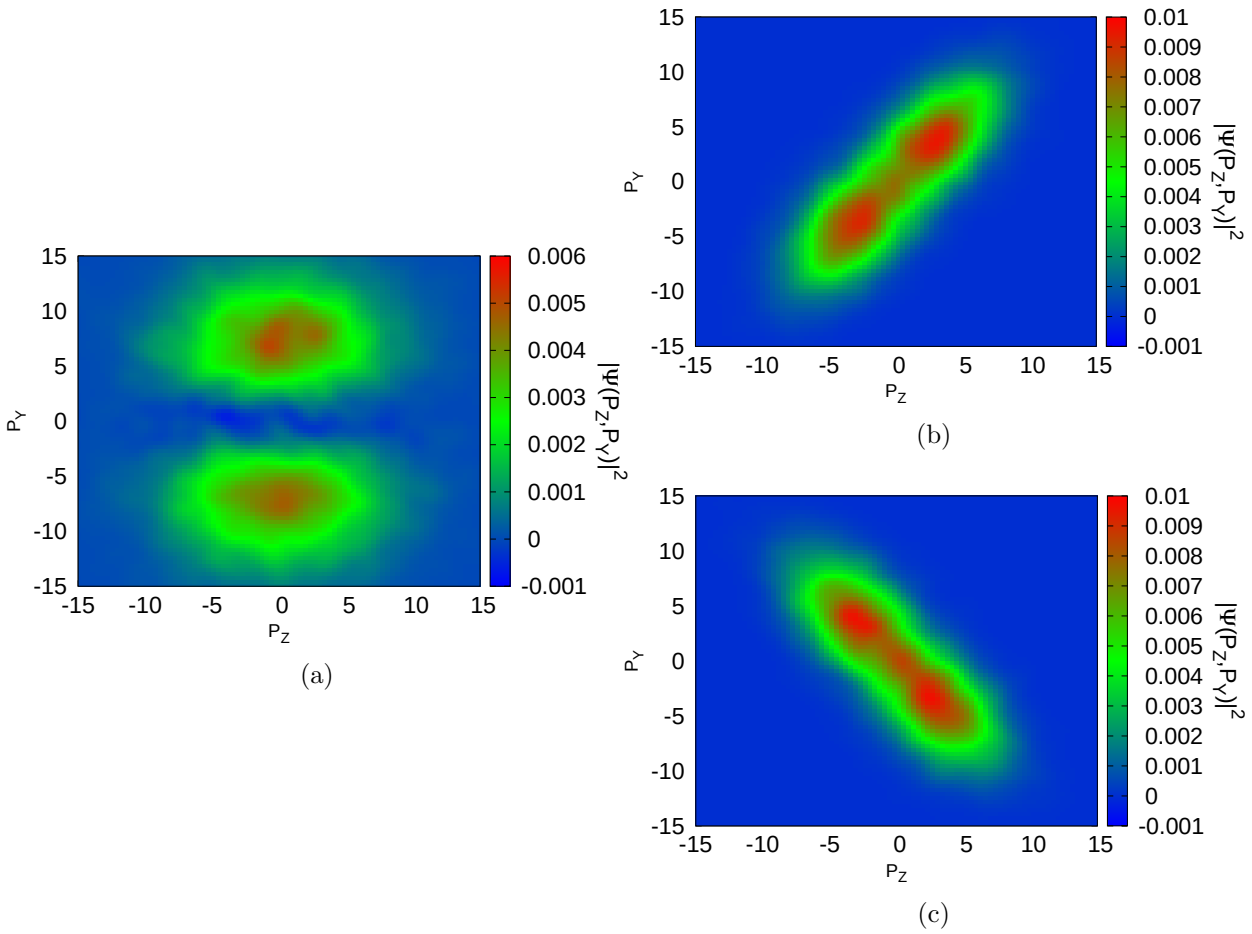


FIGURE 9.5. One quanta of excitation in the asymmetric-stretch mode momentum distributions in Cartesian coordinates shown as contour plots. Metropolis sample has 100,000 points in the normal mode phase space, results are converted to Cartesian coordinates with the normal mode transformation. (a) Oxygen atom asymmetric-stretch excitation, (b) and (c) are asymmetric-stretch excitation for each hydrogen atom.

how do these nodes, that are quantum in origin, manifest themselves in the final momenta images seen in Fig. 6.4. With these results, the impetus is placed on experimentalist to investigate these findings; experimentally imaging the vibrational nodes of the initial state in the final momenta images and comparing with these semi-classical results would give a basis for future inquiries into quantum and classical mechanics correspondence.

### 9.2. Simulation Results

Given the axial-recoil and branching ratio results in Chapter 5, three states were chosen based on their distinct dynamics to analyze how initial conditions generated from excited-Wigner distributions change the final results. First the $^1A_2$ state was chosen because as seen in Table 5.1 the majority of the $1,000$ trajectories on this surface underwent three-body dissociation. The other two states chosen were the $^1B_1$ and $2^1A_1$ because they both have appreciable percentage of two-body trajectories, while also having distinct dynamics within themselves. As seen in Table 5.1 the $^1B_1$ state has the majority of its $1,000$ trajectories following a two-body mechanism, while the $2^1A_1$ state has an considerable amount of trajectories going to both two and three-body branches. Also, Fig. 7.10 suggests that one is able to separate the two and three-body dynamics for the $2^1A_1$ state based on the dynamics' sensitivity on the initial conditions and therefore may produce markedly different branching ratios depending on which mode is excited. Since two of these states breaks the axial-recoil approximation, we present both the *molecular* frame and the COLTRIMS frame data for all the states under consideration for transparency.

We initially excite each normal mode with only one quanta of energy. Fig. 9.6 shows how the $^1A_2$ state's final momenta images are deformed due to the initial conditions having one quanta of energy in the three respected normal modes of motion. As evidenced in these figures, the nodal interference information introduced in the initial conditions is imprinted onto the final momenta image. For example in Fig. 9.6(top row), the excitation in the bending mode produces two separate islands of density counts for the deuterium ions. This shows that the structure in the initial conditions for excitation in the bending mode, shown in Figs. 9.3(b) and (c), does maintain its form and produces a similar structure in the final momenta image, only distorted by the topology of the $^1A_2$ surface. This conservation of structure is also true for the other two modes and after transforming from the molecular frame to the COLTRIMS frame producing the Newton-like images (see Chapter 6) these features are still visible. Therefore, these momenta images give a prediction that a COLTRIMS experiment measuring two protons from a vibrationally-excited water molecule should see the imaging of these interference nodes in the final momenta images.

Next we present the final momenta images after propagation of excited-initial conditions for the $^1B_1$ state in Fig. 9.7 As explored in Chapters 6 and 7, this state's trajectories flip backwards

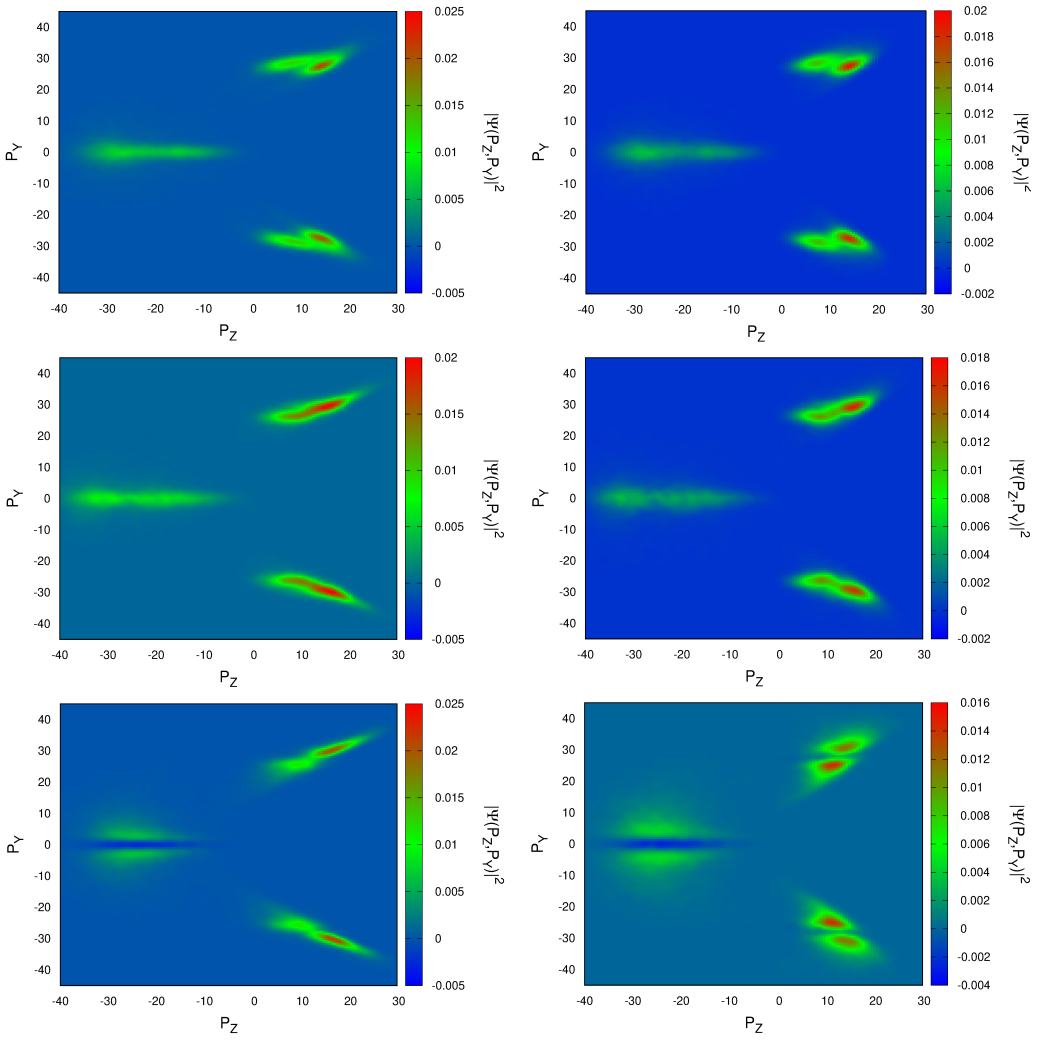


FIGURE 9.6. $^1A_2$ final momenta images after propagation of 100,000 trajectories using excited-initial conditions. Left column: molecular frame, right column: COLTRIMS frame. Top row: bend excitation, middle row: symmetric-stretch excitation, bottom row: asymmetric-stretch excitation.

and breaks the axial-recoil approximation. We see the usual *mustache* pattern (seen in Fig. 6.6) for the true molecular frame in Figs. 9.7(left column) and the illusion of the orientation of the water molecule once the COLTRIMS coordinate system is applied, in Figs. 9.7(right column). This state doesn't appear to have as clean nodal structure as the $^1A_2$ momenta images. However, there is still moderate structure that may manifest itself in a COLTRIMS measurement.

Finally, we present the final momenta images for the $2^1A_1$ state using initial conditions generated from an excited-Wigner distribution in each mode. This state produces the most interesting

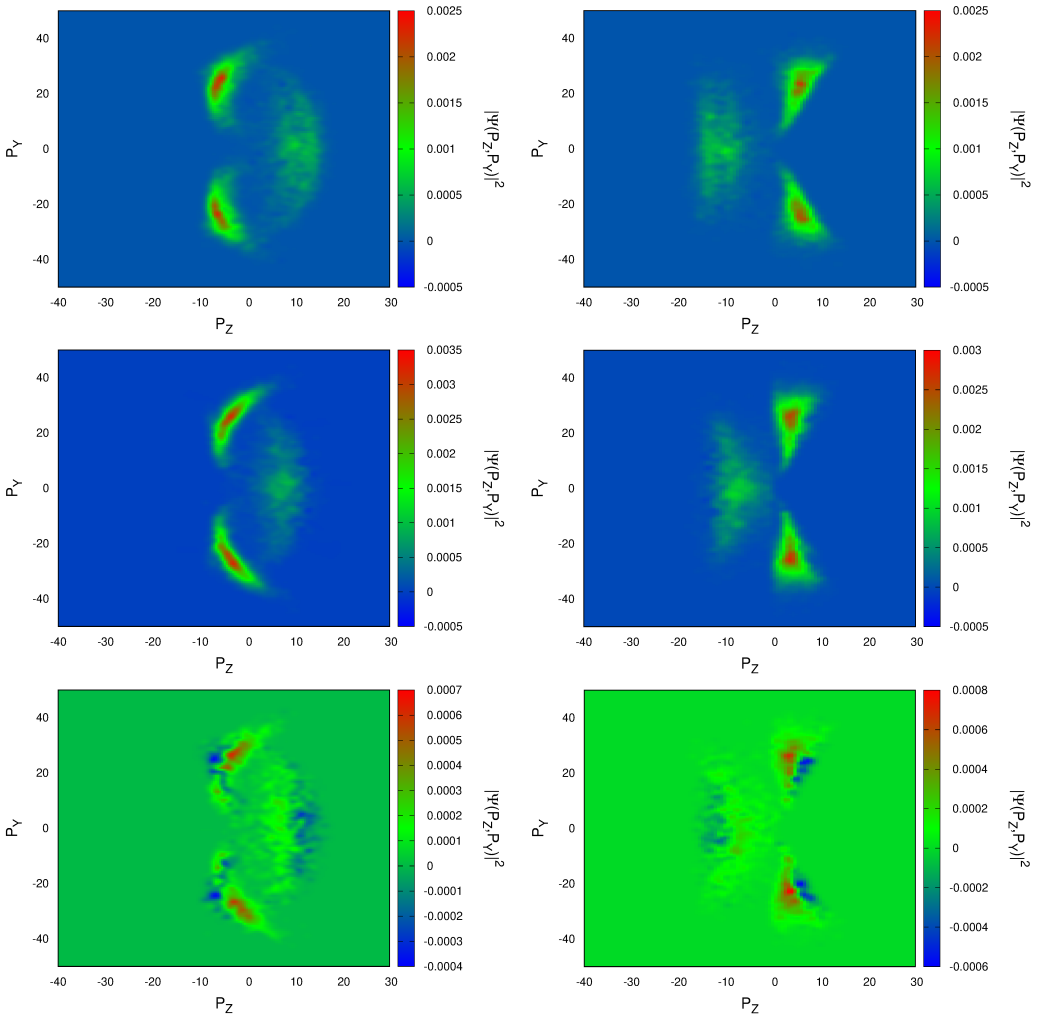


FIGURE 9.7. $^1B_1$ final momenta images after propagation of 100,000 trajectories using excited-initial conditions. Left column: molecular frame, right column: COLTRIMS frame. Top row: bend excitation, middle row: symmetric-stretch excitation, bottom row: asymmetric-stretch excitation.

molecular frame and Newton-like images out of the three but we focus on the Newton-like images seen in Fig. 9.8(right column) since we are anticipating the COLTRIMS experimental measurement. The bend excitation, Fig. 9.8(top row), doesn't appear to exhibit noticeable structure. However, Figs. 9.8(middle row) and Figs. 9.8(bottom row) both picture a bizarre Newton-like image. The symmetric-stretch excitation figure shows two separate islands for the deuterium ions with a nodal structure in the predicted neutral oxygen at around $P_z = -15$ a.u. The excitation in the asymmetric-stretch mode generating a final Newton-like image in Fig. 9.8(bottom row) has a

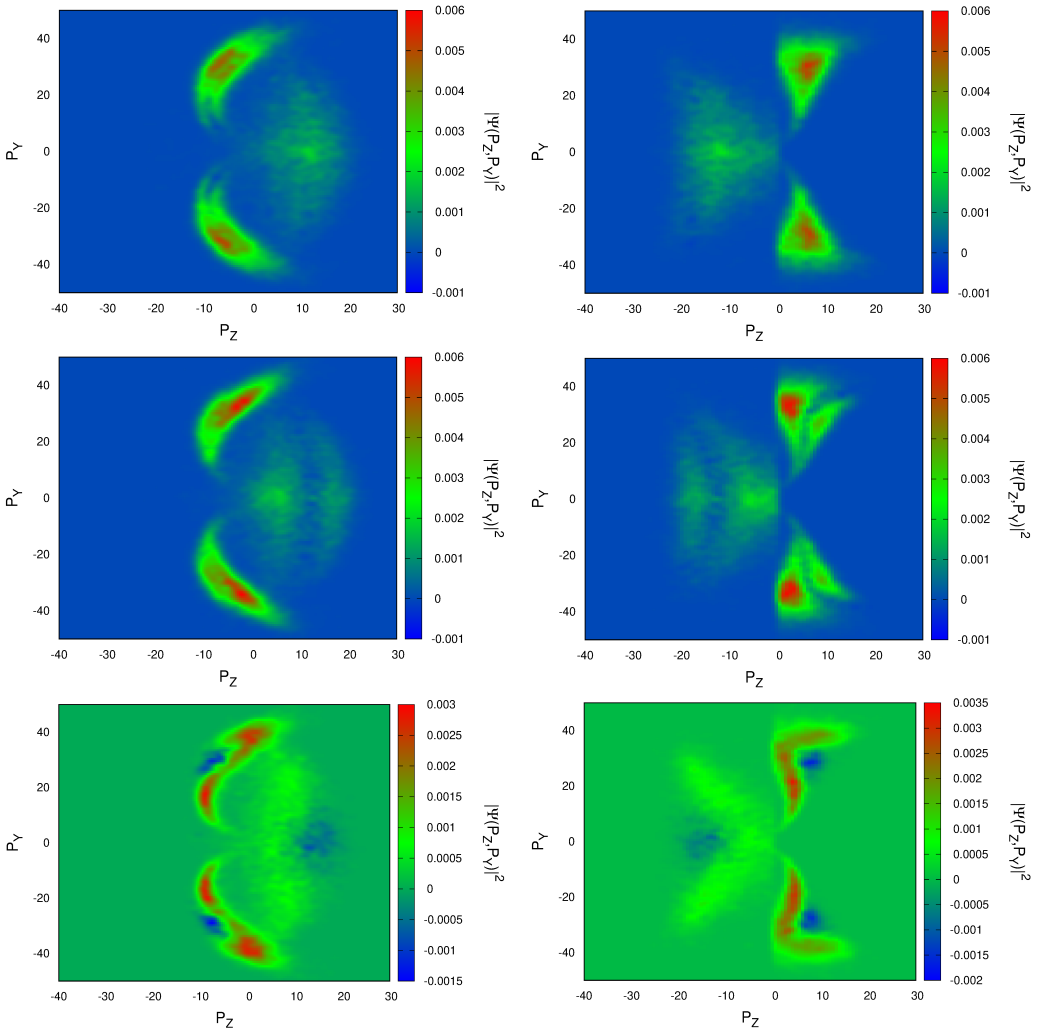


FIGURE 9.8. $2^1A_1$ final momenta images after propagation of 100,000 trajectories using excited-initial conditions. Left column: molecular frame, right column: COLTRIMS frame. Top row: bend excitation, middle row: symmetric-stretch excitation, bottom row: asymmetric-stretch excitation.

unique structure. The two deuterium ions seem to have trajectories around a point of depression in counts at about $P_z = 10$ a.u. and $P_y = \pm 30$ a.u. These negative sectors are expected to converge to zero as $1/N$, where $N$ is the sample size, when $N \to \infty$. However, it would be interesting to see if these structures manifest themselves in an experiment or if these sections of low counts are just artifacts of our semi-classical method.

These three states show that for imaging the final momenta vectors of the two deuterium ions from a vibrationally hot heavy water molecule, only from the direct breakup mechanism can one

determine which vibrational mode has been excited within a COLTRIMS experimental observation. In Fig. 9.6 for all three excitation in each mode for the $^1A_2$ state, we see essentially the same structure for the excited-initial conditions. For example, in Fig. 9.8(bottom row) we see the same node at $P_y = 0$ a.u. in the oxygen atom as in the asymmetric stretch-excitation of the initial Wigner distribution seen in Figs. 9.5(a) as Cartesian coordinates. This clear preservation of structure is lost for the more involved slingshot dynamics that the $^1B_1$ and $2^1A_1$ states undergo. In other words, the topology of these states deform the initial nodal structure to the point where easy assignment of which mode was excited just from the final Newton-like images is not feasible. For instance, Fig. 9.6(middle row) shows structure that in no way indicates the symmetric-stretch excitation based on the patterns in Figs. 9.4 alone. These observations stress the requirement of theoretical simulations guiding experimental interpretations for this proposed COLTRIMS experiment.

### 9.3. Predictions for Future Experiments

We note another experimental observable that sets a firm set of predictions for future experiments, the two and three-body branching ratios. Table 9.1 lists the branching ratios for all three states using initial conditions generated from a Wigner distributions constructed from a harmonic wave function with $n = 1$ for one of the three modes. The three electronic states have markedly different branching ratios and it's instructive to compare these results with the original results in Table 5.1. Albeit, comparing numbers in Table 5.1 to Table 9.1 is not correct because Table 9.1 has 10× more trajectories. Thus, we only note the general patterns here.

We see the branching ratio for the state that is largely three-body direct breakup in the Table 5.1, namely the $^1A_2$ state, isn't effected by one quanta excitation in any of the three modes. The $^1A_2$ branching ratio is still largely three-body when using excited-initial conditions. As noted before, the branching ratio for the $^1B_1$ state is largely two-body. With one quanta excitation in either of the three modes of motion, this state's branching ratio is still largely two-body. Looking at the potential energy slices in symmetric stretch (Fig 3.1), for example, the $^1B_1$ has a barrier to symmetric dissociation. This coupled with a larger gradient to bond opening angle was the argument for this state's dynamics to flip backwards in a slingshot motion. It's reasonable to suggest then, that there is a specific number of quanta excitation in symmetric stretch that would

TABLE 9.1. Branching ratios for two and three-body breakup channel from ensembles of 100,000 classical trajectories with initial conditions sampled from the Wigner distribution generated from one quanta, $n = 1$, excitation in the respected modes.

Bend Excitation

| $D_2O^{++}$ Electronic state | % Two-Body | % Three-Body |
|---|---|---|
| $^1A_2$ | 0 | 100 |
| $^1B_1$ | 97 | 3 |
| $2^1A_1$ | 30 | 70 |

Symmetric Stretch Excitation

| $D_2O^{++}$ Electronic state | % Two-Body | % Three-Body |
|---|---|---|
| $^1A_2$ | 0 | 100 |
| $^1B_1$ | 97 | 3 |
| $2^1A_1$ | 27 | 73 |

Antisymmetric Stretch Excitation

| $D_2O^{++}$ Electronic state | % Two-Body | % Three-Body |
|---|---|---|
| $^1A_2$ | 1 | 99 |
| $^1B_1$ | 97 | 3 |
| $2^1A_1$ | 65 | 35 |

overcome this barrier and the branching ratio would swing in favor of three-body for this state and the dynamics would proceed in a direct breakup fashion.

Finally we examine the $2^1A_1$ state's branching ratios. After 100,000 trajectories using the ground-vibrational state to model the initial conditions, the branching ratios for this state were three-body = 67.3% and two-body = 32.7%, which is consistent with Table 5.1. For this state, Table 9.1 presents branching ratios that have comparable numbers to Table 5.1 for one quanta excitation in the bend mode and in the symmetric-stretch mode. However, the branching ratios completely flip for the asymmetric-stretch mode with three-body = 35% and two-body = 65%. This indicates that the asymmetric-stretch mode is probing the separatrix [**26**] in phase space that defines the seam separating the regions of two and three-body dynamics. (In general, a separatrix is the boundary separating two modes of behaviour in a differential equation.) This

finding was hinted at in Fig. 7.10 where it was shown that this state has markedly different inital-conditions distributions for two and three-body dynamics. Therefore, this analysis shows that if an COLTRIMS experiment could excite the water molecule's asymmetric-stretch mode, the total yield of the two and three-body breakup channels would flip. The author notes that the asymmetric stretch mode has $B_2$ symmetry while the symmetric stretch and bend modes have $A_1$ symmetry. Thus an experiment that could align the water molecule with respect to the polarization, while also exciting the molecule slightly before double-photoionization, perhaps would see this effect.

It's worth mentioning within a COLTRIMS experiment the two separate islands in Fig. 9.8(right column, middle row), for example, would be interpreted as two distinct states. Clearly this is not the case if the experiment is probing a vibrationally excited-neutral-water molecule, as evident in these results. As an illustration, Fig. 9.9 shows the final Newton-like momenta images for the $^1A_2$ state with initial conditions starting from a Wigner distribution that is constructed from a $n \geq 2$ harmonic wave function. For two quanta in the asymmetric-stretch mode, Fig. 9.9(Top), we see two separate islands for the deuterium ions and two nodes in the inferred neutral oxygen. In Fig. 9.9(Bottom), the clear distinct structures start to become opaque with five quanta in the asymmetric-stretch mode. Hence, an experiment that excites one mode with multiple quanta may see the higher $n$ vibrational nodes but will lose the nodal resolution. These and previous results show that it is vital to have theoretical simulations in a coordinated effort with the experiment proposed by this chapter, to accurately interpret the resulting measurements.

As noted in the beginning of this chapter, the COLTRIMS experiment takes advantage of assuming the target is "cold" when analyzing the results. The agreement between these experimental results and theoretical simulations using initial conditions that were generated from the ground-vibrational state of water presented in previous chapters, is evidence of the validity of this assumption. Thus, the purpose of this chapter is to set the stage for a new experiment of measuring the momentum vectors of the deuterium ions after single-photon double ionization of a vibrationally-excited water molecule. The author notes that this experiment is only analyzing the nuclei and, therefore does not require, in theory, a four-fold coincidence measurement used in a COLTRIMS apparatus. Such an experiement would require one to excite the molecule using an infrared laser and probe using VUV/XUV photons, for example. One could generate these

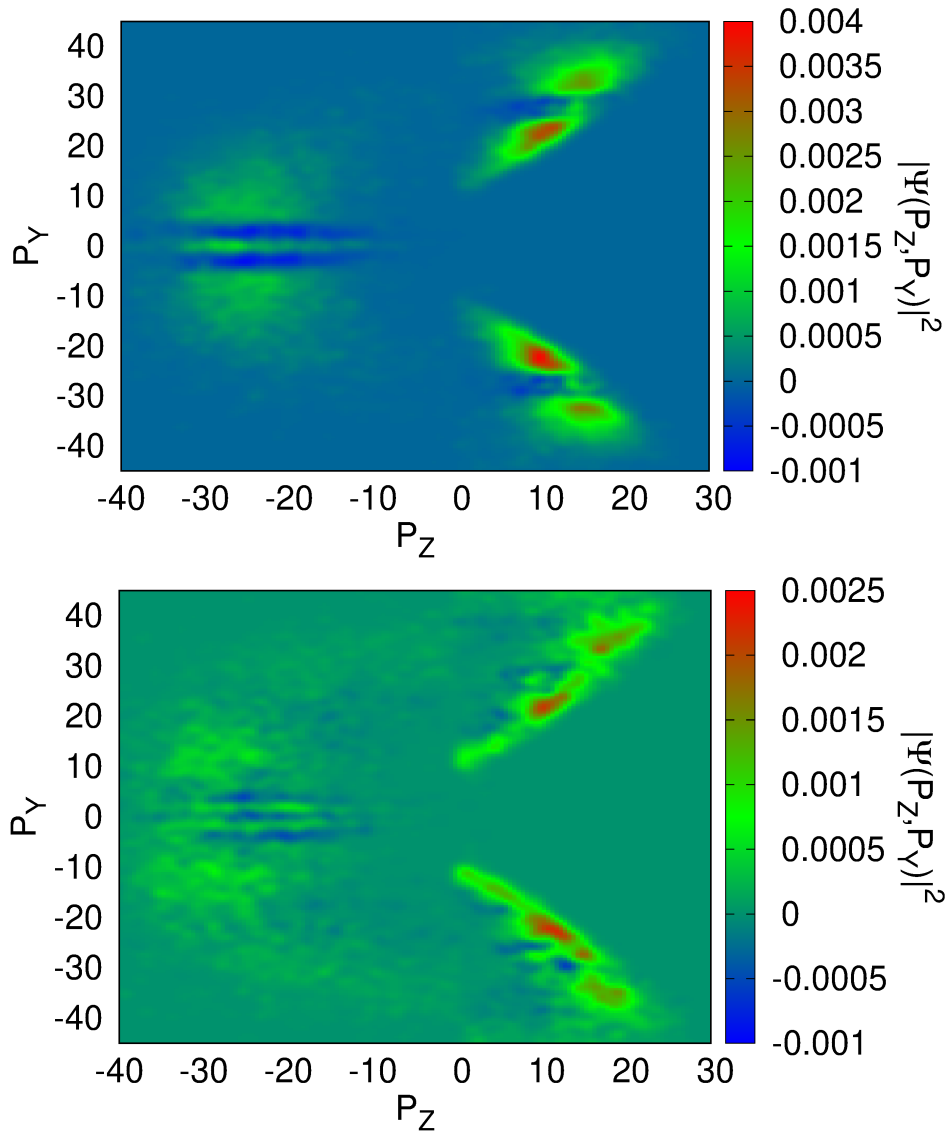


FIGURE 9.9. Newton-like momenta images for the $^1A_2$ state starting from initial conditions generated from an Wigner distribution with a variable number of quanta in the asymmetric-stretch mode. Top: $n = 2$, bottom: $n = 5$

using high-harmonic generation or if one wasn't so interested in a time-resolved measurment via a synchrotron light source. The theoretical results in this chapter show such an experiment would image the initial-vibrational node in the final measured momenta of the deuterium ions. Also, this experiment should be able see a clear signal in the asymmetric-stretch excitation by noting a complete change in the two and three-body branching ratios of the $2^1A_1$ state, allowing for tunable dynamics and perhaps more fine control over how an experiment excites the water molecule.

# Publications

(1) Zachary L. Streeter, Frank L. Yip, Robert R. Lucchese, Benoit Gervais, Thomas N. Rescigno, and C. William McCurdy, "Dissociation dynamics of the water dication following one-photon double ionization. I. Theory", Phys. Rev. A **98**, 1-10 (2018).

(2) D. Reedy, J. B. Williams, B. Gaire, A. Gatton. M. Weller, A. Menssen, T. Bauer, K. Henrichs, Ph. Burzynski, B. Berry, Z L. Streeter, J. Sartor, I. Ben-Itzhak, T. Jahnke, R. Dörner, Th. Weber, and A. L. Landers, "Dissociation dynamics of the water dication following one-photon double ionization. II. Experiment", Phys. Rev. A **98**, 053430 (2018).

(3) Larsen, Kirk A., Rescigno, Thomas N., Severt, Travis, Streeter, Zachary L., Iskandar, Wael, Heck, Saijoscha, Gatton, Averell, Champenois, Elio G., Strom, Richard, Jochim, Bethany, Reedy, Dylan, Call, Demitri and Moshammer, Robert, Dörner, Reinhard, Landers, Allen L., Williams, Joshua B., McCurdy, C. William, Lucchese, Robert R., Ben-Itzhak, Itzik, Slaughter, Daniel S. and Weber, Thorsten, "Photoelectron and fragmentation dynamics of the $H^+ + H^+$ dissociative channel in $NH_3$ following direct single-photon double ionization", Phys. Rev. Res. **2**, 043056 (2020).

(4) Kirk A Larsen, Thomas N Rescigno, Zachary L Streeter, Wael Iskandar, Saijoscha Heck, Averell Gatton, Elio G Champenois, Travis Severt, Richard Strom, Bethany Jochim, Dylan Reedy, Demitri Call, Robert Moshammer, Reinhard Dörner, Allen L Landers, Joshua B Williams, C William McCurdy, Robert R Lucchese, Itzik Ben-Itzhak, Daniel S Slaughter and Thorsten Weber, "Mechanisms and dynamics of the $NH_2^+ + H^+$ and $NH^+ + H^+ + H$ fragmentation channels upon single-photon double ionization of $NH_3$", J. Phys. B. Atom. Molec. Phys. **53**, 244003 (2020).

(5) Chuan Cheng, Zachary L. Streeter, Andrew J. Howard, Michael Spanner, Robert R. Lucchese, C. William McCurdy, Thomas Weinacht, Philip H. Bucksbaum, and Ruaridh Forbes,

"Strong Field Ionization of Water II: Electronic and Nuclear Dynamics En Route to Double Ionization", (Phys. Rev. A Accepted).

(6) Travis Severt, Zachary L. Streeter, Wael Iskandar, Kirk A. Larsen, Averell Gatton, Daniel Trabert, Bethany Jochim, Brandon Griffin, Elio G. Champenois, Matther W. Brister, Dylan Reedy, Demitri Call, Richard Strom, Allen L. Landers, Reinhard Dörner, Joshua B. Williams, Daniel S. Slaughter, Robert R. Lucchese, Thorsten Weber, C. William McCurdy and Itzik Ben-Itzhak, "Step-by-step, state-selective tracking of sequential fragmentation dynamics of water dications by momentum imaging", (PNAS submitted).

(7) W. Iskandar, T. N. Rescigno, Z. L. Streeter, C. W. McCurdy, R. R. Lucchese, K. A. Larsen, B. Griffen, J. B. Williams, B. Jochim, T. Severt, I. Ben-Itzhak, D. S. Slaughter, and Th. Weber, "Role of charge redistribution and electron transfer in the ultrafast photodissociation of the heavy water dication into $D^+ + O^+ + D$", (In preparations).

# Dissociation dynamics of the water dication following one-photon double ionization I: Theory

Zachary L. Streeter,[1,2] Frank L. Yip,[3] Robert R. Lucchese,[1] Benoit Gervais,[4] Thomas N. Rescigno,[1] and C. William McCurdy[1,2,*]

[1] *Chemical Sciences Division, Lawrence Berkeley National Laboratory, Berkeley CA 94720, USA*
[2] *Department of Chemistry, University of California, Davis, CA 95616, USA*
[3] *Department of Science and Mathematics, California State University-Maritime Academy, Vallejo, California 94590, USA*
[4] *CIMAP, Unité Mixte CEA-CNRS-ENSICAEN-UCBN 6252, BP 5133, F-14070 Caen, Cedex 05, France*

The measurement of the triple differential cross section in the body frame for double photoionization of a molecule can be made in principle by detecting the ionic fragments and the two photoelectrons in coincidence – but only if the dynamics and geometry of dissociation of the doubly charged molecular ion are known. A classical trajectory study of the nine lowest states of the water dication is presented using high quality *ab initio* potential energy surfaces. Sampling from a semiclassical initial distribution of positions and momenta is used to approximate ionization from the Frank-Condon region of the ground vibrational state of neutral $H_2O$. Excellent agreement in comparison with preliminary experimental momentum imaging measurements of double photoionization of water show that eight dication states can be unambiguously identified in the experiment with the aid of theory. The theoretical trajectory results allow body frame measurements of double photoionization to yield all eight states even though the usual assumption of direct dissociation, the "axial recoil" approximation, breaks down for three of the dication electronic states seen in the experiment.

## I. INTRODUCTION

Theoretical and experimental interest in single-photon double photoionization is motivated by the fact that this process is exquisitely sensitive to the effects of electron correlation. For that reason, one-photon double ionization is the focus of an extensive literature, of which a small sample includes experimental studies on atoms [1–9] and molecules [10–19] and theoretical studies on atoms [20–41] that form the basis for theoretical treatments of the more challenging single-photon double photoionization from molecules [42–56]. In molecular targets, the physics of double photoionization and, in particular, its sensitivity to the role of electron correlation, is by far best revealed by measurements in the molecular frame [11–18], with no averaging over orientations of the molecule, but those measurements have been almost exclusively limited to the cases of the $H_2$ and $D_2$ molecules. One-photon double photoionization of $H_2$ is followed promptly by the Coulomb explosion of the $H_2^{++}$ dication, and a coincidence measurement of the momenta of the two ejected electrons and one of the protons (together with momentum conservation) produces a kinematically complete description of the double ionization and breakup process. This technique permits reconstruction of the molecular geometry at the time of photoionization, assuming a vertical electronic transition, and allows the observation of the triply differential cross section (TDCS) in the molecular frame.

Naturally, even more can be learned about this fundamental process with more complicated molecular targets, such as the other diatomic molecules of the first row elements, which could expose the role of electron correlation in double ionization of many-electron molecules. However the ground states and first few excited states of $N_2^{++}$ and $O_2^{++}$, for example, have barriers to dissociation such that measurements are feasible only for double ionization producing higher lying excited states of the dications. Thus the TDCS for double ionization to produce the ground and low lying states of those dications, which would be the most accessible to sophisticated theoretical treatments like those that have been performed for $H_2$ and atoms, are not currently accessible by particle coincidence methods. Nonetheless, measurements of the TDCS for double photoionization of $N_2$ have been performed for randomly oriented molecules by Bolognesi, *et al.* [19] producing results suggestive of the rich physics that lies behind this process in more complicated molecules. Moreover, measurement of the TDCS in the body frame

* cwmccurdy@ucdavis.edu

of a nonlinear polyatomic molecule could provide insight into double photoionization uncomplicated by degeneracies in the states of the dication being produced. However, such a measurement requires a target molecule that dissociates upon double photoionization in such a way as to allow the complete determination of the body frame from the final momenta of the ions produced and observed in coincidence with the photoelectrons.

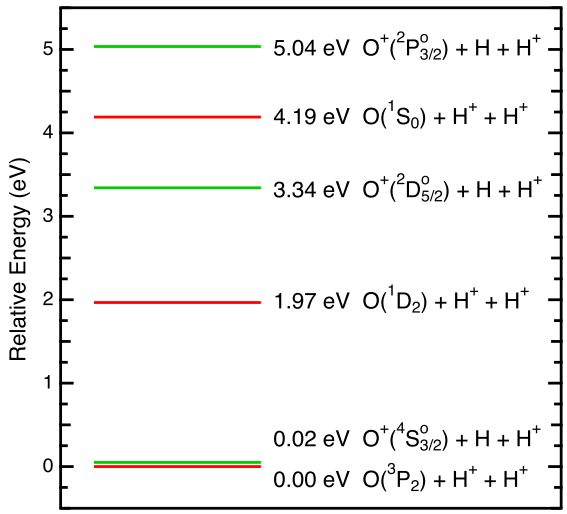


FIG. 1. (Color online) Experimental energies of the low energy asymptotes of the three-body breakup of $H_2O^{++}$ relative to the lowest state O $(^3P_2) + H^+ + H^+$ [57].

Here we explore the dissociation dynamics of doubly ionized water, a polyatomic molecule that provides a practical target for particle coincidence studies of double photoionization. With the aid of the complete nuclear dynamics we present here, the TDCS can be measured in the molecular frame for double ionization leading to the formation of eight of the lowest nine states of the $H_2O^{++}$ dication. This study focuses on the nuclear dynamics on the potential surfaces of the nine lowest states of $H_2O$, for eight of which the breakup channel producing two protons, $\gamma + H_2O \rightarrow 2H^+ + 2e^- + O$, either dominates or occurs to an experimentally measurable extent. We compare the results of our classical trajectory study with exploratory experiments using the cold target recoil momentum imaging method (COLTRIMS) that have recently yielded a complete momentum plane picture of the final momenta of

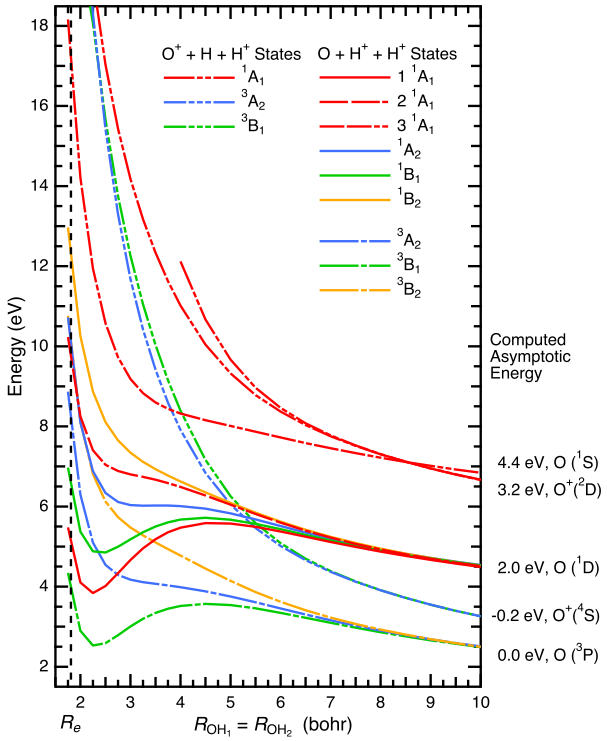


FIG. 2. (Color online) Potential curves for the symmetric breakup ($\theta_{HOH} = 104.45°$), $H_2O^{++} \rightarrow O + H^+ + H^+$ and $O^+ + H + H^+$ from internally contracted multireference configuration interaction (icMRCI) calculations, showing the nine states of the water dication that correlate with the valence states of the oxygen atom and four of the valence states that correlate with the oxygen atomic ion. The energies given on the right-hand-side of the figure indicate the computed asymptotic energies for the three particle breakup with the indicated atomic O state and the H atom, if present, in its ground state. The energies on the vertical scale on the left and the asymptotic energies on the right are relative to the $O(^3P) + H^+ + H^+$ asymptotic energy.

the protons after double ionization yielding particular states of $H_2O^{++}$. Those experimental results, including some preliminary observations of the photoelectrons that yield information about the electron dynamics, are reported in full detail in reference [58] hereafter referred to as II.

The energies of the three-body breakup asymptotes of the $H_2O^{++}$ ion are given in Fig. 1. The lowest three electronic energy terms of the oxygen atom in its ground state electronic configuration of $1s^22s^22p^4$ are the $^3P$, $^1D$ and $^1S$ levels whose degenerate components (neglecting spin-orbit cou-

pling) comprise three triplet and six singlet singlet states. When combined with two protons, these atomic states correlate with the nine lowest states of the $H_2O^{++}$ dication at the equilibrium geometry, as shown in Fig. 2. There are thus three energetic asymptotes for the process $H_2O^{++} \rightarrow H^+ + H^+ + O$ for the nine lowest states of the dication. Additionally, there are low-energy asymptotes of the form H + $H^+$ + $O^+$. The two lowest such asymptotes have the oxygen ion in either its ground state $O^+$ ($^4$S) or in its first excited state $O^+$ ($^2$D). Note that at the equilibrium geometry these state are above the nine state that connect with the $H^+$ + $H^+$ + O asymptotic states. However, as seen in Fig. 2, the states leading to H + $H^+$ + $O^+$ ($^2$D) cross the state of the same symmetry leading to the $H^+$ + $H^+$ + O ($^1$S) asymptote, although these crossing occur at fairly large separations and, as will be discussed below, are not believed to affect the nuclear dynamics on the states leading to the $H^+$ + $H^+$ + O asymptotes.

Fig. 2 suggests that the nuclear dynamics for breakup of the dication might be direct, with the two protons dissociating roughly along the OH bonds for some channels and perhaps surmounting barriers to do so for the others. However the dynamics on the full potential surfaces shows that the dynamics of three-body breakup on some of these states is substantially more complicated. The axial recoil approximation, in which the dissociation of the dication is assumed to be direct and to occur before any appreciable rotation or rearrangement of the molecule (commonly used in the interpretation of momentum imaging experiments using the COLTRIMS method) breaks down radically for some of these electronic states. Nonetheless, a quantitative understanding the nuclear dissociation dynamics opens the door to four-particle coincidence measurements detecting two protons (which can establish the molecular frame) and two electrons that will constitute the TDCS in the molecular frame of a polyatomic molecule for eight of the nine states of the water dication dissociating to the lowest three energy levels of the oxygen atom.

The outline of this paper is as follows. In Sec. II we describe the potential surfaces for the nine electronic states of the $H_2O^{++}$ dication on which we have carried out classical trajectory studies, including the calculation of one which has not appeared previously in other studies. In Sec. III we discuss intersections occurring between the highest of those states and states correlating with other asymptotes. Sec. IV describes the classical trajectory study which sampled initial conditions from the Wigner phase space distribution of neutral water in its ground state, and in Sec. V the results are compared with experimental measurements from II to establish that the calculated dynamics are indeed consistent with the momentum plane observations. In Sec. VI we summarize how the knowledge of the nuclear dynamics, including for those channels in which the dissociation is not direct and for which the "axial recoil" approximation does not hold, can be used together with experimental observations to measure the TDCS in the body frame.

## II. THE ELECTRONIC STATES OF $H_2O^{++}$

At the equilibrium geometry of $H_2O$, the lowest nine electronic states of the water dication can be described qualitatively as the states that arise from the removal of two electrons from the highest three molecular orbitals of the Hartree-Fock ground state electronic configuration, $1a_1^2\ 2a_1^2\ 1b_2^2\ 3a_1^2\ 1b_1^2$. As shown in Fig. 2, for three-body breakup the $^3B_1$, $^3A_2$ and $^3B_2$ states correlate with the three components of the $^3$P ground state of the oxygen atom. The $1^1A_1$, $^1B_1$, $2^1A_1$, $^1A_2$ and $^1B_2$ correlate with the components of the $^1$D state of oxygen. The $3^1A_1$ correlates with the oxygen $^1$S state.

In a study of the breakup of the water dication into the $H^+ + OH^+$ channel, Gervais *et al.* [59] computed potential surfaces for the eight states dissociating to the O $^3$P and $^1$D states. Those surfaces were calculated at a sophisticated level using internally contracted multireference configuration interaction (icMRCI) methods at the configuration interaction singles and doubles (CISD) level including the Davidson correction for quadruple excitations. Those accurate *ab initio* surfaces were fit to a linear combination of 100 basis functions that represent the Coulomb and polarization interactions at intermediate and long interatomic distances together with screened Coulomb and multipole interactions at short distances. The typical deviation of the fit, which is described in detail in Ref. [59], from the calculated energy points was of the order of $10^{-3}$ hartrees in that study, and the fits represent the surface for $R_{OH} > 0.8$ bohr and $\theta > 80°$. We used those surfaces for the lower eight states in the classical trajectory calculations we report here.

Since our interest is in three-body breakup of the dication, and since the preliminary experiments in II observed all three asymptotes, we calculated the

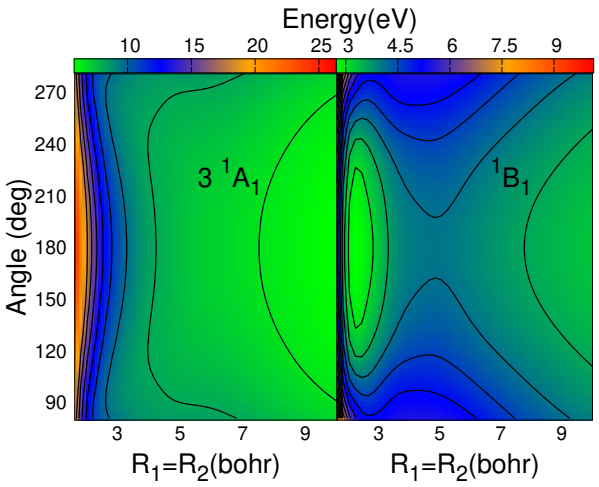


FIG. 3. (Color online) Comparison of $3^1A_1$ and $^1B_1$ potential surfaces as a function of symmetric stretch and HOH angle.

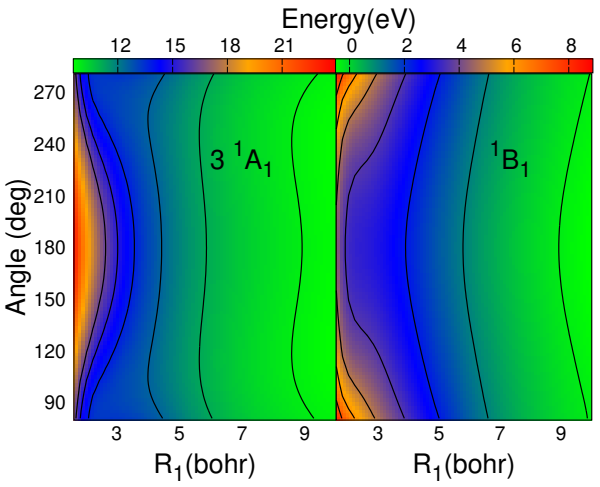


FIG. 4. (Color online) Comparison of $3^1A_1$ and $^1B_1$ potential surfaces as a function one $R_{OH}$ distance and HOH angle with the other internuclear distance fixed at $R_{OH} = 1.81$ bohr

remaining potential surface for the $3^1A_1$ state, and used the functional form developed by Gervais *et al.* to fit it. The calculations were performed with the MOLPRO [60, 61] suite of quantum chemistry programs using the same icMRCI method at the CISD level including the Davidson correction as the calculations of the other surfaces [59] employed in the classical trajectory calculations in Sec. IV. The Gaussian basis was the cc-pVTZ Dunning correlation consistent basis [62], and the MRCI calculations were based on orbitals from CASSCF calculations on the lowest $^3B_1$ state in $C_s$ symmetry with one a′ orbital frozen and six electrons in five a′ and two a″ orbitals. The grid of 4722 geometries consisted of 11 angles from 80° to 180° and values of $R_{OH}$ from 1 to 50 bohr with fine spacings at short distances.

Two comparisons of potential surfaces relevant to the dynamics in the three-body breakup channel to produce two protons are shown in Figs. 3 and 4. As we will see below in Sec. V, dissociation into the O + $H^+$ + $H^+$ arrangement is direct for some of the nine states of the dication we consider. For these dication states, the axial recoil approximation is valid and the final momenta of the two protons can be used in a COLTRIMS experiment to determine the plane of the molecule and its orientation in coincidence with the photoelectrons. But for others, in particular for the $^1B_1$ state shown in those figures, the axial recoil approximation breaks down completely, but does so in a predictable way that potentially allows the determination of the molecular frame. For both the $3^1A_1$ and $^1B_1$, a strong gradient towards symmetric dissociation is visible in Fig. 3 that is reflected also in the curves in Fig. 2. The key difference between the two potential surfaces is visible at the left hand edges of each panel of Figs. 3 and 4 where there is a strong gradient towards larger bond angles in the case of the $^1B_1$ state while the opposite is the case for the $3^1A_1$. In Fig. 5 we plot bending curves on the nine surfaces with the OH distances fixed at the equilibrium distance of the neutral and where the behavior of the $3^1A_1$ and $^1B_1$ states contrasts strongly. We can make the simple observation that at the equilibrium geometry the potential surfaces of three of the states, the $^3B_1$, $^1B_1$ and $2^1A_1$ have a strong or significant component of the gradient in the direction of larger bond angles. That observation is directly correlated with the breakdown of the axial recoil approximation that we see in the classical trajectory study of the three-body breakup channel.

We note that similar calculations of portions of the potential surfaces carried out using uncontracted multireference CISD and larger CAS choices with the Columbus suite of quantum chemistry programs [63–65] gave no significant differences with the calculations used to compute the complete surfaces for dynamics. For example, the calculations that generated the curves in Figs. 2 and 5 were also carried out with a larger CAS space in the MCSCF and larger reference space for the CISD calculation that

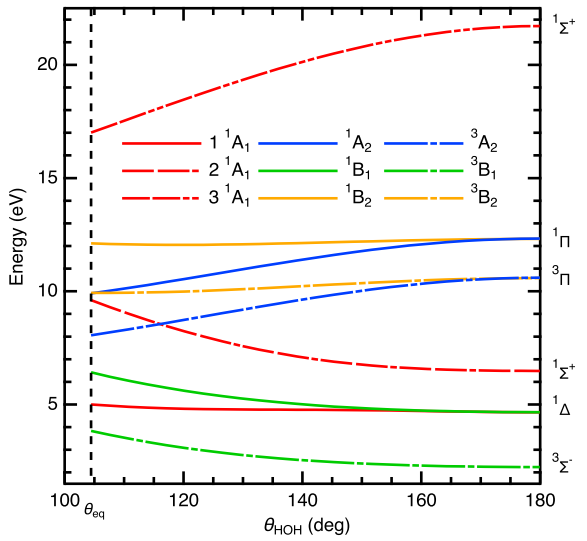


FIG. 5. (Color online) Potential curves for bending with $R_{OH} = 1.81$ bohr from multireference CISD calculations for the nine states of the water dication that correlate with the valence states of the oxygen atom (see Fig. 2).

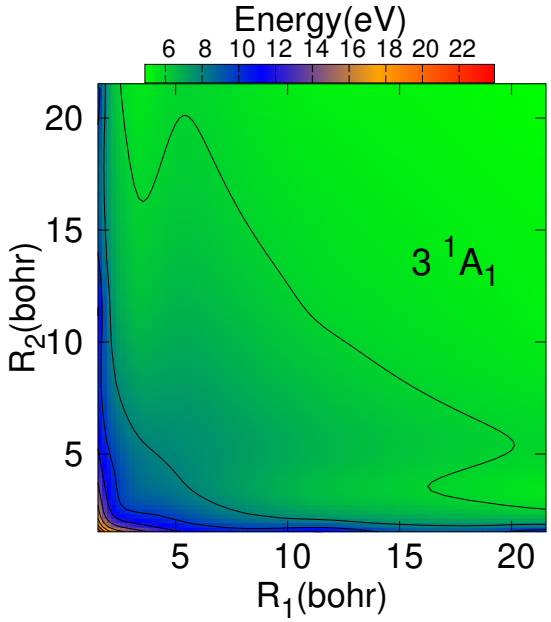


FIG. 6. (Color online) Calculated potential surface as a function of $R_{OH}$ distances with $\theta = 104.45^\circ$ showing the shallow $OH^+$ well and barrier to dissociation.

consisted of three $a_1$, two $b_1$, two $b_2$ and one $a_2$ active orbitals (with the $1a_1$ orbital frozen) and show only inconsequential overall energy shifts from the less-correlated calculations.

Finally we observe that the $OH^+ + H^+$ asymptote of the potential surface for the $3^1A_1$ ($4^1A'$) state is the $^1\Sigma^+$ state with a dominant configuration $1\sigma^2\,1\pi^4\,2\sigma^2$ which is not bound but has a barrier to symmetric dissociation, apparent in Fig. 6, of about 0.56 eV. In our study, none of the classical trajectories in the ensemble were observed to remain trapped behind the barrier.

## III. DIABATIC STATES LEADING TO $O^+ + H^+ + H$ ASYMPTOTES AND AN APPROXIMATE DIABATIC SURFACE FOR THE $3^1A_1$ STATE

In the present paper we are comparing to experiments [58] performed at a photon energy of 57 eV, which corresponds to 20.3 eV on the energy scale used in Fig. 2. At this energy the states that are diabatically connected to the $O^+ + H^+ + H$ asymptotes are not energetically accessible. However, we know from the asymptotes, illustrated in Fig. 1, that the diabatic states of $^1A'$ symmetry leading the $O^+(^2D^o_{5/2}) + H + H^+$ must cross the $^1A'$ state,

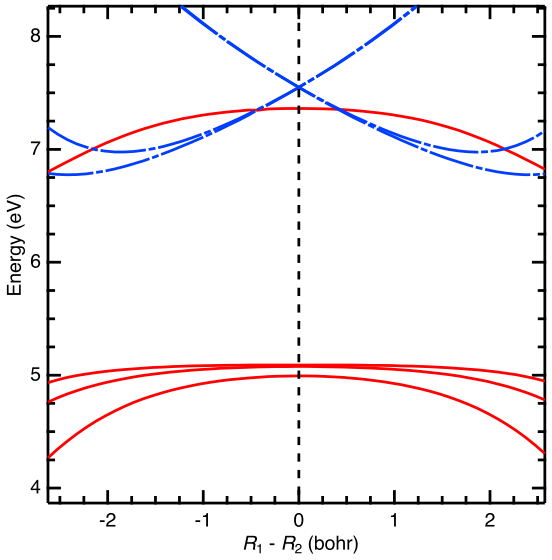


FIG. 7. (Color online) Cuts through the icMRCI diabatic PESs for the lowest eight A′ states of $H_2O^{++}$ for $\theta = 110^\circ$ with $R_{OH_1} + R_{OH_2} = 14.75$ bohr. The solid red lines are for the PESs that diabatically connect to the $O+H^+ + H^+$ asymptotes and the dashed blue lines are for the PESs that diabatically connect to the $O^+ + H^+ + H$ asymptotes.

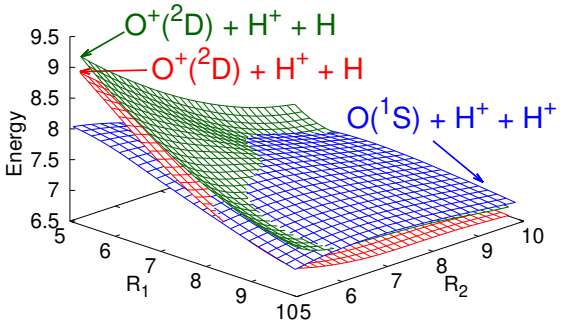


FIG. 8. (Color online) Calculated PESs in eV as a function of $R_1$(bohr) and $R_2$(bohr) distances with $\theta = 110°$. The red and green surfaces are the fifth and sixth adiabatic states of $^1A'$ symmetry in the icMRCI calculation based on five states in the SA-CASSCF calculation. The blue surface is the potential that was fit to the converged icMRCI points where the fourth $^1A'$ could be well described as being connected to the $O(^1S) + H^+ + H^+$ asymptote. This approximate diabat for the $3^1A_1$ state passes through through the two surfaces that correlate to $O^+(^2D)$ state.

which has $^1A_1$ symmetry in $C_{2v}$ geometries, that is connected to $O(^1S_0) + H^+ + H^+$. To calculate the potential energy surfaces (PESs) that are diabatically connected to both $O^+$ and O asymptotes we have performed icMRCI calculations based on orbitals from a state-average (SA) CASSCF reference wave function that had two $^3B_1$, two $^3A_2$, and one $^3B_1$ reference states. As can be seen in Fig. 2, these reference states include states that are connected to both $O^+$ and O asymptotes.

Additionally, we can see in Fig. 2 that the PESs that correlate to the $O^+(^4S)$ asymptote do not cross any of the lower triplet states correlating to the $^3P$ of neutral oxygen atom. However, the PESs that correlate to the $O^+(^2D)$ asymptote cross the $3^1A_1$ PES at 8.5 bohr. Additional insight into these different PESs is given by considering cuts of the eight lowest $^1A'$ PESs with fixed $\theta = 110°$ and constant $R_{OH_1} + R_{OH_2} = 14.75$ au shown in Fig. 7. The diabats shown there were constructed by sorting the fixed-nuclei energies into sets that gave the smoothest connected curves. We note that there was an exceeding small energy splitting found where the states connected to the different asymptotes crossed. The very weak interactions between the diabats is presumable due to the fact that any such splitting would be caused by the tunneling of an electron from an O atom to a proton at a distance of over 7 bohr.

The choice of CASSCF reference wave function in the computation of the potential surface for the $3^1A_1$ state used to study the breakup dynamics included only one state, the $^3B_1$ ground state. This reference space could adequately represent states with the $O + H^+ + H^+$ asymptote but was insufficient for converging the icMRCI calculations using MOLPRO for states dominated by configurations describing the $O^+ + H^+ + H$ asymptote. Thus there was a subset of geometries where the icMRCI did not converge to a $3^1A_1$ state with a strong overlap with the reference space. This potential was then fit using the analytical form of Gervais *et al.* [59] neglecting points at those geometries and incorporating the proton-proton repulsion at large distances.

As seen in Fig. 8, the choice of the $^3B_1$ state as the reference wave function coupled with the assumptions made in the fitting procedure provided an approximate diabat for the $3^1A_1$ state. This approximate diabatic surface allowed the calculation of classical trajectories leading to the $O + H^+ + H^+$ asymptote neglecting the effects of small couplings to states leading to the other arrangements.

## IV. CLASSICAL TRAJECTORIES SAMPLING FROM THE INITIAL VIBRATIONAL DISTRIBUTION OF NEUTRAL $H_2O$

We have calculated ensembles of classical trajectories for each state of the dication, sampling from the Wigner phase space distribution for the normal modes of vibration of the neutral water molecule. The Wigner distribution [66] is a semiclassical phase distribution that can provide a useful ensemble of initial conditions for classical trajectories that approximately represent the effects of zero point motion. For the harmonic oscillator, it is given by a familiar and everywhere positive analytical expression. For a molecule with N atoms the Wigner distribution in the harmonic approximation is

$$W(\mathbf{Q},\mathbf{P}) = \frac{1}{(\pi\hbar)^{3N-6}} \prod_{j=1}^{3N-6} \exp\left[-\frac{\omega_j}{\hbar} Q_j^2 - \frac{P_j^2}{\hbar\omega}\right], \quad (1)$$

where $Q_j$ and $P_j$ are the normal mode coordinates and momenta, respectively, and $\omega_j$ are the associated frequencies which are defined in terms of the eigenvectors and eigenvalues of the mass weighted

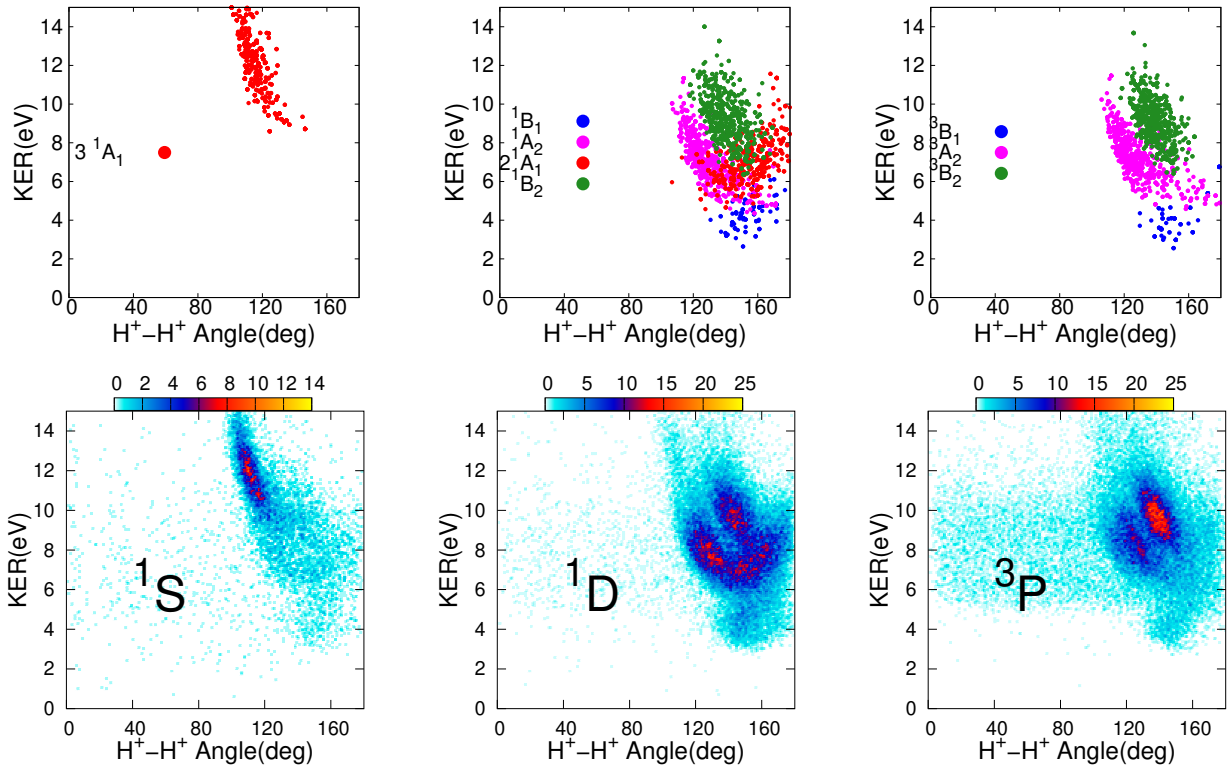


FIG. 9. (Color online) Plots of the total kinetic energy release of the atomic fragments versus the angle between the momenta of the ejected protons shown separately for the three states of the oxygen atom that can be distinguished in the experiment. Top row: classical trajectories, bottom row: histogram plot of experimental measurements.

Hessian, $B_{i,j} = (m_i m_j)^{-1/2} \partial^2 V / \partial x_i \partial x_j$,

$$\mathbf{BL} = \mathbf{L}\Lambda \tag{2}$$

with $\mathbf{L}^T\mathbf{L} = \mathbf{1}$ and $\Lambda_j = \omega_j^2$. Metropolis sampling of Eq.(1) can be used to provide initial conditions for the classical trajectories in the original cartesian coordinates and momenta, $x_i$ and $p_i$, according to

$$\begin{aligned} x_i &= x_i^{(0)} + \frac{1}{\sqrt{m_i}} \sum_{j=1}^{3N-6} L_{i,j} Q_j \\ p_i &= \sqrt{m_i} \sum_{j=1}^{3N-6} L_{i,j} P_j \ . \end{aligned} \tag{3}$$

Such an ensemble of initial conditions provides a classical approximation to the quantum dissociation dynamics initiated by an electronic transition to the double continuum governed by the Franck-Condon approximation.

Here we used the normal modes from a CASSCF calculation on neutral $H_2O$ using the same CAS choice and basis as in the calculations on the excited state ions. The calculated normal mode frequencies were 3762.7 $cm^{-1}$, 1692.8 $cm^{-1}$ and 3877.9 $cm^{-1}$, which are 3 to 6% larger than the experimental values. Gervais *et al.* [59] performed a similar sampling of the Wigner distribution in their study

TABLE I. Branching ratios for three-body breakup channel from ensembles of 1000 classical trajectories with initial conditions sampled from the Wigner distribution of the initial neutral state.

| | | |
|---|---|---|
| $^3B_1$ | 7.6 | Yes |
| $1\,^1A_1$ | 1.6 | – |
| $^1B_1$ | 15.4 | Yes |
| $2\,^1A_1$ | 67.5 | Yes |
| $^3A_2$ | 100 | No |
| $^3B_2$ | 99.8 | No |
| $^1A_2$ | 99.6 | No |
| $^1B_2$ | 99.1 | No |
| $3\,^1A_1$ | 100 | No |

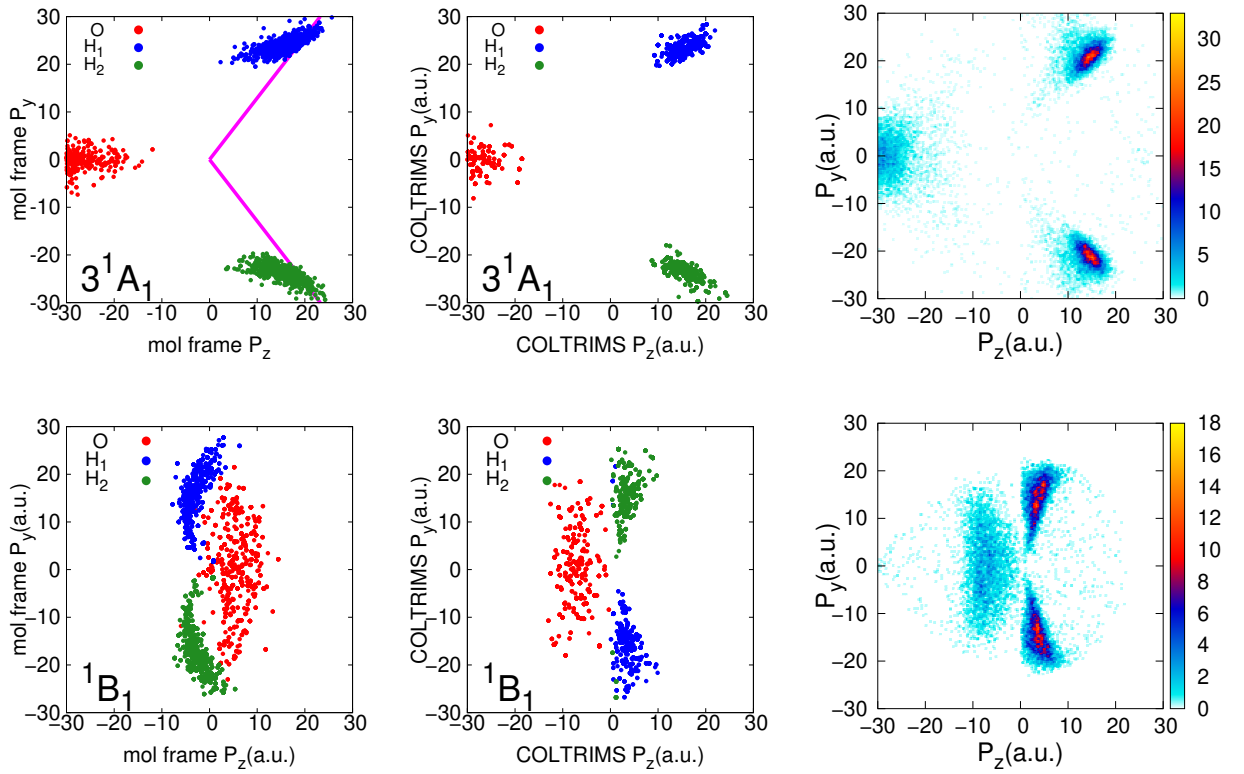


FIG. 10. (Color online) Fragment momentum distributions for $3^1A_1$ and $^1B_1$. Left panels: computed final momenta of the classical trajectories, solid lines indicate directions of strict axial recoil dynamics. Middle panels: momenta from the classical trajectories analyzed and plotted to determine the apparent molecular plane and orientation under the assumption of axial recoil as explained in the text. Right panels: COLTRIMS experimental data analyzed and plotted as in the middle panels.

of the $OH^+/H^+$ dissociation channel, but used the experimental values of the frequencies instead of the computed ones. The branching ratios into the three body arrangement from calculations using ensembles of 1000 trajectories are shown in Table I. The criterion for categorizing a trajectory as three body was that the $R_{OH}$ distance of one proton be 200 bohr or greater and that the other reach at least 50 bohr.

The calculated branching ratios generally reproduce the trends in the calculations of Gervais *et al.* for dissociation of the first eight of these states in the case of $HOD^{++}$. They point out that the branching ratios are controlled in large measure by saddle points at equal values of the ROH distance in the potential surfaces of the lower four states. Those branching ratios show a strong isotope effect and may also be sensitive to the details of the distribution of initial conditions.

## V. FINAL MOMENTUM DISTRIBUTIONS FOR THREE-BODY BREAKUP AND THE BREAKDOWN OF THE AXIAL RECOIL APPROXIMATION

Here we make two comparisons with a portion of the preliminary experimental data that is presented and analyzed fully in paper II [58] where the experimental methods are also described in detail. The first comparison is a plot of the kinetic energy release (KER, the sum of kinetic energies of the atomic fragments) versus angle between the final momenta of the two protons. As explained in Ref. [58], those data in the experiment can be separated by the final electronic state of the oxygen atom, since the two protons are observed in coincidence with the two electrons and the sum of these kinetic energies distinguishes the electronic state of the oxygen fragment.

The experimental results analyzed in that way are shown in the lower row of Fig. 9 as a density plot that represents a histogram of coincidence counts. In the upper panel, the asymptotic values for the kinetic energy release and angle between the proton momenta for the classical trajectories surviving into the three-body breakup channel are plotted as individual points.

The classical trajectory results in Fig. 9 show that the correlation between KER and $H^+$– $H^+$ angles can be used to identify initial states of the $H_2O^{++}$ ions that dominate in various regions of the plot. The agreement between the experimental and theoretical distributions in that figure demonstrates that this correlation can be used to perform that identification in other experiments in which the photoelectrons are observed in coincidence with the protons. For the purposes of measuring the TDCS for double photoionization, this analysis is key to the determination of which electronic state of the dication produced the two electrons measured in coincidence with the protons. There appears to be considerable correlation between the intensities of the features in the experimental observation and the density of classical trajectories in the upper panels of Fig. 9. However, the relative numbers of classical trajectories in each of the features is determined by the branching ratios to produce the three body channel on each dication potential surface. Only if the total double photoionization cross sections were approximately the same in magnitude for all the states would one expect the classical trajectories alone to predict the relative intensities of the experimental features. Otherwise, it would be necessary to weight the classical trajectory intensities by the relative cross sections for double ionization to produce their respective dication states.

We note that the $1^1A_1$ state produces too few trajectories in the three-body breakup channel to appear in the plot that predicts the KER versus the angle between the ejected protons for states that correlate to the $^1D$ state of the oxygen atom. The fact that there are only four features in the experimental observation in the corresponding panel (bottom middle) of Fig. 9 is consistent with the theoretical prediction based solely on the branching ratio of the classical trajectories.

The comparison in the rightmost panels of Fig. 9 of classical trajectory and experimental distributions for the $^3P$ asymptote shows two strong and one weak feature in close agreement, but the experiment displays an additional broad distribution between KER values of about 5.5 eV to 10 eV and extending over all $H^+$– $H^+$ angles. We note that the Franck-Condon region for double ionization to produce the $2^1A_1$ state corresponds to at least the upper part of that range of KER, and correlates in the two-body channel, which it produces about 33% of the time (Table I), to the $b^1\Sigma^+$ state of $OH^+$. That state is known to be predissociated by an intersystem crossing with the $A^3\Pi$ of $OH^+$ [59, 67] to produce $O(^3P)$ + $H^+$ with a lifetime of on the order of 2 picoseconds. It is reasonable therefore to speculate that this two-body dissociation channel could produce events in this fourth feature of the experimental distribution for the $O(^3P)$ three body channel. Fig. 2 suggests that a similar mechanism might connect both the $1^1A_1$ and $^1B_1$ states of $H_2O^{++}$ with the triplet three-body asymptote producing other events in this range of KER for which the axial recoil approximation would also break down.

The second comparison with the experiment described in paper II [58] is shown in Fig. 10 where the final momenta of the protons from the classical trajectories for the $3^1A_1$ and the $1^1B_1$ are plotted. In a COLTRIMS experiment, in the absence of knowledge of the dissociation dynamics, the assumption of the axial recoil approximation can be used to determine the apparent orientation of the molecule and thus locate the directions of the ejected electrons in the body frame. The meaning of "axial recoil" approximation [68] in interpreting momentum coincidence experiments in the case of diatomics is the assumption that the fragments are ejected along the direction of vibration and that the axis of the molecule does not rotate appreciably before dissociation is complete. Here, for the dissociation of the triatomic water dication, strict "axial recoil" dynamics would mean that the two protons are ejected along the bond directions as indicated in the top left panel of Fig. 10. However, for the purposes of determining the initial orientation of the symmetry axis of the molecule in this case, it suffices that the two protons be ejected symmetrically near the original bond directions.

Thus in the analysis of the experimental data shown in Fig. 10, the bisector of the angle between the momenta of the two protons determines the z axis of the momentum plane, and the directions of the momenta of the protons are assigned equal angles above and below that axes. The momentum of the oxygen is deduced by momentum conservation under the assumption of a cold target with no center of mass momentum, and thus has the opposite

sign for its $z$ component. To the degree that the dissociation is direct and symmetric, this procedure determines the plane of the molecule and its orientation in that plane for the purposes of coincidence measurements with the ejected electrons. The final momenta of computed classical trajectories can be plotted in exactly the same way to allow a direct comparison with the experiment, and this is what is also shown in Fig. 10.

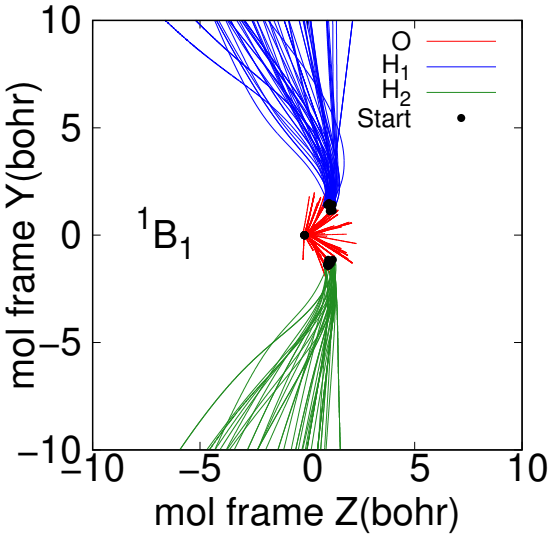


FIG. 11. (Color online) Sixty randomly sampled trajectories in the three-body breakup channel of the $^1B_1$ potential surface, showing the inversion of the original bond angle and consequent breakdown of the axial recoil approximation.

For the $3^1A_1$ state the comparison in Fig. 10 of classical trajectory results with experiment shows that the axial recoil approximation captures the majority of the physics of dissociation. Importantly, when the computed final momenta are plotted in the same way as the COLTRIMS experimental data they are little changed by the assumption of axial recoil. The agreement with the experimental data in this case is excellent.

However, for the $1^1B_1$ state the majority of the protons in the three-body channel emerge traveling towards the *opposite* side of the molecule from the one from which they originated, signaling the complete breakdown of the axial recoil approximation. The origin of this distinctive difference between the dissociation dynamics of the $1^1B_1$ and that of the $3^1A_1$ state is the strong gradient of the potential surface toward bond angle opening in the former case and the gradient toward bond angle closure in the latter. The contrast between these aspects of the two potential surfaces can be seen in Figs. 3, 4 and 5 and was described in Section II.

To illustrate how the gradient in the potential surface affects the dissociation dynamics, a random selection of a subset of the trajectories on the $1^1B_1$ potential surface is plotted in Fig. 11, showing how they invert the sense of the original bond angle of the molecule. Nonetheless, when the classical trajectories are plotted in the same way as the experimental data, under the assumption of axial recoil as described above (center panels of Fig. 10), they reproduce the experimental momentum plane image (right panels of Fig. 10), verifying that the trajectories on this potential surface accurately represent the observed dissociation dynamics. Similar results are found for all three states ($^3B_1$, $^1B_1$ and $2^1A_1$) whose potential surfaces have a strong gradient towards bond opening, as shown in Fig. 5. We note in passing that similar scissoring dynamics that invert the sense of the bond angle have been observed in dissociative attachment of electrons to water to produce oxygen anions [69].

Thus for the eight states that are evidently observed in the experiment, the three-body dissociation dynamics of five of these satisfy the axial recoil approximation, while for the other three, the axial recoil approximation breaks down completely, but does so in a particularly simple and potentially nontheless useful way. The lower panels of Fig. 10 illustrate a mapping of the experimental results analyzed under the assumption of axial recoil onto the correct momentum plane. The classical trajectory results allow the isolation of parts of the experimental observations that are dominated by trajectories that unambiguously invert the original plane of the molecule.

## VI. CONCLUSION

We have verified that the three-body dissociation dynamics of the water dication for the states that dissociate to the oxygen atom in its $^3P$, $^1D$ and $^1S$ states and two protons are well described by classical trajectories on the computed potential energy surfaces. The theoretical calculations predict the momentum plane distributions of the final states in

good agreement with preliminary experimental data, and open the way for a full experimental determination of the TDCS in the body frame for one-photon double photoionization of the water molecule. A complete comparison of theory and experiment for the remaining six states, not shown here, is given in paper II [58].

We have found that for three of those dication electronic states the axial recoil approximation, which has been the basis for the interpretation of most COLTRIMS experiments, and which previously seemed essential to the construction of body frame information from coincidence measurement of ions and photoelectrons breaks down radically. Nonetheless the analysis in Sec. V will potentially allow the measurement of the TDCS in the body frame for those states as well. Those experiments have the potential to reveal for the first time the details of double photoionization in the body frame of a polyatomic molecule.

Experiments such as these will pose a profound challenge to theory to predict the body-frame TDCS for double photoionization of water. The current state of the art for *ab initio* calculation of double photoionization amplitudes is to treat the dynamics of two active electrons completely while freezing the others in target atomic or molecular orbitals. Such calculations have only been carried out on atoms [38–41, 70–73] to our knowledge, but in those cases surprisingly good agreement with experimental angular distributions of the ejected electrons was obtained. To calculate the TDCS for one-photon double ionization of water, we can make the same two-active-electron approximation, and use the computational methods involving a single center expansion and numerical grids that we have used previously in double photoionization calculations on $H_2$ [47–50]. This approach promises to accurately describe correlation between the two outgoing electrons. A critical open question is whether the approximation of treating only two active electrons will be sufficient to describe the effects of initial state correlation on the removal of two electrons from the same orbital as well as from different orbitals of the neutral molecule to produce different states of the dication.

## ACKNOWLEDGMENTS

Work at LBNL was performed under the auspices of the US DOE under Contract DE-AC02-05CH11231 and was supported by the U.S. DOE Office of Basic Energy Sciences, Division of Chemical Sciences. Calculations presented here made use of the resources of the National Energy Research Scientific Computing Center, a DOE Office of Science User Facility. FLY was supported by the National Science Foundation, Grant No. PHY-1509971 and the U.S. DOE Office of Science, Office of Workforce Development for Teachers and Scientists (WTDS) under the Visiting Faculty Program.

[1] L. Avaldi and A. Huetz, Journal of Physics B: Atomic, Molecular and Optical Physics **38**, S861 (2005).

[2] O. Schwarzkopf, B. Krässig, J. Elmiger, and V. Schmidt, Physical Review Letters **70**, 3008 (1993).

[3] R. Dörner, T. Vogt, V. Mergel, H. Khemliche, S. Kravis, C. L. Cocke, J. Ullrich, M. Unverzagt, L. Spielberger, M. Damrau, O. Jagutzki, I. Ali, B. Weaver, K. Ullmann, C. C. Hsu, M. Jung, E. P. Kanter, B. Sonntag, M. H. Prior, E. Rotenberg, J. Denlinger, T. Warwick, S. T. Manson, and H. Schmidt-Böcking, Physical Review Letters **76**, 2654 (1996).

[4] R. Dörner, J. M. Feagin, C. L. Cocke, H. Bräuning, O. Jagutzki, M. Jung, E. P. Kanter, H. Khemliche, S. Kravis, V. Mergel, M. H. Prior, H. Schmidt-Böcking, L. Spielberger, J. Ullrich, M. Unversagt, and T. Vogt, Physical Review Letters **77**, 1024 (1996).

[5] R. Dörner, H. Bräuning, J. M. Feagin, V. Mergel, O. Jagutzki, L. Spielberger, T. Vogt, H. Khemliche, M. H. Prior, J. Ullrich, C. L. Cocke, and H. Schmidt-Böcking, Physical Review A **57**, 1074 (1998).

[6] L. Malegat, P. Selles, P. Lablanquie, J. Mazeau, and A. Huetz, Journal of Physics B: Atomic, Molecular and Optical Physics **30**, 263 (1997).

[7] H. Bräuning, R. Dörner, C. L. Cocke, M. H. Prior, B. Krässig, A. S. Kheifets, I. Bray, A. Bräuning-Demian, K. Carnes, S. Dreuil, V. Mergel, P. Richard, J. Ullrich, and H. Schmidt-Böcking, Journal of Physics B: Atomic, Molecular and Optical Physics **31**, 5149 (1998).

[8] S. Cvejanovic, J. P. Wightman, T. J. Reddish, F. Maulbetsch, M. A. MacDonald, A. S. Kheifets, and I. Bray, Journal of Physics B: Atomic, Molecular and Optical Physics **33**, 265 (2000).

[9] P. Bolognesi, V. Feyer, A. Kheifets, S. Turchini, T. Prosperi, N. Zema, and L. Avaldi, Journal of Physics B: Atomic, Molecular and Optical Physics **41**, 051003 (2008).
[10] T. J. Reddish, J. P. Wightman, M. A. MacDonald, and S. Cvejanović, Physical Review Letters **79**, 2438 (1997).
[11] R. Dörner, H. Bräuning, O. Jagutzki, V. Mergel, M. Achler, R. Moshammer, J. M. Feagin, T. Osipov, A. Bräuning-Demian, L. Spielberger, J. H. McGuire, M. H. Prior, N. Berrah, J. D. Bozek, C. L. Cocke, and H. Schmidt-Böcking, Physical Review Letters **81**, 5776 (1998).
[12] D. P. Seccombe, S. A. Collins, T. J. Reddish, P. Selles, L. Malegat, A. K. Kazansky, and A. Huetz, Journal of Physics B: Atomic, Molecular and Optical Physics **35**, 3767 (2002).
[13] T. Weber, A. Czasch, O. Jagutzki, A. Müller, V. Mergel, A. Kheifets, J. Feagin, E. Rotenberg, G. Meigs, M. H. Prior, S. Daveau, A. L. Landers, C. L. Cocke, T. Osipov, H. Schmidt-Böcking, and R. Dörner, Physical Review Letters **92**, 163001 (2004).
[14] T. Weber, A. O. Czasch, O. Jagutzki, A. K. Muller, V. Mergel, A. Kheifets, E. Rotenberg, G. Meigs, M. H. Prior, S. Daveau, A. Landers, C. L. Cocke, T. Osipov, R. Diez Muino, H. Schmidt-Bocking, and R. Dorner, Nature **431**, 437 (2004).
[15] T. Weber, L. Foucar, T. Jahnke, M. Schoeffler, L. Schmidt, M. Prior, and R. Doerner, Journal of Physics B: Atomic, Molecular and Optical Physics **50**, 164002 (2017).
[16] T. Weber, A. O. Czasch, O. Jagutzki, A. K. Muller, V. Mergel, A. Kheifets, E. Rotenberg, G. Meigs, M. H. Prior, S. Daveau, A. Landers, C. L. Cocke, T. Osipov, R. Diez Muino, H. Schmidt-Bocking, and R. Dorner, Nature **443**, 1014 (2006).
[17] M. Gisselbrecht, M. Lavollée, A. Huetz, P. Bolognesi, L. Avaldi, D. P. Seccombe, and T. J. Reddish, Physical Review Letters **96**, 153002 (2006).
[18] D. Akoury, K. Kreidi, T. Jahnke, T. Weber, A. Staudte, M. Schöffler, N. Neumann, J. Titze, L. P. H. Schmidt, A. Czasch, O. Jagutzki, R. A. C. Fraga, R. E. Grisenti, R. D. Muiño, N. A. Cherepkov, S. K. Semenov, P. Ranitovic, C. L. Cocke, T. Osipov, H. Adaniya, J. C. Thompson, M. H. Prior, A. Belkacem, A. L. Landers, H. Schmidt-Böcking, and R. Dörner, Science **318**, 949 (2007).
[19] P. Bolognesi, B. Joulakian, A. A. Bulychev, O. Chuluunbaatar, and L. Avaldi, Physical Review A **89**, 053405 (2014).
[20] F. Maulbetsch and J. S. Briggs, Journal of Physics B: Atomic, Molecular and Optical Physics **28**, 551 (1995).
[21] F. Maulbetsch and J. S. Briggs, Journal of Physics B: Atomic, Molecular and Optical Physics **27**, 4095 (1994).
[22] A. S. Kheifets and I. Bray, Physical Review A **54**, R995 (1996).
[23] S. P. Lucey, J. Rasch, C. T. Whelan, and H. R. J. Walters, Journal of Physics B: Atomic, Molecular and Optical Physics **31**, 1237 (1998).
[24] A. S. Kheifets and I. Bray, Journal of Physics B: Atomic, Molecular and Optical Physics **31**, L447 (1998).
[25] A. S. Kheifets and I. Bray, Physical Review A **57**, 2590 (1998).
[26] J. S. Briggs and V. Schmidt, Journal of Physics B: Atomic, Molecular and Optical Physics **33**, R1 (2000).
[27] L. Malegat, P. Selles, and A. Huetz, Journal of Physics B: Atomic, Molecular and Optical Physics **30**, 251 (1997).
[28] P. Selles, L. Malegat, and A. K. Kazansky, Physical Review A **65**, 032711 (2002).
[29] C. W. McCurdy, D. A. Horner, T. N. Rescigno, and F. Martín, Physical Review A **69**, 032707 (2004).
[30] D. A. Horner, J. Colgan, F. Martín, C. W. McCurdy, M. S. Pindzola, and T. N. Rescigno, Physical Review A **70**, 064701 (2004).
[31] J. Colgan, M. S. Pindzola, and F. Robicheaux, Physical Review A **72**, 022727 (2005).
[32] M. S. Pindzola, F. Robicheaux, S. D. Loch, J. C. Berengut, T. Topcu, J. Colgan, M. Foster, D. C. Griffin, C. P. Ballance, D. R. Schultz, T. Minami, N. R. Badnell, M. C. Witthoeft, D. R. Plante, D. M. Mitnik, J. A. Ludlow, and U. Kleiman, Journal of Physics B: Atomic, Molecular and Optical Physics **40**, R39 (2007).
[33] D. C. Griffin, M. S. Pindzola, C. P. Ballance, and J. Colgan, Physical Review A **79**, 023413 (2009).
[34] A. S. Kheifets, D. V. Fursa, C. W. Hines, I. Bray, J. Colgan, and M. S. Pindzola, Physical Review A **81**, 023418 (2010).
[35] M. S. Pindzola, C. P. Ballance, S. A. Abdel-Naby, F. Robicheaux, G. S. J. Armstrong, and J. Colgan, Journal of Physics B: Atomic, Molecular and Optical Physics **46**, 035201 (2013).
[36] Y. Li, M. S. Pindzola, and J. Colgan, Journal of Physics B: Atomic, Molecular and Optical Physics **49**, 195205 (2016).
[37] F. L. Yip, D. A. Horner, C. W. McCurdy, and T. N. Rescigno, Physical Review A **75**, 042715 (2007).
[38] F. L. Yip, T. N. Rescigno, and C. W. McCurdy, Physical Review A **94**, 063414 (2016).
[39] F. L. Yip, T. N. Rescigno, C. W. McCurdy, and F. Martín, Physical Review Letters **110**, 173001 (2013).
[40] F. L. Yip, C. W. McCurdy, and T. N. Rescigno, Physical Review A **81**, 063419 (2010).
[41] F. L. Yip, F. Martín, C. W. McCurdy, and T. N. Rescigno, Physical Review A **84**, 053417 (2011).
[42] J. M. Feagin, Journal of Physics B: Atomic, Molecular and Optical Physics **31**, L729 (1998).

[43] M. Walter and J. S. Briggs, Physical Review Letters **85**, 1630 (2000).
[44] A. S. Kheifets and I. Bray, Physical Review A **72**, 022703 (2005).
[45] A. S. Kheifets, Physical Review A **71**, 022704 (2005).
[46] W. Vanroose, F. Martín, T. N. Rescigno, and C. W. McCurdy, Science **310**, 1787 (2005).
[47] W. Vanroose, D. A. Horner, F. Martín, T. N. Rescigno, and C. W. McCurdy, Physical Review A **74**, 052702 (2006).
[48] D. A. Horner, W. Vanroose, T. N. Rescigno, F. Martín, and C. W. McCurdy, Physical Review Letters **98**, 073001 (2007).
[49] L. Tao, C. W. McCurdy, and T. N. Rescigno, Physical Review A **82**, 023423 (2010).
[50] D. A. Horner, S. Miyabe, T. N. Rescigno, C. W. McCurdy, F. Morales, and F. Martín, Physical Review Letters **101**, 183002 (2008).
[51] J. Colgan, M. S. Pindzola, and F. Robicheaux, Physical Review Letters **98**, 153001 (2007).
[52] T. J. Reddish, J. Colgan, P. Bolognesi, L. Avaldi, M. Gisselbrecht, M. Lavollée, M. S. Pindzola, and A. Huetz, Physical Review Letters **100**, 193001 (2008).
[53] J. Colgan, M. S. Pindzola, and F. Robicheaux, Journal of Physics B: Atomic, Molecular and Optical Physics **41**, 121002 (2008).
[54] X. Guan, K. Bartschat, and B. I. Schneider, Physical Review A **83**, 043403 (2011).
[55] I. A. Ivanov and A. S. Kheifets, Physical Review A **85**, 013406 (2012).
[56] W.-C. Jiang, L.-Y. Peng, J.-W. Geng, and Q. Gong, Physical Review A **88**, 063408 (2013).
[57] J. E. Sansonetti and W. C. Martin, Journal of Physical and Chemical Reference Data **34**, 1559 (2005).
[58] D. Reedy, J. B. Williams, T. Weber, B. Gair, A. Gatton, M. Weller, A. Menssen, T. Bauer, K. Henrichs, P. Burzynski, B. Berry, Z. L. Streeter, J. Sartor, I. Ben-Itzhak, T. Jahnke, R. Dörner, T. Weber, and A. L. Landers, Unpublished.
[59] B. Gervais, E. Giglio, L. Adoui, A. Cassimi, D. Duflot, and M. E. Galassi, The Journal of Chemical Physics **131**, 024302 (2009).
[60] H.-J. Werner, P. J. Knowles, G. Knizia, F. R. Manby, and M. Schütz, WIREs Comput Mol Sci **2**, 242 (2012).
[61] H.-J. Werner, P. J. Knowles, G. Knizia, F. R. Manby, M. Schütz, *et al.*, "Molpro, version 2015.1, a package of ab initio programs," (2015), see http://www.molpro.net.
[62] T. H. D. Jr., The Journal of Chemical Physics **90**, 1007 (1989).
[63] H. Lischka, T. Müller, P. G. Szalay, I. Shavitt, R. M.Pitzer, and R. Shepard, WIREs Comput Mol Sci **1**, 191 (2011).
[64] H. Lischka, R. Shepard, R. M. Pitzer, I. Shavitt, M. Dallos, T. Muller, P. G. Szalay, M. Seth, G. S. Kedziora, S. Yabushita, and Z. Zhang, Phys. Chem. Chem. Phys. **3**, 664 (2001).
[65] H. Lischka, R. Shepard, I. Shavitt, R. M. Pitzer, M. Dallos, T. Müller, P. G. Szalay, F. B. Brown, R. Ahlrichs, H. J. B m, A. Chang, D. C. Comeau, R. Gdanitz, H. Dachsel, C. Ehrhardt, M. Ernzerhof, P. Höchtl, S. Irle, G. Kedziora, T. Kovar, V. Parasuk, M. J. M. Pepper, P. Scharf, H. Schiffer, M. Schindler, M. Schüler, M. Seth, E. A. Stahlberg, J.-G. Zhao, S. Yabushita, Z. Zhang, M. Barbatti, S. Matsika, M. Schuurmann, D. R. Yarkony, S. R. Brozell, E. V. Beck, J.-P. Blaudeau, M. Ruckenbauer, B. Sellner, F. Plasser, and J. J. Szymczak, "Columbus, an *ab initio* electronic structure program, release 7.0," (2015).
[66] E. Wigner, Phys. Rev. **40**, 749 (1932).
[67] R. de Vivie, C. M. Marian, and S. D. Peyerimhoff, Chemical Physics **112**, 349 (1987).
[68] R. N. Zare, Mol. Photochem. **4**, 1 (1972).
[69] H. Adaniya, B. Rudek, T. Osipov, D. J. Haxton, T. Weber, T. N. Rescigno, C. W. McCurdy, and A. Belkacem, Phys. Rev. Lett. **103**, 233201 (2009).
[70] J. Colgan and M. S. Pindzola, Physical Review A **65**, 022709 (2002).
[71] D. C. Griffin, M. S. Pindzola, C. P. Ballance, and J. Colgan, Physical Review A **79**, 023413 (2009).
[72] S. A. Abdel-Naby, M. S. Pindzola, and J. Colgan, Journal of Physics B: Atomic, Molecular and Optical Physics **48**, 025204 (2015).
[73] E. Sokell, P. Bolognesi, A. Kheifets, I. Bray, S. Safgren, and L. Avaldi, Physical Review A **89**, 013413 (2014).

# Dissociation dynamics of the water dication following one-photon double ionization II: Experiment

D. Reedy[1,2], J.B. Williams[1],* B. Gaire[3], A. Gatton[3], M. Weller[3], A. Menssen[7], T. Bauer[4], K. Henrichs[4], Ph. Burzynski[4], B. Berry[5], Z.L. Streeter[3,6], J. Sartor[2], I. Ben-Itzhak[5], T. Jahnke[4], R. Dörner[4], Th. Weber[3], and A.L. Landers[2]

[1] *Department of Physics, University of Nevada, Reno, Reno, Nevada 89557, USA*
[2] *Department of Physics, Auburn University, Auburn, Alabama 36849, USA*
[3] *Lawrence Berkeley National Laboratory, Chemical Sciences and Ultrafast X-ray Science Laboratory, Berkely, California 94720, USA*
[4] *Institut für Kernphysik, J.W. Goethe Universität, Max-von-Laue-Str. 1, 60438 Frankfurt, Germany*
[5] *J.R. Macdonald Laboratory, Department of Physics, Kansas State University, Manhattan, Kansas 66506, USA*
[6] *Department of Applied Science, University of California, Davis, California 95616, USA and*
[7] *Clarendon Laboratory, Department of Physics, University of Oxford, Oxford OX1 3PU, United Kingdom*

We demonstrate the use of Cold Target Recoil Ion Momentum Spectroscopy (COLTRIMS) to perform state-selective measurements of the dissociative channels following the single-photon double ionization (PDI) of $H_2O$. The two dominant dissociation channels observed lead to two-body ($OH^+ + H^+ + 2e^-$) and three-body ($2H^+ + O + 2e^-$) ionic fragmentation channels. In the two-body case we observe the presence of an autoionization process with a double differential cross section that is similar to the PDI of helium well above threshold. In the three-body case, momentum and energy correlation maps in conjunction with new classical trajectory calculations in the companion theory paper by Streeter *et al.* [1] lead to the determination of the eight populated dication states and their associated fragmentation geometry. For the latter case, state-specific relative cross sections, median kinetic energy releases, and median angles between asymptotic proton momenta are presented. This benchmark level experiment demonstrates that, in principle, state-selective fixed-frame triple-differential cross sections can be measured for some dication states of the water molecule.

## I. INTRODUCTION

Understanding the correlated emission of electron pairs from one-, two-, or multi-center Coulomb potentials after single-photon double ionization (PDI) is a fundamental challenge both theoretically and experimentally [2–6]. There is an extensive literature on PDI for atomic targets, particularly helium, where the final state consists of three measurable continuum particles and the single initial state for the electron pair along with spherical symmetry allow for clear theoretical interpretation of experimental results [7–11]. Interpreting PDI spectra from molecules is substantially more challenging. While in atoms there is a distinct energy value above which the PDI can be initiated, this threshold is less clear for molecules. This is due to additional degrees of freedom in the binding potential which result in an entire threshold region [12]. At the upper limit of this threshold region is the direct, or vertical, ionization threshold wherein a single photon promotes a correlated electron pair to the continuum. Within the bounds of this threshold region indirect or two-step processes are possible, wherein the photon ejects one electron and leaves the cation in an excited state which, after rearrangement, can eject a second electron. In atoms, only discrete electronic states have to be taken into account, which in many cases can be clearly distinguished in the PDI measurement. However, the internuclear separation of the multi-center potential of a molecule results in a substantially more complex ground-state electronic configuration. Energy correlation maps, which depict the electron energy or electron energy sum as a function of the kinetic energy release (KER, sum of all neutral and ionic fragment kinetic energies), are one experimental tool that can probe the potential energy surfaces (PESs) and identify the electronic states involved in the dissociation; however, they are not always unambiguous, as some of the data will show below.

Larger molecules such as triatomics can break up

* jbwilliams@unr.edu

through multiple dissociation channels, further increasing the complexity of the PDI investigation. The relative populations of the final state molecular fragments are governed by the often intricate dissociation channels on the PESs of the molecule. The binding energy of these surfaces vary as a function of bending and (symmetric and asymmetric) stretching coordinates. Conical intersections and non-adiabatic transitions between the surfaces can allow energy distribution between the different modes and initiate nuclear rearrangements during the dissociation process of the molecular dication (e.g. vibration, rotation, isomerization [13], roaming [14]). Bond breakage can occur simultaneously or in a step-wise manner [15]. The number and kind of independent ways by which the dynamic nuclear system can move inherently increases the complexity of the correlated electron-pair emission process in their energy sharing and relative angles with respect to the body frame. It is therefore a challenge for theory and experiment to identify and isolate all of these different contributions.

In PDI investigations of molecular targets, both experiment and theory heavily rely on simplifying assumptions such as the Born-Oppenheimer approximation [16] and the axial-recoil approximation[17]. The axial-recoil approximation, which assumes constituent ion fragments proceed outward along bond axes following dissociation, paves the way to measure electron emission patterns in the body-fixed frame, if electrons can be detected in coincidence with the nuclear fragments [18–20]. Ideally, kinematically complete experiments can be performed, where the 3D momenta of all particles are directly measured or derived for each PDI event. This enables the deduction of the kinetic energies and relative emission angles of all particles in the final state, generating highly (or even fully) differential cross sections.

Investigation of kinematically complete PDI of the simplest molecule, $H_2$, has been performed for more than a decade. Both theory ([20–26]) and experiment ([4, 19, 27]) have sought to probe the dynamics of electron correlation in the initial and final state.

Here we guide the reader through the detailed experimental exploration of the PDI of single water molecules, i.e. a simple planar triatomic target. The PDI experiment was performed with 57 eV photons, 18 eV above the vertical double ionization threshold of 39 eV [28] for $H_2O$. In principle, the PDI of $H_2O$ can lead to dissociation into the following two- and three-body breakup channels:

$$\gamma + H_2O \rightarrow H_2^{+*} + O^{+*} + 2e^- \quad (1)$$
$$\rightarrow H^+ + OH^{+*} + 2e^- \quad (2)$$
$$\rightarrow H^+ + H^* + O^{+*} + 2e^- \quad (3)$$
$$\rightarrow 2H^+ + O^* + 2e^- \quad (4)$$
$$\rightarrow O^{2+} + 2H^* + 2e^- \quad (5)$$

where the $^*$ superscript indicates the possibility of either a ground or excited state. Of these five channels only two have been observed in our PDI experiment, namely one two-body (2) and one three-body breakup (4). Channel (1) has been observed in proton-water collisions [29, 30]. Experiments of PDI below the vertical ionization threshold of 39 eV have observed channel (3) [31], while electron ionization experiments have recorded fragments from all five channels [32]. In addition to PDI, single photoionization can produce an excited molecular fragment which later autoionizes, producing identical ion signatures as PDI processes [28]. We observed one such autoionization channel, namely:

$$\gamma + H_2O \rightarrow H^+ + OH^* + e^- \quad (6)$$

where the $OH^*$ molecule autoionizes to the $OH^+$ ion soon after.

The organization of the paper is as follows. In section II we briefly discuss the setup used to produce the experimental data. In Section III we focus on the analysis of the observed two-body breakup. We will present and discuss energy correlation maps, electron-energy sharing results as single differential cross sections (SDCS), and relative electron-electron emission angles. The same spectroscopic analysis tools will be applied to the observed three-body breakup in the first part of Section IV. In the second part of Section IV two new analysis diagrams are introduced: (a) the nuclear conformation map, i.e. the three-body yield as a function of KER and angle between asymptotic proton momenta (hereafter referred to as $\beta$), and (b) the triatomic breakup momentum plane. These new diagrams are introduced to identify and isolate, with the help of theory, all eight dication states relevant in this PDI experiment. We mention the unambiguous failure of the axial-recoil approximation, discovered and discussed in detail in the theoretical companion paper by Streeter [1]. In Section V we will conclude the investigation with a summary and outlook towards possible kinematically complete experiments on water molecules in the future.

## II. EXPERIMENT

The current experiment was conducted using beamline 10.0.1 of the Advanced Light Source (ALS) at Lawrence Berkeley National Laboratory to produce 57 eV photons for a COLTRIMS experimental chamber. A rigorous description of the COLTRIMS technique can be found in the literature [33–35]. In short, a supersonic molecular beam is crossed with a photon beam inside a spectrometer comprised of two micro-channel plate delay line anode (MCP DLA) detectors with static electric and magnetic fields used to steer the charged photo fragments onto the detectors. The expansion of the molecular beam through the nozzle and into vacuum leaves the molecules internally cold and overwhelmingly in their ground vibrational and rotational states. The ion detector had a two layer anode, while the electron detector had a three layer anode [36]. The molecular beam was produced by heating a liquid water reservoir and the input gas line to increase the vapor pressure of the water. A near $4\pi$ solid angle collection efficiency is realized for all charged particles, with detector dead-time issues preventing coincidence measurements of electrons striking the detector simultaneously in the same place. The detectors are position- and time-sensitive, allowing the full 3D momentum vectors for each charged particle to be calculated.

In the current case, up to two electrons are measured in coincidence with either a proton-$OH^+$ pair or two protons. Analysis was performed only on coincidence events including all four charged particles. For the latter measurement, a neutral (perhaps excited) oxygen atom is not measured. The large momentum difference between atomic and electronic fragments allows us to use conservation of linear momentum among atomic fragments to calculate the momentum of the neutral oxygen fragment. Broadening of momenta due to the lab-frame velocity of the gas jet was negligible. We include this calculated oxygen momentum in the analysis of the three-body breakup.

## III. TWO-BODY BREAKUP

This section focuses on the dissociation dynamics of the two-body channel resulting in a proton and an $OH^{+*}$ ion, including the auto-ionizing channel. The channel is identified by its signature in a PIPICO spectrum (Fig. 1) as the narrow circled feature associated with $H^+$ and $OH^+$ ions measured in coincidence. The horizontal and vertical stripes crossing the spectrum are random coincidences corresponding to the 328.266ns period at the ALS, while the circled round feature in the lower left corner identifies the three-body channel. Two "replicas" of the $H^+ + OH^+$ feature can be observed as well. These are identical in origin to the horizontal and vertical stripes: they are two-particle ion coincidences corresponding to the ALS bunchmarker and erroneously paired with electron background signals by the acquisition system.

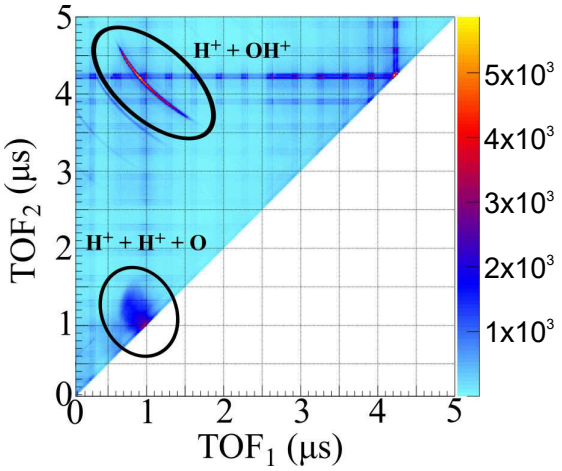


FIG. 1. Photoion-Photoion coincidence (PIPICO) spectra with the two-body and 3-body channels circled. Coincidence yields are plotted as a function of the individual ion time-of-flights (TOF).

Once the channel is isolated in the PIPICO spectrum we proceed by considering the energy correlation map, Fig. 2(a), which shows the $H^+ + OH^+$ yield as a function of KER and electron energy sum ($E_{e\,sum}$). A complementary correlation plot of the same yield as a function of KER and individual electron energy is presented in Fig. 2(b). Both electrons from the coincidence measurement are included in the second plot.

Gervais *et al* [37] performed an exhaustive study of the eight lowest $HDO^{2+}$ dication dissociation channels, four of which preferentially dissociate to the two-body channel. They found that these four dication states ($X^3A''$, $1^1A'$, $1^1A''$, and $2^1A'$ in $C_S$ symmetry) dissociated with a KER near 7 eV. In this work we found a mean KER of 6.7 eV for the bright vertical feature in Fig. 2(a) and (b), which matches reasonably well the results of Ref. [37]. The width of

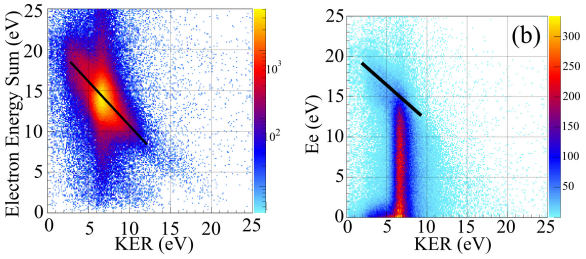


FIG. 2. (a) Energy correlation plot for the two-body breakup channel: $H^+$ + $OH^+$ yield as a function of electron energy sum ($Ee_1$ + $Ee_2$) and KER (log-yield scaling). (b) Energy correlation plot for the two-body breakup channel: yield as a function of single electron energy and KER(lin-yield scaling). Both electrons are included in the plot. Black lines are added as a visual guide to the diagonal features.

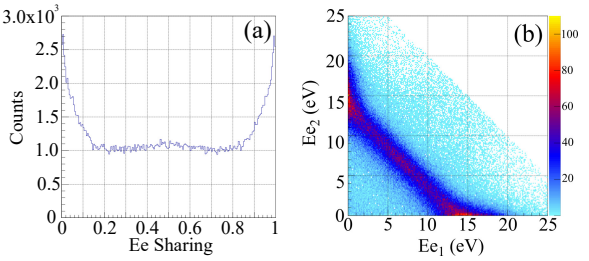


FIG. 3. Electron yield of the $H^+$ + $OH^+$ channel as a function of (a) electron energy ($E_e$) sharing ratio, $Ee_1/Ee_{sum}$. (b) Individual electron energies.

the vertical feature in electron energy is due to the separation of the potential surfaces leading to the four states: the potential surface "shapes" are similar, leading to comparable KER values, but their relative heights above the $H_2O$ ground state are different, leading to a broad range of electron energies. The extent of the vertical feature is exacerbated by electron energy resolution.

Based solely on the analysis of Ref. [37], it is unclear what the diagonal feature observed in the energy correlation maps (Fig. 2) might represent. Instead, a study of two-step PDI of water by Sann *et al* [28] using 43 eV photons provides evidence that this diagonal feature is a signature of an autoionization process. Single photoionization of the water molecule produces a proton and an excited OH fragment, which subsequently autoionizes to the $X^3\Sigma^-$ ground state of $OH^+$ once the proton is far enough away that the autoionization channel becomes energetically open. Measurement of the two ionic fragments, as well as the fast photoelectron and slow autoionization electron, is easily misinterpreted as a direct-PDI event at first inspection.

Comparing Fig. 1(b) from Ref. [28] to Fig. 2(b) offers verification that we have observed the same auto-ionization process. The excess photon energy of the current experiment (57 eV instead of 43 eV), as well as the preponderance of direct PDI, manifest in the bright vertical stripe connecting the "fast electron" (diagonal feature) and "slow electron" (horizontal feature near 0). The electron energy sharing ratio is presented as a single differential cross section in Fig. 3(a). The electron energy correlation is presented in Fig. 3(b). Features along the axes of 3(b) correspond to the fast/slow electron energy pairs, while the diagonal feature corresponds to the symmetric electron energy sharing of a PDI process. In PDI of larger molecules, for example in difluoroethylene $C_2H_2F_2$, the asymmetric energy sharing features appear below the diagonal, in contrast to the feature appearing above the diagonal in Fig 3(b) [38]. This disparity is again likely resolved by consulting with Ref. [28]. The autoionizing channel leads to the $OH^+$ ground state $X^3\Sigma^-$, while PDI channels can lead to a number of excited cation states. Higher potential surfaces leave less energy to distribute among the photoelectrons in this case, which accordingly moves the diagonal feature of 3(b) toward the origin.

The two features in Fig. 3(b) can be separated to a large extent by requiring KER <5 eV and KER >7 eV, which elucidates the asymmetric and symmetric sharing features, respectively, as shown in Fig. 4. Separation of the asymmetric electron energy sharing via a gate on KER <5 eV is consistent with techniques used in Ref. [28] which separated the autoionization channel with similar "low KER" gating.

We note that in Ref. [28], significantly less direct PDI was observed than in the current data. This is due to the lower photon energy of 43 eV being closer to the direct PDI threshold. Among the PDI events observed, there is a preference for equal electron energy sharing, which can be best observed in the small bright spot in the center of the diagonal feature in Fig. 3(b). This tendency toward equal energy sharing in the PDI case is discussed in detail in Section IV for the three-body case.

Eland *et al.* [39] and others have observed indirect dissociative double ionization processes below the vertical double ionization threshold, as low as 34 eV photon energy. The signature of such an au-

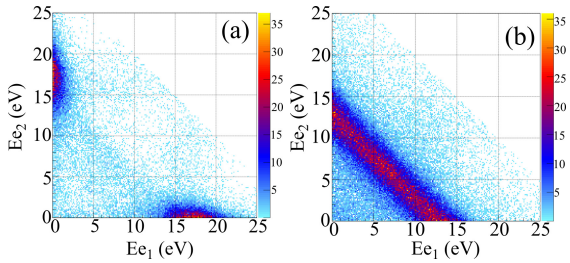


FIG. 4. Electron yield of the $H^+ + OH^+$ channel as a function of individual electron energies with (a) KER $< 5$ eV, isolating the asymmetric energy sharing contribution. (b) KER $> 7$ eV, isolating the symmetric energy sharing contribution.

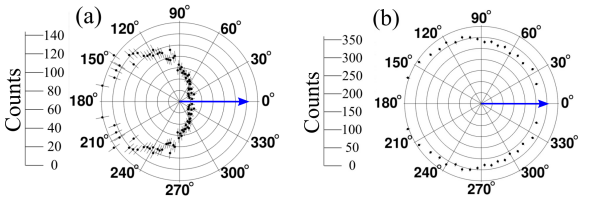


FIG. 5. Angle between the two emitted electrons. One electron is fixed at 0° (blue arrow). (a) A symmetric energy sharing electron pair, where each electron has $50\% \pm 5\% E_{sum}$, summed over all possible states. (b) An asymmetric energy sharing pair, where the fixed electron has $E_e > 90\% E_{sum}$, summed over all possible states. The distributions have been mirrored about a line between 0-180°.

toionization event is one electron with nearly all the excess photon energy paired with an electron of near 0 energy. In the current experiment, a 57 eV photon would impart ∼23 eV to the photoelectron in such a process. The current data do not display any significant signature corresponding to such a dissociation pathway.

Further separation of the PDI data in the two-body channel is extremely challenging due to lack of separable features. Gervais *et al.* [37], and more recently Ref. [1], inform us that the PDI data is likely a combination of primarily the $^3A_2$, $1\ ^1A_1$, $^1A_2$, and $2\ ^1A_1$ dication states. However, these states cannot be separated in the current data set.

Despite the difficulty in identifying individual dication states in the two-body channel, we are able to report two sets of doubly-differential cross sections (DDCS). The first is the relative electron-electron emission angle for both symmetric and highly asymmetric electron energy sharings (SDCS values of near 0.5±0.1 or near 0±0.1), shown in Fig. 5. The second is the electron emission angle relative to the polarization axis for asymmetric energy sharing pairs, shown in Fig. 6. For the PDI process, i.e. the symmetric energy sharing case, the cross sections are integrated over all possible dication states.

Figure 5(a) and (b) show the relative electron-electron emission angular distributions for symmetric and asymmetric energy sharings, respectively. The distribution for symmetric energy sharing Fig. 5(a) resembles the predictions of atomic "knock-off" (or "knock-out") models for angular distributions following double photoionization well above threshold [40]. In this case, one expects symmetric energy sharing and a billiard-ball 90° angular peak, which skews toward 180$^o$ due to Coulomb repulsion.

Fig. 5(a) represents the PDI case, where the photon promotes two correlated electrons to the continuum and a dication state is populated directly. The completeness of this particular measurement is, however, limited by electron detector dead time, particularly where equal energy electrons with nearly identical momentum vectors can hit the detector at the same place and time, causing the loss of the multi-hit event. We present the measurement here with the caveat that although general trends in this distribution are likely correct, the measurement should be confirmed in a future experiment with reduced phase-space lapse leading to multi-hit event losses.

The distribution of the angle between the photoelectrons in the case of highly asymmetric energy sharing, i.e. the auto-ionization case, is shown in Fig. 5(b). This distribution meets expectations for an auto-ionization process, where the slow electron has no "knowledge" of the fast electron's momenta and is emitted isotropically in a second step.

Figure 6(a) and (b) show the lab frame photoelectron angular distributions with respect to the photon polarization axis. Figure 6(a) is the distribution of the fast electron of an asymmetric energy sharing pair, carrying $> 90\%$ of the total electron energy. Figure 6(b) is the distribution of a slow electron in an asymmetric pair, carrying $< 10\%$ of the total electron energy. Figure 6(a) and (b) resemble the distributions presented by Knapp *et al* [41] and Colgan *et al* [21] following double photoionization of helium well above threshold. Both studies found the fast electron had a pronounced dip around 90$^o$, similar to a dipole transition to the continuum. The similarity of their finding to those of Fig. 6(a) suggest that the fast photoelectron measured here is emitted from an orbital of mainly atomic S character. In

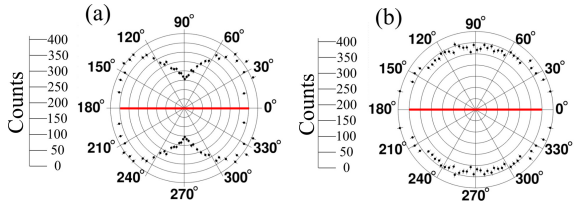


FIG. 6. Laboratory frame angular distributions of asymmetric energy sharing electron pairs for the two-body breakup. The polarization axis of the incident photon is indicated by a red line. (a) Fast electron with Ee > $0.9E_{sum}$. (b) Slow electron with Ee < $0.1E_{sum}$. The distributions have been symmetrized over the 0-180° axis.

addition, they found that the slow electron had an essentially isotropic distribution, which was also the finding in Fig. 6(b).

## IV. THREE-BODY BREAKUP

We begin the analysis by repeating the approach employed in the two-body case with energy correlation maps, electron energy sharing, and angular analysis, described in sub-section IV.A. Successful identification of features in the energy correlation map lead us in a new direction, which is described in sub-section IV.B.

### A. Energy correlation maps, electron energy sharing, and electron emission angles

Analysis of the three-body reaction channel begins with identification of the channel in the PIPICO spectrum as the broad, round feature near the origin. The next steps follow the path of the two-body channel analysis, with continuum energy correlation maps. Since the three-body breakup has an angular component among the ionic fragments, an additional spectrum is presented in Fig. 7(b), namely the $H^+ + H^+ + O^*$ yield as a function of total continuum energy (sum of KER and electron energies) and $\beta$.

In contrast with the two-body case, there are separated features in the energy correlation map shown in Fig. 7(a). Three features of distinct total continuum energy are visible. These features correspond to the lowest three energy terms of the neutral oxygen fragment: $^3P$, $^1D$, and $^1S$, the asymptotic limits of the dissociating dication potential energy surfaces leading to $H^+ + H^+ + O$ and discussed in great detail by Gervais *et al* [37] and in Ref. [1]. These features are labeled in Fig. 7(b), and their energies are shown in Table I along with NIST data by Moore [42]. The features labeled I, II, and III correspond to the O($^3P$), O($^1D$), and O($^1S$) asymptotes, respectively.

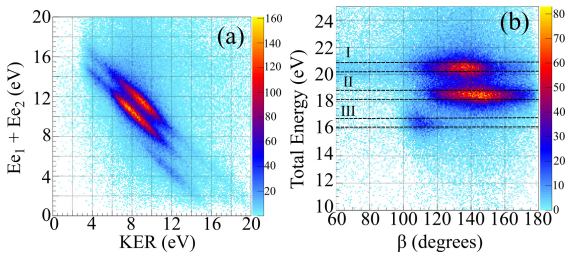


FIG. 7. Energy correlation plots for the three-body breakup, including investigation of the angle between proton momenta. (a) $H^+ + H^+ + O$ yield as a function of electron energy sum ($Ee_{sum}$) and KER. (b) Yield as a function of total energy ($Ee_{sum}$ + KER) and $\beta$ (asymptotic angle between proton momenta). The three labeled features correspond to asymptotic oxygen terms: I - $^3P$ ; II - $^1D$ ; III - $^1S$

TABLE I. Oxygen term energy separation

| Term | NIST (eV) | Expt (eV) | Label |
|---|---|---|---|
| $^3P$ | 0.0 | 0.0 | I |
| $^1D$ | 1.967 | 1.94 ± .51 | II |
| $^1S$ | 4.190 | 4.02 ± .63 | III |

The electron energy sharing SDCS for the three-body breakup in Fig. 8(a) displays a different structure than that of the two-body breakup shown in Fig. 3(a). The distribution peaks at the center, indicating a strong preference for a near-symmetric energy sharing between the photoelectrons. In contrast with the two-body breakup, the data do not reveal a different energy sharing between the photoelectrons. While autoionization to $H^+ + O^+ +$ H is energetically possible, such a breakup was not observed in this data.

We attribute the center-peaked feature of the three-body PDI channel to a reduction of the electron energy phase space due to the relatively low photon energy. The binding energy of the electrons (39 eV) is larger than the excess energy of the photoelectrons (<18 eV). The competing process to direct PDI is the recapture of one electron; near threshold, if the photoelectrons do not share energy nearly

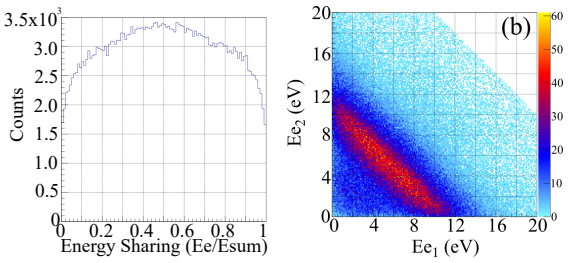


FIG. 8. $H^+ + H^+ + O$ yield as a function of (a) electron energy ($E_e$) sharing ratio, $Ee_1/Ee_{sum}$ (b) individual electron energies.

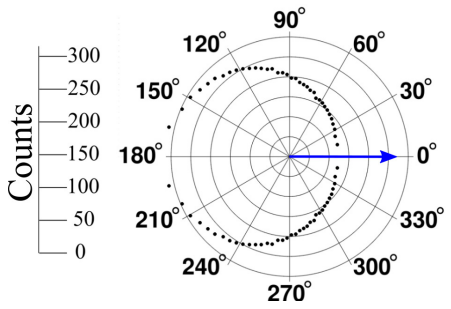


FIG. 9. Angle between the two emitted electrons. One electron is fixed at 0° (blue arrow). Data are summed over all electron energy sharings, all molecular orientations, and all possible dication states.The distribution has been mirrored about a line between 0-180°.

evenly, the slow electron can be recaptured, resulting in a single ionization or multi-step autoionization process rather than direct-PDI. The shape of the SDCS in this case is determined by the Wannier threshold geometry and energetic phase space volume [43–46]. As recapture is more likely for asymmetric electron energy sharings, symmetric sharings are measured more often and the resulting SDCS resembles the center-peaked feature observed in Fig. 8(a). Accordingly, Fig. 8(b) shows no bright features along ordinate and abscissa and only a diagonal feature which corresponds to symmetric energy sharing.

Figure 9 presents the angle between the momenta of the two electrons. This figure is similar to the findings from the two-body channel in the case where the electrons have nearly equal energy, i.e. the direct PDI case. As in the two-body case, this distribution is presented with the caveat that the angular distribution is limited by electron detector dead time and the measurement should be confirmed in future experiments with emphasis on improved resolution for equal energy sharing electron pairs.

### B. Nuclear conformation maps and molecular momentum planes

It is well known that the two hydrogen nuclei bind to the central oxygen atom via covalent bonding in the $H_2O$ electronic ground state. Interactions between the binding electrons and the nuclear charges perturb the geometry of the molecule such that the minima of the bending potential occurs at $\sim 104.5^o$. While the two-body channel offers no information regarding the bond angle at the time of photoionization, detection of the 3D momenta of the outgoing protons in coincidence allows us to infer the momentum of the oxygen atom via linear momentum conservation as described in the introduction. This enables us to determine the asymptotic angle between proton momenta, $\beta$. It is clear in Fig. 7(b) that the asymptotic limits of the dissociating dications leading to $O(^3P)$, $O(^1D)$, and $O(^1S)$ have unique $\beta$ distributions.

As the water dication populates various PESs, we should expect changes in bond angle and OH bond lengths as the dication is rearranged according to the new dication molecular potential. Changes to the bond angle and bond lengths can manifest in both KER and $\beta$. To investigate these possibilities, we visualize the yield of the three-body channel as a function of KER and $\beta$, shown in Fig. 10. Hereafter, such figures are referred to as nuclear conformation maps. Yield plots contrasting various dissociation angles and energies have been used in the literature to, for example, distinguish between concerted and step-wise bond cleavage in molecular systems [15].

Knowledge of the water dication potential surfaces and their asymptotes from Ref. [1] leads us to conclude that the features in Fig. 10 must correspond to the various dication states populated by the PDI. As each dication state dissociates to a particular total continuum energy asymptote, easily identified by the neutral oxygen term, we can produce nuclear conformation maps using the total continuum energy gates shown in Fig. 7(b). The conformation maps produced with these total continuum energy gates will then be limited to the dication states that dissociate to the corresponding oxygen asymptote. The results of these total continuum energy gates on the nuclear conformation map are shown in Fig. 11.

Before further discussion of the features in Fig.

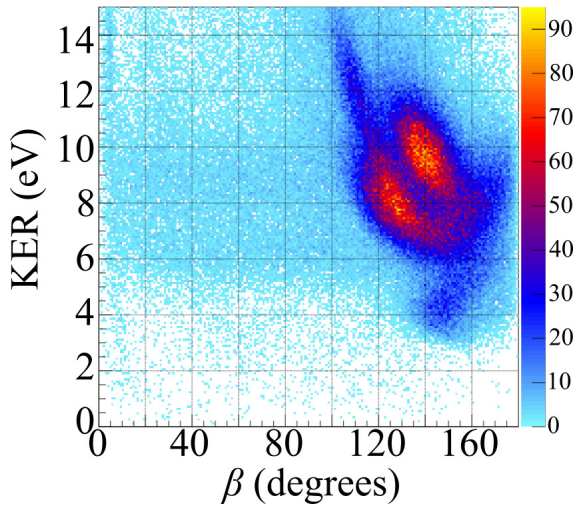


FIG. 10. $H^+ + H^+ + O$ yield as a function of KER and $\beta$, dubbed nuclear conformation map.

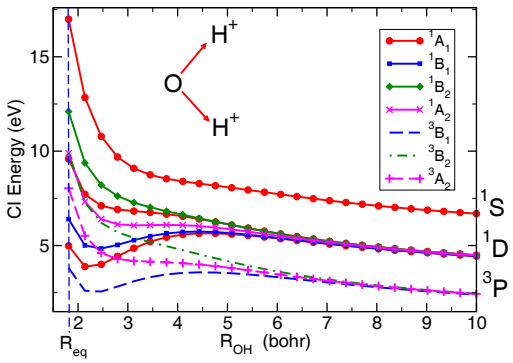


FIG. 12. A slice of the nine energetically accessible dication potential curves along a bond angle of 104.5° and under symmetric stretch ($R_1 = R_2$). The nearness of the dication curves at $R_{eq}$ suggest the origin of the overlap of the states in the nuclear conformation map.

11, it is highly informative to pause and take further guidance from the theory provided in Ref. [1], as the computed potential surfaces suggest that each oxygen asymptote is associated with specific dication states: The triplet dication states $^3B_1$, $^3A_2$, and $^3B_2$ lead to the O($^3P$) asymptote; The singlet dication states $1\,^1A_1$, $2\,^1A_1$, $^1A_2$, $^1B_1$, and $^1B_2$ lead to the O($^1D$) asymptote; one singlet dication state, $3\,^1A_1$, leads to the O($^1S$) asymptote. The asymptotic behavior of these dication states is shown in Fig. 12. Branching ratios presented in Ref. [1] and Ref. [37] suggest that the $1^1A_1$ dication dissociates nearly exclusively to the two-body channel $H^+ + OH^+$. Consequently, for a three-body dissociation, we expect three dication states to lead to the O($^3P$) asymptote, four to the O($^1D$), and one to the O($^1S$).

The nuclear conformation maps in Fig. 11, gated on the total continuum energy corresponding to each final oxygen term, match results in figure 9 of Ref. [1], wherein classical trajectory simulations were used to produce nuclear conformation maps for each of the eight anticipated dication states. These simulations were grouped by the dication states that have identical asymptotic continuum energies, i.e. by the oxygen term. In the simulations, each dication state appears to have a characteristic combination of KER and angle $\beta$.

It is now apparent that the combination of asymptotic continuum energy (corresponding to neutral oxygen term), KER, and $\beta$ might be used as a signature to select individual dication states in the data as they dissociate into the three-body channel $H^+ + H^+ + O^*$. The results from Ref. [1] show that there is some significant overlap in these states, particularly those leading to the O($^1D$) asymptote. The nearness of the $^1B_2$, $2^1A_1$, and $^1A_2$ potential surface slices, shown in Fig. 12, help visualize this overlap.

We use the prescribed combination of asymptotic continuum energy, KER, and $\beta$ from Ref. [1] to create state-selection gates for each of the eight dication states of the dissociating water molecule. The gates are polygons surrounding each dication state in the conformation map. The polygon gates are summarized in Table II and visualized in Fig. 13.

For the given data set, we chose gates to both minimize cross-state contamination and maximize total events. The application of these gates excludes

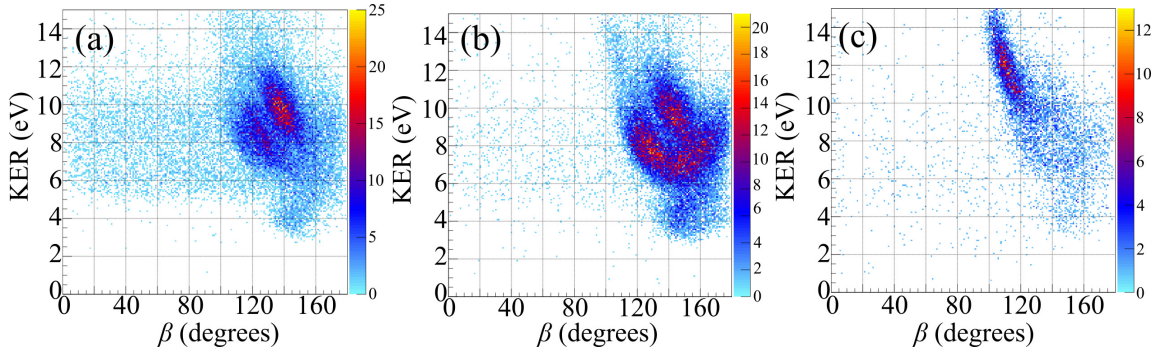


FIG. 11. Nuclear conformation maps, restricted by total continuum energy as shown in Fig. 7(b). (a) Gate I, corresponding to the O($^3P$) asymptote. (b) Gate II, corresponding to the O($^1D$) asymptote. (c) Gate III, corresponding to the O($^1S$) asymptote.

TABLE II. Gates used to state-select three-body breakup on conformation maps.

| $C_{2v}$ | Points ($\beta$,KER) |
|---|---|
| $^3B_1$ | (130,2.5),(130,4.6),(175,4.6),(175,2.5) |
| $^3A_2$ | (105,11),(107,11),(147,6.5),(147,5.2),(105,5.2) |
| $^3B_2$ | (115,12),(165,12),(165,6.4),(150,6.4),(115,10.3) |
| $^1B_1$ | (130,4.6),(175,4.6),(175,2.5),(130,2.5) |
| $^1A_2$ | (105,11),(107,11),(135,7.3),(135,5.5),(105,5.5) |
| $2\ ^1A_1$ | (150,6),(151,7.8),(180,12),(180,6) |
| $^1B_2$ | (115,12),(160,12),(160,9.4),(147,7),(115,10.5) |
| $3\ ^1A_1$ | (90,7),(90,18),(145,18),(145,7) |

some valid data from each state, while admitting some contamination from nearby states in the conformation map space. We apply the gates to classical trajectory calculations from Ref. [1] to characterize the quality of the state-selection in two ways. First, we observe the distribution of the different states present in the gated data, i.e. the state prevalence. Second, we observe the amount of the selected state present in the gate as a fraction of the total number of simulated events for that state, i.e. the state fraction. Table III shows the state prevalence and state fraction for each selected state. The left-most column displays the selected state's $C_{2v}$ symbol. The right-most column is the state fraction. The central columns indicate the prevalence of each state.

With the gates from Table II, the states are selected with better than 91% targeted state prevalence for all states except the $2\ ^1A_1$. We anticipate that with a more robust data set and more refined gates, many of these values can be improved. From visual inspection of Fig. 13 and Fig. 9 in Ref. [1] it is clear that we lose a significant number of events from all dication states leading to the O($^1D$) asymptote due to their overlap in the conformation map around KER = 6 eV and $\beta = 140°$.

Using the state-selection gates listed in Table II, we present relative cross sections for the states as approximate percentages of all three-body data in Table IV. These relative cross sections are produced by applying the state-selection gates for each of the eight dication states and reporting the fractional yield of the coincidence measurement.

In addition to relative cross sections, we report the peak values for the KER and $\beta$ for each dication state, presented in Table V. The standard deviation for each gated distribution is reported along with the peak value.

It bears repeating that for Tables IV and V, the quality of the state-specific separations of the data vary. We have quantified the severity of cross-state contamination in Table III. Despite this caveat, agreement with results from Ref. [1] for KER and $\beta$ values are encouraging.

In addition to KER, $\beta$, and fractional yield measurements, knowledge of the 3D momentum vectors of each molecular fragment gives us access to another powerful analysis tool. The momenta of the particles can be visualized in the molecular momentum plane defined by the proton momenta. Specifically, we define the $z$-axis for the molecular plane as

$$\frac{\hat{p}_1 + \hat{p}_2}{|\hat{p}_1 + \hat{p}_2|} = \hat{z}_{mol} \tag{7}$$

The $y$-axis is defined as the perpendicular co-planar axis, as shown in the center of Fig. 15. This al-

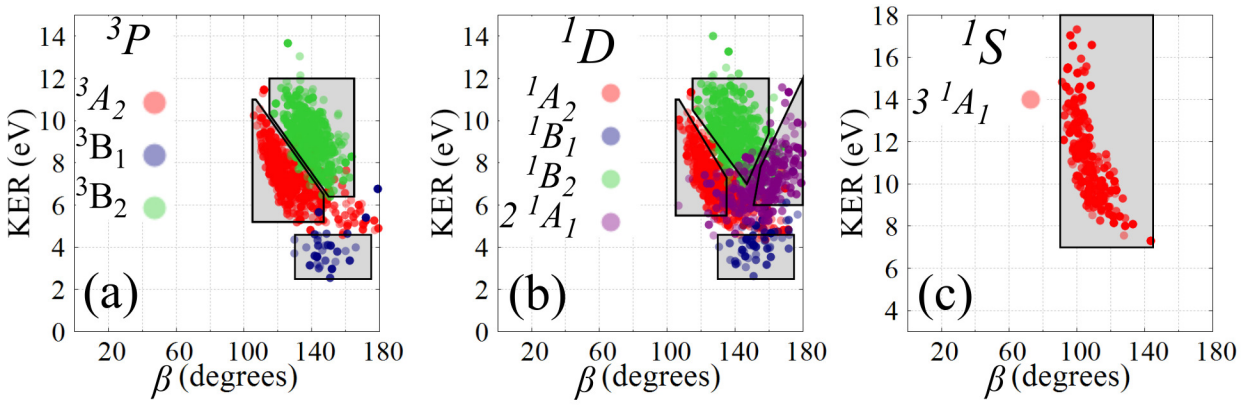


FIG. 13. Gates are constructed as polygons of connected points surrounding each dication state in conformation map space. Table II lists the points used to construct each polygon.

TABLE III. Dication prevalence and fraction by state-selection gate (%)

| | | State Prevalence (%) | | | | | | | | Fraction |
|---|---|---|---|---|---|---|---|---|---|---|
| | | $^3B_1$ | $^3A_2$ | $^3B_2$ | $^1B_1$ | $^1A_2$ | $2\ ^1A_1$ | $^1B_2$ | $3\ ^1A_1$ | % |
| Selected State | $^3B_1$ | 96.7 | 3.3 | 0 | - | - | - | - | - | 67.8 |
| | $^3A_2$ | 0.4 | 98.3 | 1.3 | - | - | - | - | - | 84.8 |
| | $^3B_2$ | 0 | 4.7 | 95.3 | - | - | - | - | - | 93.6 |
| | $^1B_1$ | - | - | - | 94.0 | 6.0 | 0 | 0 | - | 59.5 |
| | $^1A_2$ | - | - | - | 0 | 91.2 | 8.0 | 0.8 | - | 77.5 |
| | $2\ ^1A_1$ | - | - | - | 2.5 | 3.9 | 83.8 | 9.8 | - | 53.1 |
| | $^1B_2$ | - | - | - | 0 | 2.4 | 3.9 | 93.7 | - | 81.9 |
| | $3\ ^1A_1$ | - | - | - | - | - | - | - | 100 | 100 |

lows us to form a Newton-like plot of the fragments in the molecular-dissociation plane. Under the axial-recoil approximation, such plots would reveal the dynamics of the dissociating water dication in the rest frame of the molecule. However, results from Ref. [1] suggest that the axial-recoil approximation fails, in some cases dramatically, for the PDI of water. As a result, the Newton-like plots serve as a visual guide to the asymptotic dissociation and a probe for theoretical results without reliance on the axial-recoil approximation. The current experiment and analysis produce asymptotic momenta for each particle and, as a result, the experiment itself is unable to determine whether the axial-recoil approximation has failed or not without input from theory.

The Newton-like momentum plot, integrated over all dication states, is presented in Fig. 14. From previous analysis of the conformation maps in this paper we expect that this Newton-like plot should have distinct values of momenta and $\beta$ for each dication state. Separation of the individual dication states in the Newton-like plot is achieved by the application of the state-selection gates reported in Table II. These state-selected Newton-like plots are presented in Fig. 15.

Using all the tools developed in subsection IV.B and guidance from Ref. [1], Fig. 15 provides dissociation frame momentum plots which separate each of the eight dication states. These figures are produced by limiting the total continuum asymptotic energy as in Fig. 7(b) and by limiting the KER and $\beta$ according to the unique features of the nuclear confor-

TABLE IV. Approximate state specific relative cross sections for the three-body breakup.

| $C_{2v}$ Symmetry | % of 3-Body Data ($\sqrt{N}$) |
|---|---|
| $1\ ^1A_1$ | - |
| $^3B_1$ | 1.45 (0.05) |
| $^3A_2$ | 12.75 (0.15) |
| $^3B_2$ | 25.28 (0.21) |
| $^1B_1$ | 2.93 (0.07) |
| $^1A_2$ | 13.77 (0.15) |
| $2\ ^1A_1$ | 13.24 (0.15) |
| $^1B_2$ | 20.87 (0.19) |
| $3\ ^1A_1$ | 9.71 (0.13) |

TABLE V. Peak KERs and $\beta$s from experimental data (E.) and simulations [1] for the three-body breakup.

| $C_{2v}$ | E. KER ($\sigma$) | KER | E. $\beta$ ($\sigma$) | $\beta$ |
|---|---|---|---|---|
| $^3B_1$ | 4.29 (0.42) | 4.2 | 145.9 (8.7) | 152.2 |
| $^3A_2$ | 7.99 (1.14) | 7.3 | 121.4 (9.8) | 129.0 |
| $^3B_2$ | 9.66 (1.22) | 9.2 | 138.6 (10.7) | 138.5 |
| $^1B_1$ | 4.26 (0.41) | 4.2 | 148.3 (10.1) | 154.9 |
| $^1A_2$ | 7.58 (0.98) | 7.2 | 125.5 (8.0) | 130.0 |
| $2^1A_1$ | 7.65 (1.03) | 7.1 | 163.6 (6.7) | 155.8 |
| $^1B_2$ | 9.81 (1.11) | 9.3 | 142.9 (9.3) | 140.5 |
| $3^1A_1$ | 11.4 (1.83) | 11.4 | 110.8 (11.4) | 106.0 |

mation maps identified using the classical trajectory simulations from Ref. [1]. The details of these gates are shown in Table II and Fig. 13. The assignment of particular dication state labels follows guidance from Ref. [1].

Simulation results from Ref. [1] were used to reproduce the Newton-like figures, shown in Fig. 16. These figures provide further evidence that the state-selection gates in Table II are separating the correct dication states. The axial recoil approximation was not needed to make this comparison, as Ref. [1] reproduced the results of the direct physical observable, e.g. the asymptotic momenta.

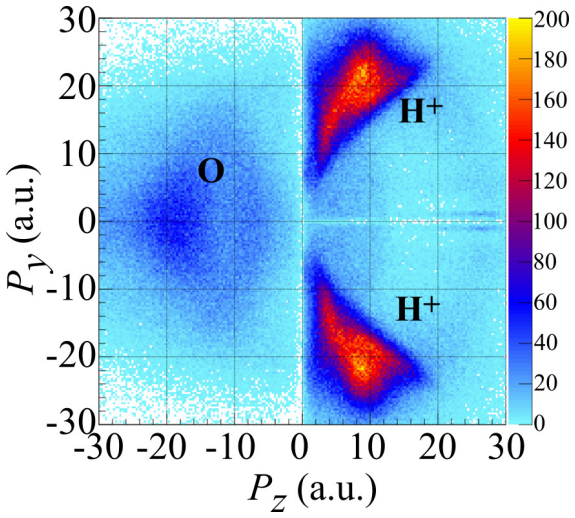


FIG. 14. Newton-like plot of the dissociating water molecule, in the molecular dissociation frame, for the three-body breakup. The horizontal axis is along the sum of the proton unit momenta. Protons are by definition in the first or second quadrant, while the oxygen momentum is in the third and fourth quadrants.

## V. CONCLUSIONS

We have measured the 3D momenta of two ionic fragments and two electrons in coincidence following the PDI of water molecules with single linearly polarized photons of 57 eV. The analysis was split to focus separately on (a) the observed two-body reaction channel, $H^+ + OH^+$, and (b) three-body channel, $H^+ + H^+ + O^*$.

**(a)** Energy correlation maps (Fig. 2), single differential cross sections (Fig. 3), double differential cross sections of electron-electron emission angles and electron angular distributions with respect to the polarization axis (Fig. 5,6) revealed a rich body of data due to at least four dication states and $OH^+$ fragment vibronic and rotational excitation. Furthermore, it was found that the PDI channel was overlayed with an auto-ionization process. Unique single differential cross section distributions were observed for states dissociating via auto-ionization and those dissociating via direct PDI. Identification of dication states $X^3A''$, $1^1A'$, $1^1A''$ and $2^1A'$ could not be realized without more separable data or guidance from theory. Since measurements of the final state dissociation angles are not a measurable quantity in the two-body breakup, only a highly resolved measurement of the energy correlation map (Fig. 2)

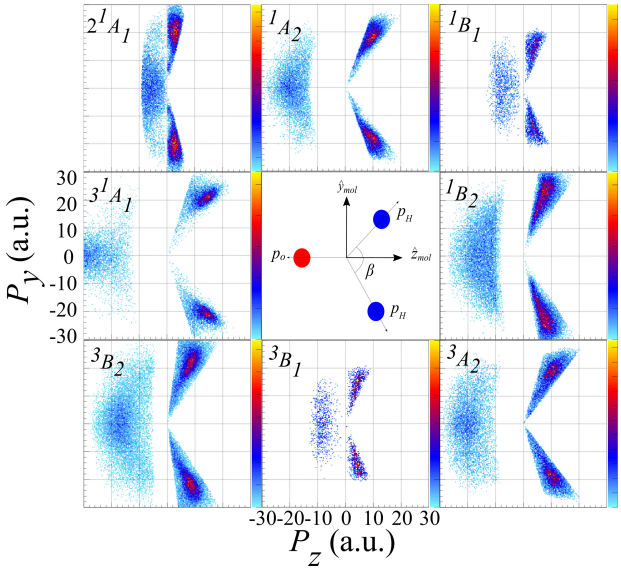


FIG. 15. Momentum plots as in Fig. 14 with gates of total energy (Fig. 7(b) and KER and $\beta$ given in Table II applied to separate the individual dication states. The selected state of each pane is noted in the upper left corner. The cartoon in the center reminds the reader about the dissociation frame axes and the positions of the oxygen (red dot) and protons (blue dots). Axes scales are identical in each pane, but are provided only once to improve visual clarity.

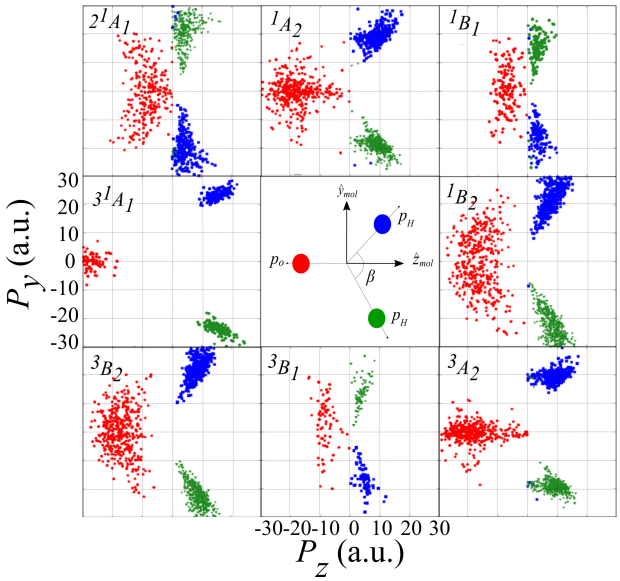


FIG. 16. Momentum plots as in Fig. 14 for all eight dication states using classical trajectory simulation results from Ref. [1] for the three-body breakup and in the experimental dissociation frame. The state of each pane is noted in the upper left corner. The cartoon in the center reminds the reader about the experimental dissociation frame axes and the positions of the oxygen (red) and protons (blue, green). Axes scales are identical in each pane, but are provided only once to improve visual clarity.

might offer access to these states. This would require a larger data set than was realized in this experiment.

**(b)** Similar spectra as in (a) were used to investigate the dissociation dynamics, as well as new nuclear conformation map (Fig. 10) and Newton-like plots (Fig. 14). Analysis of the electron single and double differential cross sections (Fig. 8,9) were similar to those of the two-body channel for equal energy sharing, but showed no signs of extreme electron energy asymmetry following indirect autoionization channels. Nuclear conformation maps and guidance from Ref. [1] provided a way to state-select the three-body fragmentation. The most contaminated data following state-selection was the 2 $^1A_1$ state, which included no more than ∼83% of the selected state following the application of the gate. In contrast, the other seven gates provided better than ∼91% state prevalence in each case. With the state-selection gates, we extracted state-specific peak kinetic energy releases (KER) and $\beta$s, and compared them to the results from classical trajectory simulations in Ref. [1]. Furthermore, we have presented the first experimental relative cross sections for these eight dication states following further guidance from Ref. [1].

In principle, the experimental selection and molecular plane orientation of the dication states can be used to make state-selected, fixed dissociation-frame triply differential cross section (TDCS) measurements. Results from Ref. [1] suggest that three states, namely the 2 $^1A_1$, $^1B_1$, and $^3B_1$, cannot be described as adhering to the axial-recoil approximation in any way. The rest of the states can be state-selected and body-frame oriented. From the gates presented in Section IV.B, we can determine state-selected and body-frame oriented TDCSs. These cross sections, typically presented as an angle between photoelectrons with the energy-sharing ratio and body-frame fixed, are exquisitely sensitive to electron-electron correlation as determined by the initial two-electron wave function, selection rules based on parity and angular momentum conservation depending on the energy sharing of the two electrons, symmetry effects of the populated molecular dication state, and Coulomb interactions of all free charged particles. While the measurement of TDCSs has been nicely realized in great detail for the PDI of $H_2$ (resp. $D_2$) [4, 19, 20, 26, 27], such investigations already become demanding for the PDI of diatomics like $N_2$ and $O_2$ due to the multitude of electronic states involved in the near threshold region. Few successful experiments have been performed on these diatomic systems [47, 48]. Advancing towards such highly detailed PDI studies of small polyatomics represents a challenge for theory and experiment alike. The new spectroscopic analysis tools presented here will be used to produce clean and powerful TDCS measurements in future investigations.

### A. Acknowledgments

Work performed at University of Nevada, Reno was supported by University of Nevada, Reno and the National Science Foundation Grant No. NSF-PHY-1807017. Work at LBNL was performed under the auspices of the US Department of Energy (DOE) under Contract No. DEAC02-05CH11231, using the Advanced Light Source (ALS) and National Energy Research Computing Center (NERSC), and was supported by the ALS US. DOE Office of Basic Energy Sciences, Division of Chemical Sciences. We thank the staff of the ALS, in particular beamline 10.0.1 scientists for their outstanding support. JRML personnel were supported by Grant No. DE-FG02-86ER13491 from the same funding agency. A.S. Gatton acknowledges financial support from the ALS via the Doctoral Fellowship in Residence. Our collaborators from Goethe University Frankfurt acknowledge support by DAAD and BMBF. We are indebted to the RoentDek Company for long-term support with detector hardware and software.

[1] Z. L. Streeter, F. L. Yip, R. R. Lucchese, B. Gervais, and C. W. McCurdy, Physical Review A (2018).
[2] A. Kheifets, Physical Review A **71**, 022704 (2005).
[3] L. Malegat, P. Selles, and A. Huetz, J. Phys. B: At. Mol. Opt. Phys. **30**, 251 (1997).
[4] M. Waitz, D. Metz, J. Lower, C. Schober, M. Keiling, M. Pitzer, K. Mertens, M. Martins, J. Viefhaus, S. Klumpp, T. Weber, H. Schmidt-Böcking, L. P. H. Schmidt, F. Morales, S. Miyabe, T. N. Rescigno, C. W. McCurdy, F. Martín, J. B. Williams, M. S. Schöffler, T. Jahnke, and R. Dörner, Phys. Rev. Lett. **117**, 083002 (2016).
[5] D. Akoury, K. Kreidi, T. Jahnke, T. Weber, A. Staudte, M. Schöffler, N. Neumann, J. Titze,

L. P. H. Schmidt, A. Czasch, O. Jagutzki, R. A. C. Fraga, R. E. Grisenti, R. D. Muiño, N. A. Cherepkov, S. K. Semenov, P. Ranitovic, C. L. Cocke, T. Osipov, H. Adaniya, J. C. Thompson, M. H. Prior, A. Belkacem, A. L. Landers, H. Schmidt-Böcking, and R. Dörner, Science **318**, 949 (2007).

[6] L. Cederbaum, F. Tarantelli, A. Sgamellotti, and J. Schirmer, The Journal of Chemical Physics **85**, 6513 (1986).

[7] R. Dörner, H. Bräuning, J. M. Feagin, V. Mergel, O. Jagutzki, L. Spielberger, T. Vogt, H. Khemliche, M. H. Prior, J. Ullrich, C. L. Cocke, and H. Schmidt-Böcking, Phys. Rev. A **57**, 1074 (1998).

[8] H. Bräuning, R. Dörner, C. L. Cocke, M. H. Prior, B. Krässig, A. Bräuning-Demian, K. Carnes, S. Dreuil, V. Mergel, P. Richard, J. Ullrich, and H. Schmidt-Böcking, Journal of Physics B: Atomic, Molecular and Optical Physics **30**, L649 (1997).

[9] P. Bolognesi, R. Camilloni, M. Coreno, G. Turri, J. Berakdar, A. S. Kheifets, and L. Avaldi, Journal of Physics B: Atomic, Molecular and Optical Physics **34**, 3193 (2001).

[10] J. S. Briggs and V. Schmidt, Journal of Physics B: Atomic, Molecular and Optical Physics **33**, R1 (2000).

[11] H. Bräuning, R. Dörner, C. L. Cocke, M. H. Prior, B. Krässig, A. S. Kheifets, I. Bray, A. Bräuning-Demian, K. Carnes, S. Dreuil, V. Mergel, P. Richard, J. Ullrich, and H. Schmidt-Böcking, Journal of Physics B: Atomic, Molecular and Optical Physics **31**, 5149 (1998).

[12] D. Winkoun, G. Dujardin, L. Hellner, M. J. Besnard, J. Phys B: Atomic, Molecular, Optical Physics **21**, 1385 (1988).

[13] Y. H. Jiang, A. Rudenko, O. Herrwerth, L. Foucar, M. Kurka, K. U. Kühnel, M. Lezius, M. F. Kling, J. V. Tilborg, A. Belkacem, K. Ueda, S. Düsterer, R. Treusch, C. D. Schröter, R. Moshammer, and J. Ullrich, Physical Review Letters **105**, 263002 (2010).

[14] A. G. Suits, Accounts of Chemical Research **41**, 873 (2008).

[15] J. Rajput, T. Severt, B. Berry, B. Jochim, P. Feizollah, B. Kaderiya, M. Zohrabi, U. Ablikim, F. Ziaee, K. Raju P., D. Rolles, A. Rudenko, K. D. Carnes, B. D. Esry, and I. Ben-Itzhak, Phys. Rev. Lett. **120**, 103001 (2018).

[16] A. Tachibana and T. Iwai, Physical Review A **33**, 2262 (1986).

[17] R. M. Wood, Q. Zheng, A. K. Edwards, and M. A. Mangan, Review of Scientific Instruments **68**, 1382 (1997).

[18] A. Landers, T. Weber, I. Ali, A. Cassimi, M. Hattass, O. Jagutzki, A. Nauert, T. Osipov, A. Staudte, M. H. Prior, H. Schmidt-Böcking, C. L. Cocke, and R. Dörner, Phys. Rev. Lett. **87**, 013002 (2001).

[19] T. Weber, A. Czasch, O. Jagutzki, A. Müller, V. Mergel, A. Kheifets, J. Feagin, E. Rotenberg, G. Meigs, M. H. Prior, S. Daveau, A. L. Landers, C. L. Cocke, T. Osipov, H. Schmidt-Böcking, and R. Dörner, Physical Review Letters **92**, 163001 (2004).

[20] W. Vanroose, F. Martin, T. Rescigno, and C. McCurdy, Science **310**, 1787 (2005).

[21] J. Colgan and M. S. Pindzola, Journal of Physics B: Atomic, Molecular and Optical Physics **37**, 1153 (2004).

[22] J. Colgan, M. S. Pindzola, and F. Robicheaux, Physical Review Letters **98**, 153001 (2007).

[23] J. Colgan, M. Foster, M. S. Pindzola, and F. Robicheaux, Journal of Physics B: Atomic, Molecular and Optical Physics **40**, 4391 (2007).

[24] D. A. Horner, W. Vanroose, T. N. Rescigno, F. Martín, and C. W. McCurdy, Physical Review Letters **98**, 073001 (2007).

[25] W. Vanroose, D. A. Horner, F. Martín, T. N. Rescigno, and C. W. McCurdy, Physical Review A **74**, 052702 (2006).

[26] T. J. Reddish, J. Colgan, P. Bolognesi, L. Avaldi, M. Gisselbrecht, M. Lavollée, M. S. Pindzola, and A. Huetz, Phys. Rev. Lett. **100**, 193001 (2008).

[27] M. Gisselbrecht, M. Lavollée, A. Huetz, P. Bolognesi, L. Avaldi, D. P. Seccombe, and T. J. Reddish, Phys. Rev. Lett. **96**, 153002 (2006).

[28] H. Sann, T. Jahnke, T. Havermeier, K. Kreidi, C. Stuck, M. Meckel, M. S. Schöffler, N. Neumann, R. Wallauer, S. Voss, A. Czasch, O. Jagutzki, T. Weber, H. Schmidt-Böcking, S. Miyabe, D. J. Haxton, A. E. Orel, T. N. Rescigno, and R. Dörner, Phys. Rev. Lett. **106**, 133001 (2011).

[29] I. Ben-Itzhak, A. Max Sayler, M. Leonard, J. W. Maseberg, D. Hathiramani, E. Wells, M. A. Smith, X. Jiangfan, P. Wang, K. D. Carnes, and B. D. Esry, Nuclear Instruments and Methods in Physics Research B: Beam Interactions with Materials and Atoms **233**, 284 (2005).

[30] A. M. Sayler, M. Leonard, K. D. Carnes, R. Cabrera-Trujillo, B. D. Esry, and I. Ben-Itzhak, Journal of Physics B: Atomic, Molecular and Optical Physics **39**, 1701 (2006).

[31] P. J. Richardson, J. H. D. Eland, P.G. Fournier, D. L. Cooper, Journal of Chemical Physics **84**, 3189 (1986).

[32] King, S.J and Price, S.D., International Journal of Mass Spectrometry **277**, 84 (2008).

[33] R. Dörner, V. Mergel, O. Jagutzki, L. Spielberger, J. Ullrich, R. Moshammer, H. Schmidt-Böcking, Physics Reports **330**, 95 (2000).

[34] T. Jahnke, T. Weber, T. Osipov, A. Landers, O. Jagutzki, L. Schmidt, C. Cocke, M. Prior, H. Schmidt-Böcking, R. Dörner, and et al., Journal of Electron Spectroscopy and Related Phenomena **141**, 229 (2004).

[35] J. Ullrich, R. Moshammer, A. Dorn, R. Dörner, L. P. H. Schmidt, and H. Schmidt-Böcking, Reports on Progress in Physics **66**, 1463 (2003).
[36] O. Jagutzki, A. Cerezo, A. Czasch, R. Dörner, M. Hattas, M. Huang, V. Mergel, U. Spillmann, K. Ullmann-Pfleger, T. Weber, H. Schmidt-Böcking, and G. Smith, IEEE Transactions on Nuclear Science **49**, 2477 (2002).
[37] B. Gervais, E. Giglio, L. Adoui, A. Cassimi, D. Duflot, and M.E. Galassi, Journal of Chemical Physics **131**, 024302 (2009).
[38] B. Gaire, I. Bocharova, F. P. Sturm, N. Gehrken, J. Rist, H. Sann, M. Kunitski, J. Williams, M. S. Schöffler, T. Jahnke, B. Berry, M. Zohrabi, M. Keiling, A. Moradmand, A. L. Landers, A. Belkacem, R. Dörner, I. Ben-Itzhak, and T. Weber, Phys. Rev. A **89**, 043423 (2014).
[39] J.H.D. Eland, Chemical Physics , 391 (2006).
[40] T. Schneider, P. L. Chocian, and J.-M. Rost, Physical Review Letters **89**, 073002 (2002).
[41] A. Knapp, M. Walter, T. Weber, A. L. Landers, S. Schössler, T. Jahnke, M. Schöffler, J. Nickles, S. Kammer, O. Jagutzki, L. P. H. Schmidt, T. Osipov, J. Rösch, M. H. Prior, H. Schmidt-Böcking, C. L. Cocke, J. Feagin, and R. Dörner, Journal of Physics B: Atomic, Molecular and Optical Physics **35**, L521 (2002).
[42] C. Moore, *CRC Series in Evaluated Data in Atomic Physics* (CRC Press, 1993) p. 339.
[43] R. Wehlitz, F. Heiser, O. Hemmers, B. Langer, A. Menzel, and U. Becker, Physical Review Letters **67**, 3764 (1991).
[44] M. Pont and R. Shakeshaft, Physical Review A **54**, 1448 (1996).
[45] A. S. Kheifets and I. Bray, Physical Review A **75**, 042703 (2007).
[46] R. Dörner, J. M. Feagin, C. L. Cocke, H. Bräuning, O. Jagutzki, M. Jung, E. P. Kanter, H. Khemliche, S. Kravis, V. Mergel, M. H. Prior, H. Schmidt-Böcking, L. Spielberger, J. Ullrich, M. Unversagt, and T. Vogt, Physical Review Letters **77**, 1024 (1996).
[47] A. Ponzi, C. Angeli, R. Cimiraglia, S. Coriani, and P. Decleva, The Journal of Chemical Physics **140**, 204304 (2014).
[48] P. O'Keeffe, P. Bolognesi, A. Moise, R. Richter, Y. Ovcharenko, and L. Avaldi, The Journal of Chemical Physics **136**, 104307 (2012).

# Photoelectron and fragmentation dynamics of the $H^+ + H^+$ dissociative channel in $NH_3$ following direct single-photon double ionization

Kirk A. Larsen,[1,2,*] Thomas N. Rescigno,[2,†] Travis Severt,[3] Zachary L. Streeter,[2,4] Wael Iskandar,[2] Saijoscha Heck,[2,5,6] Averell Gatton,[2,7] Elio G. Champenois,[1,2] Richard Strom,[2,7] Bethany Jochim,[3] Dylan Reedy,[8] Demitri Call,[8] Robert Moshammer,[5] Reinhard Dörner,[6] Allen L. Landers,[7] Joshua B. Williams,[8] C. William McCurdy,[2,4] Robert R. Lucchese,[2] Itzik Ben-Itzhak,[3] Daniel S. Slaughter,[2] and Thorsten Weber[2,‡]

[1] *Graduate Group in Applied Science and Technology, University of California, Berkeley, CA 94720, USA*
[2] *Chemical Sciences Division, Lawrence Berkeley National Laboratory, Berkeley, CA 94720, USA*
[3] *J.R. Macdonald Laboratory, Physics Department, Kansas State University, Manhattan, Kansas 66506, USA*
[4] *Department of Chemistry, University of California, Davis, CA 95616, USA*
[5] *Max-Planck-Institut für Kernphysik, Saupfercheckweg 1, 69117 Heidelberg, Germany*
[6] *J.W. Goethe Universität, Institut für Kernphysik, Max-von-Laue-Str. 1, 60438 Frankfurt, Germany*
[7] *Department of Physics, Auburn University, Alabama 36849, USA*
[8] *Department of Physics, University of Nevada Reno, Reno, Nevada 89557, USA*

(Dated: August 18, 2021)

We report measurements on the $H^+ + H^+$ fragmentation channel following direct single-photon double ionization of neutral $NH_3$ at 61.5 eV, where the two photoelectrons and two protons are measured in coincidence using 3-D momentum imaging. We identify four dication electronic states that contribute to $H^+ + H^+$ dissociation, based on our multireference configuration-interaction calculations of the dication potential energy surfaces. The extracted branching ratios between these four dication electronic states are presented. Of the four dication electronic states, three dissociate in a concerted process, while the fourth undergoes a sequential fragmentation mechanism. We find evidence that the neutral NH fragment or intermediate $NH^+$ ion is markedly ro-vibrationally excited. We also identify differences in the relative emission angle between the two photoelectrons as a function of their energy sharing for the four different dication states, which bare some similarities to previous observations made on atomic targets.

## I. INTRODUCTION

Photo-Double-Ionization (PDI) is a process in which two electrons are ejected from an atom or molecule by absorption of a single photon. The resulting dication can be produced through either an indirect or a direct process. In the indirect process [1, 2], the target is first ionized to produce a photoelectron and a singly-charged, excited cation. Subsequently, the cation decays by autoionization to produce a second continuum electron. The secondary electrons in indirect PDI have a unique signature, i.e. often a very narrow kinetic energy distribution and a rather isotropic angular emission pattern, which allows the process to be uniquely identified in a two-electron energy- or momentum-coincidence spectrum. In contrast to the indirect process, direct PDI involves simultaneous projection of two bound electrons to a correlated pair of continuum states. The interaction of the two electrons makes PDI an ideal process for studying electron-electron correlation [3–7].

Because of the repulsive Coulomb interaction between singly charged ions that is active over very large internuclear distances, the vertical double ionization thresholds of small molecules generally lie above the dissociation limits corresponding to formation of singly charged fragments. Since the dissociative electronic states of a polyatomic dication can possess various fragmentation pathways involving different numbers of bodies, distinct fragment species can be measured depending on various factors. Studying the photoelectron pair and various ionic fragments in coincidence can provide information on electron-electron correlation, the features of dication potential energy surfaces, and the nuclear dynamics involved in the dication breakup. The

* klarsen@lbl.gov
† tnrescigno@lbl.gov
‡ tweber@lbl.gov

molecular fragmentation that typically follows direct PDI can be broadly described as occurring in a single step (concerted), where all charged and neutral fragments are born simultaneously, or occurring in multiple steps (sequential), where first a portion of the charged and neutral fragments are generated, leading to a metastable intermediate moiety, which then undergoes further dissociation to produce the final set of fragments [8, 9].

In sequential fragmentation, the decay of the metastable intermediate(s) can be facilitated by various mechanisms, such as internal conversion or intersystem crossing to a dissociative state. Although spin-orbit coupling is generally weak in low-Z systems, intersystem crossing can in certain instances be the primary decay mechanism of metastable intermediates in a sequential dissociation process. Due to the weak coupling, the rate of intersystem crossing can be low, which leads to a significant period spent in the intermediate, providing time for the metastable fragments to rotate between the two fragmentation steps.

Distinguishing between concerted and sequential fragmentation channels is crucial in certain types of measurements, as concerted fragmentation channels can enable body-fixed frame photoelectron angular distributions to be retrieved, which carry far more information content than laboratory frame angular distributions. These body-fixed frame photoelectron angular distributions can, in most cases, only be reconstructed if the dication dissociates promptly along the relevant internuclear axes relative to rotation of those axes, allowing the molecular orientation at the instant of the PDI to be determined. This requirement is known as the axial recoil approximation [10]. Since measuring body-frame photoelectron angular distributions following PDI poses a great experimental challenge, there exists only a small body of literature covering this topic, primarily focused on $H_2$ [6, 7, 11–13]. Various experimental methods such as particle coincidence 3-D momentum imaging, including COLd Target Recoil Ion Momentum Spectroscopy (COLTRIMS), allow measurements to be made in the molecular frame, but are predicated on the axial recoil approximation, hence it is useful to first determine which dication states exhibit concerted fragmentation mechanisms. The body-fixed frame electron emission pattern, or Molecular Frame Photoelectron Angular Distributions (MFPADs), can be established if the complete structure of the molecule at the time of dissociation can be reconstructed from the detected heavy ionic fragments. However, if a dissociative channel produces more than two (undetected) neutral fragments, or results in a polyatomic fragment with unknown orientation, only the Recoil Frame Photoelectron Angular Distribution (RFPAD) can be reconstructed. The latter represents the electron emission pattern with respect to a distinguished axis or plane spanned by the (detected) charged fragments. R/MFPADS are particularly sensitive to electron-electron correlation in both the initial and final states.

Various experimental and theoretical studies spanning a few decades have investigated the different dication electronic states and dissociation channels present in $NH_3$ following PDI, electron impact double ionization, and double ionization via double-charge-transfer spectroscopy [14–29]. Most of these studies have focused on determining the appearance energies of the different fragments and the energetic locations of the dication electronic states. Among these investigations, no study, to our knowledge, has examined the $H^+ + H^+$ fragmentation channels of ammonia.

In this work, we investigate $H^+ + H^+$ dissociation following direct valence PDI of neutral $NH_3$ at 61.5 eV, approximately 27 eV above the PDI threshold [30], where both the photoelectron and proton pairs are measured in coincidence using COLTRIMS. Based on Multi-Reference Configuration-Interaction (MRCI) calculations of dication Potential Energy Surfaces (PESs), we identify four dication electronic states that contribute to the $H^+ + H^+$ fragmentation. Our measurement provides the branching ratios between the four involved dication electronic states. As will be detailed below, of these four states, one appears to dissociate via a sequential mechanism and three dissociate in a concerted mechanism. Two of the three concerted dissociative states fragment at geometries near that of the ground state of neutral $NH_3$, where the axial recoil approximation appears valid, while the third state undergoes a significant change in nuclear geometry prior to fragmentation. By measuring the correlated electron and ion fragment momenta, we determine that the neutral NH fragment or charged intermediate $NH^+$ cation is rovibrationally excited with considerable internal energy, in some cases more than 2 eV.

## II. EXPERIMENT

The $H^+ + H^+$ fragmentation channel following valence PDI at 61.5 eV was investigated using

COLTRIMS [31, 32], where the two photoelectrons and two protons were collected with full $4\pi$ solid angle, and their 3-D momenta were measured in coincidence, on an event-by-event basis. These four charged particles were guided using weak static parallel electric and magnetic fields, 11.4 V/cm and 10.0 G, respectively, to multi-hit position- and time-sensitive detectors at opposite ends of the spectrometer. Each detector comprised a Multi-Channel Plate (MCP) stack in chevron configuration for time readout, together with a delay-line anode, which decoded the hit position of each particle [33]. The electron and ion delay-line detectors were a hex-anode with an 80 mm MCP stack and a quad-anode with a 120 mm MCP stack, respectively. This system encodes a charge particle's 3-D momentum into its hit position on the detector and Time-of-Flight (TOF) relative to each ionizing extreme ultraviolet (XUV) pulse emitted by the synchrotron. These detectors have a small but significant dead-time following each detected particle, therefore they are subject to limited multi-hit capability [33]. This problem is most prominent in the electron pair detection, due to the small differences in the electron arrival times and hit positions at the detector. This dead-time effect can influence measured relative electron-electron angular distributions and is thus important to quantify, in order to distinguish real features from those that may emerge due to the detection scheme. We point out that the photoions do not suffer from this dead-time problem to the same degree as the electrons, as they are much more spread out in TOF and hit position on the ion detector. The electron-pair resolution is estimated by simulating the charged particle motion in the spectrometer fields with various sum kinetic energies and in various energy sharing conditions of the electron pair. For each pair of trajectories, the relative hit position and time-of-flight is computed, which is used to determine the fraction of simulated electron-pair events lost due to an estimated detector response, and thus approximate the fraction of actual losses.

The PDI experiment was performed using a tunable monochromatic linearly polarized beam of XUV photons produced at beamline 10.0.1.3. at the Advanced Light Source (ALS) synchrotron located at Lawrence Berkeley National Laboratory. The beamline monochromator was configured to provide 61.5 eV photons to the experiment, with an energy resolution narrower than $\pm 50$ meV. The photon energy of 61.5 eV was chosen to be near the maximum of the PDI cross section of $NH_3$, while at the same time providing electron kinetic energies that can be detected with full solid angle and adequate energy resolution (around 1:10). Moreover, it is beneficial to keep the electron sum energy greater than $\sim 5$ eV in order to utilize a large region of the 3D electron pair detection phase space, minimizing losses due to the electron detector dead-time (this will be apparent in Fig. 4 later in the discussion).

A beam of rotationally and vibrationally cold neutral $NH_3$ ($\sim$80 K) was produced by an adiabatic expansion of the pressurized target gas ($\sim$35 psi) through a 50 $\mu$m nozzle, and collimated by a pair of downstream skimmers. The first skimmer has a diameter of 0.3 mm and the second skimmer has a diameter of 0.5 mm. The first skimmer is placed 8 mm downstream of the nozzle and in the zone of silence of the supersonic expansion. The second skimmer is 10 mm downstream of the first skimming stage. The resulting supersonic jet of target molecules propagated perpendicular to the photon beam, where the two beams crossed at the interaction region ($\sim 0.15 \times 0.15 \times 1.0$ mm$^3$) inside the 3-D momentum imaging spectrometer, where PDI of the neutral ammonia in its ground state occurs at an average rate of less than 0.01 events per XUV pulse, assuring unambiguous coincidence conditions.

The TOF and hit position of the charge particles produced by PDI were recorded in list mode on an event-by-event basis, enabling relevant events to be selected and examined in a detailed off-line analysis. For each PDI event, the kinetic energies and emission angles of the photoelectrons were determined from the 3-D photoelectron momenta, while the orientation of the recoil frame and the kinetic energy release (KER) of the fragmentation were determined using the measured 3-D momenta of the two protons. We infer the momentum of the center of mass of the remaining neutral NH radical by assuming momentum conservation between it and the two measured protons, treating the fragmentation as three-body breakup (even if the NH diatom fragments to N + H).

## III. THEORY

Most previous work on the ammonia dication have been experimental in nature. Of the earlier theoretical studies, most have focused on computing the vertical double ionization energy of neutral ammonia [30, 34]. Tarantelli *et al.* [35] computed excited state excitation energies of $NH_3^{2+}$ at the equi-

librium geometry of $NH_3$ (see also Table I), but to our knowledge no earlier calculations of $NH_3^{2+}$ potential surfaces have been reported. The electron configuration of $NH_3$ in its ground-state is $(1a_1)^2(2a_1)^2(1e)^4(3a_1)^2$. At a photon energy of 61.5 eV, there are nine dication states which are energetically accessible following a vertical transition. In order to determine which of these states correlate with the three-body NH + $H^+$ + $H^+$ fragmentation channel, we carried out a series of electronic structure calculations. At each molecular geometry considered, we generated a set of molecular orbitals from a two-state, Complete Active Space (CAS) Multi-Configuration Self-Consistent Field (MCSCF) calculation on the lowest triplet ($^3$E) states of the dication. We kept one orbital (N 1s) frozen and included seven orbitals in the active space. We then performed MRCI calculations including all single and double excitations from the CAS reference space to generate 1-D cuts through the PESs. All bond angles were frozen at the equilibrium geometry of neutral ammonia ($107^o$), as was one hydrogen ($H_{III}$) bond length (1.9138 Bohr), while two hydrogen bonds ($H_I$) and ($H_{II}$) were symmetrically stretched. The results of the calculations are shown in Fig. 1 with the electron configuration and state labels of each dication PES cut identified in the legend. The PES cuts were calculated out to a symmetric stretch N-$H_I$/N-$H_{II}$ distance of 50.0 bohr and extrapolated to infinity under the assumption of a purely repulsive Coulomb interaction between the positively charged fragments. The vertical energies at the neutral $NH_3$ geometry and the energies at the asymptotic limits are given in Table I. Note that here we do not explicitly consider cuts through the dication PESs where only one NH bond is stretched, as that is the subject of a future paper.

Our calculations reveal that there are only three three-body proton-proton dissociative limits. Of the three-body proton-proton channels, two are singlet states and one is a triplet state. The two singlet states leave the remaining neutral NH molecule in a $^1\Delta$ or a $^1\Sigma^+$ state, while the triplet leaves the neutral NH fragment in a $^3\Sigma^-$ state. In order to produce the two experimentally observed protons in the fragmentation, the implication is that an excitation must access one of these three dissociative limits, or undergo a four-body fragmentation mechanism that yields two protons, i.e. results in the fragments N + H + $H^+$ + $H^+$.

We identify three relevant singlet states, $(1e^{-2})$ $^1$E, $(1e^{-2})$ $^1A_1$, and $(2a_1^{-1}, 3a_1^{-1})$ $^1A_1$, shown in Fig. 1 (a) as solid curves (magenta, green and red), and a fourth relevant triplet state, $(1e^{-2})$ $^3A_2$, shown as a dashed curve (cyan). The curves in Fig. 1 (a) are color-coded to be consistent with the experimental features to be discussed in the following section. Since spin-orbit coupling, required for an intersystem crossing, is expected to be weak, the triplet state must dissociate to a triplet fragment state. However, Fig. 1 shows that the $^3A_2$ state (cyan dashed) actually correlates with the $NH^+(^2\Pi)$+$H^+$+H($^2$S) dissociation channel (cyan dashed in the Fig. 1 (b) inset). To reach the $NH(^3\Sigma^-)$+$2H^+$ limit (black curve in the inset) requires a charge exchange, which is possible at N-H separations greater than 18 Bohr where the $^3$E ($^3A''$) and $^3A_2$ ($^3A''$) states become nearly degenerate in energy across a range of geometries (see cyan dashed and black curves in Fig. 1 (b)). This can result in charge exchange over a large range of distances along the asymmetric stretch coordinate that the dissociating wave packet traverses. We have observed an analogous asymptotic charge-exchange mechanism at such large N-H distances in an earlier study of dissociative electron attachment to ammonia [36].

For singlet states accessible in the Franck-Condon (FC) region as depicted in Fig. 1 (a), there are two different proton-proton limits (red and green curves). The $(1e^{-2})$ $^1A_1$ state (green) is seen to cross two other dissociative $^1A_1$ states (green and red), which correlate with the products NH ($^1\Delta$) or NH ($^1\Sigma^+$) plus two protons, respectively. Conical intersections (CIs) between the dissociative states and the initially excited $^1A_1$ state can result in dissociation to either of the singlet limits. Since the location of the CIs cannot be determined from 1-D energy cuts (although numerous avoided crossing are observed), we must rely on the experimental findings to see which of the singlet limits are populated.

Previous experimental observations have indicated that PDI to the $(1e^{-2})$ $^1$E state is associated with the $NH^+$ + $H^+$ + H fragmentation channel [15]. Since the dissociative limit of the $(1e^{-2})$ $^1$E state does not directly yield two protons, excitation to this state must undergo a nonadiabatic transition to either of the two $^1A_1$ excited dication states, or the $NH^+$ fragment it produces must dissociate to N + $H^+$, in order to result in the measured two-proton coincidence.

The $(1e^{-2})$ $^1$E state, doubly degenerate in $C_{3v}$ geometry, splits into A′ and A″ states when two N-H bonds are symmetrically stretched. Of these two states, the upper state has A″ symmetry. Accord-

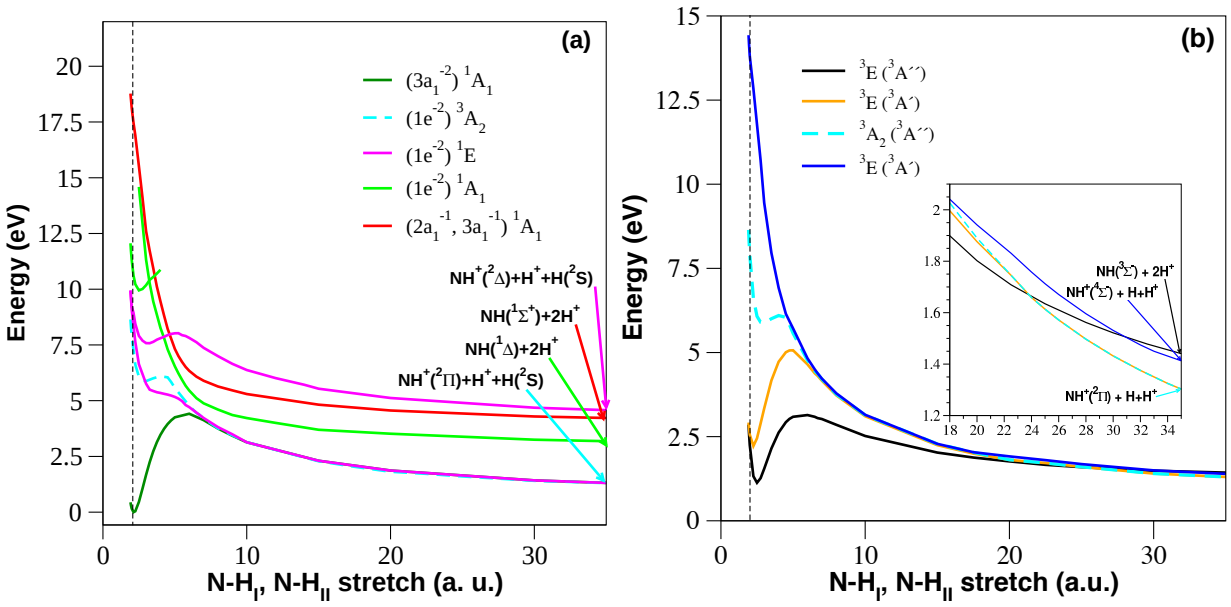


FIG. 1. PES cuts of the $NH_3$ dication generated from MRCI calculations as described in the text. Here, two protons are symmetrically stretched while the third remains fixed , with all internal angles frozen at the geometry of neutral ammonia. The zero of energy is set at the ground-state ($^1A_1$) of the ammonia dication at the geometry of neutral ammonia, which lies 34.8 eV below the dication [30]. On this energy scale, the 61.5 eV photon energy lies at 26.7 eV. The dashed vertical line indicates the equilibrium geometry of neutral ammonia. (a) Cuts of the experimentally identified relevant states; (b) detail of PES cuts for selected $NH_3$ dication triplet states. The inset indicates a region of large symmetric stretch distances where charge exchange may occur, as discussed in the text.

| State | Vertical Energy (eV) | Asymptote | Adiabatic Limit Energy (eV) |
|---|---|---|---|
| $(1e^{-2})^3A_2$ (cyan) | 8.64 (8.23)* | $NH(^3\Sigma^-)+H^+ +H^+$ | 0.96 |
| $(1e^{-2})^1E$ (magenta) | 9.94 (9.91)* | $NH^+(^2\Pi)+H+H^+$ | 0.52 |
| $(1e^{-2})^1A_1$ (green) | 11.94 (11.77)* | $NH(^1\Delta[^1\Sigma^+])+H^+ +H^+$ | 2.69 [3.74] |
| $(2a_1^{-1},3a_1^{-1})^1A_1$ (red) | 18.94 (19.33)* | $NH(^1\Sigma^+)+H^+ +H^+$ | 3.74 |

TABLE I. Ammonia dication vertical energies at neutral $NH_3$ geometry and asymptotic three-body limits extrapolated from *ab initio* calculations at $N\text{-}H_I/N\text{-}H_{II}$ distances of 50.0 bohr. Note that for the $^1A_1$ state (green), two possible asymptotic limits are given (see text). *Values in parentheses are configuration interaction results from Ref. [35].

ingly, internal conversion to either of the $^1A'$ states that have limits producing NH + $H^+$ + $H^+$ is unfavorable. Dissociation on the lower curve yields an $NH^+$ fragment in its $X^2\Pi$ ground state. If the $NH^+$ fragment is produced with sufficient internal energy, it can dissociate to $N^+(^3P)$+ $H(^2S)$ or through intersystem crossing to another $NH^+$ state, to $N(^4S)$ + $H^+$. In the latter case this results in the production of two protons via a sequential four-body breakup $NH_3^{++} \rightarrow NH^+ + H^+ + H \rightarrow N + 2H^+ + H$. This sequential breakup process will be examined in detail below.

## IV. RESULTS AND DISCUSSION

Using the insights gained from the calculations on dication electronic states described in the previous section, we provide a detailed discussion of the experimental results below, which has been divided into three sub-sections. In the first sub-section, we present and discuss the energetics of the photoelectrons and photoions, identifying features which correspond with the states outlined in the previous section. In the second sub-section, we address the details of the dissociation dynamics by analyzing the relative emission angle between the two protons in each of these states. Lastly, we present results on

the photoelectron dynamics via an analysis of the relative emission angle between the two photoelectrons for the four dication states in different energy sharing conditions of the electron pair.

### A. Photoelectron and photoion energetics

The $H^+ + H^+$ fragmentation following PDI of $NH_3$ at 61.5 eV, ∼27 eV above the PDI threshold, is identified and isolated by selecting the two charged fragments in the time-of-flight spectrum and then in momentum space, and by enforcing that two electrons are measured in coincidence with the two ionic fragments. First, we plot the PDI yield as a function of the energy difference between the two particles of the proton pair and the energy sum of the photoelectron pair. This plot is shown in Fig. 2.

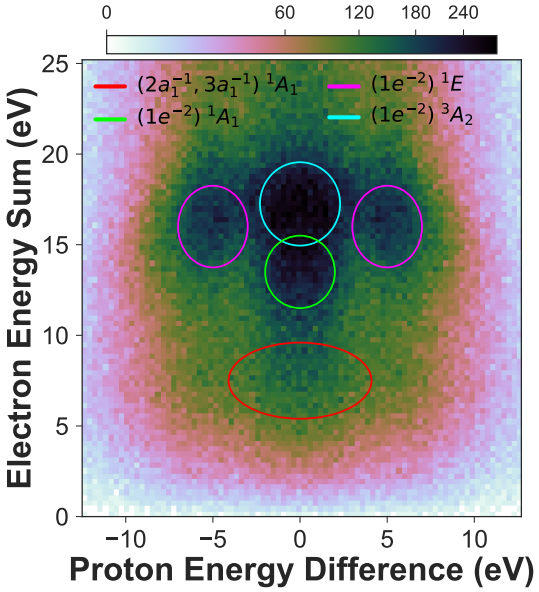


FIG. 2. The yield of $H^+ + H^+$ after valence PDI of $NH_3$ as a function of the energy difference of the proton pair and the energy sum of the photoelectron pair. The four color-coded ellipses guide the eye to the relevant features and dication states discussed in the text. The data has been mirrored about zero proton energy difference, as there is no physical meaning to the order in which the two proton are detected.

Here we are able to identify four features, which we attribute to the four different dication electronic states calculated and tabulated in the previous section, resulting in photoelectron pairs with energy sums centered around 7.3 eV, 14.1 eV, 16.7 eV, and 17.6 eV. These features are indicated by ellipses to guide the eye and color-coded to be consistent with the calculated values of 7.8, 14.8, 16.8 and 18.1 eV listed in Table I. The measured and calculated values are in excellent agreement and are consistent with the state assignments. Note that the ellipses do not reflect the actual software gates used in the data analysis. In the offline analysis, we choose each of these states by selecting carefully around the center of each feature in Fig. 2, while additionally placing constraints on the proton energy sum (which aids in separating the low and high KER features). Enforcing conditions in a multitude of dimensions in this fashion enables us to separate these four features for subsequent analysis.

Each of these four features possesses a Full Width at Half Maximum (FWHM) in electron energy sum of roughly 6.2 eV, 2.1 eV, 4.2 eV, and 2.4 eV, respectively. The FWHM of the electron energy sum of each dication state roughly indicates the magnitude of the gradient of the PES in the FC region, provided the electron detector energy resolution is smaller than the width of the feature in question. To estimate the expected spread of observed photoelectron energies for the various dication states, we use a variant of the so-called reflection approximation [37]. The range of detectable KERs is determined by the FC envelope of the initial (neutral) vibrational state reflected onto the final dication PESs. We approximate the initial vibrational wavefunction with a harmonic oscillator function $\chi_0$, obtained from a fit of the ground state energy of ammonia as a function of the symmetric stretch coordinate. If we assume that the PDI cross section varies little over the FC region and that the final continuum vibrational wavefunctions can be approximated by delta functions about the classical turning points on the dication PESs [7], then the envelope of the expected photoelectron energies is given by the values of the vertical PDI energies as a function of the symmetric-stretch coordinate, weighted by the square of the symmetric-stretch vibrational wavefunction. We find that $|\chi_0|^2$ reaches half its maximum value at a symmetric-stretch displacement of approximately ±0.11 Bohr from equilibrium, and we have used these values to calculate the FWHM of the photoelectron distributions. According to this procedure we find widths of 5.1 eV, 1.9 eV, 3.1 eV and 2.2 eV, respectively, which are in good agreement with the measurement (see also Table II). From this we find that, given our photoelectron spectral resolu-

tion of roughly $\Delta E/E \sim 0.1$, the measured FWHM of each state does indeed roughly correspond with the gradient of its PES in the FC region.

We present the 1-D photoelectron energy sum spectrum in Fig. 3, where each feature we identified in Fig. 2 has been indicated by the color-coded distribution. The peak value of each distribution has been indicated in Table II, where it is also compared with the theoretically calculated value. We find good agreement between the measurement and calculations. We can clearly identify the feature with a photoelectron energy sum centered near 7.3 eV, while the three higher photoelectron energy features appear clustered together. The branching ratios between the four measured features that correspond with the four dication states are estimated from the relative yield of these four features, and they are presented in Table III. The method for extracting these branching ratios is discussed later.

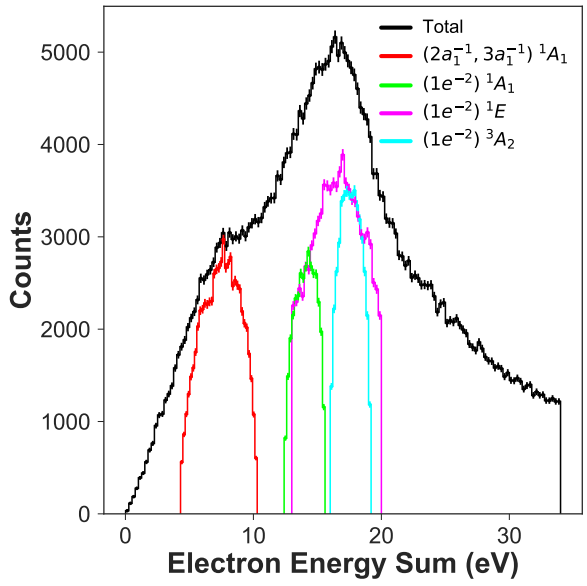


FIG. 3. The $NH_3$ PDI yield of the $H^+ + H^+$ channel as a function of the photoelectron energy sum integrated over all features (black) as well as for the four color-coded features corresponding with the identified dication states. The electron energy sum distributions for the four features have been scaled by a factor of four, for better visibility.

The yields of the $H^+ + H^+$ channels as a function of the kinetic energy of the first and second detected electron are plotted in the electron-electron energy correlation map shown in Fig. 4. Since the two electrons are indistinguishable particles, the labeling (as 1 and 2) is arbitrary and the figure has been symmetrized across the diagonal (the line $E_2 = E_1$) to account for this.

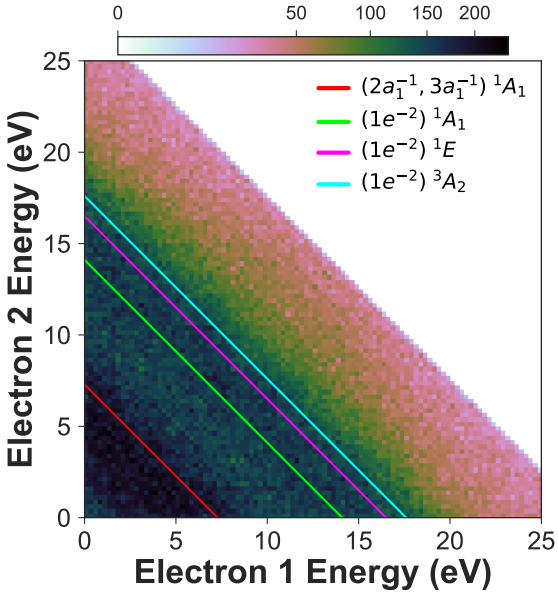


FIG. 4. Electron-electron energy correlation map for the $H^+ + H^+$ channels of the PDI of $NH_3$. The four identified dication states are color-coded and indicated by diagonal lines.

The four different features that correspond to the dication electronic states identified in Figs. 2 and 3 are indicated as color-coded diagonal lines (which take the form $E_2 = -E_1 + E_{sum}$, where $E_{sum}$ is the photoelectron energy sum corresponding to that feature) in Fig. 4. We point out that the red diagonal line appears to be off the center of the diagonal feature, even though this location represents the peak. This is because there are fewer bins along a given constant electron energy sum (i.e. a diagonal of the form $E_2 = -E_1 + E_{sum}$) as the photoelectron energy sum decreases. Since the length of a constant energy diagonal line scales as $\sqrt{2}E_{e^-}$, the number of available bins that events can populate decreases with decreasing $E_{e^-}$. This leads to the counts at low constant electron energy sums to be concentrated in just a small number of bins, which can render the true location of the peak obscured in this 2-D spectrum, while it is well represented in Fig. 3.

All four dication states are accessed via direct PDI, as indicated by the uniform diagonal features (taking the form $E_2 = -E_1 + E_{sum}$) and the absence

of any Auger or autoionization lines, which would appear with vertical or horizontal characteristics at very unequal energy sharing due to the autoionization electron possessing a narrow constant (low) energy. The uniformity of the diagonal features in Fig. 4 indicates that the two photoelectrons do not exhibit a strong preference towards either equal or unequal energy sharing, but rather exhibit roughly constant $H^+ + H^+$ yield as a function of the electron energy sharing (see also Fig. 12). The photoelectron energy sharing distributions for each of the four states will be presented and discussed in more detail in the final sub-section C.

The same four features, corresponding with those seen in Fig. 2, are present in the proton-proton energy correlation map given in Fig. 5. As in the electron-electron energy correlation map of Fig. 4, the two protons are indistinguishable particles, hence the labeling is arbitrary and the figure has been symmetrized across the diagonal (the line $E_2 = E_1$). We have removed events that lie in the low energy corner of Fig. 5, as the events that lie within this region originate from false coincidences. For each proton-pair we compute the KER by treating the process as a three-body fragmentation and by inferring the momentum of the N-H center of mass via momentum conservation. Each feature seen in Fig. 5 possesses a different KER distribution centered around 12.7 eV, 5.9 eV, 7.7 eV, and 5.5 eV, each with a FWHM of roughly 6.1 eV, 2.2 eV, 3.0 eV, and 2.0 eV, respectively. These KER distributions are discussed in more detail later. The three KER features we have associated with the $(2a_1^{-1}, 3a_1^{-1})$ $^1A_1$, $(1e^{-2})$ $^1A_1$ and $^3A_2$ states exhibit a tendency towards equal energy sharing between the two protons, consistent with a concerted breakup mechanism. The fourth KER feature, associated with the $^1E$ state, exhibits highly unequal energy sharing between the two protons, indicative of a sequential breakup mechanism.

Theoretical KER values are obtained by subtracting the asymptotic energies from the associated vertical PDI energies in Table I, while theoretical photoelectron energy sum values are computed by subtracting these vertical PDI energies and the double ionization threshold from the photon energy. These results are displayed in Table II. For the concerted breakup channels theory gives 15.2, 8.2, and 7.7 eV for the $(2a_1^{-1}, 3a_1^{-1})$ $^1A_1$, $(1e^{-2})$ $^1A_1$, and $(1e^{-2})$ $^3A_2$ dication states, respectively. (Note that the NH($^1\Sigma^+$) asymptote has been used for both $^1A_1$ states.) These values are uniformly higher, by 2.5, 2.3 and 2.2 eV, respectively, than the measured values. This discrepancy is either due to calculated dissociation energies that are all uniformly too small by approximately 2 eV, or can arise if the NH fragment in all three concerted breakup channels is produced with approximately 2 eV of ro-vibrational energy. The energy balance of the sequential breakup is consistent with high internal energy of the NH fragment. For the sequential $^1E$ breakup channel, theory gives a KER value of 9.4 eV, which is 1.7 eV higher than the measured value. This corresponds to a four-body breakup mechanism, discussed in detail in Section IV B.

The FWHM of the KER distribution associated with each dication state carries similar information as the electron sum energy FWHM (see also Table II), indicating the steepness of the potential energy surfaces in the FC region, convoluted with the energy resolution of the ion spectrometer (estimated to be on the order of 100 meV). These values are indicated in Table II.

We show the 1-D KER spectrum in Fig. 6, where each feature we identified in Fig. 5 has been indicated by the color-coded distribution. The peak value of each distribution is listed in Table II, where it is also compared with our theoretical results. The differences between the measured and calculated values in Table II are consistent with the molecular fragments containing roughly 2 eV of internal energy (or the aforementioned four-body breakup mechanism, which is discussed below), not explicitly accounted for in our theory which only considers fragments in their rotational and vibrational ground states.

The estimated branching ratios between these four dication states are displayed in Table III. These branching ratios are approximated by simultaneously fitting each feature in Fig. 2 with a 2-D Gaussian distribution (although the distributions may not be explicitly Gaussians, this is nonetheless a good approximation). The fitting procedure varied the widths along each dimension independently, while also including a varying constant background offset. Following this fitting procedure, we integrate the fit for each feature individually to estimate its contribution to the total $H^+ + H^+$ yield. The main contribution to the uncertainty of the branching ratio is rooted in the aforementioned electron pair deadtime, which influences the detection yield of the electron-ion coincidences for each dication state as a function of the electron sum energy. Applying the simulation mentioned above, we estimate the total

| State | Photoelectron Energy Sum (eV) | | KER (eV) | |
|---|---|---|---|---|
| | Experiment (FWHM) | Theory (FWHM) | Experiment (FWHM) | Theory* (FWHM) |
| $(1e^{-2})^3A_2$ (cyan) | 17.6 (2.4) | 18.1 (2.2) | 5.5 (2.0) | 7.7 (2.2) |
| $(1e^{-2})^1E$ (magenta) | 16.7 (4.2) | 16.8 (3.1) | 7.7 (3.0) | 9.4 (3.1) |
| $(1e^{-2})^1A_1$ (green) | 14.1 (2.1) | 14.8 (1.9) | 5.9 (2.2) | 8.2 (1.9) |
| $(2a_1^{-1},3a_1^{-1})^1A_1$ (red) | 7.3 (6.2) | 7.8 (5.1) | 12.7 (6.1) | 15.2 (5.1) |

TABLE II. The measured and calculated photoelectron energy sum and KER centroids for each of the four identified features from $H^+ + H^+$ fragmentation following PDI of $NH_3$ at 61.5 eV. The asterisk marking the theoretical KER values indicates that these are calculated assuming ro-vibrational ground state fragments, i.e. assuming maximum KER with no energy channeled into internal excitations. The theoretical KER values are all roughly 2 eV higher than the measured values, which is consistent with the dissociation producing fragments possessing approximately 2 eV of ro-vibrational energy (as explained in the text).

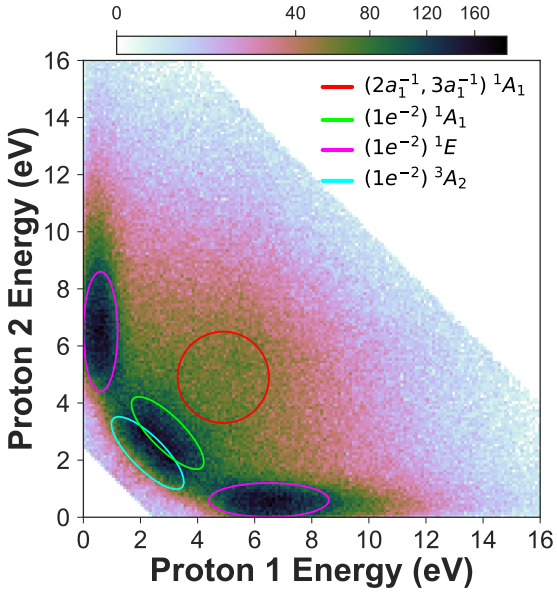


FIG. 5. Proton-proton energy correlation map for the $H^+ + H^+$ fragmentation channels of the valence PDI of $NH_3$. The four identified dication states are color-coded and indicated by ellipses to guide the eye.

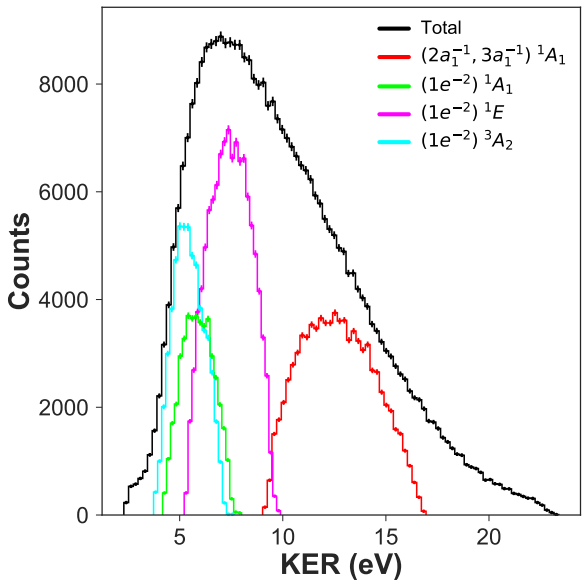


FIG. 6. The yield of $H^+ + H^+$ fragmentation channel of the valence PDI of $NH_3$ as a function of KER, shown for the total yield (black), as well as for the four color-coded features corresponding to the identified relevant dication states. The KER distributions for the four features have been scaled by a factor of five, for better visibility.

possible loss in PDI yield for electron sum energies of 7.3 eV ($(2a_1^{-1}, 3a_1^{-1})\ ^1A_1$), 14.1 eV ($(1e^{-2})\ ^1A_1$), 16.7 eV ($(1e^{-2})\ ^1E$), and 17.6 eV ($(1e^{-2})\ ^3A_2$) to be 27.2%, 10%, 8.1%, and 7.5%, respectively. This translates to an error of up to 5% in the branching ratio. Errors due to deviations from the assumed Gaussian shape of each feature in the fitting process and the quality of the fit are estimated to be small (<1% and <0.3%, respectively).

Last, we plot the $H^+ + H^+$ yield as a function of the energy at the adiabatic limit $E_{inf}$ and the energy above the double ionization threshold $E_i$. This plot is shown in Fig. 7, with $E_i = \hbar\omega - DIP - (E_{e_1} + E_{e_2})$ and $E_{inf} = \hbar\omega - DIP - (E_{e_1} + E_{e_2} + KER)$, where DIP is the Double Ionization Potential. As a guide to the eye, each of the four identified features have been indicated by ellipses. This plot indicates for each state and its dissociative limit where the $NH_3^{++}$ is excited to upon PDI, relative to the dication ground state. The circled features can be directly compared with the calculated vertical energy and adiabatic energy values shown in Table I, which

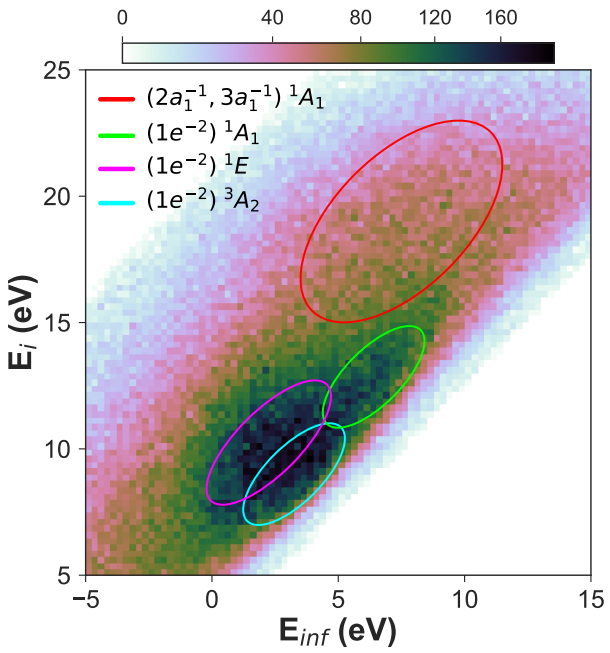


FIG. 7. The PDI yield of $NH_3$ at 61.5 eV as a function of the energy above the double ionization threshold at the adiabatic limit following dissociation, $E_{inf}$, and the energy above the double ionization threshold, $E_i$, for each of the four identified relevant dication states from the $H^+ + H^+$ fragmentation channel. The four identified dication states are color-coded and indicated by ellipses to guide the eye.

| State | Branching Ratio |
|---|---|
| $(2a_1^{-1}, 3a_1^{-1})\ ^1A_1$ | 14.6% |
| $(1e^{-2})\ ^1A_1$ | 4.5% |
| $(1e^{-2})\ ^1E$ | 18.1% |
| $(1e^{-2})\ ^3A_2$ | 62.8% |

TABLE III. The branching ratios for the four dication states contributing to the $H^+ + H^+$ dissociation channel following PDI of $NH_3$ at 61.5 eV. The errors on these fractions are estimated to be up to 5% (see text).

show good agreement with our theoretical results. As mentioned above, the measured energies $E_{inf}$ are each approximately 2 eV higher than what is theoretically predicted for rotationally and vibrationally cold fragments, whereas the molecular fragments in the experiment can carry away this amount of energy internally, as we think is plausible from our analysis presented in section IV B.

### B. Photodissociation dynamics: distinguishing concerted and sequential fragmentation

To examine the connection between the measured KER and the molecular geometry in each dication electronic state, we plot the yield as a function of cosine of the measured angle between the momenta of the two protons, $\cos\theta_{p_1,p_2} = \boldsymbol{p_1}\cdot\boldsymbol{p_2}/|\boldsymbol{p_1}||\boldsymbol{p_2}|$, and the KER, as shown in Fig. 8. It should be mentioned that due to the Coulomb repulsion between the two photoions, the measured proton-proton angle is an asymptotic dissociation angle, hence its value will be slightly larger than the true angle at which the fragmentation transpires. Although we do not have an exact estimate of how significantly the asymptotic dissociation angles differ from the true bond angles, our analysis carries useful information that differentiates the dissociation dynamics for each of the four features. In Fig. 8, the neutral ground state geometry of $NH_3$ (specifically the H-N-H bond angle) is indicated by the vertical black dashed line. First, we point out that of the four dication states three - the $(2a_1^{-1}3a_1^{-1})\ ^1A_1$, $(1e^{-2})\ ^1A_1$, and $(1e^{-2})\ ^3A_2$ states - exhibit decreasing KER with increasing measured dissociation angle between the protons, as seen in Fig. 8. Qualitatively, if the angle between the two protons increases due to nuclear motion in the dication, e.g. the $NH_3$ umbrella opening, their separation increases and their Coulomb repulsion correspondingly decreases, resulting in the negative bivariate correlation between the KER and the proton-proton angle, $\theta_{p_1,p_2}$. Although this type of nuclear motion was not addressed in our calculations (which kept bond angles frozen), we still bring forward this qualitative picture as a possible explanation for the observed correlation. This also gives further support to the notion that these three dication states dissociate via a concerted mechanism, where the two protons are simultaneously eliminated from the dication.

We also point out that the features associated with the $(2a_1^{-1}, 3a_1^{-1})\ ^1A_1$ state and the $(1e^{-2})\ ^1A_1$ state dissociate at angles closer to the neutral ground state geometry of the $NH_3$ molecule (H-N-H bond angle $\sim 107°$) than the feature associated with the $(1e^{-2})\ ^3A_2$ state, which tends to fragment at angles approaching 180°. Although the distributions for the $(1e^{-2})\ ^1A_1$ and $(1e^{-2})\ ^3A_2$ states appear similar in shape, each state's fragmentation dynamics can be distinguished as different by the location of their respective peaks in the measured proton-proton angle. This suggests that the $(2a_1^{-1}, 3a_1^{-1})\ ^1A_1$ and

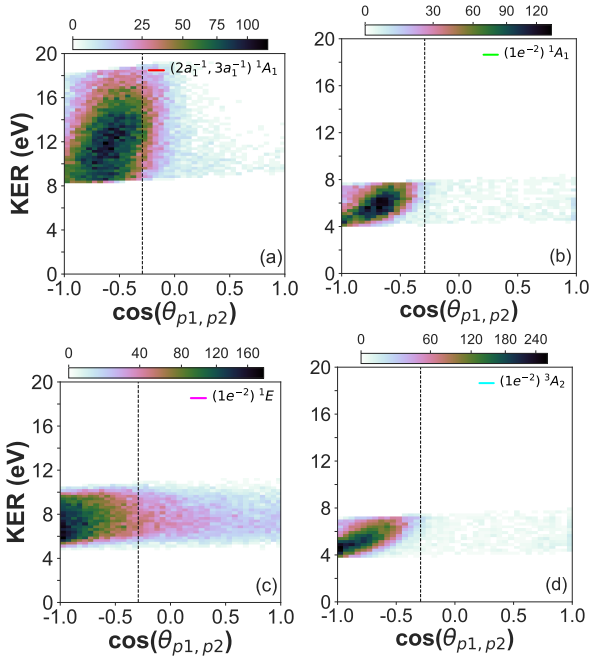


FIG. 8. The PDI yield of $NH_3$ as a function of cosine of the measured proton-proton angle, $\cos\theta_{p_1,p_2}$, and KER for each of the four dication states from the $H^+ + H^+$ fragmentation channel at 61.5 eV. The dashed black vertical line indicates the neutral ground state H-N-H angle.

the $(1e^{-2})$ $^1A_1$ states exhibit prompt fragmentation, while the molecular structure in the $(1e^{-2})$ $^3A_2$ state evolves further away from the neutral configuration, driven towards larger bond angles between the two protons, prior to dissociation. This is indeed consistent with the asymptotic charge exchange mechanism, described in Section III, that couples the $^3A_2$ ($^3A''$) and $^3E$ ($^3A''$) states (PES cuts inset in Fig. 1(b)). The dissociation on the $(2a_1^{-1}, 3a_1^{-1})$ $^1A_1$ and $(1e^{-2})$ $^1A_1$ states result in the direct elimination of two protons, which are light and depart fast, providing little time for the molecular structure to evolve away from the neutral equilibrium geometry during the fragmentation. In contrast, the fragmentation on the $(1e^{-2})$ $^3A_2$ state initially involves a heavier $NH^+$ ion preceding the charge exchange mechanism that produces a light proton. Thus the initial dissociation on the $(1e^{-2})$ $^3A_2$ state (prior to the charge exchange) is slower due to the increased mass of one of the charged fragments.

Although our calculations keep the bond angles frozen, it is known that for molecules of the form $AH_3$, ionization from the $1e$ orbital (as in the case of the $(1e^{-2})$ $^3A_2$ state) drives the molecule towards a planar configuration, i.e. larger H-N-H bond angles (this can be seen in a Walsh diagram, see Ref. [38]). The increased fragmentation time leads to an increased likelihood for processes such as the aforementioned charge exchange to take place, as well as more time for the molecular geometry to evolve away from the neutral equilibrium geometry towards larger H-N-H angles, preceding the dissociation. The timescale for a wave packet in the $(1e^{-2})$ $^3A_2$ state to reach the geometry where charge exchange can occur, as well as other details of the dissociation dynamics, precisely explaining the propensity towards fragmentation at H-N-H angles approaching 180° (beyond our qualitative description), would need to be addressed in a future study requiring time-dependent calculations that include non-adiabatic coupling.

In contrast to the three states in Fig. 8 discussed above, the $(1e^{-2})$ $^1E$ state in Fig. 8 (c) displays a band of KER over a wide distribution of $\theta_{p_1,p_2}$ extending all the from zero to 180° and smoothly peaked towards 180°. This distribution is consistent with the sequential dissociation mechanism discussed below in detail, namely $NH_3^{++} \rightarrow NH^+ + H^+ + H \rightarrow N + 2H^+ + H$. If prior to the second step of this process the $NH^+$ fragment rotates freely before dissociating via a crossing with another electronic state, the $H^+$ is ejected in a random direction in the body frame of the $NH^+$ molecule. However that is not a random direction in the laboratory frame because the $NH^+$ fragment is translating with a center of mass momentum opposite to the sum of the momenta of the H and $H^+$ atoms produced in the first step, presumably ejected near the directions of the original NH bonds. The diatom's center of mass is therefore moving away from the $H^+$ ion produced in the first step, and consequently the random angular distribution of the proton ejected from the moving $NH^+$ shifted in the direction opposite the direction of the first $H^+$ ion. A similar effect has been seen in dissociation of the water dication following one-photon double ionization, in which a sequential dissociation channel involving dissociation of $OH^+$ is seen [39, 40].

Other evidence also suggests that the different fragmentation dynamics of the $(1e^{-2})$ $^1E$ state can be specifically attributed to a sequential dissociation mechanism involving four bodies in the final set of fragments. Here, we do not consider the possibility of a sequential dissociation process first resulting in $NH_2^+ + H^+$ fragmentation, with the $NH_2^+$ subsequently dissociating to $NH + H^+$ or $N + H + H^+$.

Our interpretation does not include these channels, as we have analyzed the $NH_2^+ + H^+$ dissociation channel (which is the subject of a future paper) and did not observe any electron-ion momentum correlation consistent with shared dication electronic states producing both $NH + H^+ + H^+$ or $NH_2^+ + H^+$ fragments. However, we cannot totally rule out these possibilities, as the lifetime of the intermediate $NH_2^+$ fragment may be too short for these fragments to survive the flight time to the ion detector. However, if intermediate $NH_2^+$ fragments dissociate during their flight to the detector, the secondary ion momenta should exhibit a broad spread in momentum. Since this is not observed, we argue in favor of a different sequential dissociation mechanism.

Previous measurements have found that PDI to the $(1e^{-2})$ $^1$E state produces the fragments $NH^+ + H^+ + H$, where the bound $NH^+$ ion is in its ground state, i.e. the X $^2\Pi$ state [15]. Although the dissociative limit of the $NH^+$ $^2\Pi$ state results in $N^+(^3P) + H(^2S)$ fragmentation, it has been shown that the X $^2\Pi$ state crosses the a $^4\Sigma^-$ state in the FC region and that population transfer between the X and a states can occur via spin-orbit coupling [41–45]. As seen in Fig. 9, the $NH^+$ a $^4\Sigma^-$ state dissociates to $H^+ + N(^4S)$ with a dissociation energy that is roughly 1 eV smaller than the X $^2\Pi$ state dissociation energy. Thus, high-lying vibrational states of the $NH^+$ fragment that are initially bound in the X $^2\Pi$ state can undergo intersystem crossing to the a $^4\Sigma^-$ state, yielding the final fragments of the reaction $NH_3^{++} \rightarrow N(^4S) + H(^2S) + H^+ + H^+$. In the present context, population transfer can occur along the inner wall of the quasi-degenerate $NH^+$ states when the initial breakup of the $(1e^{-2})$ $^1$E state produces $NH^+(^2\Pi)$ ions with internal energy that lies within the *appearance window* shown in Fig. 9. We can estimate the location of the four-body limit by first extrapolating the MRCI energy for the $^3$E state (Fig. 1 blue curve) to infinite separation of the N-H bonds. This places the $NH^+(^4\Sigma^-) + H + H^+$ limit at 0.63 eV. Adding to this the 3.66 eV dissociation energy of $NH^+(^4\Sigma^-)$ places the four-body limit at 4.29 eV, directly in the center of the *appearance window*. This four-body breakup mechanism also explains why the theoretical KER value of 9.42 eV gleaned from Table I is higher than the measured value of 7.7 eV. From Fig. 9 we see that the $NH^+$ fragment must have a minimum internal energy of 3.7 eV to dissociate to $N + H^+$ at the lower end of the appearance window to produce a fast proton with (9.42–3.7 eV) = 5.72 eV and a zero energy proton. At the upper end of the *appearance window* we get a fast proton with (9.42–4.5 eV) = 4.92 eV and a slow proton with 1 eV. This interpretation appears to be consistent with the measured particle energy balance and prompts us to believe that each NH fragment in the three concerted dissociation channels was produced with a distribution of ro-vibrational energy around 2 eV, while the $NH^+$ fragment in the sequential dissociation channel was produced with a distribution of ro-vibrational energy that extends well beyond 3.7 eV, enabling the second fragmentation step. These results are also consistent with a previous theoretical treatment of the dissociation of $H_2O^{++}$ [46], where the internal energy distribution of the $OH^+$ fragment in the $H^+ + OH^+$ two-body dissociation channel was observed to span approximately 3–5 eV.

Although the initial set of photoions produced via excitation to the $(1e^{-2})$ $^1E$ state would not produce the four-particle (two-electron, two-proton) coincidence we measure, highly vibrationally excited ground state $NH^+$ fragments (lying within the *appearance window*) can spin-orbit couple to a state where a fragmentation, producing a second proton, is possible, yielding the necessary two-proton coincidence. Since the spin-orbit coupling is weak, and the ensuing dissociation is not instantaneous, the intermediate $NH^+$ fragment can rotate prior to coupling to the dissociative state, which results in a proton-proton angular distribution that differs from the other three dication states that involve fewer fragmentation steps. The lifetime of the excited intermediates in the *appearance window* in the $X(^2\Pi)$ state is determined by the strength of the spin-orbit coupling but not deduced in our experiment. It could potentially be measured using a different detection scheme or calculated using a different theoretical approach than the one taken in this study.

We discuss the cases of excitations below and above the *appearance window* next. Excitations initially prepared in the $X^2\Pi$ state that lie above the *appearance window* directly dissociate to produce $N^+(^3P) + H^+ + H(^2S) + H(^2S)$. Indeed, this is supported by our measurements by analyzing the $N^+ + H^+$ dissociation channel, which is briefly addressed here. The same procedure used to select the $H^+ + H^+$ dissociation channel and described at the beginning of this sub-section is used to select the $N^+ + H^+$ channel. We plot the PDI yield of the $N^+ + H^+$ fragmentation as a function of the photoelectron energy sum and photoion energy sum, shown in Fig. 10. In this fragmentation channel we observe a single

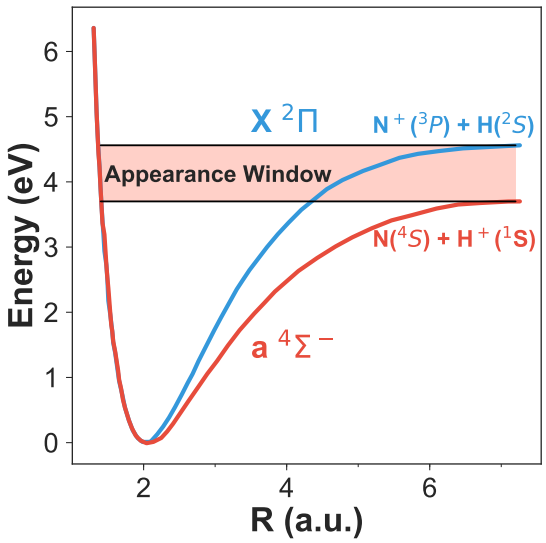


FIG. 9. The potential energy curves for the $X^2\Pi$ ground state and the $a^4\Sigma^-$ state of $NH^+$, extracted from Ref. [42]. Population transfer may occur between these states via spin-orbit coupling, where initially bound excitations on the $X^2\Pi$ state can dissociate on the $a^4\Sigma^-$ state. Only diatomic $NH^+$ fragments with internal energy within (or above) the *appearance window* will dissociate.

feature (seen in Fig. 10), which we attribute to a single contributing dication electronic state. We argue that this feature corresponds with the magenta color-coded $(1e^{-2})$ $^1$E state. This feature possesses an electron energy sum of 16.7 eV, which exactly coincides with the electron energy sum measured for the feature in the $H^+ + H^+$ dissociation channel corresponding with the $(1e^{-2})$ $^1$E state. From this evidence we suggest that the single feature observed in the $N^+ + H^+$ channel corresponds with the same dication electronic state that contributes to the sequential $H^+ + H^+$ dissociation mechanism. Comparing the $H^+ + H^+$ and $N^+ + H^+$ yields following PDI to the $(1e^{-2})$ $^1$E state indicates that roughly the same amount of population ends up above the *appearance window* as compared to within it. As for excitations initially prepared in the X $^2\Pi$ state that lie below the *appearance window*, these will remain as bound $NH^+$ fragments. This is also supported by our measurements by analyzing the $NH^+ + H^+$ dissociation channel (which is the topic of a future paper and thus not presented here). In this dissociation channel we also identify a feature corresponding with the $(1e^{-2})$ $^1$E state. These results are entirely consistent with the explanation presented in the paragraph above, where the PDI to the $(1e^{-2})$ $^1$E state produces the fragments $NH^+$ $^2\Pi$ + $H^+$ + H for which the excitation in the $NH^+$ ion can lie below, within, or above the *appearance window*. All three of these cases are observed in our measurement and illustrate the various levels of complexity in the dissocation dynamics of simple polyatomic molecules that can occur following valence PDI to just a single state.

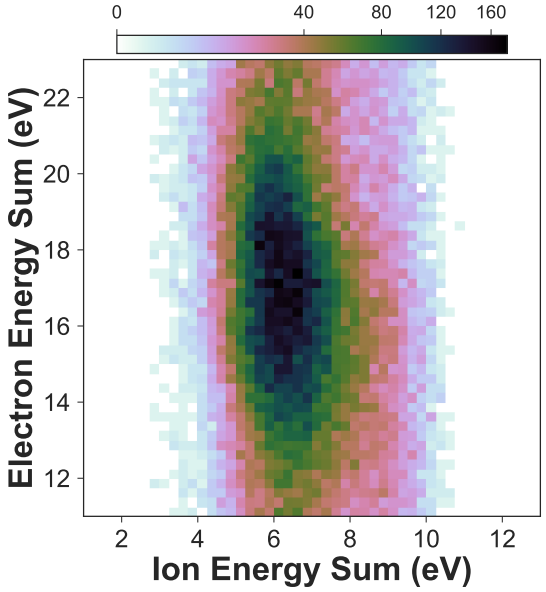


FIG. 10. The yield of $N^+ + H^+$ after valence PDI of $NH_3$ as a function of photoelectron pair energy sum and photoion pair energy sum for the $(1e^{-2})$ $^1$E dication state.

To further support the claim that the $H^+ + H^+$ fragmentation on the $(1e^{-2})$ $^1$E state occurs via the four-body mechanism discussed above, we analyze the slow proton emerging from the dissociation on the $(1e^{-2})$ $^1$E state, using its momentum to infer the KER of the dissociation of the $NH^+$ fragment, shown in Fig. 11. Since two neutral particles are left undetected (N and H), and simple conservation of momentum can thus not be applied, this is realized by assuming that the momentum of the undetected neutral N atom is approximately that of the N-H center of mass, inferred from the two proton momenta. We find the inferred KER to peak at 0.61 eV (FWHM 0.71 eV), which lies below the ~1 eV maximum KER permitted by the locations of the two adiabatic limits of the $X^2\Pi$ and $a^4\Sigma^-$ states,

i.e. the *appearance window* (see Fig. 9). This supports the assumption that the slow proton emerges from a dissociation on the $a^4\Sigma^-$ state. Since our measurement also indicates that the $(1e^{-2})$ $^1$E state contributes to the $NH^+ + H^+ + H$ fragmentation channel (the topic of another manuscript, currently in preparation), which is in agreement with previous measurements [15], we believe that some small fraction of the $NH^+$ fragments of this three-body fragmentation channel can decay through intersystem crossing and feed into the four-body $N + H + H^+ + H^+$ fragmentation channel. This conclusion is also corroborated by our analysis of the $N^+ + H^+$ dissociation channel, which shows that the $(1e^{-2})$ $^1$E state also feeds into this four-body fragmentation channel and corresponds with the initial excitations in the $NH^+$ $^2\Pi$ ion that lie above the *appearance window*.

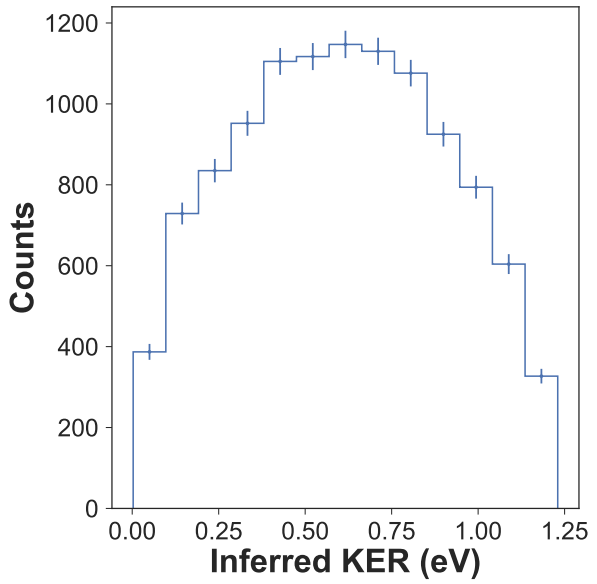


FIG. 11. The inferred KER from the dissociation of the $NH^+$ fragment, involving the measured slow proton and the nitrogen following PDI of $NH_3$ at 61.5 eV to the $(1e^{-2})$ $^1$E state, resulting in the four-body fragmentation $N + H + H^+ + H^+$. The KER peaks at 0.61 eV, with a FWHM of 0.71 eV.

### C. Photoelectron dynamics

Next, we display in Fig. 12 the photoelectron energy sharing distributions for the four dication states. We define the electron energy sharing as:

$$\rho = \frac{E_{e_1}}{E_{e_1} + E_{e_2}}, \tag{1}$$

where $E_{e_1}$ and $E_{e_2}$ are the energies of electron 1 and 2, respectively. Values of $\rho$ near 0.5 indicate equal energy sharing between the two photoelectrons, while values near 0 or 1 indicate unequal energy sharing between the two photoelectrons. In all four dication states we do not observe a strong enhancement in yield for any particular values of $\rho$. The distributions are nearly flat. In the absence of autoionization, this is similar to the PDI of atoms and molecules in this excess energy range (see e.g. [47, 48]). The exception is the $(1e^{-2})$ $^3A_2$ state (cyan) and perhaps the $(1e^{-2})$ $^1$E state (magenta), which show some propensity towards increased yield at values of $\rho$ near 0.5. This is surprising since the $(1e^{-2})$ $^3A_2$ and the $(1e^{-2})$ $^1$E state dication states correspond to the highest electron sum energies (see Fig. 3). A maximum PDI yield at equal energy sharing, if any, would be expected for the lowest electron sum energies according the the Wannier threshold law [49], which favors the emission of two electrons with the same energy and back-to-back close to the PDI threshold. However, the electron pair emission patterns are subject to selection rules that are specific to each dication state and the molecular orientation with respect to the polarization vector; they inherently influence the electron energy sharing to a certain degree. The detailed investigation of this complex problem requires M/RFPADs and is beyond the scope of this work. These distributions have all been normalized to the same value and have been placed in ascending order, based on the corresponding photoelectron energy of the state (the state with the lowest photoelectron energy sum is placed near the bottom and the state with the highest photoelectron energy sum is placed at the top).

Lastly, we plot in Fig. 13 the yield of the $H^+ + H^+$ fragmentation as a function of cosine of the relative emission angle between the two photoelectrons and in different energy sharing conditions of the electron pair for the four dication states, integrated over all molecular orientations relative to the polarization vector of the incoming light and with no restrictions on the emission direction of either electron. The relative electron-electron angles are plotted for $0.425 < \rho < 0.575$ (shown in red) and for $\rho < 0.05$ or $\rho > 0.95$ (shown in blue). We point out that our measurement suffers from some multi-hit detector dead-time effects, which influence the measured

yields of the photoelectrons emitted in the same direction with similar kinetic energies. For equal energy sharing between the two emitted electrons and for $\theta_{e_1,e_2} \leq 90°$ (emission into the same hemisphere), we can expect to fail to detect up to $\sim 52\%$ events for the $(1e^{-2})\ ^3A_2$ state, $\sim 27\%$ for the $(1e^{-2})\ ^1E$ state, $\sim 23\%$ for the $(1e^{-2})\ ^1A_1$ state, and $\sim 22\%$ for the $(2a_1^{-1}, 3a_1^{-1})\ ^1A_1$ state. Note that we estimate these losses for the "worst case" isotropic relative electron-electron emission, which very well represents autoionization processes that are sequential in nature and are subject to unequal energy sharing between the electrons. The equal energy sharing case on the other hand is dominated by knock-out processes with very few electron pairs emitted into the same hemisphere. The actual losses are expected to be closer to the losses for the case of unequal electron energy sharing reported below.

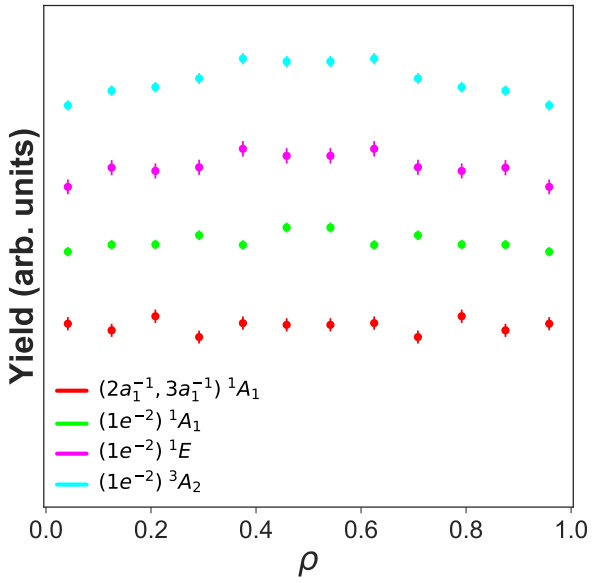


FIG. 12. The yield of the $H^+ + H^+$ fragmentation after PDI of $NH_3$ at 61.5 eV as a function of photoelectron energy sharing for each of the four relevant dication states. Here the y-axis indicates the PDI yield in arbitrary units on a linear scale. The distributions are not internormalized. They have been staggered in order based on their respective electron energy sum for better visibility (i.e. the states are placed in ascending order with respect to their respective photoelectron energy sum).

The relative angles between the two photoelectrons under unequal energy sharing conditions (blue circles in Fig. 13) are rather isotropic for all four

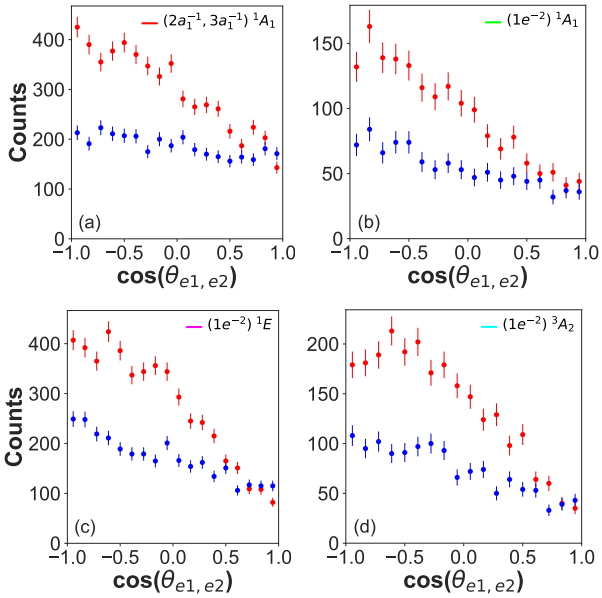


FIG. 13. The cosine of the relative emission angle between the two photoelectrons for two different energy sharing conditions for each of the four dication states of $NH_3$ following PDI at 61.5 eV. Electron energy sharing between 0.425 and 0.575 is shown in red, and energy sharing less than 0.05 or greater than 0.95 is shown in blue.

dication states, where there is a slight propensity towards back-to-back emission (or in other words a lack of events with electrons emitted into the same direction), which we partly attribute to the dead-time problem at relative electron-electrons angles below 90° (emission into the same hemisphere). The simulated losses of events with unequal energy sharing amount to $\sim 26.1\%$ for the $(1e^{-2})\ ^3A_2$ state, $\sim 8.4\%$ for the $(1e^{-2})\ ^1E$ state, $\sim 5.2\%$ for the $(1e^{-2})\ ^1A_1$ state, and $\sim 4.2\%$ for the $(2a_1^{-1}, 3a_1^{-1})\ ^1A_1$ state. Evidently the small anisotropies in the relative angular distributions for the unequal electron energy sharing case (blue), presented in Fig. 13 for all four dication states, are accounted for by the detector dead-time limitations, and are otherwise consistent with isotropic relative angular distributions. As there is no hint for autoionzation visible in the electron-electron energy correlation map depicted in Fig. 4, the unequal electron energy sharing case is likely dominated by knock-out processes, as reasoned below.

In contrast, the photoelectron dynamics for equal energy sharing conditions (red in Fig. 13) reveals

anisotropic angular distributions that are different for all four dication states and exceed the anisotropy expected from dead-time effects alone. For this case the relative angle between the two photoelectrons producing the $(2a_1^{-1}, 3a_1^{-1})$ $^1A_1$ state exhibits a preference towards back-to-back emission. The emission angle between the two photoelectons from the $(1e^{-2})$ $^3A_2$ state increases starting at 0° and peaks at an angle of roughly 125° before decreasing as the angle approaches 180°. The photoelectrons that produce the $(1e^{-2})$ $^1E$ state have relative emission angles that increase starting at 0°, which then begin to level out at 100°, increasing at a slower rate as the angle approaches 180°. Last, the relative electron-electron emission angle of the $(1e^{-2})$ $^1A_1$ state increases starting at 0° and peaks at an angle of roughly 150° before decreasing as the angle approaches 180°. All four dication states show a non-vanishing PDI yield for small electron-electron angles close to 0°. This contribution is mainly due to the finite angular bin size accepting differences in the relative emission angles of up to 27° at these values, as well as residual background from random coincidences underneath the features visible in e.g. Fig. 2.

These trends in the relative electron-electron angular distributions as a function of the electron energy sharing possess similarities to prior observations made in the PDI of atomic and molecular targets [6, 50–52]. In the valence PDI experiments for helium [50], which is dominated by knock-out processes, rich photoelectron angular distributions emerge due to selection rules and symmetry considerations. It has been seen that for equal energy sharing conditions and the first detected electron fixed along the polarization vector of the ionizing field, the relative emission angle between the photoelectrons can be quite anisotropic and peaked at angles between 90° and 180° due to selection rules for dipole allowed transitions, whereas in unequal energy sharing conditions, the relative angle between the electrons can become more isotropic with a smaller peak at 180°. In the atomic case for equal electron energy sharing, there can be a node at a relative electron-electron angle of 180°, regardless of the emission direction of either of the two electrons. This is for instance true for the PDI of He and is due to a selection rule based on parity conservation in one photon transitions. Such a scenario is in general not well pronounced in the PDI of (polyatomic) molecules, and rather resembles the distributions for all cases presented in Fig. 13. In addition to the finite angular bin size, again accepting differences in the relative emission angles of up to 27° at 180°, we attribute this to the fact that we have not enforced any conditions on the molecular orientation or direction of the polarization vector of the XUV field. Integrating over all molecular orientations and the direction of the polarization vector is prone to wash out sharp features in the electron relative angular distribution, since angular momentum can be transferred to the nuclear systems and softens the aforementioned selection rules (as seen and discussed in Refs. [6, 7]), in addition to other features. The limited number of events in the present data set does not allow conditions to be enforced on the molecular orientation or emission direction of one of the photoelectrons with high statistical significance. Future COLTRIMS studies could be directed towards the states that obey the axial recoil approximation to gather appreciable statistics, in order to produce photoelectron angular distributions in the molecular frame, which inter alia would help to study and understand the role of selection rules in the PDI of a symmetric top molecule with respect to the polarization vector of the incoming light.

## V. CONCLUSION

We have performed state-selective measurements on the $H^+ + H^+$ dissociation channel of $NH_3$ following direct valence PDI at 61.5 eV, where the two photoelectrons and two protons were measured in coincidence on an event-by-event basis using COLTRIMS. With the assistance of theoretical MRCI calculations of dication PES cuts, we identified the four participating dication electronic states that lead to $H^+ + H^+$ fragmentation, which correspond with the four features we observed and have estimated their branching ratios.

The PDI yield as a function of KER and the measured proton-proton angle indicates that three of the four dication states dissociate in a concerted mechanism, while the fourth state, the $(1e^{-2})$ $^1E$ state, dissociates via a sequential process, with the intermediate ro-vibrationally excited $NH^+$ fragment ion decaying through an intersystem crossing that leads to a four-body breakup. Two of the dication states, the $(2a_1^{-1}, 3a_1^{-1})$ $^1A_1$ and $(1e^{-2})$ $^1A_1$ states, exhibit concerted dissociation mechanisms that fragment near the ground state geometry (axial recoil approximation applies). The third state, the $(1e^{-2})$ $^3A_2$ state, undergoes appreciable evolution in

its molecular geometry and an asymptotic electron transfer from H to $NH^+$ at distances greater than 18 Bohr in the dissociating dication, preceding the three-body breakup. Differences between the MRCI calculations and the measured KER suggest that the neutral NH fragment in each of the three-body dissociation channels is highly ro-vibrationally excited.

The relative emission angle between the two photoelectrons as a function of their energy sharing has some resemblance to prior measurements made on atomic and molecular targets, in spite of integrating over all molecular orientations and emission angles of the first photoelectron, relative to the XUV polarization. While the present study has focused on PDI processes that result in proton-proton breakup channels, we are presently analyzing the two- and three-body PDI breakup channels that produce $NH_2^+$ + $H^+$ and $NH^+$ + H + $H^+$, which is the topic of a future manuscript.

## VI. ACKNOWLEDGMENTS

Work at LBNL was performed under the auspices of the US Department of Energy (DOE) under Contract DE-AC02-05CH11231, using the Advanced Light Source and National Energy Research Computing Center, and was supported by the U.S. DOE Office of Basic Energy Sciences, Division of Chemical Sciences. JRML personnel were supported by the same US DOE funding source under Award No. DE-FG02-86ER13491. A.G. was supported by the ALS through a Doctoral Fellowship in Residence. Personnel from the University of Nevada, Reno was supported by the National Science Foundation Grant No. NSF-PHY-1807017. The Frankfurt group acknowledges the support of the Deutsche Akademische Austausch Dienst (DAAD) and the Deutsche Forschungsgemeinschaft (DFG). We thank the staff at the Advanced Light Source for operating the beamline and providing the photon beam. Moreover, we thank the RoentDek GmBH for long-time support with detector hardware and software.

[1] P. Lablanquie, J. Delwiche, M.-J. Hubin-Franskin, I. Nenner, P. Morin, K. Ito, J. H. D. Eland, J.-M. Robbe, G. Gandara, J. Fournier, and P. G. Fournier, Phys. Rev. A **40**, 5673 (1989).

[2] H. Sann, T. Jahnke, T. Havermeier, K. Kreidi, C. Stuck, M. Meckel, M. S. Schöffler, N. Neumann, R. Wallauer, S. Voss, A. Czasch, O. Jagutzki, T. Weber, H. Schmidt-Böcking, S. Miyabe, D. J. Haxton, A. E. Orel, T. N. Rescigno, and R. Dörner, Phys. Rev. Lett. **106**, 133001 (2011).

[3] V. Mergel, M. Achler, R. Dörner, K. Khayyat, T. Kambara, Y. Awaya, V. Zoran, B. Nyström, L. Spielberger, J. H. McGuire, J. Feagin, J. Berakdar, Y. Azuma, and H. Schmidt-Böcking, Phys. Rev. Lett. **80**, 5301 (1998).

[4] C. W. McCurdy, D. A. Horner, T. N. Rescigno, and F. Martín, Phys. Rev. A **69**, 032707 (2004).

[5] F. L. Yip, T. N. Rescigno, C. W. McCurdy, and F. Martín, Phys. Rev. Lett. **110**, 173001 (2013).

[6] T. Weber, A. Czasch, O. Jagutzki, A. Müller, V. Mergel, A. Kheifets, J. Feagin, E. Rotenberg, G. Meigs, M. H. Prior, S. Daveau, A. L. Landers, C. L. Cocke, T. Osipov, H. Schmidt-Böcking, and R. Dörner, Phys. Rev. Lett. **92**, 163001 (2004).

[7] W. Vanroose, D. A. Horner, F. Martín, T. N. Rescigno, and C. W. McCurdy, Phys. Rev. A **74**, 052702 (2006).

[8] B. Gaire, S. Y. Lee, D. J. Haxton, P. M. Pelz, I. Bocharova, F. P. Sturm, N. Gehrken, M. Honig, M. Pitzer, D. Metz, H.-K. Kim, M. Schöffler, R. Dörner, H. Gassert, S. Zeller, J. Voigtsberger, W. Cao, M. Zohrabi, J. Williams, A. Gatton, D. Reedy, C. Nook, T. Müller, A. L. Landers, C. L. Cocke, I. Ben-Itzhak, T. Jahnke, A. Belkacem, and T. Weber, Phys. Rev. A **89**, 013403 (2014).

[9] J. Rajput, T. Severt, B. Berry, B. Jochim, P. Feizollah, B. Kaderiya, M. Zohrabi, U. Ablikim, F. Ziaee, K. Raju P., D. Rolles, A. Rudenko, K. D. Carnes, B. D. Esry, and I. Ben-Itzhak, Phys. Rev. Lett. **120**, 103001 (2018).

[10] R. N. Zare, Molecular Photochemistry **4**, 1 (1972).

[11] T. Weber, A. O. Czasch, O. Jagutzki, A. Müller, V. Mergel, A. Kheifets, E. Rotenberg, G. Meigs, M. H. Prior, S. Daveau, *et al.*, Nature **431**, 437 (2004).

[12] D. Akoury, K. Kreidi, T. Jahnke, T. Weber, A. Staudte, M. Schöffler, N. Neumann, J. Titze, L. P. H. Schmidt, A. Czasch, *et al.*, Science **318**, 949 (2007).

[13] T. J. Reddish, J. Colgan, P. Bolognesi, L. Avaldi, M. Gisselbrecht, M. Lavollée, M. S. Pindzola, and A. Huetz, Phys. Rev. Lett. **100**, 193001 (2008).

[14] D. Winkoun and G. Dujardin, "Zeitschrift für Physik D Atoms, Molecules and Clusters" **4**, 57 (1986).
[15] M. Stankiewicz, P. A. Hatherly, L. J. Frasinski, K. Codling, and D. M. P. Holland, Journal of Physics B: Atomic, Molecular and Optical Physics **22**, 21 (1989).
[16] R. Locht, M. Davister, W. Denzer, H. Jochims, and H. Baumgärtel, Chemical Physics **138**, 433 (1989).
[17] R. Locht and J. Momigny, Chemical Physics Letters **138**, 391 (1987).
[18] J. H. Eland, Chemical Physics **323**, 391 (2006).
[19] J. A. Samson, G. Haddad, and L. Kilcoyne, The Journal of chemical physics **87**, 6416 (1987).
[20] J. Appell and J. Horsley, The Journal of Chemical Physics **60**, 3445 (1974).
[21] T. Märk, F. Egger, and M. Cheret, The Journal of Chemical Physics **67**, 3795 (1977).
[22] M. Langford, F. Harris, P. Fournier, and J. Fournier, International journal of mass spectrometry and ion processes **116**, 53 (1992).
[23] W. Griffiths and F. Harris, Rapid Communications in Mass Spectrometry **4**, 366 (1990).
[24] R. Locht, C. Servais, M. Ligot, F. Derwa, and J. Momigny, Chemical physics **123**, 443 (1988).
[25] J. White, R. Rye, and J. Houston, Chemical Physics Letters **46**, 146 (1977).
[26] R. Camilloni, G. Stefani, and A. Giardini-Guidoni, Chemical Physics Letters **50**, 213 (1977).
[27] M. T. Økland, K. Fægri Jr, and R. Manne, Chemical Physics Letters **40**, 185 (1976).
[28] D. R. Jennison, Physical Review A **23**, 1215 (1981).
[29] R. Boyd, S. Singh, and J. Beynon, Chemical physics **100**, 297 (1985).
[30] R. Locht and J. Momigny, Chemical Physics Letters **138**, 391 (1987).
[31] R. Dörner, V. Mergel, O. Jagutzki, L. Spielberger, J. Ullrich, R. Moshammer, and H. Schmidt-Böcking, Physics Reports **330**, 95 (2000).
[32] J. Ullrich, R. Moshammer, A. Dorn, R. Dörner, L. P. H. Schmidt, and H. Schmidt-Böcking, Reports on Progress in Physics **66**, 1463 (2003).
[33] O. Jagutzki, A. Cerezo, A. Czasch, R. Dorner, M. Hattas, M. Huang, V. Mergel, U. Spillmann, K. Ullmann-Pfleger, T. Weber, *et al.*, IEEE Transactions on Nuclear Science **49**, 2477 (2002).
[34] S. A. Pope, I. H. Hillier, M. F. Guest, and J. Kendric, Chem. Phys. Lett. **95**, 247 (1983).
[35] F. Tarantelli, A. Tarantelli, A. Sgamellotti, J. Schirmer, and L. S. Cederbaum, Chem. Phys. Lett. **117**, 577 (1985).
[36] T. N. Rescigno, C. S. Trevisan, A. E. Orel, D. S. Slaughter, H. Adaniya, A. Belkacem, M. Weyland, A. Dorn, and C. W. McCurdy, Phys. Rev. A **93**, 052704 (2016).
[37] T. N. Rescigno and B. I. Schneider, J. Phys. B: At. Mol. Opt. Phys. **21**, L691 (1988).
[38] J. Higuchi, The Journal of Chemical Physics **24**, 535 (1956).
[39] Z. L. Streeter, F. L. Yip, R. R. Lucchese, B. Gervais, T. N. Rescigno, and C. W. McCurdy, Physical Review A **98**, 053429 (2018).
[40] I. Ben-Itzhak and T. Severt, private communication (2020).
[41] H. Liu and G. Verhaegen, The Journal of Chemical Physics **53**, 735 (1970).
[42] J. M . Amero, and G. J. Vázquez, International Journal of Quantum Chemistry **99**, 353 (2004); *ibid* **101**, 396 (2005).
[43] K. Kawaguchi and T. Amano, The Journal of chemical physics **88**, 4584 (1988).
[44] R. Colin and A. Douglas, Canadian Journal of Physics **46**, 61 (1968).
[45] R. Tarroni, P. Palmieri, A. Mitrushenkov, P. Tosi, and D. Bassi, The Journal of chemical physics **106**, 10265 (1997).
[46] B. Gervais, E. Giglio, L. Adoui, A. Cassimi, D. Duflot, and M. Galassi, The Journal of chemical physics **131**, 024302 (2009).
[47] J. Andersson, S. Zagorodskikh, A. H. Roos, O. Talaee, R. Squibb, D. Koulentianos, M. Wallner, V. Zhaunerchyk, R. Singh, J. Eland, *et al.*, Scientific Reports **9**, 1 (2019).
[48] D. Reedy, J. Williams, B. Gaire, A. Gatton, M. Weller, A. Menssen, T. Bauer, K. Henrichs, P. Burzynski, B. Berry, *et al.*, Physical Review A **98**, 053430 (2018).
[49] G. H. Wannier, Physical Review **90**, 817 (1953).
[50] H. Bräuning, R. Dörner, C. L. Cocke, M. H. Prior, B. Krässig, A. S. Kheifets, I. Bray, A. Bräuning-Demian, K. Carnes, S. Dreuil, V. Mergel, P. Richard, J. Ullrich, and H. Schmidt-Böcking, Journal of Physics B: Atomic, Molecular and Optical Physics **31**, 5149 (1998).
[51] A. Knapp, B. Krässig, A. Kheifets, I. Bray, T. Weber, A. L. Landers, S. Schössler, T. Jahnke, J. Nickles, S. Kammer, O. Jagutzki, L. P. H. Schmidt, M. Schöffler, T. Osipov, M. H. Prior, H. Schmidt-Böcking, C. L. Cocke, and R. Dörner, Journal of Physics B: Atomic, Molecular and Optical Physics **38**, 645 (2005).
[52] J. M. Randazzo, G. Turri, P. Bolognesi, J. Mathis, L. U. Ancarani, and L. Avaldi, Phys. Rev. A **101**, 033407 (2020).

# Mechanisms and dynamics of the $NH_2^+ + H^+$ and $NH^+ + H^+ + H$ fragmentation channels upon single-photon double ionization of $NH_3$

Kirk A. Larsen,[1,2,*] Thomas N. Rescigno,[2,†] Zachary L. Streeter,[2,3] Wael Iskandar,[2] Saijoscha Heck,[2,4,5] Averell Gatton,[2,6] Elio G. Champenois,[1,2] Travis Severt,[7] Richard Strom,[6] Bethany Jochim,[7] Dylan Reedy,[8] Demitri Call,[8] Robert Moshammer,[4] Reinhard Dörner,[5] Allen L. Landers,[6] Joshua B. Williams,[8] C. William McCurdy,[2,3] Robert R. Lucchese,[2] Itzik Ben-Itzhak,[7] Daniel S. Slaughter,[2] and Thorsten Weber[2,‡]

[1] *Graduate Group in Applied Science and Technology, University of California, Berkeley, CA 94720, USA*
[2] *Chemical Sciences Division, Lawrence Berkeley National Laboratory, Berkeley, CA 94720, USA*
[3] *Department of Chemistry, University of California, Davis, CA 95616, USA*
[4] *Max-Planck-Institut für Kernphysik, Saupfercheckweg 1, 69117 Heidelberg, Germany*
[5] *J.W. Goethe Universität, Institut für Kernphysik, Max-von-Laue-Str. 1, 60438 Frankfurt, Germany*
[6] *Department of Physics, Auburn University, Alabama 36849, USA*
[7] *J.R. Macdonald Laboratory, Physics Department, Kansas State University, Manhattan, Kansas 66506, USA*
[8] *Department of Physics, University of Nevada Reno, Reno, Nevada 89557, USA*

(Dated: August 18, 2021)

We present state-selective measurements on the $NH_2^+ + H^+$ and $NH^+ + H^+ + H$ dissociation channels following single-photon double ionization at 61.5 eV of neutral $NH_3$, where the two photoelectrons and two cations are measured in coincidence using 3-D momentum imaging. Three dication electronic states are identified to contribute to the $NH_2^+ + H^+$ dissociation channel, where the excitation in one of the three states undergoes intersystem crossing prior to dissociation, producing a cold $NH_2^+$ fragment. In contrast, the other two states directly dissociate, producing a ro-vibrationally excited $NH_2^+$ fragment with roughly 1 eV of internal energy. The $NH^+ + H^+ + H$ channel is fed by direct dissociation from three intermediate dication states, one of which is shared with the $NH_2^+ + H^+$ channel. We find evidence of autoionization contributing to each of the double ionization channels. The distributions of the relative emission angle between the two photoelectrons, as well as the relative angle between the recoil axis of the molecular breakup and the polarization vector of the ionizing field, are also presented to provide insight on both the photoionization and photodissociation mechanisms for the different dication states.

## I. INTRODUCTION

Molecular dissociation of polyatomic systems that follows single Photon Double Ionization (PDI) can involve an excitation to a given dication electronic state reaching its own respective adiabatic limit or undergoing non-adiabatic transitions between states preceding the fragmentation [1–3]. Non-adiabatic dynamics, e.g. ultrafast state coupling via Conical Intersections (CIs) in polyatomic molecules, occur often. CIs are degeneracies between Born-Oppenheimer Potential Energy Surfaces (PESs) that result in non-adiabatic transitions between excited states. They can be facilitated via (a) internal conversion, where two interacting hypersurfaces have the same multiplicity, or (b) intersystem crossing processes, where the multiplicity is different and spin-orbit coupling is required. Both flavors (a) and (b) represent a breakdown of the Born-Oppenheimer approximation [4]. CIs have been observed in numerous instances to significantly shape the molecular fragmentation processes occurring in the molecular dication, influencing the branching ratios, energy dispersion, breakup kinematics, and timescales [1–3]. However, identifying the flavor of the CI, i.e. distinguishing between type (a) and (b), by precisely tracing the electron and nuclear dynamics between the instant of PDI and when the dissociation has set in, is very challenging. This is because polyatomic molecules can break up in many different ways after PDI, and each reaction channel inherently carries different coupled rovibrational degrees of freedom that can be excited. Some of these non-adiabatic fragmentation dynamics leave their fingerprint in the energy or momentum domain of the

* klarsen@lbl.gov
† tnrescigno@lbl.gov
‡ tweber@lbl.gov

emitted particles, and they can be determined if the 3-D momenta of the photoelectron-pair and the recoiling fragments can be measured in coincidence to produce highly differential observables, which is the aim of this work. In this paper we report on the PDI of $NH_3$ and reveal the role and flavor of a non-adiabatic transition occurring in a select two-body breakup channel, while identifying the other two- and three-body breakup channels as direct, in a combined effort of experiment and theory.

The electronic states of $NH_3^{2+}$ and its dissociation channels have been studied in detail experimentally following PDI, electron impact double ionization, and double-charge-transfer spectroscopy, as well as theoretically [5–21]. These studies have largely focused on establishing the appearance energies of the various dissocation channels and the relative energies of the dication electronic states. Early experimental studies on the two-body $NH_2^+ + H^+$ dissociation channel in a narrow photon energy range near the PDI threshold revealed that intersystem crossing from the X $(3a_1^{-2})$ $^1A_1$ to the A $(3a_1^{-1}, 1e^{-1})$ $^3E$ state can facilitate fragmentation [21]. However, non-adiabatic effects have remained unobserved in any of the other fragmentation channels, whether near or well above the double ionization threshold. Additionally, to our knowledge, no study to date has examined the exact nature of the PDI mechanisms in $NH_3$ in detail, e.g. the level at which autoionization contributes to the PDI, if at all, or if the PDI is primarily based on an electron-electron knock-out process (so called Two-Step 1 interaction [22]).

In our recent study [23], hereafter referred to as [I], we reported the photoionization mechanisms and photodissociation dynamics of the $H^+ + H^+$ fragmentation channels of $NH_3^{2+}$ following PDI of neutral $NH_3$ molecules at 61.5 eV. In that study we observed non-adiabatic dynamics that enables both a sequential dissociation mechanism and a charge transfer process. In this report we extend our investigation to the $NH_2^+ + H^+$ and $NH^+ + H^+ + H$ dissociation channels of $NH_3^{2+}$ following PDI of $NH_3$ molecules at 61.5 eV, approximately 27 eV above the PDI threshold, where both the photoelectron- and cation-pair are measured in coincidence using charged particle 3-D momentum imaging.

## II. EXPERIMENT

Both the $NH_2^+ + H^+$ and $NH^+ + H^+ + H$ fragmentation channels of $NH_3^{2+}$ following PDI of neutral $NH_3$ molecules at 61.5 eV were investigated using COLd Target Recoil Ion Momentum Spectroscopy (COLTRIMS) [24, 25], where the two photoelectrons and two cations produced by PDI are detected with full $4\pi$ solid angle, and their 3-D momenta are measured in coincidence on an event-by-event basis. The photoelectron- and cation-pair were guided using static parallel electric and magnetic fields, 11.4 V/cm and 10.0 G, respectively, to multi-hit capable position- and time-sensitive detectors. The detectors comprised a Multi-Channel Plate (MCP) stack in chevron configuration, backed by a delay-line anode readout, each at opposite ends of the spectrometer. The electron and ion delay-line detectors were a three-layer hex-anode with an 80 mm MCP stack and a two-layer quad-anode with a 120 mm MCP stack, respectively. This system encodes a charged particle's 3-D momentum into its hit position on the detector and Time-of-Flight (TOF) relative to the incoming XUV light pulses. These detectors are subject to multi-hit dead-time effects that are most prominent in the electron pair detection, due to the small variation in the electron's arrival times and hit positions on the detector [26], whereas the dead-time effects play a negligible role for the detection of the cation pair. This dead-time effect can influence the measured relative electron-electron angular distribution, hence it is important to quantify this deficiency, in order to distinguish real features from those which originate from the underperforming detection scheme. The electron-pair resolution is estimated by simulating the relative motion of the electron pair in the spectrometer fields with various electron sum kinetic energies and in various electron energy sharing conditions. For each pair of electron trajectories, the relative hit position and TOF is computed, which is used to determine the fraction of simulated electron-pair events lost due to an estimated detector response, and thus approximate the fraction of actual losses.

PDI was performed using a linearly polarized tunable monochromatic beam of extreme ultraviolet (XUV) photons produced at beamline 10.0.1.3. at the Advanced Light Source (ALS), located at Lawrence Berkeley National Laboratory. The beamline monochromator was configured to provide 61.5 eV photons to the experiment with an energy resolution of less than $\pm 50$ meV. The photon energy of 61.5 eV was chosen to be near the maximum of the PDI cross section of $NH_3$, while at the same time providing electron kinetic energies that can be detected with full solid angle and adequate energy

resolution (around 1:10). Moreover, it is beneficial to keep the electron sum energy greater than $\sim 5$ eV in order to utilize a large region of the 3D electron pair detection phase space, minimizing losses due to the electron detector dead-time.

A beam of rotationally and vibrationally cold ($\sim$80 K) $NH_3$ molecules (Praxair, anhydrous ammonia >99% purity) was produced by an adiabatic expansion of pressurized gas through a 50 $\mu$m nozzle and collimated by a pair of downstream skimmers. The first skimmer had a diameter of 0.3 mm, and the second skimmer had a diameter of 0.5 mm. The first skimmer was placed 8 mm downstream of the nozzle and in the zone of silence of the supersonic expansion. The second skimmer was 10 mm downstream of the first skimming stage. This supersonic gas jet propagated perpendicular to the photon beam, where the two beams crossed at the interaction region ($\sim 0.15 \times 0.15 \times 1.0$ mm$^3$) inside the 3-D momentum imaging spectrometer, resulting in the PDI of neutral ammonia in its ground state at an average rate of less than 0.01 events per XUV pulse, assuring unambiguous coincidence conditions. The pressure in the target chamber was $\sim 2 \times 10^{-8}$ Torr with the supersonic beam running, and was approximately a factor of 2 lower without the jet. The target gas itself was delivered through a room temperature injection line using Swagelok connections. Background water in the target chamber was the largest contaminating species, and was minimized through the use of a cold trap filled with liquid nitrogen.

The TOF and hit position of charge particles produced by the PDI were recorded in list mode on an event-by-event basis, enabling relevant events to be captured and examined in a detailed off-line analysis, using the LMF2Root software package [27] described in Ref. [28]. After cleaning, calibrating, and sorting the data set, for each PDI event the photoelectron kinetic energy was determined from the 3-D photoelectron momentum, while the Kinetic Energy Release (KER) of the fragmentation was determined from the 3-D momenta of the two cations. We inferred the momentum of the neutral H fragment in the three-body dissociation channel from momentum conservation.

## III. THEORY

The electron configuration of neutral $NH_3$ in its ground-state is $(1a_1)^2(2a_1)^2(1e)^4(3a_1)^2$. Nine low-lying singlet and triplet states of the ammonia dication can be formed by distributing six electrons over the outer 1e and/or $3a_1$ orbitals, all of which are accessible by single photon absorption at an energy of 61.5 eV. In order to determine which of these states correlate with the two-body $NH_2^+ + H^+$ dissociation channel and three-body $NH^+ + H^+ + H$ fragmentation channel, we carried out a series of electronic structure calculations, analogous to those described in [I]. As in our recent work, the molecular orbitals at each geometry considered were generated from state-averaged, Complete Active Space (CAS) Multi-Configuration Self-Consistent Field (MCSCF) calculations on the two lowest triplet ($^3$E) states of the dication, keeping one orbital (N 1s) frozen and including seven orbitals in the CAS space. These were followed by Multi-Reference Configuration-Interaction (MRCI) calculations, including all single and double excitations from the CAS reference space, to generate cuts through the calculated Potential Energy Surfaces (PESs). As in [I], all bond angles were frozen at the equilibrium geometry of neutral ammonia ($107^o$), as was one hydrogen bond length (1.9138 Bohr), while either one or two hydrogen bonds were stretched. The results of the calculations are shown in Fig. 1(a) and (b), respectively. The electron configuration and state labels of each dication PES are given in the legend. The vertical energies at the neutral $NH_3$ geometry and the energies at the asymptotic limits (extrapolated from 30 Bohr to infinity under the assumption of a purely repulsive Coulomb interaction between the positively charged fragments) are given in Table I.

Our calculations reveal that there are five relevant dication electronic states accessible in the Franck-Condon (FC) region. Three of these states are singlets, $(3a_1^{-2})\ ^1A_1$, $(3a_1^{-1}, 1e^{-1})\ ^1E$, and $(1e^{-2})\ ^1E$, shown as solid curves (black, green, and gold), while two are triplets, $(3a_1^{-1}, 1e^{-1})\ ^3E$, and $(1e^{-2})\ ^3A_2$ shown as dashed curves (red and cyan).

In the case of stretching a single proton (asymmetric stretch), Fig. 1(a) shows that the three $NH_3^{2+}$ states $(3a_1^{-2})\ ^1A_1$, $(3a_1^{-1}, 1e^{-1})\ ^3E$, and $(3a_1^{-1}, 1e^{-1})\ ^1E$ correlate with the $^1$A$_1$, $^3$B$_1$, and $^1$B$_1$ states of $NH_2^+$, respectively. The $(3a_1^{-2})\ ^1A_1$ state is evidently predissociated by the A$'$ component of the $^3$E state, which can lead to a non-adiabatic transition between these states via intersystem crossing.

In the case of symmetric stretch of two hydrogen bonds, it can be seen in Fig. 1(b) that the $^1$A$'$ components of the $(3a_1^{-1}, 1e^{-1})\ ^1E$, $(1e^{-2})\ ^1E$ states, as well as the $^3$A$''$($(1e^{-2})\ ^3$A$_2$) state, all dissociate to

| State | Vertical Energy (eV) | Asymptote | Adiabatic Limit Energy (eV) |
|---|---|---|---|
| | | Two-Body Channels | |
| $(3a_1^{-2})^1A_1$ (black) | 0.44 | $NH_2^+(^1A_1)+H^+$ | -4.61 |
| $(1e^{-1},3a_1^{-1})^3E$(red) | 2.97 | $NH_2^+(^3B_1)+H^+$ | -5.23 |
| $(1e^{-2})^1E$ (gold) | 5.74 | $NH_2^+(^1B_1)+H^+$ | -3.09 |
| | | Three-Body Channels | |
| $(3a_1^{-2})^1A_1$ (black) | 0.44 | $NH^+(^2\Pi)+H^++H$ | 0.52 |
| $(1e^{-1},3a_1^{-1})^1E[A']$ (green) | 5.74 | $NH^+(^2\Pi)+H^++H$ | 0.52 |
| $(1e^{-1},3a_1^{-1})^1E[A'']$ (green) | 5.74 | $NH^+(^2\Delta)+H^++H$ | 3.78 |
| $(1e^{-1},3a_1^{-1})^3A_2$ (cyan) | 8.64 | $NH^+(^2\Pi)+H^++H$ | 0.52 |
| $(1e^{-2})^1E[A']$ (gold) | 10.39 | $NH^+(^2\Pi)+H^++H$ | 0.52 |
| $(1e^{-2})^1E[A'']$ (gold) | 10.39 | $NH^+(^2\Delta)+H^++H$ | 3.78 |

TABLE I. Ammonia dication vertical energies at neutral $NH_3$ geometry and asymptotic two- and three-body dissociation limits extrapolated from *ab initio* calculations at N-H distances of 30.0 bohr (see text). The zero of energy is set to the ground-state ($^1A_1$) of the ammonia dication at the geometry of the neutral ammonia molecule.

the three-body channel $NH^+$ ($^2\Pi$) + $H^+$ + H. The two $A''$ symmetry components of the $(3a_1^{-1}, 1e^{-1})$ $^1E$ and $(1e^{-2})$ $^1E$ dication states dissociate to $NH^+$ ($^2\Delta$) + $H^+$ + H. Previous measurements have also indicated that the $(1e^{-2})$ $^1E$ dication state dissociates to the $NH^+$ + $H^+$ + H channel [6].

To get theoretical estimates of the expected spread of the observed photoelectron energies for the various dication states, we use a variant of the so-called reflection approximation [29]. The range of detectable KERs is determined by the FC envelope of the initial (neutral) vibrational state reflected onto the final dication PESs. For the initial vibrational wavefunction we use a harmonic oscillator function $\chi_0$, obtained from a fit of the ground state energy of ammonia as a function of the symmetric stretch. If we assume that the PDI cross section varies little over the FC region (which is a good approximation, since there are no resonances or near-threshold effects at the chosen photon energy) and that the final continuum vibrational wavefunctions can be approximated by delta functions about the classical turning points on the dication PESs [30], then the envelope of the expected photoelectron energies is given by the values of the vertical PDI energies as a function of the symmetric-stretch coordinate, weighted by the square of the symmetric-stretch vibrational wavefunction. We find that $|\chi_0|^2$ reaches half its maximum value at a symmetric-stretch displacement of approximately $\pm 0.11$ Bohr from equilibrium, and we have used these values to calculate the FWHM of the photoelectron distributions below.

## IV. RESULTS

The $NH_2^+$ + $H^+$ two-body and $NH^+$ + $H^+$ + H three-body dissociation channels of $NH_3^{2+}$, following PDI of $NH_3$ at 61.5 eV, $\sim$27 eV above the PDI threshold, are identified and isolated by selecting the two charged fragments in the PhotoIon-PhotoIon COincidence (PIPICO) TOF spectrum and then in momentum space. Moreover, we also enforce that two electrons are measured in coincidence with the two ionic fragments. We show the PIPICO spectrum in Fig. 2, where the photoion-photoion coincidence yield is shown on a logarithmic scale. Here we observe four photoion-photoion coincidence features following PDI of $NH_3$ molecules, two of which are addressed in this report, $NH_2^+$ + $H^+$ and $NH^+$ + $H^+$, while the other two coincidence features, $H^+$ + $H^+$ and $N^+$ + $H^+$, are the topic of manuscript [I]. The $N^+$ + $H^+$ channel is very faint and diffuse, which renders it difficult to visually identify in the PIPICO spectrum alone, however it emerges upon further analysis (examined in [I]). The vertical and horizontal features, as well as the periodically repeating features, are the result of false coincidences, which are removed later in our analysis. We first begin with a discussion of the $NH_2^+$ + $H^+$ two-body fragmentation channel before turning to the $NH^+$ + $H^+$ + H three-body channel. By inspecting the yield of the two features in the PIPICO corresponding with $NH_2^+$ + $H^+$ and $NH^+$ + $H^+$ coincidences, we find the approximate branching ratio between the $NH_2^+$ + $H^+$ two-body and the $NH^+$ + $H^+$ + H three-body dissociation channels to be 86:14.

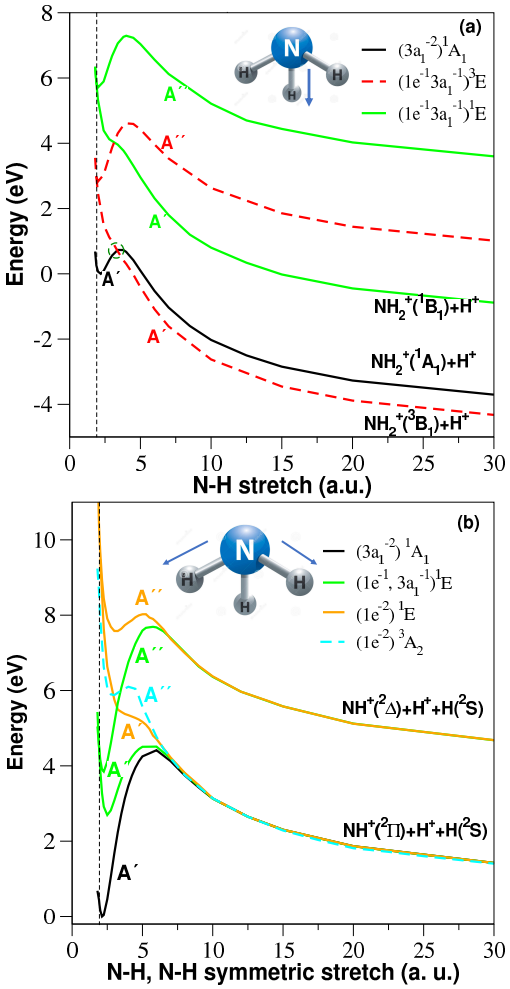


FIG. 1. PES cuts of the experimentally identified states of the $NH_3$ dication generated from MRCI calculations as described in the text. In panel (a) one hydrogen is stretched while the other two hydrogens remain fixed, with all internal angles frozen at the geometry of neutral ammonia. In panel (b) two hydrogens are symmetrically stretched while the third hydrogen remains fixed, with all internal angles frozen at the geometry of neutral ammonia. The dissociation limits are given in Table I. The zero of energy is set to the ground-state ($^1A_1$) of the ammonia dication at the geometry of the neutral ammonia molecule, which lies 34.8 eV below the dication ground state [8]. On this energy scale, the 61.5 eV photon energy falls at 26.74. The green dashed circle in panel (a) indicates the region where intersystem crossing may occur. The broken vertical lines indicate the equilibrium geometry of neutral $NH_3$.

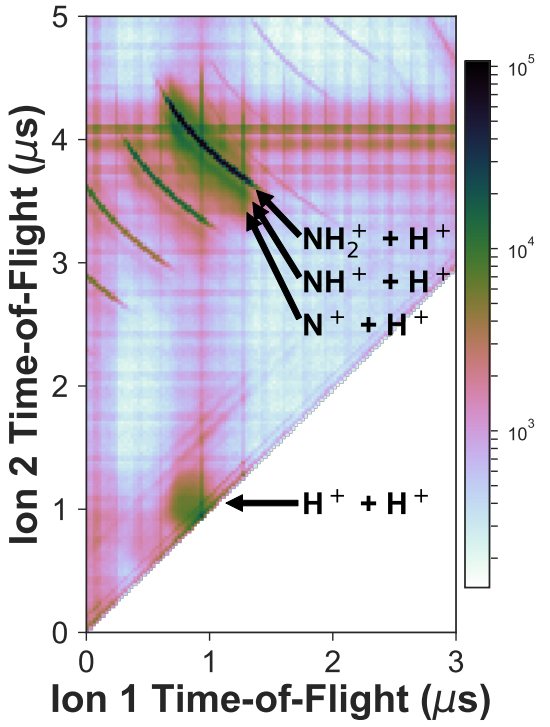


FIG. 2. The photoion-photoion time-of-flight coincidence map (PIPICO spectrum), shown on a logarithmic scale. The observed photoion-photoion coincidences from the respective breakup channels following PDI of $NH_3$ at 61.5 eV are indicated by the black arrows and text. Two of these channels ($H^+ + H^+$ and $N^+ + H^+$) are the topic of paper [I].

### A. Two-body breakup channel: $NH_2^+ + H^+$

We plot the PDI yield of the $NH_2^+ + H^+$ fragmentation channel of $NH_3^{2+}$ as a function of the kinetic energy of the first and second detected electrons, to produce an electron-electron energy correlation map, as shown in Fig. 3. Since the two electrons are indistinguishable particles, the labeling (as 1 and 2) is arbitrary, and the figure has been symmetrized across the diagonal (the line $E_1 = E_2$) to account for this. With the guidance of the calculated PES cuts, we identify three features corresponding with three different $NH_3^{2+}$ electronic states that feed into the $NH_2^+ + H^+$ two-body fragmentation channel. Although difficult to visually identify here, these three features are better separated in different spectra that are shown below in Fig. 4. Each of these three features correspond to two photoelectrons with energy

sums centered around 26.9 eV, 23.9 eV, and 21.4 eV, with a Full Width at Half Maximum (FWHM) of roughly 1.5 eV, 2.0 eV, and 1.7 eV, respectively. These features, indicated as diagonal lines (which take the form $E_2 = -E_1 + E_{sum}$, where $E_{sum}$ is the photoelectron energy sum corresponding to that feature), have been color-coded as black, red, and green to guide the eye. In the offline analysis we choose each of these three features by selecting carefully around the center of each feature in Fig. 4. Enforcing conditions in a multitude of observables and dimensions (particle energy and momenta) in this fashion enables us to separate these three features for subsequent in-depth analysis.

The FWHM of the electron energy sum of each dication state roughly corresponds with the magnitude of the gradient of the PES in the FC region (convoluted with the energy resolution of the electron detector). The characteristics of the three features suggest that the three dication states are accessed via direct PDI, as indicated by the uniformity of the negatively sloped diagonal features in Fig. 3, and also appear to be populated through autoionization, the signature being the two sharp features located at the end of the diagonals, where one of the electrons possesses nearly zero kinetic energy. The branching ratio between these three measured channels that correspond with the three dication states shown in Table II is estimated from the relative yield of these three features. The branching ratios and the method used to estimate them are discussed below.

Next we plot the yield of the $NH_2^+ + H^+$ dissociation channel as a function of the KER and the kinetic energy sum of the photoelectron pair, in order to generate an electron-ion energy correlation map. Three features corresponding with the three color-coded diagonals in Fig. 3 are present in the electron-nuclei energy correlation map, shown in Fig. 4. These three features are marked by ellipses in their respective color-codes to guide the eye (note: these ellipses do not reflect the actual momentum gates of the analysis). The feature circled by the green ellipse is comparatively faint and can be mistaken as a part of the feature circled by the red ellipse, however it is identified as a state with the assistance of the calculated PES cuts. Here we see that each dication state possesses a different distribution of KER centered around 5.7 eV, 6.7 eV, and 6.7 eV, each with a FWHM of roughly 1.0 eV, 1.3 eV, and 1.2 eV, respectively. The FWHM of the KER of each dication state carries similar information as the electron sum energy FWHM, indicating the steepness of the PESs in the FC region (convoluted with the energy resolution of the ion spectrometer).

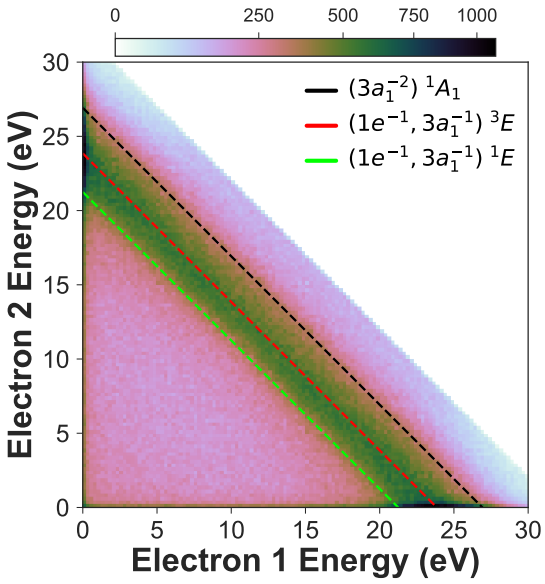


FIG. 3. The $NH_2^+ + H^+$ yield as a function of the kinetic energy of the first and second photoelectron after PDI of $NH_3$ at 61.5 eV. The three features indicating the active dication states are color-coded (black, red, and green) and shown as diagonal lines to guide the eye. Electrons with energy sums beyond 35 eV were not detected with full $4\pi$ solid angle and are hence omitted.

We present the $NH_2^+ + H^+$ yield as a function of the photoelectron energy sum in Fig. 5, where each active dication state we identified in Fig. 4 has been indicated in Fig. 5 by a distribution in its corresponding color. In the total yield we observe an asymmetric monomodal distribution, exhibiting a rapid rise in yield on the low energy side of the peak and a slower decay in yield on the high energy side of the peak. The wings on the distribution originate from false coincidences and background events that are challenging to completely eliminate in the analysis, resulting in a near-uniform background (clearly visible in Fig. 3) underlying the spectrum that causes exaggerated wings.

We show the $NH_2^+ + H^+$ yield as a function of KER in Fig. 6, where each dication state we identified in Fig. 4 has been indicated by a distribution in its corresponding color. In the total yield we observe another broad asymmetric monomodal KER distribution with a rapid increase in yield on the low energy side of the peak and a slower decay in yield towards high energy. Both the experimental and

| State | Photoelectron Energy Sum (eV) | | KER (eV) | | Branching Fraction | $\beta_2$ |
|---|---|---|---|---|---|---|
| | Experiment | Theory[a] | Experiment | Theory[a,b] | | |
| $(3a_1^{-2})\ ^1A_1$ (black) | 26.9 (1.5) | 26.5 (1.5) | 5.7 (1.0) | 5.5 (1.5) | 13% ± 3% | -0.30 ± 0.01 |
| $(3a_1^{-1}, 1e^{-1})\ ^3E$ (red) | 23.9 (2.0) | 23.5 (2.0) | 6.7 (1.3) | 8.2 (2.0) | 44% ± 3% | -0.12 ± 0.01 |
| $(3a_1^{-1}, 1e^{-1})\ ^1E$ (green) | 21.4 (1.7) | 21.0 (2.4) | 6.7 (1.2) | 7.5 (2.4) | 43% ± 3% | -0.18 ± 0.01 |

TABLE II. The measured and calculated photoelectron energy sum and KER for each of the three identified features from $NH_2^+ + H^+$ fragmentation following PDI of $NH_3$ at 61.5 eV, as well as the estimated branching ratios and $\beta_2$ anisotropy parameter (see text). The energy widths (FWHM) are in parentheses. [a]Theoretical FWHM values estimated from the square of the symmetric stretch vibrational wavefunction of $NH_3$ projected onto the respective dication state (see text). [b]Theoretical KER values are calculated assuming ro-vibrational ground state fragments, i.e. assuming maximum KER with no energy channeled into internal excitations.

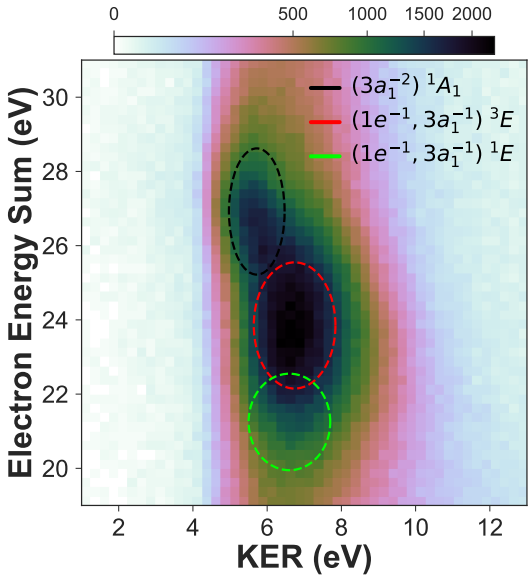


FIG. 4. The $NH_2^+ + H^+$ yield as a function of the KER and the kinetic energy sum of the photoelectron pair after PDI of $NH_3$ at 61.5 eV. The three features indicating the active dication states are color-coded (black, red, and green) and shown as ellipses to guide the eye (they only approximately represent the software gates).

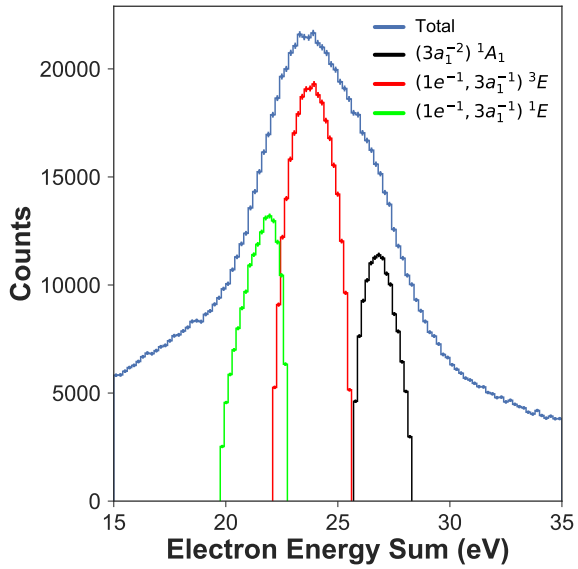


FIG. 5. The $NH_2^+ + H^+$ yield as a function of the kinetic energy sum of the photoelectron pair after PDI of $NH_3$ at 61.5 eV (shown in blue). The distributions for the three contributing dication states are shown in their respective color-codes (shown in black, red, and green, and multiplied by a factor of 1.6 for improved visibility). Contributions from individual dication states are extracted with gates as indicated in Fig. 4, and hence their sum does not reflect the total (blue) yield (see text). The statistical error bars are on the order of the line width.

theoretically calculated photoelectron energy sums and KERs are shown in Table II, which show good agreement.

These three corresponding dication states were identified using MRCI calculations, as discussed in Section III, and are consistently color-coded throughout the paper. The $(3a_1^{-2})\ ^1A_1$ state is shown in black, the $(3a_1^{-1}, 1e^{-1})\ ^3E$ state in red, and the $(3a_1^{-1}, 1e^{-1})\ ^1E$ state in green. Our ion yield measurements suggest that the branching ratios for these three dication states, shown in Table II, are approximately $13\% \pm 3\%$ for the $(3a_1^{-2})\ ^1A_1$ state, $44\% \pm 3\%$ for the $(3a_1^{-1}, 1e^{-1})\ ^3E$ state, and $43\% \pm 3\%$ for the $(3a_1^{-1}, 1e^{-1})\ ^1E$ state. These branching ratios and errors (plus/minus one standard deviation) are estimated by simultaneously fitting each feature in Fig. 4 with separate 2-D Gaussian distributions (although the distributions may not be explicitly Gaussian, this is nonetheless a good

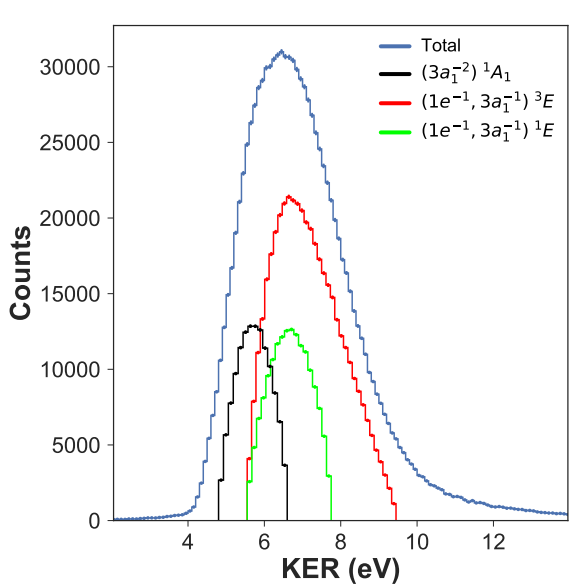


FIG. 6. The $NH_2^+ + H^+$ yield as a function of the KER after PDI of $NH_3$ at 61.5 eV (shown in blue). The distributions for the three contributing dication states are shown in their respective color-codes (shown in black, red, and green, and multiplied by a factor of 1.6 for improved visibility). Contributions from the individual dication states are extracted with gates as indicated in Fig. 4, and hence their sum does not reflect the total (blue) yield (see text). The statistical error bars are on the order of the line width.

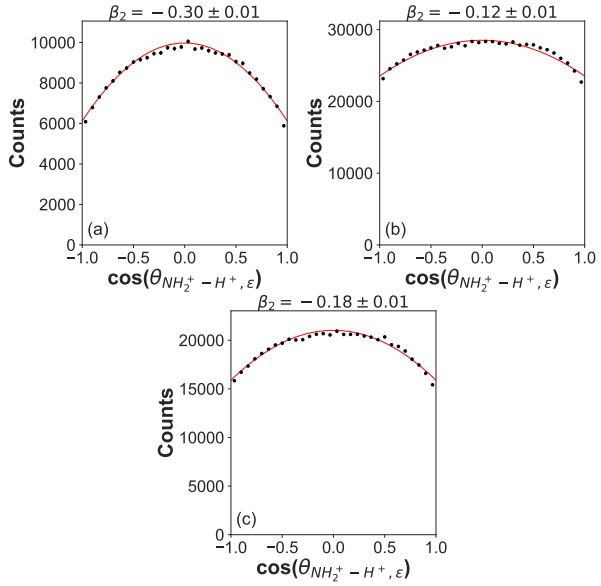


FIG. 7. The yield of $NH_2^+ + H^+$ dissociation after PDI of $NH_3$ at 61.5 eV as a function of the cosine of the measured relative angle between the $NH_2^+$-$H^+$ recoil axis and XUV polarization vector $\varepsilon$ for the (a) $(3a_1^{-2})\ ^1A_1$, (b) $(3a_1^{-1}, 1e^{-1})\ ^3E$, and (c) $(3a_1^{-1}, 1e^{-1})\ ^1E$ dication states. The fits, representing the parametrizations in terms of the anisotropy (see Eq. 1), are shown in red, where the retrieved $\beta_2$ value is shown above each plot.

approximation). The fitting procedure varied the widths along each dimension independently, while also including a varying constant background offset. Following this fitting procedure, we integrate the fit for each dication state to estimate its contribution to the total $NH_2^+ + H^+$ yield. The main contribution to the uncertainty of the branching ratio is rooted in the aforementioned electron pair dead-time, which influences the detection yield of the electron-ion coincidences for each dication state as a function of the electron sum energy. Applying the simulation mentioned above, we estimate the total possible loss in PDI yield for electron sum energies of 26.9 eV ($(3a_1^{-2})\ ^1A_1$), 23.9 eV ($(3a_1^{-1}, 1e^{-1})\ ^3E$), and 21.4 eV ($(3a_1^{-1}, 1e^{-1})\ ^1E$) to be 4.5%, 5.2%, and 5.9%, respectively. This translates to an error of up to 3% in the branching ratio. Errors due to deviations from the assumed Gaussian shape of each feature in the fitting process and the quality of the fit are estimated to be small (both <1%).

From the PES cuts shown in Fig. 1(a) and the energetics presented in Fig. 4 and Table II, we conclude that the $(3a_1^{-2})\ ^1A_1$ state dissociates to the $NH_2^+(^3B_1) + H^+$ limit, the $(3a_1^{-1}, 1e^{-1})\ ^3E$ state directly dissociates to this very same limit, and the $(3a_1^{-1}, 1e^{-1})\ ^1E$ state directly dissociates to the $NH_2^+(^1B_1) + H^+$ limit. Here the $(3a_1^{-2})\ ^1A_1$ dication state must undergo an intersystem crossing preceding the dissociation, as the measured KER indicates that it does not reach its adiabatic limit (which would only produce ∼5.05 eV of KER). In Fig. 1(a) it can be seen that the $(3a_1^{-2})\ ^1A_1$ dication state is bound in the FC region and can predissociate by the $A'$ symmetry curve of the $(3a_1^{-1}, 1e^{-1})\ ^3E$ dication state. This enables a non-adiabatic population transfer mechanism that has been observed previously in near-threshold measurements [5, 6]. In Ref. [5] it was suggested that for excitation energies well above the PDI threshold of $NH_3$, direct dissocation would dominate over the predissociation, which is enabled by spin-orbit coupling. Our measurement, performed ∼27 eV above the double ionization threshold, is at odds with this proposition, as we observe the predissociation via intersystem cross-

ing dominating over direct dissociation. Further, based on the measured KER, we conclude that this coupling mechanism outcompetes the dissociation from the population tunneling through the barrier of the $(3a_1^{-2})\ ^1A_1$ dication state along the asymmetric stretch coordinate, since dissociation via tunneling would result in a lower KER than what is measured. Comparing the measured and calculated KERs for the $(3a_1^{-2})\ ^1A_1$ state (see Table II) indicates that the resulting $NH_2^+$ fragment is formed in a relatively cold ro-vibrational state. In contrast to the $(3a_1^{-2})\ ^1A_1$ state, the $(3a_1^{-1}, 1e^{-1})\ ^3E$ state directly dissociates on the $A'$ curve, producing an $NH_2^+$ fragment with approximately 1.5 eV of ro-vibrational energy, which we infer by comparing the measured KER to the theoretical KER calculated for $NH_3^{2+}$ ground state fragments. However, the $(3a_1^{-1}, 1e^{-1})\ ^3E$ state also exhibits contributions from ro-vibrationally cold $NH_2^+$ fragments that reside in the long tail of the KER toward high energy values at constant electron sum energy. Here, a population transfer from the dissociative $(3a_1^{-1}, 1e^{-1})\ ^3E$ dication state to the $(3a_1^{-2})\ ^1A_1$ state is unlikely, as this would involve a non-adiabatic transition between states of different spin symmetry, and the wavepacket would only encounter the coupling region once as it dissociates. Similarly, the $(3a_1^{-1}, 1e^{-1})\ ^1E$ dication state also directly dissociates on its $A'$ curve, producing an $NH_2^+$ fragment with approximately 0.8 eV of ro-vibrational energy. We point out that the direct dissociation, producing a ro-vibrationally excited fragment, is consistent with the results in [I].

In order to assess if there are preferred molecular orientations at which PDI of $NH_3$ occurs for each of the three $NH_3^{2+}$ dication states, we plot in Fig. 7(a), (b), and (c) the yield of the $NH_2^+ + H^+$ two-body fragmentation as a function of the cosine of the relative angle between the recoil axis of the molecular breakup ($NH_2^+$-$H^+$) and the XUV polarization $\varepsilon$. For the features corresponding with the $(3a_1^{-2})\ ^1A_1$, and $(3a_1^{-1}, 1e^{-1})\ ^3E$, and $(3a_1^{-1}, 1e^{-1})\ ^1E$ dication states, we observe an enhancement in PDI for molecular orientations where the recoil axis is aligned at $\sim 90^\circ$ angle with respect to the polarization vector. Here, this enhancement in PDI yield is strongest in the $(3a_1^{-2})\ ^1A_1$ state, weaker in the $(3a_1^{-1}, 1e^{-1})\ ^1E$ state, whereas the distribution of the $(3a_1^{-1}, 1e^{-1})\ ^3E$ dication state is the most isotropic of the three (its $\beta_2$ value is the closest to zero). This perpendicular orientation of the recoil axis with respect to the polarization vector roughly coincides with the $C_{3v}$ symmetry axis of the $NH_3$ molecule. In all dication states the PDI involves the $3a_1$ orbital, i.e. the lone-pair, which is aligned along the molecular $C_{3v}$ axis. This could explain the enhancement at geometries where the polarization vector of the ionizing field is directed along this orbital and the stronger effect in the $(3a_1^{-2})\ ^1A_1$ state, where both holes are created in the $3a_1$ orbital, as opposed to the $(3a_1^{-1}, 1e^{-1})\ ^3E$ and $(3a_1^{-1}, 1e^{-1})\ ^1E$ states, where a hole is created in each of the $3a_1$ and $1e$ orbitals.

These photofragment angular distributions have been fitted (solid red line) using the familiar parameterization:

$$\frac{d\sigma}{d\Omega} = \frac{\sigma_0}{4\pi}[1 + \beta_2 P_2(\cos\theta)], \tag{1}$$

which describes the fragment angular distribution from the dissociation of a rigid rotor, where $\sigma_0$ is the total cross section, $\beta_2$ is the anisotropy parameter, $P_2$ is the second order Legendre polynomial, and $\theta$ is the angle between the recoil axis of the molecular two-body breakup and the polarization vector of the ionizing field [31, 32]. The retrieved $\beta_2$ parameter is shown above each plot, while the data is fitted using the projection method discussed in [33], where the error of $\beta_2$ is determined via statistical bootstrapping [34]. We find $\beta_2$ values of $-0.30 \pm 0.01$, $-0.12 \pm 0.01$, and $-0.18 \pm 0.01$ for the $(3a_1^{-2})\ ^1A_1$, $(3a_1^{-1}, 1e^{-1})\ ^3E$, and $(3a_1^{-1}, 1e^{-1})\ ^1E$ dication states, respectively. These values are also listed in Table II.

Next, we display the yield of the $NH_2^+ + H^+$ two-body channel as a function of the energy sharing $\rho$ between the two photoelectrons for the three features that correspond with the three $NH_3^{2+}$ states. We define the electron energy sharing as:

$$\rho = \frac{E_{e_1}}{E_{e_1} + E_{e_2}}, \tag{2}$$

where $E_{e_1}$ and $E_{e_2}$ are the kinetic energies of electron 1 and 2, respectively. Values of $\rho$ near 0.5 indicate equal energy sharing between the two photoelectrons, while values near 0 or 1 indicate unequal energy sharing between the two photoelectrons. The results are shown in Fig. 8(a), (b), and (c).

We attribute the sharp features near 0 and 1, observed in Fig. 8(a), (b), and (c), to the PDI of $NH_3$ via autoionization, corresponding with a fast photoelectron and slow electron emerging from the autoionization. The fraction of PDI via autoionization relative to direct PDI is appoximately 1.9%±1.0% in

the $(3a_1^{-2})\ ^1A_1$ state, 4.4%±0.7% in the $(3a_1^{-1}, 1e^{-1})\ ^3E$ state, and 6.2% ± 0.9% in the $(3a_1^{-1}, 1e^{-1})\ ^1E$ state. This is estimated by extrapolating the average number of counts in the equal energy sharing condition across all $\rho$ and then subtracting this value from the bins where $\rho$ is near 0 or 1 (the unequal energy sharing condition). Computing this residue gives an estimate on how many counts are associated with autoionization relative to the direct PDI of $NH_3$. The error in the autoionization fraction is determined from the error in the average number of counts in the equal energy sharing condition (which is extracted from Poisson statistics).

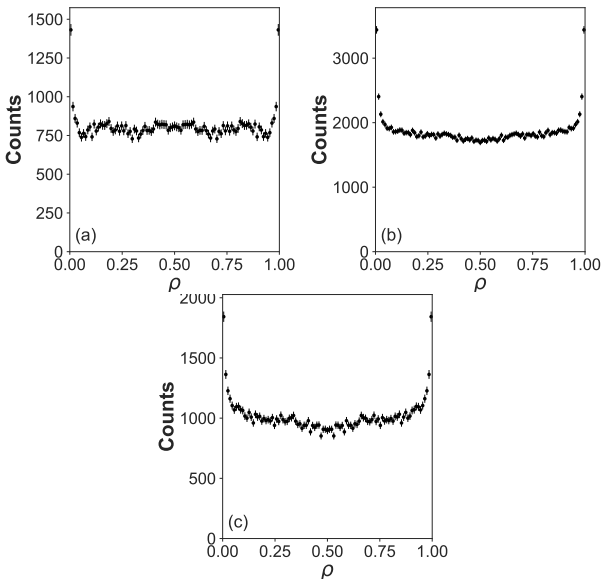


FIG. 8. The yield of the $NH_2^+ + H^+$ two-body breakup after PDI of $NH_3$ at 61.5 eV as a function of the electron energy sharing $\rho$ (see Eq. 2) for the (a) $(3a_1^{-2})\ ^1A_1$, (b) $(3a_1^{-1}, 1e^{-1})\ ^3E$, and (c) $(3a_1^{-1}, 1e^{-1})\ ^1E$ dication states.

Finally, we plot in Fig. 9, Fig. 10, and Fig. 11 the yield of the $NH_2^+ + H^+$ dissociation channel as a function of the cosine of the relative emission angle between the two photoelectrons, (a) integrated over all energy sharing conditions and (b) for equal energy sharing condition for the three $NH_3^{2+}$ states. In these figures, there are no conditions enforced on either the molecular orientation or the emission angle of the first detected photoelectron relative to the polarization vector of the XUV beam. In the equal energy sharing case the relative angle is plotted for $0.475 < \rho < 0.525$. We point out that our measurement suffers from some multi-hit detector deadtime effects, which influence the measured yield of photoelectrons emitted in the same direction with similar kinetic energies. In the equal energy sharing condition and for the emission into the same hemisphere $\theta_{e_1,e_2} \leq 90°$, this corresponds, in worst case, to a loss of ∼15% of the events for the $(3a_1^{-2})\ ^1A_1$ state, ∼16% for the $(3a_1^{-1}, 1e^{-1})\ ^3E$ state, and ∼18% for the $(3a_1^{-1}, 1e^{-1})\ ^1E$ state. This worst-case scenario is simulated for an isotropic relative electron-electron emission, which very well represents autoionization processes that are sequential in nature and are subject to unequal energy sharing between the electrons. The equal energy sharing case on the other hand is dominated by knock-out processes with very few electron pairs emitted into the same hemisphere. The actual losses are hence believed to be smaller by at least a factor of 2, i.e. closer to the simulated losses for unequal electron energy sharing. We refrain from showing the measured photoelectron angular distribution in the unequal energy sharing case, which captures the autoionization feature, as there is a significant contribution due to direct PDI that pollutes the autoionization signal considerably and prevents a clear analysis of the relative angular distribution for this indirect ionization process.

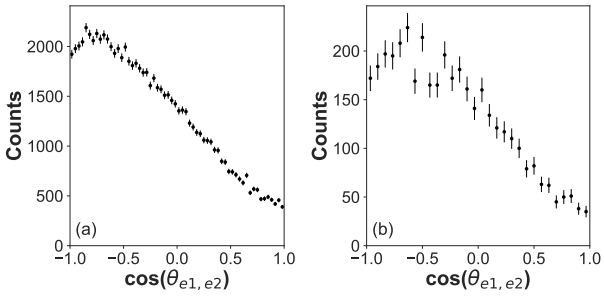


FIG. 9. The yield of the $NH_2^+ + H^+$ two-body breakup, after PDI of $NH_3$ at 61.5 eV, as a function of the cosine of the relative emission angle between the two photoelectrons for the $(3a_1^{-2})\ ^1A_1$ dication state (a) integrated over all possible electron energy sharing and (b) for equal energy sharing ($\rho = 0.5 \pm 0.025$).

The relative angles between the two electrons, integrated over all energy sharing cases, show a preferred emission of the two electrons into opposite hemispheres. The distribution for the $(3a_1^{-2})\ ^1A_1$ dication state [Fig. 9(a)] peaks at 145° with a notable dip at 180° corresponding to a back-to-back emission. The $(3a_1^{-1}, 1e^{-1})\ ^3E$ state [Fig. 10(a)] peaks at 125° and has a similar dip at 180°. The $(3a_1^{-1}, 1e^{-1})\ ^1E$ state [Fig. 11(a)] peaks at 120°, with a slight increase at 180° compared to the two other dication

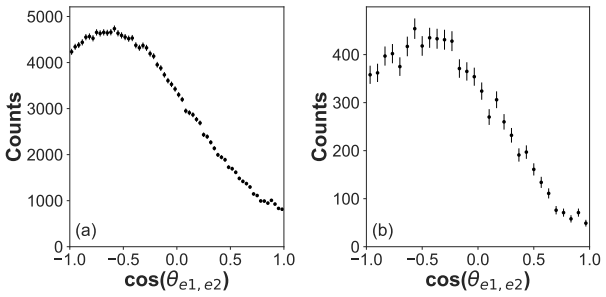


FIG. 10. The yield of the $NH_2^+ + H^+$ two-body breakup, after PDI of $NH_3$ at 61.5 eV, as a function of the cosine of the relative emission angle between the two photoelectrons for the $(3a_1^{-1}, 1e^{-1})$ $^3E$ dication state (a) integrated over all possible electron energy sharing and (b) for equal energy sharing ($\rho = 0.5 \pm 0.025$).

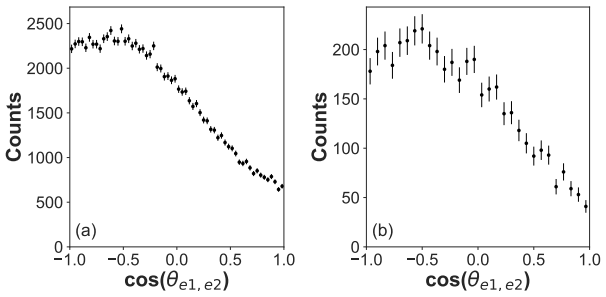


FIG. 11. The yield of the $NH_2^+ + H^+$ two-body breakup, after PDI of $NH_3$ at 61.5 eV, as a function of the cosine of the relative emission angle between the two photoelectrons for the $(3a_1^{-1}, 1e^{-1})$ $^1E$ dication state (a) integrated over all possible electron energy sharing and (b) for equal energy sharing ($\rho = 0.5 \pm 0.025$).

states.

The photoelectron dynamics in the equal energy sharing condition ($\rho = 0.5 \pm 0.025$) reveals similar anisotropic angular distributions depicted in Fig. 9(b), Fig. 10(b), and Fig. 11(b), which possess minima near 0° relative emission angle in all three states and peak at relative angles near 130° in the $(3a_1^{-2})$ $^1A_1$ state, 125° in the $(3a_1^{-1}, 1e^{-1})$ $^3E$ state, and 120° in the $(3a_1^{-1}, 1e^{-1})$ $^1E$ state. All three distributions show a dip at 180°. This relative electron emission pattern is reminiscent of a knock-out double ionization process as found in other valence PDI investigations of atomic and molecular targets [35–38]. In all three cases the likelihood for emission in the same direction is roughly a factor of 10 less likely than emission at the peak angle.

### B. Three-body breakup channel: $NH^+ + H^+ + H$

As in the previous section, we plot in Fig. 12 the PDI yield of the $NH^+ + H^+ + H$ channel as a function of the kinetic energy of the first and second detected electrons, to produce the electron-electron energy correlation map. As before, the figure has been symmetrized across the diagonal (the line $E_1 = E_2$) to account for the indistinguishability of the two photoelectrons. With the guidance of the calculated PES cuts, we identify three features corresponding with three $NH_3^{2+}$ dication electronic states that feed the three-body $NH^+ + H^+ + H$ fragmentation channel. Again, although these features are difficult to visually identify here, they are better separated in different spectra that are shown below in Fig. 13. The photoelectrons associated with these features have energy sums centered around 19.7 eV, 18.3 eV, and 16.8 eV, and a FWHM of roughly 2.5 eV, 2.3 eV, and 2.1 eV, respectively. These features, indicated by diagonal lines (taking the form $E_2 = -E_1 + E_{sum}$), are color-coded as green, cyan, and gold to guide the eye (the same green color used in the two-body breakup section is applied here because the same dication state contributes to both the two- and three-body fragmentation channels, as discussed below). Using the same protocol as described in the two-body breakup section, we choose each of these three features by selecting carefully around the center of each feature in Fig. 13. As in the two-body breakup channel, these three states are accessed via direct PDI and also evidently through autoionization.

Three corresponding features are present in the electron-nuclei energy correlation map, shown in Fig. 13, which are circled by their respective color-codes to guide the eye (as before, these ellipses do not reflect the actual momentum gates). The feature circled by the cyan ellipse can be mistaken as a part of the feature circled by either the green or gold ellipse, however it is identified as a state with the assistance of the calculated PES cuts. Each feature possesses a different KER distribution centered around 6.4 eV, 7.1 eV, and 9.4 eV, each with a FWHM of roughly 1.1 eV, 1.4 eV, and 2.4 eV, respectively.

We present the $NH^+ + H^+ + H$ three-body yield as a function of the photoelectron energy sum in Fig. 14, where each feature we identified in Fig. 13 has been indicated by a distribution in its corresponding color. In the total yield we observe a slightly asymmetric monomodal distribution. As in the two-body channel, the wings on the distribution

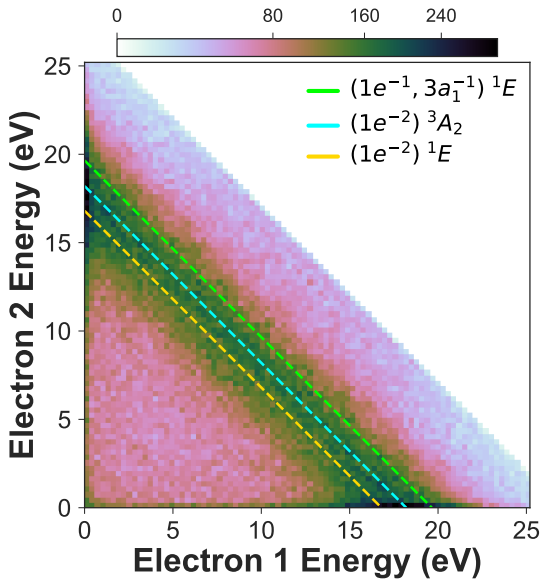


FIG. 12. The $NH^+ + H^+ + H$ three-body yield, after PDI of $NH_3$ at 61.5 eV, as a function of the kinetic energy of the first and second photoelectron. The three contributing dication states are color-coded (green, cyan, and gold) and shown as diagonal lines to guide the eye. Electron sum energies beyond 27 eV are omitted for visual clarity.

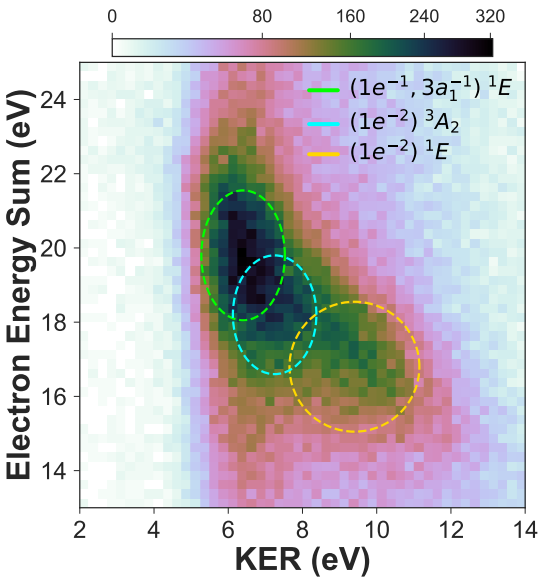


FIG. 13. The $NH^+ + H^+ + H$ three-body yield, after PDI of $NH_3$ at 61.5 eV, as a function of the KER and the kinetic energy sum of the photoelectron pair. The three contributing dication states are color-coded (green, cyan, and gold) and shown as ellipses to guide the eye (they only approximately represent the software gates).

originate from false coincidences and background events that are challenging to completely eliminate in the analysis, causing a near-uniform background (clearly visible in Fig. 12) to underlie the spectrum, resulting in exaggerated wings.

Next, we show the $NH^+ + H^+ + H$ yield as a function of KER in Fig. 15, following the color code of Fig. 13. In the total yield we observe a broad asymmetric bimodal structure in the KER distribution. This bimodal distribution shows a rapid increase in yield on the low energy side of the peak and a slow decay in yield towards high KER, where the second mode is located. Both, the experimental and calculated photoelectron energy sums and KERs for each dication state are listed in Table III, showing good agreement for the $(1e^{-2})\ ^3A_2$ (cyan) and $(1e^{-2})\ ^1E$ (gold) dication states. In the case of the $(3a_1^{-1}, 1e^{-1})\ ^1E$ state (green), the agreement between experiment and theory is not as close, although the two values lie within the theoretically estimated FWHM. It is noteworthy that Fig. 1(b) indicates that the $(3a_1^{-1}, 1e^{-1})\ ^1E$ state possesses a barrier to dissociation when starting from the neutral equilibrium geometry, which is lifted when starting from geometries where the two N-H distances are compressed. This is consistent with the fact that for this state the calculated vertical photoelectron energy is greater than the measured value, whereas the calculated KER is smaller than the measured value. Consequently, PDI at geometries with contracted bond lengths are more likely to undergo three-body dissociation, as these excitations can directly fragment over the barrier. We point out that the difference in electron energy sum between the measurement and calculation is approximately the same as the difference in KER, which further supports this interpretation.

The three contributing dication states were also identified using MRCI calculations, as highlighted in the theory section, and are consistently color-coded throughout the paper, where the green state corresponds with the $(3a_1^{-1}, 1e^{-1})\ ^1E$ state (the same as in the two-body breakup section), the cyan state corresponds with the $(1e^{-2})\ ^3A_2$ state, and the gold state with the $(1e^{-2})\ ^1E$ state. The ion yield measurements estimate the branching ratios for these three dication states, listed in Table III, to be approximately $29\% \pm 4\%$ for the $(3a_1^{-1}, 1e^{-1})\ ^1E$ state, $24\% \pm 4\%$ for the $(1e^{-2})\ ^3A_2$ state, and $47\% \pm 4\%$

| State | Photoelectron Energy Sum (eV) | | KER (eV) | | Branching Fraction | $\beta_2$ |
|---|---|---|---|---|---|---|
| | Experiment | Theory[a] | Experiment | Theory[a,b] | | |
| $(3a_1^{-1}, 1e^{-1})\ ^1E$ (green) | 19.7 (2.5) | 21.0 (2.4) | 6.4 (1.1) | 5.2 (2.4) | 29% ± 4% | -0.27 ± 0.01 |
| $(1e^{-2})\ ^3A_2$ (cyan) | 18.3 (2.3) | 18.1 (3.3) | 7.1 (1.4) | 7.7 (3.3) | 24% ± 4% | -0.17 ± 0.01 |
| $(1e^{-2})\ ^1E$ (gold) | 16.8 (2.1) | 16.8 (3.4) | 9.4 (2.4) | 9.4 (3.4) | 47% ± 4% | 0.04 ± 0.01 |

TABLE III. The measured and calculated photoelectron energy sum and KER for each of the three active dication states leading to $NH^+ + H^+ + H$ fragmentation following PDI of $NH_3$ at 61.5 eV, as well as the estimated branching fractions and $\beta_2$ anisotropy parameter (see text). [a]Theoretical FWHM values estimated from square of symmetric stretch vibrational wavefunction of $NH_3$ projected onto dication state (see text). [b]Theoretical KER values are calculated assuming ro-vibrational ground state fragments, i.e. assuming maximum KER with no energy channeled into internal excitations.

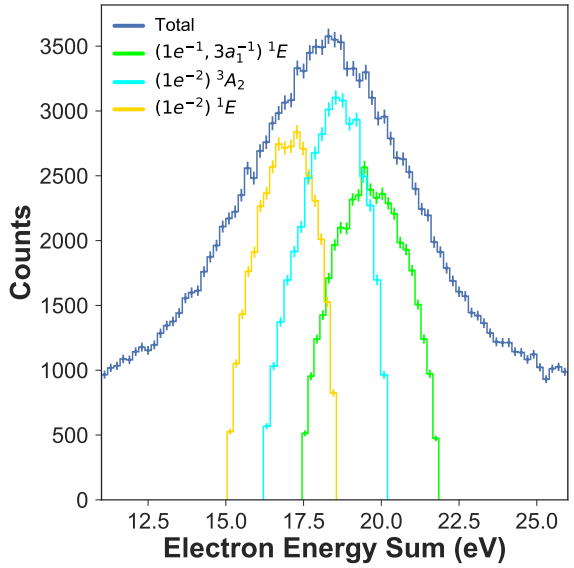


FIG. 14. The $NH^+ + H^+ + H$ three-body yield, after PDI of $NH_3$ at 61.5 eV, as a function of the electron kinetic energy sum (shown in blue). The distributions for the three contributing dication states are shown in their respective color-codes (shown in green, cyan, and gold, and multiplied by a factor of 1.5 for improved visibility). Contributions from the individual dication states are extracted with gates as indicated in Fig. 13, and hence their sum does not reflect the total (blue) yield (see text).

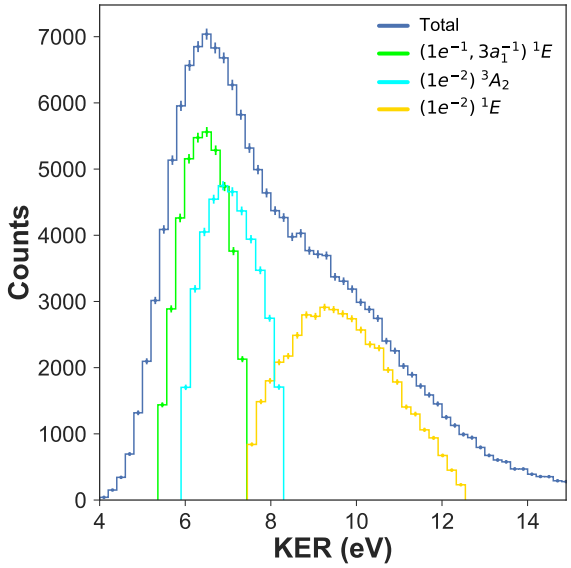


FIG. 15. The $NH^+ + H^+ + H$ three-body yield, after PDI of $NH_3$ at 61.5 eV, as a function of the KER (shown in blue). The distributions for the three contributing dication states are shown in their respective color-codes (shown in green, cyan, and gold, and multiplied by a factor of 1.5 for improved visibility). Contributions from the individual dication states are extracted with gates as indicated in Fig. 13, and hence their sum does not reflect the total (blue) yield (see text).

for the $(1e^{-2})\ ^1E$ dication state. These branching ratios are derived in the same manner as described in the two-body breakup section. As before, the main contribution to the uncertainty of the branching ratio is rooted in the aforementioned electron pair dead-time, which influences the detection yield of the electron-ion coincidences for each dication state as a function of the electron sum energy. Applying the simulation mentioned above, we estimate the total possible loss in PDI yield for electron sum energies of 19.7 eV ($(3a_1^{-1}, 1e^{-1})\ ^1E$), 18.3 eV ($(1e^{-2})\ ^3A_2$), and 16.8 eV ($(1e^{-2})\ ^1E$) to be 6.5%, 7.1%, and 7.9%, respectively. This translates to an error of up to 4% in the branching ratio. Errors due to deviations from the assumed Gaussian shape of each feature in the fitting process and the quality of the fit are estimated to be small (both <1%).

The energetics observed in the PES cuts of

Fig. 1(b), Fig. 13, and Table III indicate that the $(3a_1^{-1}, 1e^{-1})$ $^1E$ dication state dissociates to the $NH^+(^2\Pi) + H^+ + H(^2S)$ limit, with the $(1e^{-2})$ $^3A_2$ and $(1e^{-2})$ $^1E$ states dissociating to this very same limit. This finding suggests that following PDI of $NH_3$ to either of these $E$ symmetry dication states, i.e. the $(3a_1^{-1}, 1e^{-1})$ $^1E$ and $(1e^{-2})$ $^1E$ states, three-body dissociation ensues on the $A'$ symmetry PESs, shown in Fig. 1(b). In the case of the $(3a_1^{-1}, 1e^{-1})$ $^1E$ dication state, the $A''$ symmetry curve possesses a large barrier to dissociation, whereas fragmentation on the $A'$ symmetry curve is much more favorable. As for the $(1e^{-2})$ $^1E$ state, we do not observe fragmentation on the $A''$ symmetry curve, although the PES cuts shown in Fig. 1(b) indicate that the excitation lies above the shallow barrier of this curve. However, similar to the case of the $(3a_1^{-1}, 1e^{-1})$ $^1E$ dication state the fragmentation on the $A'$ symmetry curve is favored in the $(1e^{-2})$ $^1E$ state. Populating the $(1e^{-2})$ $^3A_2$ dication state results in direct three-body fragmentation on the PES (which is not doubly degenerate in the FC region like the $E$ symmetry states), reaching the $NH^+(^2\Pi) + H^+ + H(^2S)$ limit. We point out that at large internuclear separations (>18 Bohr) a charge-exchange mechanism was observed between the $NH^+$ and H fragments in this dication state, which produces the fragments $NH + H^+ + H^+$ and is discussed in detail in [I]. An analogous asymptotic electron transfer mechanism has also been observed in dissociative electron attachment to $NH_3$ [39].

To determine if there are preferred molecular orientations where PDI of $NH_3$ occurs for each of the three dication states, we plot in Fig. 16(a), (b), and (c) the yield of the $NH^+ + H^+ + H$ three-body fragmentation as a function of the cosine of the relative angle between the recoil axis of the charged fragments of the molecular breakup ($NH^+$-$H^+$) and the XUV polarization ($\varepsilon$). While in a three-body breakup all particles carry away momentum, we can deduce from the PIPICO spectrum, presented in Fig. 2, that for the most part the charged fragments solely compensate their momenta, while the third particle (the neutral H atom) takes on a spectator role. This becomes apparent by examining the TOF correlation of the $NH^+ + H^+ + H$ channel, which is almost as wide in the TOF difference and as narrow in the TOF sum as the $NH_2^+ + H^+$ two-body fragmentation. This underlines that the charged fragments of the three-body breakup repel each other and interact with each other via the Coulomb force over a long range of internuclear distances. Thus, their recoil axis, which is calculated via the difference of the measured momenta, appears to be an appropriate choice for a distinguished axis. We will see later that the relative angle between the charged fragments almost exclusively peaks at 180° and the neutral H fragment carries away rather little kinetic energy (Fig. 17), further supporting this selection.

Eq. 1 is valid for any vectorial quantity arising from single-photon ionization of a randomly oriented sample by linearly polarized light. Consequently it can be applied to the recoil axis of the charged fragments $H^+ + NH^+$ of the three-body breakup channel as well. For the $(3a_1^{-1}, 1e^{-1})$ $^1E$ and $(1e^{-2})$ $^3A_2$ dication states, we observe an enhancement in PDI for molecular orientations where the $NH^+ + H^+$ recoil axis is orientated at a $\sim 90°$ angle with respect to the polarization vector. As in the two-body breakup case, this roughly coincides with the $C_{3v}$ symmetry axis of the molecule. We find a $\beta_2$ value of $-0.27 \pm 0.01$. In the $(3a_1^{-1}, 1e^{-1})$ $^1E$ dication state, the PDI involves the $3a_1$ orbital, which is aligned along the molecular $C_{3v}$ axis. This could explain the enhancement in PDI at geometries where the polarization vector of the ionizing field is directed along this orbital, and why this enhancement is reduced in the $(1e^{-2})$ $^3A_2$, where the ionization no longer involves the $3a_1$ orbital. The $\beta_2$ value was determined to be $-0.17 \pm 0.01$. The anisotropy parameter for both states are also listed in Table III.

In contrast, the $(1e^{-2})$ $^1E$ dication state appears to exhibit a small enhancement in PDI for orientations where the recoil axis of the charged $NH^+$ and $H^+$ fragments is orientated at a $\sim 35°$ and $\sim 145°$ angle with the polarization vector [see Fig. 16(c)]. The angular distribution is nearly isotropic, appearing almost flat, meaning that compared to the other two dication states of the three-body breakup, we observe a lower likelihood of PDI where the recoil axis of the charged fragments $NH^+$ and $H^+$ is orientated perpendicular to the polarization vector in the $(1e^{-2})$ $^1E$ state. Here, since the PDI of $NH_3$ no longer involves the $3a_1$ orbital, enhancement near the $C_{3v}$ axis is suppressed. Because the PDI only involves the $1e$ orbital, which lies along the N-H bonds of the molecule, we observe an enhancement in PDI for molecular orientations near angles where the recoil axis of the charged fragments $NH^+$ and $H^+$ lies along the XUV polarization vector. We point out that this interpretation is qualitative and does not explain the aforementioned differences between the $(1e^{-2})$ $^3A_2$ and $(1e^{-2})$ $^1E$ states, which both invoke ionization from solely the $1e$ orbital. We find a $\beta_2$

value of $0.04 \pm 0.01$.

The angular distribution of Fig. 16(c) may be influenced by a breakdown of the axial recoil approximation during the dissociation [40], which can occur for select dication states and has been identified in the PDI of water molecules for a similar photon energy recently [41]. Given the purely statistical error bars, the measured angular distribution for the $(1e^{-2})\ ^1E$ state is somewhat inconsistent with the $\beta_2$ functional form, while for the $(3a_1^{-1}, 1e^{-1})\ ^1E$ and $(1e^{-2})\ ^3A_2$ states, the angular distributions can be accurately fitted by Eq. 1. The inconsistency (Fig. 16(c)) is rather insensitive to fine details of the momentum calibration, and does not appear to be subject to multi-hit problems of the ion and electron detectors, all of which were inspected thoroughly. We could not identify any problems in these analysis domains that could explain the small deviation of the measured angular distribution in Fig. 16(c) from the flat or shallow parabolic form of Eq. 1, but we need to point out that the KER and electron sum energy distributions for the weak $(1e^{-2})\ ^1E$ dication state are quite broad and may overlap with the distributions of the $(1e^{-2})\ ^3A_2$ dication state, as apparent in Fig. 13.

The diffuse features corresponding to the weak $(1e^{-2})\ ^1E$ dication state may also contain background contributions from false coincidences with parent $NH_3^+$ ions and background $H^+$ as well as $H_2^+$ ions (observed as the horizontal and vertical features in Fig. 2). Moreover, a small number of events from the $NH_2^+ + H^+$ two-body breakup channel, which lies adjacent to the $NH^+ + H^+ + H$ channel in the PIPICO spectrum (seen in Fig. 2), can be falsely assigned and may contribute to the two small peaks. The spread in TOF of the $NH_2^+ + H^+$ coincidence feature in Fig. 2 may result in a false assignment of some $NH_2^+ + H^+$ fragment pairs to any of the 3-body channels. Both of the latter two sources of background, although largely eliminated in the calibration and analysis, can be challenging to completely remove in some cases, which can result in select ionization channels being contaminated by a few percent of erroneously assigned events. Since the two small peaks in Fig. 16(c) lie only a few ($\sim 5\% \pm 1\%$) percent above the isotropic distribution, we speculate that these features arise from any of the three forms of pollution mentioned above, and do not point towards some unusual dissociation mechanism or previously unobserved photodissociation dynamics of the $(1e^{-2})\ ^1E$ dication state of $NH_3$.

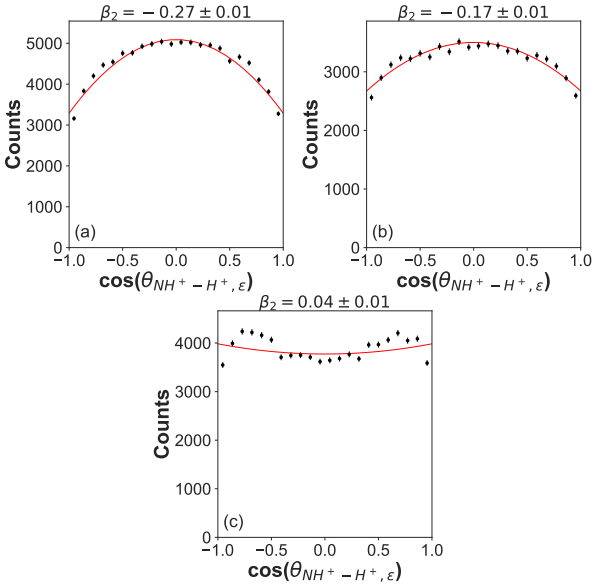


FIG. 16. The $NH^+ + H^+ + H$ three-body fragmentation yield, after PDI of $NH_3$ at 61.5 eV, as a function of the cosine of the measured relative angle between the $NH^+$-$H^+$ recoil axis and the XUV polarization vector $\varepsilon$ for the (a) $(3a_1^{-1}, 1e^{-1})\ ^1E$, (b) the $(1e^{-2})\ ^3A_2$, and (c) the $(1e^{-2})\ ^1E$ dication states. The fits, representing the parametrizations in terms of the anisotropy (see Eq. 1), are shown in red, where the retrieved $\beta_2$ value is shown above each plot.

In Fig. 17 we plot on a logarithmic scale the $NH^+ + H^+ + H$ three-body fragmentation yield, following the PDI of $NH_3$ by 61.5 eV photons, as a function of the cosine of the measured relative angle between the $NH^+$ and $H^+$ ion momenta, and the kinetic energy of the neutral H fragment. The triangular shape of the distribution is governed by momentum conservation of the three fragments, and we use it to elucidate the interaction between the heavy particles during the dissociation as a function of the $NH_3^{2+}$ state. All three distributions are peaked at 180°, indicating a preferred back-to-back emission between the photoions with the neutral H largely spectating. However, as the H fragment receives more kinetic energy from the dissociation, the relative angle between the two $NH^+$ and $H^+$ ionic fragments correspondingly opens up, which becomes nicely apparent in this 2D-spectrum. We observe that the range of angles spanned between the two photoions, following the PDI to the $(3a_1^{-1}, 1e^{-1})\ ^1E$ and $(1e^{-2})\ ^3A_2$ dication states [Fig. 17(a) and (b)], is broader than in the $(1e^{-2})\ ^1E$ state [Fig. 17(c)]. The range of ki-

netic energies spanned by the neutral H fragment is broader in the $(1e^{-2})\ ^1E$ dication state [Fig. 17(c)] compared with the $(3a_1^{-1}, 1e^{-1})\ ^1E$ and $(1e^{-2})\ ^3A_2$ dication states [Fig. 17(a) and (b)]. We also observe a difference in the correlation between the kinetic energy of the neutral H and the measured relative angle between the $NH^+$ and $H^+$ photoions. The dashed silver lines in Figs. 17(a), (b), and (c) are intended to guide the eye towards the slope of the features and improve the visibility of the energy-angle correlations. In the $(3a_1^{-1}, 1e^{-1})\ ^1E$ and $(1e^{-2})\ ^3A_2$ dication states [Fig. 17(a) and (b)] the angle between the $NH^+$ and $H^+$ fragments opens up more rapidly than in the $(1e^{-2})\ ^1E$ state [Fig. 17(c)], as the neutral H fragment takes away more kinetic energy. This suggests that the neutral H fragment acts more like a passive spectator in the dissociation that ensues following PDI to the $(1e^{-2})\ ^1E$ dication state as compared to the dissociation from the $(3a_1^{-1}, 1e^{-1})\ ^1E$ and $(1e^{-2})\ ^3A_2$ dication states, which show a stronger influence of the kinetic energy of the neutral H fragment on the relative angle between the photoions.

Next, we display the $NH^+ + H^+ + H$ three-body fragmentation yield as a function of the energy sharing between the two photoelectrons for the three features that correspond with the three dication states. These results are shown in Fig. 18(a), (b), and (c). As before, we attribute the sharp features near 0 and 1, observed in Fig. 18(a), (b), and (c), to an autoionization process, corresponding with a fast photoelectron and slow electron emerging from autoionization. The fraction of PDI via autoionization relative to direct PDI is $\sim 5.6\% \pm 2.0\%$ in the $(3a_1^{-1}, 1e^{-1})\ ^1E$ state, $\sim 7.6\% \pm 1.1\%$ in the $(1e^{-2})\ ^3A_2$ state, and $\sim 7.7\% \pm 2.1\%$ in the $(1e^{-2})\ ^1E$ dication state. This fraction is estimated using the same protocol described in the two-body breakup section.

Lastly, we plot in Fig. 19, Fig. 20, and Fig. 21 the $NH^+ + H^+ + H$ three-body fragmentation yield as a function of the cosine of the relative emission angle between the two photoelectrons, (a) integrated over all energy sharing conditions and (b) in an equal energy sharing condition for the three dication states. There are no conditions enforced on either the molecular orientation nor the emission angle of the first detected photoelectron relative to the polarization vector of the XUV beam. In the equal energy sharing case the relative angle is plotted for $0.425 < \rho < 0.575$. As pointed out in the two-body breakup section, our measurement suffers from some multi-hit detector dead-time effects, in-

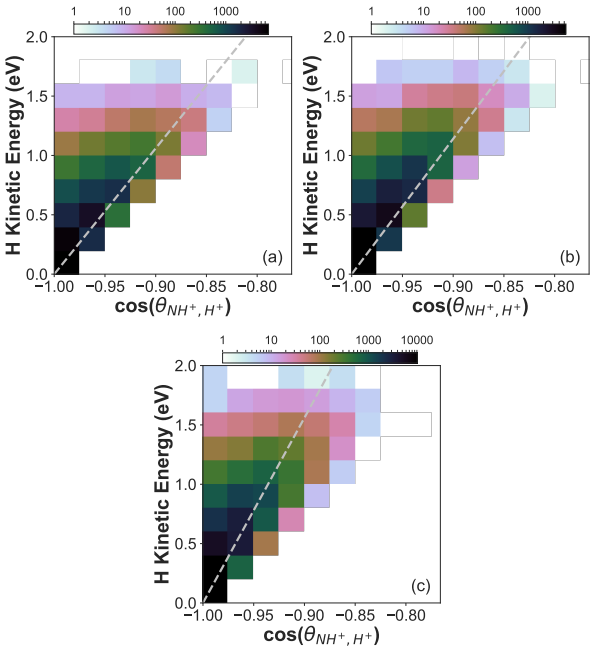


FIG. 17. The $NH^+ + H^+ + H$ three-body fragmentation yield after PDI of $NH_3$ at 61.5 eV as a function of the cosine of the measured relative angle between the $NH^+$ and $H^+$ fragment momentum vectors and the kinetic energy of the neutral H fragment, for the (a) the $(3a_1^{-1}, 1e^{-1})\ ^1E$ , (b) the $(1e^{-2})\ ^3A_2$, and (c) the $(1e^{-2})\ ^1E$ dication states. The dashed silver line in each figure serves to guide to the eye towards the slope of the feature.

fluencing the measured yield of photoelectrons emitted in the same direction with similar kinetic energies. In the equal energy sharing condition and for $\theta_{e_1,e_2} \leq 90°$ this corresponds with a maximum loss of $\sim$20% of the events for the $(3a_1^{-1}, 1e^{-1})\ ^1E$ state, $\sim$21% for the $(1e^{-2})\ ^3A_2$ state, and $\sim$23% for the $(1e^{-2})\ ^1E$ state. Like in the two-body breakup case we believe that the actual loss is at least a factor of two smaller than the worst-case scenario listed above, i.e. closer to our simulated results for the unequal electron energy sharing case. As in the two-body breakup section, we refrain from showing the photoelectron angular distribution of the unequal energy sharing case, which captures the autoionization feature, as there is a significant contribution due to direct PDI that significantly pollutes the autoionization signal and prevents a clear analysis of this relative angular distribution.

The relative angles between the two electrons, integrated over all energy sharing cases, show a preferred emission of the two particles into opposite

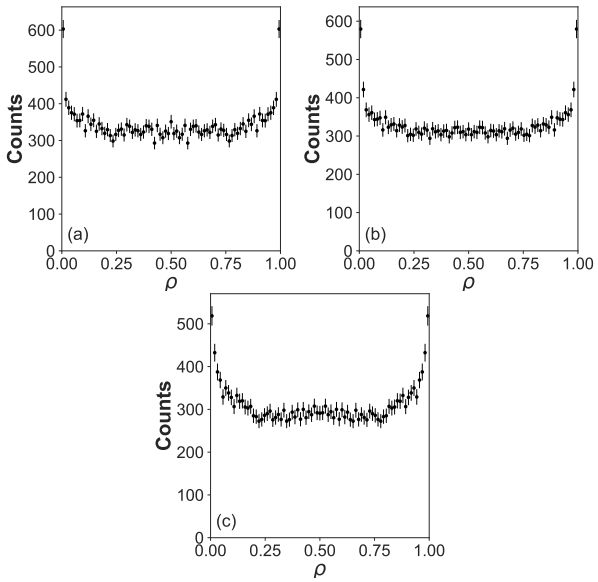


FIG. 18. The $NH^+ + H^+ + H$ three-body fragmentation yield, after PDI of $NH_3$ at 61.5 eV, as a function of the electron energy sharing $\rho$ (Eq. 2) for the (a) $(3a_1^{-1}, 1e^{-1})$ $^1E$, (b) the $(1e^{-2})$ $^3A_2$, and (c) the $(1e^{-2})$ $^1E$ dication states.

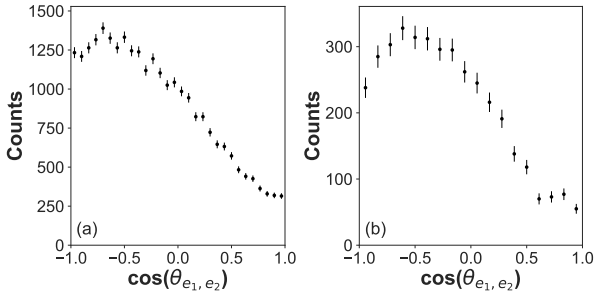


FIG. 19. The $NH^+ + H^+ + H$ three-body fragmentation yield, after PDI of $NH_3$ at 61.5 eV, as a function of cosine of the relative emission angle between the two photoelectrons for the $(3a_1^{-1}, 1e^{-1})$ $^1E$ dication state, (a) integrated over all possible electron energy sharing and (b) for equal energy sharing ($\rho = 0.5 \pm 0.075$).

hemispheres. The distribution for the $(3a_1^{-1}, 1e^{-1})$ $^1E$ dication state [Fig. 19(a)] peaks at 135° with a notable dip at 180° corresponding to a back-to-back emission. The $(1e^{-2})$ $^3A_2$ state [Fig. 20(a)] peaks at 130° with a slight increase at 180° compared to the $(3a_1^{-1}, 1e^{-1})$ $^1E$ dication state. The $(1e^{-2})$ $^1E$ state [Fig. 21(a)] has a peak at 120°, but now exhibits dominating back-to-back emission between the two electrons.

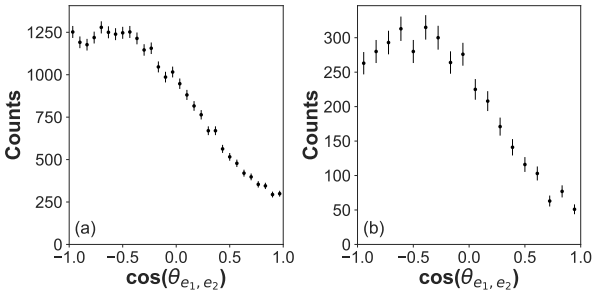


FIG. 20. The $NH^+ + H^+ + H$ three-body fragmentation yield, after PDI of $NH_3$ at 61.5 eV, as a function of the cosine of the relative emission angle between the two photoelectrons in two different energy sharing conditions for the $(1e^{-2})$ $^3A_2$ dication state, (a) integrated over all possible electron energy sharing and (b) for equal energy sharing ($\rho = 0.5 \pm 0.075$).

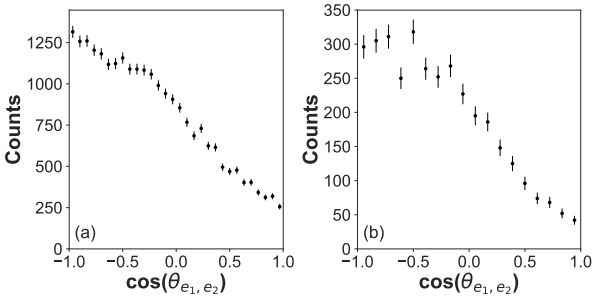


FIG. 21. The $NH^+ + H^+ + H$ three-body fragmentation yield, after PDI of $NH_3$ at 61.5 eV, as a function of the cosine of the relative emission angle between the two photoelectrons in two different energy sharing conditions for the $(1e^{-2})$ $^1E$ dication state, (a) integrated over all possible electron energy sharing and (b) for equal energy sharing ($\rho = 0.5 \pm 0.075$).

The photoelectron dynamics in the equal energy sharing condition [Fig. 19(b), Fig. 20(b), and Fig. 21(b)], again, reveals similar anisotropic angular distributions, which possess node-like features near 0° relative electron-electron emission angle and a peak at approximately 125° for the $(3a_1^{-1}, 1e^{-1})$ $^1E$ state, 115° for the $(1e^{-2})$ $^3A_2$ state, and 120° for the $(1e^{-2})$ $^1E$ state. A dip at 180° remains visible. All three dication states resemble the dynamics of a knock-out double ionization process. In all three cases, the likelihood for an emission of the two electrons in the same direction is roughly a factor of 10 less likely than the emission at peak angle.

## V. CONCLUSION

In this experiment we performed state-selective measurements on the two-body $NH_2^+ + H^+$ and three-body $NH^+ + H^+ + H$ dissociation channels of neutral $NH_3$, following PDI at 61.5 eV, where the two photoelectrons and two cations were detected in coincidence on an event-by-event basis using charged particle 3-D momentum imaging. With the help of theory, five dication states could be identified as active in this photon energy range and assigned to the two different breakup channels. Three of these PDI channels produce ro-vibrationally excited ionic fragments, where the $(3a_1^{-1}, 1e^{-1})$ $^1E$ and $(3a_1^{-1}, 1e^{-1})$ $^3E$ dication states lead to hot $NH_2^+$ fragments, while the $(1e^{-2})$ $^3A_2$ dication state leads to a hot $NH^+$ fragment.

Our measurement identifies three dication electronic states that dissociate to $NH_2^+ + H^+$ fragments, which are populated via direct PDI as well as through autoionization. We observe that the initial excitations in one of these dication states, the $(3a_1^{-2})$ $^1A_1$ state, undergoes intersystem crossing preceding dissociation. This effect has been observed before, but only close to the PDI threshold. By plotting the relative angle between the recoil axis of the molecular breakup and polarization vector of the XUV beam, we see an anisotropic PDI yield that illustrates the connection between the molecular orbitals participating in the PDI and the molecular orientations experiencing enhanced PDI.

In the three-body dissociation channel of $NH_3^{2+}$ we identify three contributing dication states, two of which are different from the states of the two-body breakup channel, that dissociate to $NH^+ + H^+ +$ H fragments. However, these state are also populated via the same ionization mechanisms, i.e. direct PDI and autoionization. In contrast to the two-body fragmentation channel, in this three-body breakup channel we observe that the three contributing dication states directly dissociate without any non-adiabatic transitions preceding the fragmentation. Plotting the relative angle between the recoil axis of the charged fragments of the breakup and the polarization vector of the XUV beam again demonstrates the connection between the molecular orbitals participating in the PDI and the molecular orientations experiencing enhanced PDI. Moreover, the dissociation of the two dication states of the three-body fragmentation result in different spectator roles of the neutral H atom.

Lastly, we presented the relative electron-electron angular distribution of all dication electronic states for all and equal electron-electron energy sharing. The distributions indicate the dominance of a knock-out PDI mechanism in all cases, and they are similar to the kinematics reported for the PDI of atoms (He) and small molecules ($D_2$ and $H_2O$) for comparable excess energies [35, 36, 42, 43].

## VI. ACKNOWLEDGMENTS

Work at LBNL was supported by the U.S. Department of Energy, Office of Science, Office of Basic Energy Sciences, Division of Chemical Sciences, Biosciences, and Geosciences under contract No. DE-AC02-05CH11231 and used the Advanced Light Source and National Energy Research Computing Center. JRML personnel were supported by the same US DOE funding source under Award No. DE-FG02-86ER13491. A.G. was supported by the ALS through a Doctoral Fellowship in Residence. Personnel from the University of Nevada, Reno was supported by the National Science Foundation Grant No. NSF-PHY-1807017. The Frankfurt group acknowledges the support of the Deutsche Akademische Austausch Dienst (DAAD) and the Deutsche Forschungsgemeinschaft (DFG). We thank the staff at the Advanced Light Source for operating beamline 10.0.1.3 and providing the photon beam. Moreover, we thank the RoentDek GmBH for longtime support with detector hardware and software.

[1] B Gaire, DJ Haxton, FP Sturm, J Williams, A Gatton, I Bocharova, N Gehrken, M Schöffler, H Gassert, S Zeller, et al. Auger decay and subsequent fragmentation pathways of ethylene following k-shell ionization. *Physical Review A*, 92(1):013408, 2015.

[2] B Gaire, I Bocharova, FP Sturm, N Gehrken, J Rist, H Sann, M Kunitski, J Williams, MS Schöffler, T Jahnke, et al. Hydrogen and fluorine migration in photo-double-ionization of 1, 1-difluoroethylene (1, 1-c 2 h 2 f 2) near and above threshold. *Physical Review A*, 89(4):043423, 2014.

[3] B Gaire, SY Lee, DJ Haxton, PM Pelz, I Bocharova, FP Sturm, N Gehrken, M Honig, M Pitzer, D Metz, et al. Photo-double-ionization of ethylene and acetylene near threshold. *Physical Review A*, 89(1): 013403, 2014.

[4] David R Yarkony. Diabolical conical intersections. *Reviews of Modern Physics*, 68(4):985, 1996.

[5] D. Winkoun and G. Dujardin. Fragmentation of doubly charged ammonia cations nh3++studied by the photoion-photoion coincidence (pipico) method. *Zeitschrift für Physik D Atoms, Molecules and Clusters*, 4(1):57–64, Mar 1986. ISSN 1431-5866. doi: 10.1007/BF01432498. URL https://doi.org/10.1007/BF01432498.

[6] M Stankiewicz, P A Hatherly, L J Frasinski, K Codling, and D M P Holland. The double photoionisation of NH3using the triple coincidence (PEPIPICO) technique. *Journal of Physics B: Atomic, Molecular and Optical Physics*, 22(1):21–31, jan 1989. doi:10.1088/0953-4075/22/1/006. URL https://doi.org/10.1088%2F0953-4075%2F22%2F1%2F006.

[7] R. Locht, M. Davister, W. Denzer, H.W. Jochims, and H. Baumgärtel. About the double ionization of ammonia and carbon dioxide. a comparison between photoionization and electron impact. *Chemical Physics*, 138(2):433 – 440, 1989. ISSN 0301-0104. doi:https://doi.org/10.1016/0301-0104(89)87149-6. URL http://www.sciencedirect.com/science/article/pii/0301010489871496.

[8] R. Locht and J. Momigny. The double ionization of ammonia. its dissociation into the doubly ionized fragment n2+. *Chemical Physics Letters*, 138(5):391 – 396, 1987. ISSN 0009-2614. doi:https://doi.org/10.1016/0009-2614(87)80527-4. URL http://www.sciencedirect.com/science/article/pii/0009261487805274.

[9] John H.D. Eland. Double photoionisation spectra of methane, ammonia and water. *Chemical Physics*, 323(2):391 – 396, 2006. ISSN 0301-0104. doi: https://doi.org/10.1016/j.chemphys.2005.09.047. URL http://www.sciencedirect.com/science/article/pii/S0301010405004829.

[10] F. Tarantelli, A. Tarantelli, A. Sgamellotti, J. Schirmer, and L.S. Cederbaum. On the doubly ionized states of ammonia. *Chemical Physics Letters*, 117(6):577 – 582, 1985. ISSN 0009-2614. doi:https://doi.org/10.1016/0009-2614(85)80305-5. URL http://www.sciencedirect.com/science/article/pii/0009261485803055.

[11] James AR Samson, GN Haddad, and LD Kilcoyne. Absorption and dissociative photoionization cross sections of nh3 from 80 to 1120 å. *The Journal of chemical physics*, 87(11):6416–6422, 1987.

[12] J Appell and JA Horsley. Electronic states of doubly ionized ammonia. *The Journal of Chemical Physics*, 60(9):3445–3448, 1974.

[13] TD Märk, F Egger, and M Cheret. Ionization of ammonia and deuterated ammonia by electron impact from threshold up to 180 ev. *The Journal of Chemical Physics*, 67(8):3795–3802, 1977.

[14] ML Langford, FM Harris, PG Fournier, and J Fournier. Determination of singlet-and triplet-state energies of the doubly ionized ammonia molecule by double-charge-transfer spectroscopy. *International journal of mass spectrometry and ion processes*, 116(1):53–69, 1992.

[15] WJ Griffiths and FM Harris. An experimental determination of the energy of the first triplet doubly-ionized state of ammonia. *Rapid Communications in Mass Spectrometry*, 4(10):366–368, 1990.

[16] Robert Locht, Ch Servais, M Ligot, Fr Derwa, and J Momigny. The dissociative electroionization of ammonia and ammonia-d3. i. the nh+ and nh2+ dissociation channels. *Chemical physics*, 123(3): 443–454, 1988.

[17] JM White, RR Rye, and JE Houston. Experimental auger electron spectrum of ammonia. *Chemical Physics Letters*, 46(1):146–150, 1977.

[18] R Camilloni, G Stefani, and A Giardini-Guidoni. The measured auger electron spectrum of ammonia vapour. *Chemical Physics Letters*, 50(2):213–217, 1977.

[19] Martin T Økland, Knut Fægri Jr, and Rolf Manne. Calculated auger emission spectrum of ammonia. *Chemical Physics Letters*, 40(2):185–188, 1976.

[20] Dwight R Jennison. Initial-state relaxation effects in molecular auger spectra. *Physical Review A*, 23 (3):1215, 1981.

[21] RK Boyd, S Singh, and JH Beynon. Delayed predissociation and collision-induced processes of the ammonia di-cation nh32+. *Chemical physics*, 100 (2):297–314, 1985.

[22] T Ishihara, K Hino, and JH McGuire. Photoionization of two electrons in helium. *Physical Review A*, 44(11):R6980, 1991.

[23] Kirk A. Larsen, Thomas N. Rescigno, Travis Severt, Zachary L. Streeter, Wael Iskandar, Saijoscha Heck, Averell Gatton, Elio G. Champenois, Richard Strom, Bethany Jochim, Dylan Reedy, Demitri Call, Robert Moshammer, Reinhard Dörner, Allen L. Landers, Joshua B. Williams, C. William McCurdy, Robert R. Lucchese, Itzik Ben-Itzhak, Daniel S. Slaughter, and Thorsten Weber. Photoelectron and fragmentation dynamics of the $h^+ + h^+$ dissociative channel in $nh_3$ following direct single-photon double ionization. *Phys. Rev. Research*, 2:043056, Oct 2020. doi:10.1103/PhysRevResearch.2.043056. URL https://link.aps.org/doi/10.1103/PhysRevResearch.2.043056.

[24] R. Dörner, V. Mergel, O. Jagutzki, L. Spielberger, J. Ullrich, R. Moshammer, and H. Schmidt-Böcking. Cold Target Recoil Ion Momentum Spectroscopy: a 'momentum microscope' to view

atomic collision dynamics. *Physics Reports*, 330(2-3):95–192, June 2000. ISSN 0370-1573. doi:doi: DOI: 10.1016/S0370-1573(99)00109-X. URL http://www.sciencedirect.com/science/article/B6TVP-401HH57-1/2/587a27ccbfe492bcbe5b72191579ddbd.

[25] Joachim Ullrich, Robert Moshammer, Alexander Dorn, Reinhard Dörner, L Ph H Schmidt, and H Schmidt-Böcking. Recoil-ion and electron momentum spectroscopy: reaction-microscopes. *Reports on Progress in Physics*, 66(9):1463, 2003.

[26] Ottmar Jagutzki, Alfred Cerezo, Achim Czasch, R Dorner, M Hattas, Min Huang, Volker Mergel, Uwe Spillmann, Klaus Ullmann-Pfleger, Thorsten Weber, et al. Multiple hit readout of a microchannel plate detector with a three-layer delay-line anode. *IEEE Transactions on Nuclear Science*, 49(5): 2477–2483, 2002.

[27] A. Czasch, T. Jahnke, and M. Shoeffler. Lmf2root v1.6 (2008–2013). URL http://www.atom.uni-frankfurt.de/czasch/default_files/software/LMF_tools/lmf2root/.

[28] Till Jahnke. Lmf2root 2... in a nutshell. 2013. *LMF2Root Dokumentation*.

[29] T. N. Rescigno and B. I. Schneider. *J. Phys. B: At. Mol. Opt. Phys.*, 21:L691, 1988.

[30] W. Vanroose, D. A. Horner, F. Martín, T. N. Rescigno, and C. W. McCurdy. Double photoionization of aligned molecular hydrogen. *Phys. Rev. A*, 74:052702, Nov 2006. doi: 10.1103/PhysRevA.74.052702. URL https://link.aps.org/doi/10.1103/PhysRevA.74.052702.

[31] Richard N Zare. Angular momentum. *Understanding Spatial Aspects in Chemistry and Physics*, 1988.

[32] Chris H Greene and Richard N Zare. Photofragment alignment and orientation. *Annual Review of Physical Chemistry*, 33(1):119–150, 1982.

[33] X-J Liu, R R Lucchese, A N Grum-Grzhimailo, Y Morishita, N Saito, G Prümper, and K Ueda. Molecular-frame photoelectron and electron-frame photoion angular distributions and their interrelation. *Journal of Physics B: Atomic, Molecular and Optical Physics*, 40(3):485–496, jan 2007. doi: 10.1088/0953-4075/40/3/004. URL https://doi.org/10.1088%2F0953-4075%2F40%2F3%2F004.

[34] Bradley Efron. Bootstrap methods: another look at the jackknife. In *Breakthroughs in statistics*, pages 569–593. Springer, 1992.

[35] H Bräuning, R Dörner, C L Cocke, M H Prior, B Krässig, A S Kheifets, I Bray, A Bräuning-Demian, K Carnes, S Dreuil, V Mergel, P Richard, J Ullrich, and H Schmidt-Böcking. Absolute triple differential cross sections for photo-double ionization of helium - experiment and theory. *Journal of Physics B: Atomic, Molecular and Optical Physics*, 31(23):5149–5160, dec 1998. doi: 10.1088/0953-4075/31/23/012. URL https://doi.org/10.1088%2F0953-4075%2F31%2F23%2F012.

[36] Th. Weber, A. Czasch, O. Jagutzki, A. Müller, V. Mergel, A. Kheifets, J. Feagin, E. Rotenberg, G. Meigs, M. H. Prior, S. Daveau, A. L. Landers, C. L. Cocke, T. Osipov, H. Schmidt-Böcking, and R. Dörner. Fully differential cross sections for photo-double-ionization of $d_2$. *Phys. Rev. Lett.*, 92:163001, Apr 2004. doi:10.1103/PhysRevLett.92.163001. URL https://link.aps.org/doi/10.1103/PhysRevLett.92.163001.

[37] Thorsten Weber, Achim O Czasch, Ottmar Jagutzki, AK Müller, Volker Mergel, Anatoli Kheifets, Eli Rotenberg, George Meigs, Mike H Prior, Sebastian Daveau, et al. Complete photofragmentation of the deuterium molecule. *Nature*, 431(7007):437–440, 2004.

[38] Dominique Akoury, K Kreidi, T Jahnke, Th Weber, A Staudte, M Schöffler, N Neumann, J Titze, L Ph H Schmidt, A Czasch, et al. The simplest double slit: interference and entanglement in double photoionization of h2. *Science*, 318(5852):949–952, 2007.

[39] T. N. Rescigno, C. S. Trevisan, A. E. Orel, D. S. Slaughter, H. Adaniya, A. Belkacem, Marvin Weyland, Alexander Dorn, and C. W. McCurdy. Dynamics of dissociative electron attachment to ammonia. *Phys. Rev. A*, 93:052704, May 2016. doi:10.1103/PhysRevA.93.052704. URL https://link.aps.org/doi/10.1103/PhysRevA.93.052704.

[40] T Peter Rakitzis and Richard N Zare. Photofragment angular momentum distributions in the molecular frame: determination and interpretation. *The Journal of chemical physics*, 110(7):3341–3350, 1999.

[41] Zachary L Streeter, Frank L Yip, Robert R Lucchese, Benoit Gervais, Thomas N Rescigno, and C William McCurdy. Dissociation dynamics of the water dication following one-photon double ionization. i. theory. *Physical Review A*, 98(5):053429, 2018.

[42] J. M. Randazzo, G. Turri, P. Bolognesi, J. Mathis, L. U. Ancarani, and L. Avaldi. Photo-double-ionization of water at 20 ev above threshold. *Phys. Rev. A*, 101:033407, Mar 2020. doi:10.1103/PhysRevA.101.033407. URL https://link.aps.org/doi/10.1103/PhysRevA.101.033407.

[43] A Knapp, B Krässig, A Kheifets, I Bray, Th Weber, A L Landers, S Schössler, T Jahnke, J Nickles, S Kammer, O Jagutzki, L Ph H Schmidt, M Schöffler, T Osipov, M H Prior, H Schmidt-Böcking, C L Cocke, and R Dörner. Photo double ionization of helium 100 eV and 450 eV above threshold: III. gerade and ungerade amplitudes and their relative phases. *Journal of Physics B: Atomic, Molecular and Optical Physics*, 38(6):645–657, mar 2005. doi: 10.1088/0953-4075/38/6/003. URL https://doi.

org/10.1088%2F0953-4075%2F38%2F6%2F003.

# Strong Field Ionization of Water II: Electronic and Nuclear Dynamics En Route to Double Ionization

Chuan Cheng,[1] Zachary L. Streeter,[2,3] Andrew J. Howard,[4,5] Michael Spanner,[6,7] Robert R. Lucchese,[2] C. William McCurdy,[2,3] Thomas Weinacht,[1] Philip H. Bucksbaum,[4,5,8] and Ruaridh Forbes[4,8,9,*]

[1] *Department of Physics, Stony Brook University, Stony Brook, NY 11794, USA*
[2] *Chemical Sciences Division, Lawrence Berkeley National Laboratory, Berkeley, CA 94720, USA*
[3] *Department of Chemistry, University of California, Davis, CA 95616, USA*
[4] *Stanford PULSE Institute, SLAC National Accelerator Laboratory 2575 Sand Hill Road, Menlo Park, CA 94025, USA*
[5] *Department of Applied Physics, Stanford University, Stanford, CA 94305, USA*
[6] *National Research Council of Canada, 100 Sussex Drive, Ottawa K1A 0R6, Canada*
[7] *Department of Physics, University of Ottawa, Ottawa K1N 6N5, Canada*
[8] *Department of Physics, Stanford University, Stanford, CA 94305, USA*
[9] *Linac Coherent Light Source, SLAC National Accelerator Laboratory, Menlo Park, California 94025, USA*

We investigate the role of nuclear motion and strong-field-induced electronic couplings during the double ionization of deuterated water using momentum-resolved coincidence spectroscopy. By examining the three-body dicationic dissociation channel, $D^+/D^+/O$, for both few- and multi-cycle laser pulses, strong evidence for intra-pulse dynamics is observed. The extracted angle- and energy-resolved double ionization yields are compared to classical trajectory simulations of the dissociation dynamics occurring from different electronic states of the dication. In contrast with measurements of single photon double ionization, pronounced departure from the expectations for vertical ionization is observed, even for pulses as short as 10 fs in duration. We outline numerous mechanisms by which the strong laser field can modify the nuclear wavefunction en-route to final states of the dication where molecular fragmentation occurs. Specifically, we consider the possibility of a coordinate-dependence to the strong-field ionization rate, intermediate nuclear motion in monocation states prior to double ionization, and near-resonant laser-induced dipole couplings in the ion. These results highlight the fact that, for small and light molecules such as $D_2O$, a vertical-transition treatment of the ionization dynamics is not sufficient to reproduce the features seen experimentally in the strong field coincidence double-ionization data.

## I. Introduction

Investigations into the mechanisms of strong-field ionization (SFI) remain an important cornerstone in ultrafast science research due to its central role in strong-field induced phenomena such as high-harmonic generation [1–3], laser-induced electron diffraction [4–6] and Coulomb-explosion imaging [7, 8]. SFI has also been used as a "pump" for experiments that aim to study charge transfer or charge migration in molecular cations [9–12]. For molecular systems this continued interest is in part due to the complexity of the SFI process when compared with atomic systems [13, 14]. Critical differences that are partially responsible for this are: the spatial arrangement of the nuclei that give rise to the molecular structure; the presence of internal degrees of freedom, vibrations and rotations; and the significantly higher density of electronic states that are typically found in these systems [15, 16].

For many experiments, the ideal scenario is that SFI serves as a "sudden" transition, where the nuclei do not move during the pulse that induces the ionization [17–19]. The electron rearrangement that accompanies sudden transitions can be compared to the "vertical" transitions that describe weak-field perturbative ionization, where a portion of the ground state vibrational wave function is projected onto the electronic states of the mono- or dication. The notion of a vertical transition is based on the idea that the transition dipole moment for the coupling of two electronic states by a weak (perturbative) external field is roughly independent of nuclear coordinate over the extent of the initial wave function. This allows one to factor the coupling matrix element into an electronic term which is multiplied by an overlap of the initial vibrational wave function with the vibrational eigenstates of the upper electronic state, and thus the initial vibrational wave function is simply "vertically lifted" and pro-

* ruforbes@stanford.edu

jected (mapped) onto the excited state potential energy surface (PES). This assumption is frequently described in terms of the Franck-Condon principle [20].

Nuclear motion during the pulse is not the only mechanism for non-vertical ionization. Coordinate-dependent strong-field ionization rates [21, 22] and impulsive Raman excitation in one of the electronic states could also result in deviations from vertical ionization [23, 24].

Recent work that considered the single-photon double ionization of water showed excellent agreement between the measured and calculated momentum resolved yield of fragment ions assuming vertical ionization [25, 26]. Here we explore the extent to which SFI with short pulses can be considered vertical. Using a combination of coincidence velocity map imaging of fragment ions and trajectory calculations for the three body dissociation dynamics of the molecular dication, we demonstrate that even for very short pulses ($<$ 10 fs), the ionization cannot be considered to be "vertical", but involves reshaping (changes to the first and second moments of the distribution) of the vibrational wavefunction during the ionization dynamics. We discuss different contributions to the wave function reshaping during ionization.

Our measurements, calculations and analysis may help interpret previous work that made use of SFI as probe of excited state dynamics [27–29] and for vibrational wave packet holography [30]. In the case of probing excited state dynamics, while SFI produced qualitatively similar time dependent yields as weak field or single photon ionization, quantitative agreement was not possible [27]. We argue that this is due to variation in SFI rates with nuclear geometry and reshaping of the vibrational wave packet during SFI. While the holography measurements showed very nice agreement between the experiment and theory in terms of the interference fringe positions and visibility, details of the comparison were not perfect due to the limited ion imaging ability and the assumption of vertical ionization. Our work directly examines this assumption and can be thought of as characterizing the instrument response function associated with SFI as a probe. Particularly for early time delays in pump probe experiments, where the initial and final PESs vary significantly with nuclear coordinate, SFI can differ from vertical ionization significantly. Also, for high intensities, one can see enhancement of ionization to higher charge states through charge resonance enhanced ionization, which also violates the notion of vertical ionization [31, 32]. Finally, for pulses longer than 10 fs, experiments and simulations are greatly affected by laser-induced dynamic alignments and couplings between different electronic states [33–36].

In terms of theoretical investigations into the SFI dynamics of water, recent frozen-nuclei time-dependent R-matrix *ab initio* ionization computations on $H_2O$ [37] suggest that laser coupling in the ion can significantly modify the angular dependence of the ionization dynamics when using multi-cycle pulses. However, if intermediate motion takes place on the ionic surface, adding the laser coupling during the ionizing pulse without also including nuclear motion on the laser-coupled ionic states becomes suspect. Motion on the ionic states will affect the phases and populations on each laser-coupled surface, which can in turn affect the ionization dynamics. The current alternative approach to modelling ionization in multi-cycle strong fields when motion in the ion states is present can be seen in studies of $N_2^+$ lasing, where the strategy is to compute half-cycle ionization yields which are then used as inputs into separate laser-coupled ion dynamics computation [38, 39]. This is the approach that we adopt in the present manuscript—our half-cycle ionization yields were presented in a previous paper [36], and herein we carry out the laser-driven ionic dynamics. A more rigorous treatment could involve adding the ionization contributions from different half-cycles to the laser-coupled ion dynamics simulation through inclusion of a source term in a density matrix approach [40].

## II. Experiment

Two similar apparatuses were used to carry out the measurements. Since they are almost the same, we provide a description for the apparatus used to carry out the 10 fs pulse measurements (described in detail in previous work [41, 42]) and indicate any differences for the apparatus used for the 40 fs pulse measurements. Briefly, the output from a commercial amplified Ti:sapphire laser system (1 mJ, 780 nm, 1 kHz) is spectrally broadened using filamentation in Ar gas, and compressed to $\sim$10 fs using chirped mirrors and an acousto-optic pulse shaper [43]. The laser pulses are directed into a vacuum chamber (base pressure of $10^{-10}$ mbar) and focused at the center of a velocity-map imaging (VMI) spectrometer using an in-vacuum concave silver mirror ($f$ = 5 cm). The *in situ* intensity was calibrated by SFI of argon, measuring the classical $2U_p$ cut-

| $C_s$ sym | spin state order | $C_{2\nu}$ sym | $C_{2\nu}$ config | 2-body branching ratio [%] | 3-body branching ratio [%] |
|---|---|---|---|---|---|
| $X^3A"$ | $T_0$ | $^3B_1$ | $(3a_1 1b_1)^{-1}$ | 92 | 8 |
| $2^3A"$ | $T_1$ | $^3A_2$ | $(1b_2 1b_1)^{-1}$ | 0 | 100 |
| $1^3A'$ | $T_2$ | $^3B_2$ | $(1b_2 3a_1)^{-1}$ | 0 | 100 |
| $1^1A'$ | $S_0$ | $1^1A_1$ | $(1b_1)^{-2}$ | 100 | 0 |
| $1^1A"$ | $S_1$ | $^1B_1$ | $(3a_1 1b_1)^{-1}$ | 87 | 13 |
| $2^1A'$ | $S_2$ | $2^1A_1$ | $(3a_1)^{-2}$ | 26 | 74 |
| $2^1A"$ | $S_3$ | $^1A_2$ | $(1b_2 1b_1)^{-1}$ | 0 | 100 |
| $3^1A'$ | $S_4$ | $^1B_2$ | $(1b_2 3a_1)^{-1}$ | 0 | 100 |
| $3^1A"$ | $S_5$ | $3^1A_1$ | $(1b_2)^{-2}$ | 0 | 100 |

TABLE I. Table of electronic states of the water dication in different conventions. Branching ratios are for the dissociation dynamics on the *ab initio* potential surfaces with initial conditions from the Wigner phase space distribution of the ground vibrational state, calculated from $10^5$ trajectories on each potential surface, similar to the calculations in [25, 26].

off for field-ionized electrons from argon [44] at low pulse energies and extrapolating to higher ones (using a procedure outlined in Ref. [45] for the 40 fs measurements). The estimated intensities for the 10 fs and 40 fs measurements are 400 TW/cm$^2$ and 600 TW/cm$^2$, respectively.

Target $D_2O$ molecules are expanded into a separate source chamber and subsequently skimmed to yield an effusive molecular beam [41]. This beam intersects the focused laser at the center of the electrostatic lens stack of the VMI spectrometer [41]. The extracted ions and electrons are recorded using a microchannel plate (MCP), phosphor screen, and Timepix3 camera with 1.5 ns time resolution (a Roentdek hexanode detector, with a time resolution of <1 ns [46] was used for the 40 fs pulse measurements).

In order to ensure the low count rates required for coincident detection of all charged particles, a working pressure of $4\times10^{-10}$ Torr was used throughout the experiment (with a base pressure of about $1\times10^{-10}$ Torr). The adopted pressure resulted in an average event rate of approximately 0.8 per laser shot, which in turn corresponded to an event rate of $< 0.1$ per shot for the double-ionization channels considered in this work. Presented in Table II are the experimentally extracted yields and branching ratios for the dissociation channels following strong-field double ionization. Two-body fragmentation into $OD^+/D^+$ is the dominant channel followed by three-body fragmentations into $D^+/D^+/O$ and $D^+/D/O^+$. In the present work we focus our discussion on the three body $D^+/D^+/O$ fragmentation channel. A detailed analysis of fragmentation into $OD^+/D^+$ was included in an earlier publication, which investigated the roles of dynamic and geometric alignment during water double ionization [35]. We note that our extracted ratios differ significantly in some channels from reported values for single photon double ionization [47] and, more critically, SFI with higher intensity longer duration pulses [48]. Furthermore, we note the absence of the weak $D_2^+/O^+$ channel observed in Ref. [48] for our data recorded with 10 fs pulses. A detailed investigation into the pulse duration dependence of double ionization branching ratios is beyond the scope of the present work.

| channels | counts: uncorrected | efficiency: uncorrected | counts: corrected | efficiency: corrected |
|---|---|---|---|---|
| $D^+/OD^+$ | 6.5x10$^4$ | 0.632 | 3.7x10$^5$ | 0.702 |
| $D^+/D^+/O$ | 3.0x10$^4$ | 0.288 | 8.8x10$^4$ | 0.165 |
| $D^+/O^+/D$ | 8.2x10$^3$ | 0.080 | 7.0x10$^4$ | 0.133 |

TABLE II. Table of branching ratio of relevant water dication dissociation channels. The detection efficiency of different ions are estimated to be 0.58($D^+$), 0.2($O^+$) and 0.3($OD^+$).

## III. Trajectory Calculations

Classical trajectory calculations simulate the conditions of single-photon double ionization of the ground state of $D_2O$ in which the molecule undergoes a Franck-Condon transition to the doubly ionized excited state. The trajectories are propagated on the field free potential surfaces of the lowest nine states of the water dication. Those states are created, in the simple molecular orbital picture, by removing two electrons in all possible ways from the highest three filled molecular orbitals of the neutral as indicated in Table I, leaving the $D_2O^{++}$ ion in all possible spin states for each configuration. The

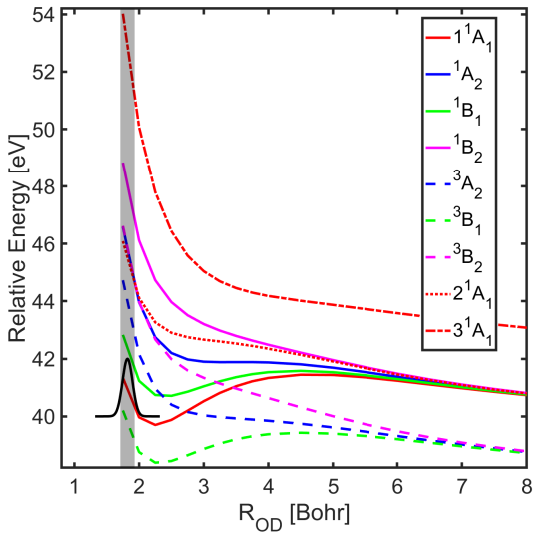


FIG. 1. Potential energy curves for the first nine states of the $D_2O$ di-cation as a function of the symmetric stretch coordinate $R_{OD}$, together with the neutral ground state wave function (solid black line). The vertical shaded grey line illustrates the extent of the ground state wave function. The curves included in this figure are reproduced from Ref. [25].

surfaces were calculated earlier [25, 49] with MOLPRO [50, 51] using internally contracted multireference configuration interaction (icMRCI) methods at the configuration interaction singles and doubles (CISD) level, including the Davidson correction to the CI energy. The full dimensional surfaces were then fitted using a functional form which is a fit (linear least squares) to an accurate form involving 100 basis functions developed by Gervais *et al.* [49].

The trajectory calculations assumed the neutral water molecule is initially in its ground vibrational state with zero total rotational angular momentum. The initial conditions for $10^5$ trajectories on each potential surface were sampled from the Wigner phase space distribution for the computed normal modes of the ground electronic state in icMRCI calculations. The Phase space distribution has the form

$$W(\mathbf{Q},\mathbf{P}) = \frac{1}{(\pi\hbar)^{3N-6}} \prod_{j=1}^{3N-6} e^{-\frac{\omega_j}{\hbar}Q_j^2 - \frac{1}{\hbar\omega_j}P_j^2} \qquad (1)$$

where $N$ is the number of atoms, $w_j$ are the associated frequencies, and the vectors $\mathbf{Q}$ and $\mathbf{P}$ are the normal mode coordinates and momenta, respectively, and is positive definite for the case of the ground state. A similar trajectory study was performed for double ionization of $H_2O$ previously [25] and compared extensively with experimental momentum images [26] from single photon double ionization measurements using the cold target recoil ion momentum spectroscopy (COLTRIMS) technique [52–54]. That comparison validated the accuracy of this *ab initio* treatment of the dissociation of the cation in all but its finest details. The present calculations differ only in the masses of the atoms (D versus H) and the larger number of trajectories on each surface ($10^5$ versus $10^3$). They thus show small quantitative differences from the previous work, for example in the two-body versus three-body dissociation branching ratios.

Classical trajectory calculations with initial rotational angular momentum which are not equal to zero and in the range of angular momenta thermally populated in a supersonic expansion were performed. This additional rotational degree of freedom produces negligible differences from the final momentum distributions of the atomic fragments computed with zero total angular momentum. Further, the importance of rotational dynamics of molecules in the context of strong field ionization was deeply investigated in an earlier publication [35].

The potential energy curves along the symmetric stretch coordinate of the first 9 states of dication are shown in the Fig. 1. The state characters are labelled according to $C_{2\nu}$ symmetry in that figure. Outlined in Table I are the equivalent labelling conventions in other symmetries, together with the dominant electronic configurations for these states near the equilibrium geometry of neutral molecule and the associated two- and three-body theoretical branching ratios for the present case of $D_2O$. The criterion for categorizing a trajectory as three body in this work was that the $R_{OD}$ distance of one deuterium be 200 Bohr or greater and that the other reach at least 50 Bohr. The long distances used for the criterion to separate two-body from three-body dissociation channels are chosen because the diatomic fragments can be produced with vibrational excitation near their dissociation limits. High vibrational and rotational excitation in the products produced by dynamics on several of the potential surfaces is discussed by [49] who compute the internal energy distributions of the diatomic fragments in the two-body channels. In other words, it is long propagation time (1.5ps in this simulation) for three body dissociation but not long enough for the sequential break up. Moreover, the $D^+/O^+/D$ channels are spin for-

bidden from the inital populated states unless the molecule goes through a non-adiabatic transition in the sequential process which is not included in the present simulations but further discussed in [25, 49].

## IV. Measurements

Given the agreement between the trajectory calculations and the single photon double ionization measurements described above, the question we address here is whether strong-field double ionization prepares a similar superposition of states of the dication, and whether the wave packet launched on each state via SFI is similar to the one launched by single photon (weak field) ionization - i.e. can the SFI process be thought of as vertical? We therefore compare the calculated double ionization yield as a function of $\beta$ and KER with our measurements. Fig. 2 shows the measured and calculated $D^+/D^+/O$ yield. Panel (a) shows the measured yield as a function of $\beta$ and KER. Panel (b) shows the calculated yield vs $\beta$ and KER assuming vertical ionization with equal population of the di-cation states. Panel (c) shows the same results as panel (b) with coefficients for the first 9 states of the dication fitted to achieve the best agreement with the measurements. Panel (d) shows the calculated results accounting for experimental broadening of the features due to the limited resolution of our VMI apparatus. Details of which are discussed below.

In the fitting procedure, due to the lack of the spin state information about the oxygen atom, states of the the same $C_{2\nu}$ symmetry (e.g. $^1B_1$ and $^3B_1$) have been grouped together since they are not separable in the $\beta$-KER plot [25]. From now on we just use the word "state" to represent different $C_{2\nu}$ symmetries. As can be seen from Fig. 9, each state populates a distinct region ("island") of the $\beta$-KER plot. More details on the island assignments can be found in Refs. [25, 26] as well as in Appendix A. Based on these islands, a simple principle component analysis (PCA) procedure that minimizes the residual was used to reproduce the $\beta$-KER plot. Different states population have been fitted and the reconstructed $\beta$-KER plot is shown as Fig. 2(c). The fitted relative state population has been listed as the table in the figure as well. The coefficients from the fit are decreasing with increasing ionization potential, roughly in agreement with expectations from a simple quasi-static tunnel ionization model of Ammosov-Delone-Krainov (ADK theory [55]). An interesting observation is that while the relative weights for states that involve removing electrons from different orbitals are in reasonable agreement with predictions from ADK theory, the relative weights for singlet states that involve removing two electrons from the same orbital with opposite spins are significantly higher than predictions based on ADK theory. This observation may indicate cooperative behavior, or non-sequential double ionization to states of the dication that involve removing two electrons from the same orbital.

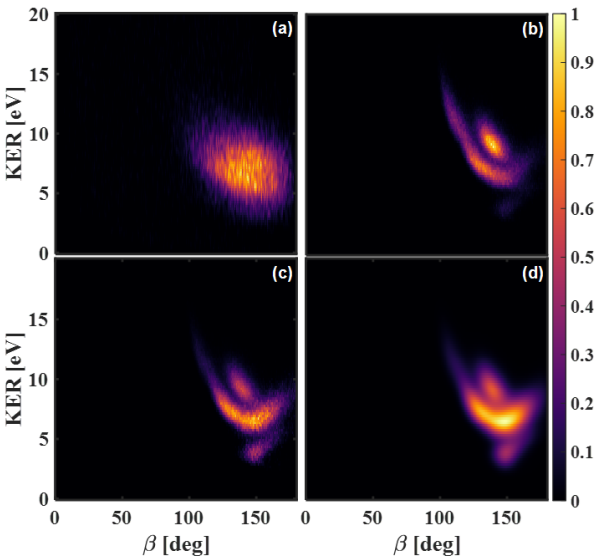


| State | *$B_1$ | $2^1A_1$ | *$A_2$ | *$B_2$ | $3^1A_1$ |
|---|---|---|---|---|---|
| Weight | 1 | 0.804 | 0.287 | 0.163 | 0.092 |

FIG. 2. Measured and calculated $D^+/D^+/O$ yield as a function of angle between the two $D^+$ ions' momentum, $\beta$, and the kinetic energy release (KER). Panel (a) Measured coincidence $D^+/D^+/O$ yield as a function of $\beta$ and KER for laser parameters described in the text; (b) Simulated $D^+/D^+/O$ yield as a function of $\beta$ and KER for equal population of each of the first nine states of the dication; (c) simulation $\beta$-KER with fit; (d) simulation $\beta$-KER with experimental resolution included. The table at the bottom lists the relative fitting populations for each states where the states are labeled with their $C_{2\nu}$ symmetry due to lack of the spin information in the observable. Details are outlined in the text.

The fitting in Fig. 2(c) only coarsely matches the measurements shown in Fig. 2(a). Although the experimental yield shows a center of mass similar to the calculations, the distinct state resolved features in the $\beta$-KER plot are not captured in the SFI results. An important first check that we carried

out in addressing this discrepancy is to determine whether our experimental resolution broadens the features such that they are no longer resolved. Using the coincidence events from 2 body dissociation channel ($D^+/OD^+$), we obtained an uncertainty for the measured $D^+$ momentum of 2.7 a.u by checking their nature of momentum conservation in all three dimensions ($p_x$, $p_y$ and $p_z$). The energy of each $D^+$ ion in the 3 body channel is about 4.5 eV. Thus the uncertainty of KER is calculated to be $\delta\text{KER} = \sqrt{2}p\delta p/m = 0.99$ eV. Similarly one can obtain the uncertainty of angle between the two $D^+$ momentum to be $\delta\beta = \sqrt{2}\delta p/p = 6.24°$.

Applying the PCA, together with the experimental resolution correction, yields Fig. 2(d). The agreement between theory and experiment is still relatively poor: Notably, the islands corresponding to the $^1B_1$ and $^3B_1$ states are absent in the measurements (see Appendix A). In the panel Fig. 2(d), where the states are blurred according to our instrument response function, the state islands feature are still present. This is completely at odds with the experimental yield shown in Fig. 2(a), where no discrete features are present. Thus, we conclude that there has to be some mechanism that drives the difference between simulation and the experiment. We note that this disagreement between experiment and theory is independent of exactly what representation one chooses (i.e. which observables to look at), and a number of different data representations are shown in the Appendix Sec. B.

## V. Dynamics Calculations and Discussion

The calculated and measured $\beta$-KER plots show some rough agreement, but disagree on many details, so it is natural to ask whether the discrepancies can be due to dynamics occurring during the SFI process. In particular, we consider the role of wave-packet reshaping (due to coordinate-dependent ionization rates for example) and nuclear dynamics (such as bending or rotation). As a first test of how much displacement the wave packet would need to alter the $\beta$-KER plot, we mapped the correlation between initial and final values for the distribution of sample points used in the classical trajectory calculations. As the dynamics calculations include an ensemble of initial and final coordinate values, we can plot the final values as a function of the initial ones, allowing us to see if there are correlations between them that lead the strong field reshaping of the ground state wave function to smear out the features in the measured $\beta$-KER plot.

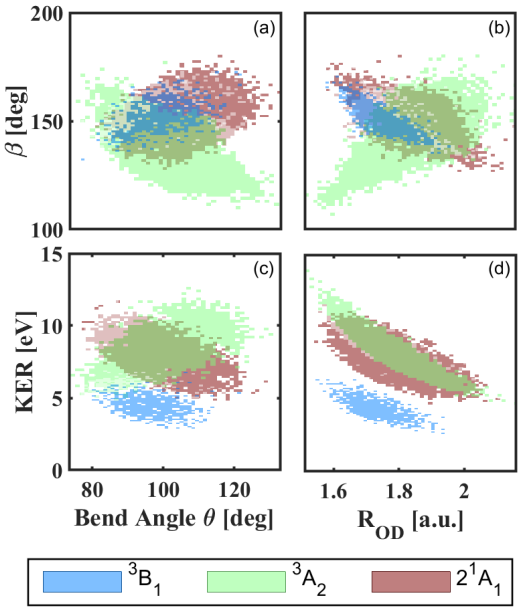


FIG. 3. Calculated $D^+/D^+/O$ yield as a function of KER, $\beta$ and initial O-D separation or D-O-D bend angle $\theta$ for three states. The top left panel (a) shows the $D^+/D^+/O$ yield as a function of initial D-O-D angle and final $\beta$. Panel (b) shows the $D^+/D^+/O$ yield as a function of initial O-D distance and final $\beta$. Panel (c) shows the $D^+/D^+/O$ yield as a function of initial D-O-D angle and final KER. Panel (d) shows the $D^+/D^+/O$ yield as a function of initial O-D distance and final KER. The color coding here is consistent with Fig. 9.

Based on the simulation we constructed the correlation maps shown in Fig. 3. Presented are correlation maps for three different electronic states, illustrating the correlation between initial opening angle and symmetric stretch coordinate with respect to the final $\beta$ and KER. The correlation between initial symmetric stretch coordinate $R_{OD}$ and final $\beta$ and KER, or initial DOD angle and final $\beta$ and KER are a result of the finite width of the initial wave function and the nonzero slope of the dicationic PES at the Franck Condon location.

The upper row in Fig. 3, which shows how the final $\beta$ values depend on the initial coordinates, exhibits a strong state dependence. The $^3B_1$ and $2^1A_1$ states show a positive correlation between the final $\beta$ value and the initial opening angle, while the $^3A_2$ state shows a negative correlation. The behavior with respect to the initial O-D distance is the opposite. This illustrates how reshaping or motion of the initial ground state wavefunction can

result in different $\beta$ distributions than those predicted for single photon ionization. The bottom row in Fig. 3 shows the KER dependence on the initial coordinates. Again, there is a significant dependence of the KER on initial bend angle and O-D distance, illustrating how reshaping or motion of the initial ground state wavefunction can distort the KER distributions predicted for single photon ionization. These plots motivate an examination of the different strong-field mechanisms that can result in non-vertical ionization and the measured $\beta$-KER plots. The sensitivity of the correlation between initial and final coordinates to electronic state is related to the breakdown of the axial recoil approximation and "slingshot" motion of the $D^+$ ions for the $^3B_1$ and $2^1A_1$ states, as discussed in more detail in [25].

The calculated $\beta$-KER plot shown in Fig. 2 (b) and Fig. 9 are results of applying one-photon perturbation theory to describe the transition from the initial neutral directly into the dication states, which is then followed by classical propagation to compute the final fragment energies and angles. In this treatment, the initial Wigner function launched on the dication states is then simply the Wigner function corresponding to the normal-mode ground state of the neutral species, that is, the Franck-Condon wave packet. While this treatment is applicable to weak-field ionization where one-photon perturbation theory is applicable, additional effects are present during SFI that modifies the initial neutral ground-state wavepacket before it arrives on the dication surfaces. First, the SFI rate can depend strongly on the nuclear coordinates, an effect which can reshape the initial ground state nuclear wavepacket during ionization. Second, multiple ionization via SFI is typically a sequential process where there is a time delay between the ejection of each liberated electron, thereby giving the nuclei a chance to relax and rearrange in between different ionization events. Finally, since there is still a strong-field present during this time delay, near-resonant laser-driven electronic transitions can occur, causing additional non-ionizing electronic transitions that reshape the nuclear wave packets while the molecule is in an intermediate ionic state.

We now outline each of these effects in more detail. We do not attempt a complete treatment of $D_2O$ double ionization in strong-fields with all degrees of freedom active, which although desirable, represents a massive theoretical and computational task. Rather, we limit ourselves to outlining each effect using simplified reduced-dimensionality models.

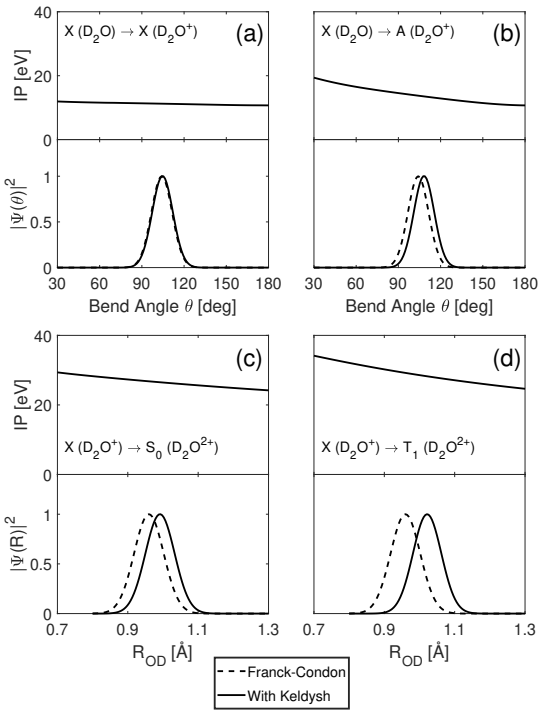


FIG. 4. Modification of the nuclear wave packet due to the coordinate-dependent Keldysh ionization rate. Panels (a) and (b) show the effect of the Keldysh weighing on the bending coordinate during the single ionization event to both the X and A cation states. The panels plot both the ionization potentials (IP) for the transitions in question, the unmodified initial neutral (i.e. Franck-Condon) wave packet, and the nuclear wave packet after applying the Keldysh weighting. Panels (c) and (d) show the effects of the Keldysh weighting for two examples of single-to-double ionizing transitions (indicated in the figures) as a function of $R_{OH}$ bond length of the symmetric stretch mode. All probability densities $|\Psi|^2$ have been normalized have a maximum of 1.

Since ionization to both the X and A cation states is expected to occur [36], modifications and dynamics arising from ionization to both X and A are used to exemplify these effects.

*Coordinate-dependence of the SFI rate*: SFI with low-frequency fields can be envisioned as a quasistatic tunnel ionization process where the ionization rate depends exponentially on the ionization potential (IP) through the Keldysh tunneling rate $\Gamma(\mathbf{R}, t)$ [21, 56–58]. In this description, ionization occurs in short sub-cycle bursts near the peaks of the laser oscillations. With the assumption that the nuclei remain stationary during a single ionization

burst, the ionized wave packet after the burst can be written as

$$\Psi_K(\mathbf{R}) = \Gamma(\mathbf{R}, t)\Psi_0(\mathbf{R}). \quad (2)$$

where $\Psi_0(\mathbf{R})$ is the initial nuclear wave packet before ionization and $\mathbf{R}$ stands for all nuclear coordinates. If ionized from the neutral at equilibrium, $\Psi_0(\mathbf{R})$ is often called the Franck-Condon wavepacket. The Keldysh rate is given by

$$\Gamma(\mathbf{R}, t) = \mathcal{P} \exp\left[-\frac{2}{3}\frac{(2\ \mathrm{IP}(\mathbf{R}))^{3/2}}{|F(t)|}\right] \quad (3)$$

where $\mathcal{P}$ is a slowly-varying (i.e. non-exponential) prefactor that depends weakly on IP, $F$, and $\mathbf{R}$. Here $F$ denotes the amplitude of the electric field. In molecular systems, the $\mathcal{P}$ prefactor would also encode the molecular orientation dependence of SFI as well as other molecular effect such as enhanced ionization, and accurate computation of $\mathcal{P}$ would require some form of *ab initio* numerical simulation of the ionization process. In the following we set $\mathcal{P} = 1$ for simplicity and consider only the effects of the Keldysh exponent. Eq.(2) shows that the Keldysh rate can modify the spatial structure of Franck-Condon wave packet through the coordinate-dependence of the IP.

Fig. 4 shows examples of the Keldysh rate modifying the initial Franck-Condon wave packet in $D_2O$. Fig. 4a shows the IPs for the first ionization step from the neutral to the X state of the ion along the bend coordinate $\theta$ together with cuts through the nuclear wave function both with and without applying the Keldysh weighting applied. Fig. 4b plots the same but for the neutral to A state. While very little change in the wave function occurs for X ionization along this coordinate, it can be seen that the Keldysh weighting has the effect of shifting the Franck-Condon wave packet along the bend coordinate. Panels c and d plot similar cuts for two transitions of the second ionization steps, X$\rightarrow$ $1^1A_1$ ($S_0$) and X$\rightarrow$ $^3A_2$ ($T_1$), but now taken along the symmetric stretch coordinate. Due to the increased magnitude and steep coordinate dependence of the IPs for these transitions, the Keldysh-induced shifts of the wave function are more pronounced compared to the previous single-ionization examples.

*Few-cycle nuclear motion in the ion*: Following the first ionization event, the nuclear wave packet can begin to move on the cationic surfaces before the second ionization occurs. This intermediate motion can change the nuclear wave packets before being projected onto the dicationic states. From our investigations of the cationic surfaces, the dominant motion is expected to be along the bend coordinate. In reality the motion in the cation occurs in the presence of the laser field, but we first consider the effects of field-free motion, which alone can already cause pronounced reshaping of the wave packets. Laser-driven motion in the cation is considered below.

The bending wavepacket dynamics on the $X^2B_1$ and $A^2A_1$ cationic surfaces is simulated using the following simplified model of $D_2O^+$. First, the bond lengths are fixed at the neutral equilibrium values, $R_{eq}$, throughout the dynamics. Second, the bending is restricted to a single plane of motion, where the overall rotational motion about the center-of-mass is not considered during these wavepacket simulation. Finally, the mass of the oxygen atom is assumed to be infinite, which significantly simplifies the corresponding kinetic energy operator. With these restrictions, the Hamiltonian of the model system is written (in atomic units) as

$$\widehat{H}(\theta, t) = \begin{bmatrix} -\frac{1}{2\mu R_{eq}^2}\frac{\partial^2}{\partial\theta^2} + V_X(\theta) & 0 \\ 0 & -\frac{1}{2\mu R_{eq}^2}\frac{\partial^2}{\partial\theta^2} + V_A(\theta) \end{bmatrix}, \quad (4)$$

where $\mu = m_D/2$ is the reduced mass of the bend coordinate, $m_D$ is the mass of atomic deuterium, while $V_X(\theta)$ and $V_A(\theta)$ are the potential energy surfaces of the $X^2B_1$ and $A^2A_1$ states. This Hamiltonian is used to solve the time-dependent Schrödinger equation (TDSE) $i\partial_t\Psi(\theta, t) = \widehat{H}(\theta, t)\Psi(\theta, t)$. In order to investigate the effect of wave-packet motion as separate from the Keldysh effects discussed above, we populate both the X and A surfaces during the ionization event starting from the unchanged Franck-Condon wave packet, and hence the initial condition for $\Psi(\theta, t)$ at the moment of ionization is taken to be the bending ground state, $\psi_0(\theta)$, on the neutral surface. The TDSE is solved using the Fourier-split-operator technique [59].

The first three panels of Fig. 5 show the effects of intermediate field-free few-cycle motion on the X and A cation surfaces. Fig. 5a shows the Wigner function of the initial Franck-Condon wave packet. This is the initial state of the bending coordinate that is used in the $\beta$-KER trajectory simulations. Figs. 5b and c plot Wigner functions after this initial state has propagated field-free for a time corresponding to 2 laser cycles of the 780 nm field (2×2.6 fs) on the X and A states, respectively. The X-state Wigner has undergone a little acceleration and motion as can be seen by the small shift of the center of the Wigner function, but there is still significant

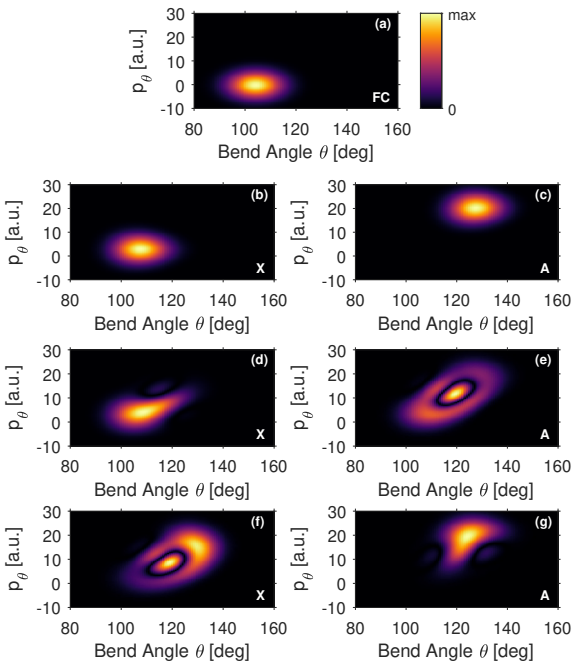


FIG. 5. Wigner functions demonstrating the effects of nuclear dynamics in the cation. (a) Wigner function of the Franck-Condon wave packet. (b) & (c) Wigner functions after field-free propagation on the X and A states respectively for a time equal to 2 cycles of the laser. (d) & (e) Wigner functions on the X and A states after laser-driven propagation for a time of 2 laser cycles with the initial population starting on the X state. The simulation was started at the peak of the pulse ($t = 0$) with the laser parameter $\lambda_0$=780 nm, $I_0 = 400$ TW/cm$^2$, and $\tau$=10 fs. (f) & (g) Same as previous two panels but now with initial population on the A state. Note that in all cases the magnitude of the Wigner function is shown.

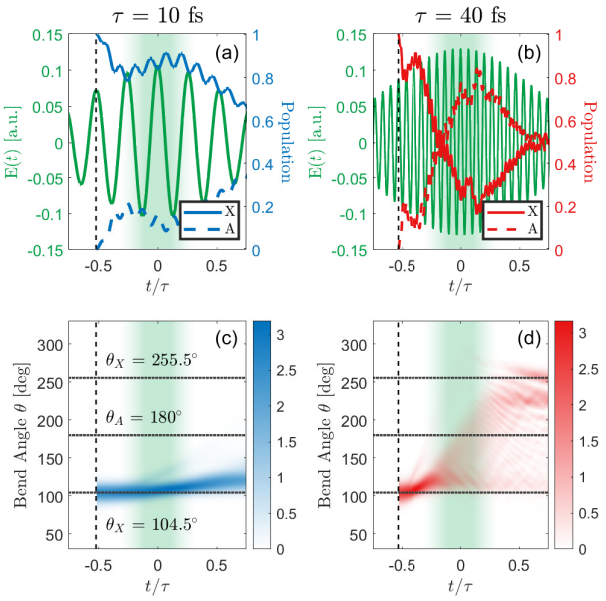


FIG. 6. Time-resolved simulations of the strong-field coupling between the X state of the water cation and the A state in the presence of (a) the 10 fs pulse with $\lambda_0 = 780$ nm and $I_0 = 400$ TW/cm$^2$ and (b) the 40 fs pulse with central wavelength $\lambda_0 = 800$ nm and peak intensity $I_0 = 600$ TW/cm$^2$ (parameters chosen to match the experiments). In each case, the cation is initiated in the X state (red/blue solid line) at a local peak in electric field (solid green line) that roughly corresponds to the point at which the pulse intensity is half it's maximum value: $t/\tau \approx$ -0.5. Due to the presence of the field, the X population couples to the A state (red/blue dashed line). Plotted below each of these figures is the probability distribution over bend angle, $\theta$, for the mixture of states displayed above, shown separately for (c) the case of a 10 fs pulse (blue) and (d) the case of a 40 fs pulse (red). In each case, dotted gray lines denote the equilibrium bend-angles for the X and A states. In all four panels, green shading roughly indicates the window in time over which the second ionization event in sequential double-ionization is expected to occur.

overlap between the propagated and initial Wigner functions in this case. However, the 2-cycle field-free propagation on the A-state substantially modifies the initial Wigner function, which now has effectively zero overlap with the initial state. The remaining panels of Fig. 5 pertain to laser-driven motion in the ion, which is outlined in the following.

*Near-resonant dipole coupling in the ion*: At 780 nm, the laser induces a near-resonance one-photon coupling between the X and A states. This coupling is included in the wave packet simulation by adding off-diagonal dipole terms to the Hamiltonian, which then becomes

$$\widehat{H}(\theta,t) = \begin{bmatrix} -\frac{1}{2\mu R_{eq}^2}\frac{\partial^2}{\partial\theta^2} + V_X(\theta) & -F(t)\cdot d_{XA}(\theta) \\ -F(t)\cdot d_{XA}(\theta) & -\frac{1}{2\mu R_{eq}^2}\frac{\partial^2}{\partial\theta^2} + V_A(\theta) \end{bmatrix}, \quad (5)$$

where $d_{XA}(\theta)$ is the transition dipole between these states, and $F(t)$ is the electric field of the laser which is chosen to be parallel to $d_{XA}(\theta)$, i.e perpendicular to the molecular plane. The electric field of the laser

is taken to have a Gaussian envelope

$$F(t) = \mathcal{F}_0 \exp\left[-4\ln 2\left(\frac{t}{\tau\sqrt{2}}\right)^2\right]\cos(\omega_0 t) \quad (6)$$

where $\omega_0$ is the carrier frequency, $\mathcal{F}_0$ is the peak electric field magnitude, and $\tau$ is the full width at half maximum of the corresponding intensity envelope $|F(t)|^2$.

The effects of the dipole coupling on the Wigner functions can be seen in Figs. 5(d)-(g), while a more complete picture of the laser-driven dynamics is shown in Fig. 6. We first consider the Wigner functions. Figs. 5(d) and (e) plot the Wigner functions on the X and A states respectively after the system was initialized with the Franck-Condon wave packet on the X state at the peak ($t$=0) of a laser pulse with $\tau$ = 10 fs and intensity of 400 TW/cm$^2$, and allowed to propagate for 2 cycles of the laser. Initially only the X state is populated, but due to the near-resonant dipole coupling some population is transferred to the A state, which is discussed further below. In addition to the modifications due to field-free propagation, seen in Figs.5(b) and (c), both of the Wigner functions on the X and A states have acquired additional structures after the laser-driven propagation. These structures arise due to light-induced potentials created by the strong near-resonant laser field that modify the field-free potential energy surfaces, an effect known as bond softening [60, 61]. Additionally, the transfer of population from one state back to the other, which occurs through cascaded one-photon transitions between the X and A states induced by the strong near-resonant laser, also contributes to these structures. Figs.5(f) and (g) plot Wigner functions for the same scenario but now with the initial population starting on the A state. Again, it is seen that new structure not present in the Franck-Condon wave packet have developed.

For the dipole moment effect on the nuclear dynamics simulation, a simple simulation was carried out and negligible change on the simulated dynamics has been seen. Other non-adiabatic or non-Born-Oppenheimer couplings, like the non-laser-induced non-adiabatic couplings are also considered. The assumption in our calculations is that these couplings are negligible so they are not included. These non-adiabatic couplings were also neglected in the classical trajectory simulations, so the two simulation sections in the paper are consistent in this regard. More specifically in the classical trajectories, they were performed field free and sampled from the Wigner

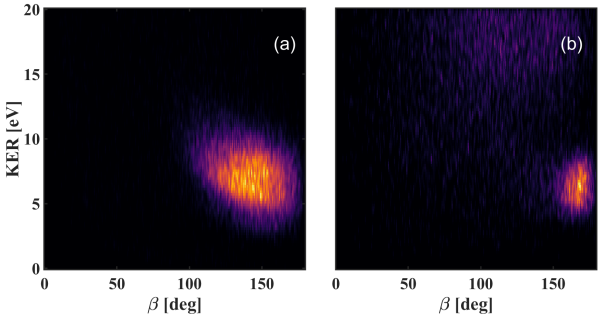


FIG. 7. $\beta$-KER plot for SFI with (a) 10 fs and (b) 40 fs pulse durations. A higher kinetic energy feature is observed for the longer pulses in panel (b). This feature can be assigned to trication formation and fragmentation via the $D^+/D^+/O^+$channel. A discussion of which is presented in Appendix C.

distribution of the initial ground state. No nonadiabatic coupling between the nine potential surfaces was included, nor coupling to other states that have conical intersections with some of these states which occur at geometries that are not probed by the classical trajectories. These points are discussed in [25, 49]. Both works also neglected nonadiabatic transitions in the dissociation dynamics of the water dication. Comparison with experiment for one photon double ionization verify that nondiabatic effects do not appreciably change the final momentum distributions in the channels producing $O/D^+/D^+$ or $OD^+/D^+$. However, those effects can be important for the production of the products $O^+/D^+/D$, which are minor channels beyond the scope of this work.

In order to put things into perspective, we compare the amount of X to A coupling that occurs in a 10 fs pulse to a significantly longer pulse with a duration of 40 fs. Fig 6 shows a broader picture of the laser-driven dynamics. The top panels show the population of ground and first excited states of the monocation together with the laser field as a function of time for 10 fs (top left) and 40 fs (top right) laser pulses. The bottom two panels show the corresponding probability density as a function of D-O-D angle and time. The figures illustrate the fact that while population transfer and nuclear dynamics can take place during a 10 fs pulse, they have a much more dramatic effect for a 40 fs pulse.

The calculations described above suggest that in a longer pulse, dynamics in the monocation en route to the dication during a longer pulse also leads to significant unbending and a $\beta$-KER plot that is shifted to larger angles. We therefore compare the $\beta$-KER

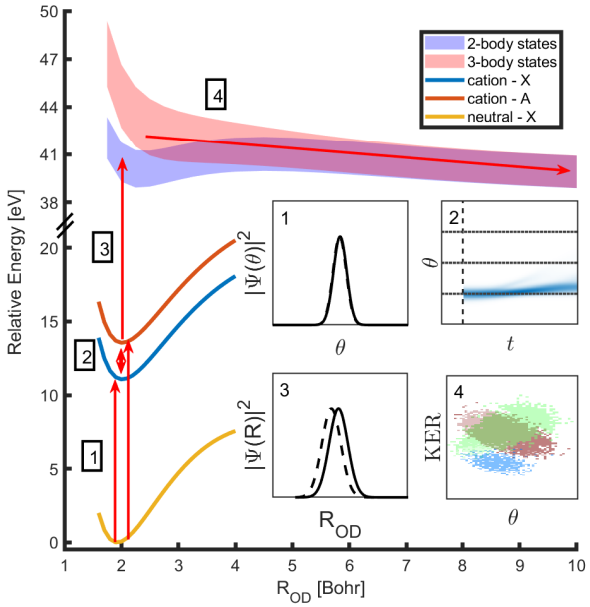


FIG. 8. Concluding figure with PES of relevant states. Four different steps are participating in the strong field double ionization of water: 1- Tunnel ionization to X and A states of monocation, which involves reshaping of wave function due to R-dependent ionization; 2- near resonant coupling of X and A states as well as motion on A state's potential; 3- ionization to the dication, which also involves reshaping of wave function; 4- dication dissociation, which can be simulated through trajectory calculations.

plot for 10 and 40 fs pulses as a test of the conclusions of the theoretical results. Fig. 7 shows this comparison, which bears out the predictions based on the calculations above. We note that the comparison shows that 40 fs tend to have larger $\beta$ angles and also the lower KER. The former is what we expected from the simulation while the latter is not easy to explain. Nevertheless, this comparison provides strong evidence that while there is rough agreement between the measured and calculated momentum resolved fragment ion yields for sub 10-fs pulses assuming vertical ionization, reshaping of the wave packet and nuclear dynamics during ionization can lead to significant differences between strong- and weak-field ionization. And one needs to understand the strong-field dynamics in order to predict the reaction products in an SFI measurement. Finally, a weak diffuse feature at higher KER (∼20 eV) and smaller $\beta$ values is observed for 40-fs pulses, which is notably absent for the short pulse case. This feature can readily be assigned to trication Coulomb explosion and is discussed in detail in Appendix C.

## VI. Conclusion

In conclusion, while we find rough agreement between measurements of the $D^+/D^+/O$ yield as a function of $\beta$ and KER for double ionization of $D_2O$ with 10 fs laser pulses and calculations of the same yield assuming weak-field/vertical ionization, there are significant differences in the details. Even after careful analysis on the state population in the strong field ionization and taking into account our experimental resolution, the experimental results still show discrepancies compared with theoretical expectations. As summarized in the Fig. 8, these differences may be ascribed to different physical processes leading to wave packet reshaping. The R-dependent single and double ionization induced by strong-field ionization and nuclear dynamics induced by resonance coupling during the pulse are believed to drive the wave packet away from the initial form. Such modifications to the wave form have a great influence on the initial conditions of the trajectory calculations on dicationic states. Thus the final experimental $\beta$-KER yield is different from the theoretical predictions from the simple single photon double ionization. These result in SFI being a non-vertical transition, with an understanding of the strong-field dynamics being important for the calculation of the fragment ion yield momentum distributions.

Our simple calculations indicate that the coordinate dependence of the tunnel ionization rate plays an important role in reshaping the initial wave packet, particularly for the second ionization step in a sequential double ionization process. Meanwhile, the monocation dynamics in the presence of the strong laser field indicate that field dressed nuclear dynamics can also reshape the vibrational wave packet. These observations are supported by measurements of the double ionization yield as a function of $\beta$ and KER for 10 fs and 40 fs pulses. This comparison has significant bearing on the use of SFI as a probe of molecular structure and dynamics, and indicates that while very short pulses ($<$ 10 fs) can minimize nuclear dynamics during the pulse, wave packet reshaping by the strong field of the laser can still result in significant distortion of the initial wave function of the molecule. We believe this work will have important consequences for pump-probe techniques, such as time-resolved Coulomb explosion imaging (CEI), that aim to track nuclear dynamics

during excited state photochemical processes.

These results showcase the need for a more comprehensive theoretical description of SFI processes, which include the role of nuclear motion occurring during the ionizing laser pulse duration. As outlined in the introduction, such nuclear dynamics could have implications for computations of SFI from multi-cycle pulses when invoking the frozen-nuclei approximation, such as recent state-of-the-art time-dependent R-matrix ionization computations for $H_2O$ that highlighted modifications to the angular dependence of ionization when significant laser coupling in the ion is present for the frozen-nuclei case. Further experimental investigations into the pulse shape and intensity dependence of SFI processes in water may help to target future modelling of these dynamics.


### Acknowledgments

We would like to thank Brian M. Kaufman and Yusong Liu for technical support, Spiridoula Matsika and James Cryan for useful discussions. RF, AJH, and PHB were supported by the National Science Foundation. AJH was additionally supported under a Stanford Graduate Fellowship as the 2019 Albion Walter Hewlett Fellow. CC and TW gratefully acknowledge support from the Department of Energy under Award No. DE-FG02-08ER15984. Work at LBNL was performed under the auspices of the U.S. Department of Energy (DOE), Office of Science, Office of Basic Energy Sciences, Chemical Sciences, Geosciences, and Biosciences Division under Contract No. DEAC02-05CH11231, using the National Energy Research Computing Center (NERSC), a DOE Office of Science User Facility, and the Lawrencium computational cluster resource provided by LBNL.


### A. Individual dication state contributions to $\beta$-KER plot

In order to try to connect the observed dissociation features in our strong-field double ionization experiment to specific dication states we adopted a similar methodology to Refs. [25, 26]. In those studies, the $H^+/H^+/O$ yield following single photon double ionization of $H_2O$ were compared against classical trajectory simulations on various electronic states of water diction. By comparing theoretical kinetic energy releases (KERs) and relative angle correlations (between the two $H^+$ fragments) to the experimental data, it was unambiguously shown that specific features could be connected to dissociation occurring on different electronic states of the dication.

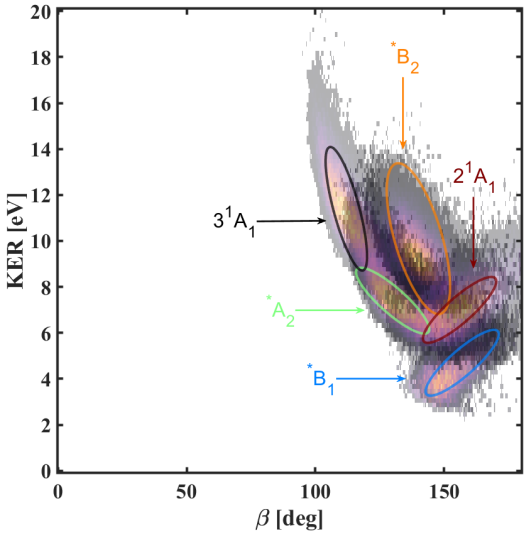


FIG. 9. Transparent theoretical $\beta$-KER plot generated from the simulations outlined in Sec. III. Annotations of the specific states associated with each distinct spectral feature are shown (ovals). A state dependent color coding consistent with Fig. 3 is adopted for clarity.

Classical trajectory simulations of three-body dissociation of $D_2O^{2+}$ into $D^+/D^+/O$ were performed using a methodology briefly outlined in Sec. III. In Fig. 3 theoretical KERs and $D^+/D^+$ relative angles, $\beta$, from these calculations are shown alongside the experimental data. In order to connect the features observed in theory to the dication states that are expected undergo three-body decay (see Table I), Fig. 9 shows the $\beta$-KER plot with annotated regions corresponding to specific final states. For clarity we adopt the same state specific color scheme outlined in Fig. 3.

### B. Alternative representations of the $D^+/D^+/O$ channel

In Sec. II it was briefly outlined that by exploiting the Timepix3 camera in conjunction with a voltage switching VMI apparatus it is possible to coincidentally detect all charge particles (electrons and ions) following strong-field double ionization, provided a suitably low number ($\ll$1) of double-ionization events per laser shot is achieved. For the

ions, the time-stamping capabilities of the camera permit the three-dimensional vector momenta of all fragments to be extracted. This information permits observables, such as the relative angles between fragments or total KERs, to determined. As is outlined in the main text of manuscript, as well as Appendix A, a particularly useful way to view the data associated with the $D^+/D^+/O$ channel is to consider the relative angle between the two $D^+$ ions, $\beta$, as a function of KER. We note, however, that there exists a large number of possible representations of the data due to three-dimensional correlated information extracted during the experiment. To highlight this, Fig. 10 shows various cuts of the full data set along the KER, $\beta$, $E_{D1}$ and $E_{share}$ coordinates. Here $E_{D1}$ and $E_{share}$ refer to the kinetic energy of the one of deuterons and the sharing of kinetic energy between both the deuterons, respectively. In Fig. 11 the equivalent plots for the theoretical simulations outlined in Sec. III are presented.

Similar to the discussion of the $\beta$-KER plot in the main text there exists some coarse agreement between theory and experiment in several of the panels. However, it is apparent that the well-resolved features in Fig. 11 are absent in the experimental data. This is likely due to the mechanisms outlined in Sec. V. A particularly noteworthy region of disagreement is observed in the panel where the yield is plotted as a function of $E_{share}$ and $\beta$. A weak feature extending over all angles at $E_{share} = 0$ and 1 is seen experimentally but has no analogous signature in the theory. In Fig. 12 a zoomed $\beta$-$E_{share}$ plot is presented to highlight this discrepancy. We attribute this large angular spread in $\beta$ to a process by which $D_2O^{2+}$ initially undergoes two-body decay into $D^+/OD^+$ but subsequently fragments into three-bodies ($D^+/D^+/O$) via a sequential break-up mechanism. A corresponding feature was observed in the $H^+/H^+/O$ yield following single-photon double ionization [26] and has also been observed in SFI induced fragmentation of triatomic molecules such as OCS [62].

### C. Signatures of trication formation in 40-fs pulse data

The comparison of the $\beta$-KER plot for the cases of short (10 fs) and long (40 fs) pulse durations (see Fig. 7) provided experimental support for the role of nuclear motion occurring during double ionization process. These data highlighted two significant differences. The first is a shifting of the feature observed at ∼7.5 eV to higher $\beta$ angles. This, as discussed in the main text, can be attributed to unbending dynamics that result in the water dication undergoing fragmentation from geometries close to linear. A second, higher KER, feature is discernible in the 40 fs data but is notably absent for the case of shorter pulses.

In Fig. 13 we present $\beta$-angle-integrated KER spectra for the two pulse durations. A striking difference is observed between the spectra, with the majority of the 40 fs counts originating from the feature centred at ∼20 eV. Given the significantly higher KER, a likely origin of this is fragmentation occurring from a more highly charged water ion and a missing coincidence partner ion (due to the limited detection efficiency of our apparatus). In order to verify this, we examined the $D^+/D^+/O^+$ coincidence channel and can unambiguously assign the origin of the higher KER feature to such a process.


[1] P.-M. Paul, E. S. Toma, P. Breger, G. Mullot, F. Augé, P. Balcou, H. G. Muller, and P. Agostini, Observation of a train of attosecond pulses from high harmonic generation, Science **292**, 1689 (2001).

[2] T. Popmintchev, M.-C. Chen, D. Popmintchev, P. Arpin, S. Brown, S. Ališauskas, G. Andriukaitis, T. Balčiunas, O. D. Mücke, A. Pugzlys, *et al.*, Bright coherent ultrahigh harmonics in the keV X-ray regime from mid-infrared femtosecond lasers, Science **336**, 1287 (2012).

[3] J. Marangos, Development of high harmonic generation spectroscopy of organic molecules and biomolecules, J. Phys. B: At. Mol. Phys. **49**, 132001 (2016).

[4] M. Meckel, D. Comtois, D. Zeidler, A. Staudte, D. Pavičić, H. Bandulet, H. Pépin, J. Kieffer, R. Dörner, D. Villeneuve, *et al.*, Laser-induced electron tunneling and diffraction, Science **320**, 1478 (2008).

[5] K. Amini, M. Sclafani, T. Steinle, A.-T. Le,

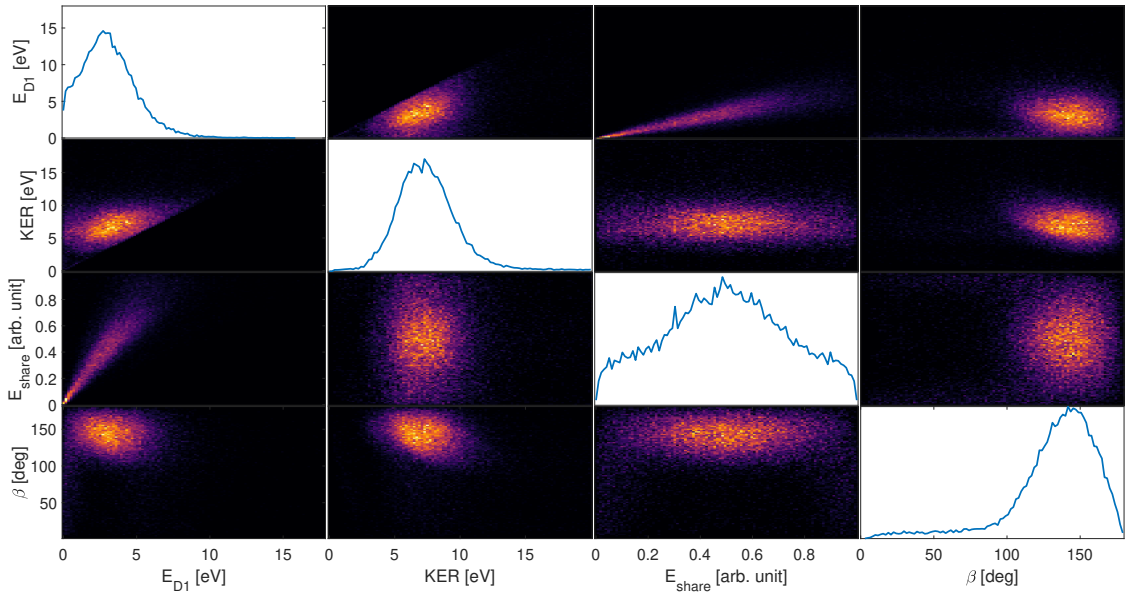


FIG. 10. Representations of the multi-dimensional $D^+/D^+/O$ coincidence data along various coordinates. Shown are KER, $\beta$, $E_{D1}$ and $E_{share}$ cuts of the data along each of these coordinates in a matrix style plot. Here the diagonal represents the one-dimensional normalized line-out along each of the aforementioned axes.


A. Sanchez, C. Müller, J. Steinmetzer, L. Yue, J. R. M. Saavedra, M. Hemmer, *et al.*, Imaging the Renner–Teller effect using laser-induced electron diffraction, Proc. Natl. Acad. Sci. **116**, 8173 (2019).

[6] C. I. Blaga, J. Xu, A. D. DiChiara, E. Sistrunk, K. Zhang, P. Agostini, T. A. Miller, L. F. DiMauro, and C. Lin, Imaging ultrafast molecular dynamics with laser-induced electron diffraction, Nature **483**, 194 (2012).

[7] H. Stapelfeldt, E. Constant, H. Sakai, and P. B. Corkum, Time-resolved coulomb explosion imaging: A method to measure structure and dynamics of molecular nuclear wave packets, Phys. Rev. A **58**, 426 (1998).

[8] I. Bocharova, R. Karimi, E. F. Penka, J.-P. Brichta, P. Lassonde, X. Fu, J.-C. Kieffer, A. D. Bandrauk, I. Litvinyuk, J. Sanderson, *et al.*, Charge resonance enhanced ionization of $CO_2$ probed by laser coulomb explosion imaging, Phys. Rev. Lett. **107**, 063201 (2011).

[9] P. M. Kraus, B. Mignolet, D. Baykusheva, A. Rupenyan, L. Hornỳ, E. F. Penka, G. Grassi, O. I. Tolstikhin, J. Schneider, F. Jensen, *et al.*, Measurement and laser control of attosecond charge migration in ionized iodoacetylene, Science **350**, 790 (2015).

[10] M. Kübel, R. Siemering, C. Burger, N. G. Kling, H. Li, A. Alnaser, B. Bergues, S. Zherebtsov, A. Azzeer, I. Ben-Itzhak, *et al.*, Steering proton migration in hydrocarbons using intense few-cycle laser fields, Phys. Rev. Lett. **116**, 193001 (2016).

[11] M. Sabbar, H. Timmers, Y.-J. Chen, A. K. Pymer, Z.-H. Loh, S. G. Sayres, S. Pabst, R. Santra, and S. R. Leone, State-resolved attosecond reversible and irreversible dynamics in strong optical fields, Nat. Phys. **13**, 472 (2017).

[12] K. Ramasesha, S. R. Leone, and D. M. Neumark, Real-time probing of electron dynamics using attosecond time-resolved spectroscopy, Annu. Rev. Phys. Chem. **67**, 41 (2016).

[13] T. K. Kjeldsen and L. B. Madsen, Strong-field ionization of diatomic molecules and companion atoms: Strong-field approximation and tunneling theory including nuclear motion, Phys. Rev. A **71**, 023411 (2005).

[14] K. Lin, X. Jia, Z. Yu, F. He, J. Ma, H. Li, X. Gong, Q. Song, Q. Ji, W. Zhang, *et al.*, Comparison study of strong-field ionization of molecules and atoms by bicircular two-color femtosecond laser pulses, Phys. Rev. Lett. **119**, 203202 (2017).

[15] M. Lezius, V. Blanchet, D. Rayner, D. Villeneuve, A. Stolow, and M. Y. Ivanov, Nonadiabatic multielectron dynamics in strong field molecular ionization, Phys. Rev. Lett. **86**, 51 (2001).

[16] T. K. Kjeldsen, C. Z. Bisgaard, L. B. Madsen, and H. Stapelfeldt, Influence of molecular symmetry on strong-field ionization: Studies on ethylene, benzene, fluorobenzene, and chlorofluorobenzene, Phys. Rev. A **71**, 013418 (2005).

[17] L. Holmegaard, J. L. Hansen, L. Kalhøj, S. L. Kragh, H. Stapelfeldt, F. Filsinger, J. Küpper,

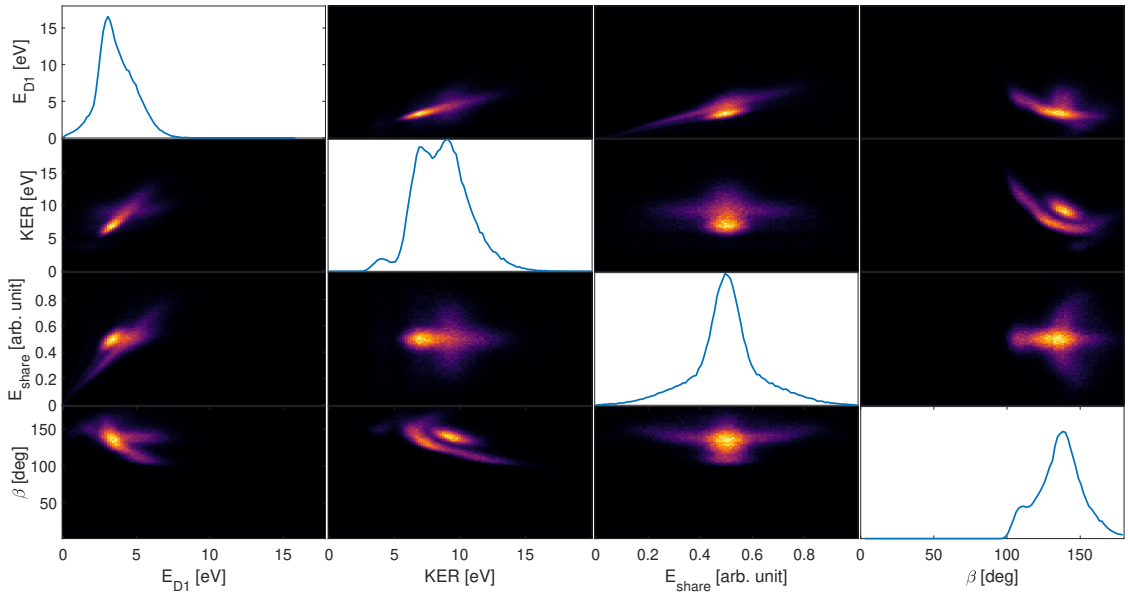


FIG. 11. Cuts of theoretical results along the same coordinates outlined in Fig. 10 for the $D^+/D^+/O$ fragmentation channel in the classical trajectory simulations. Details of constraints used to classify the trajectories into specific channels are outlined in Sec. III.

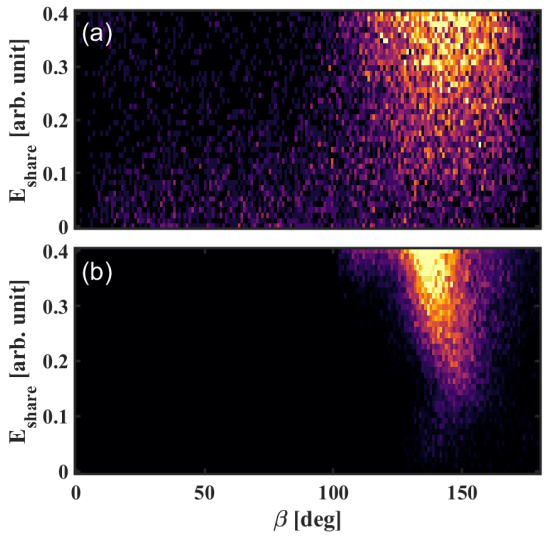


FIG. 12. Zoomed version of the $\beta$-$E_{share}$ plots shown in Figs. 10 and 11. A broad feature in angle is observed at $E_{share} < 0.2$ experimentally (a), which in notably absent in the theoretical results (b). This features can be assigned to a sequential dissociation pathway involving predissociation of $OD^+$ as discussed in the main text.

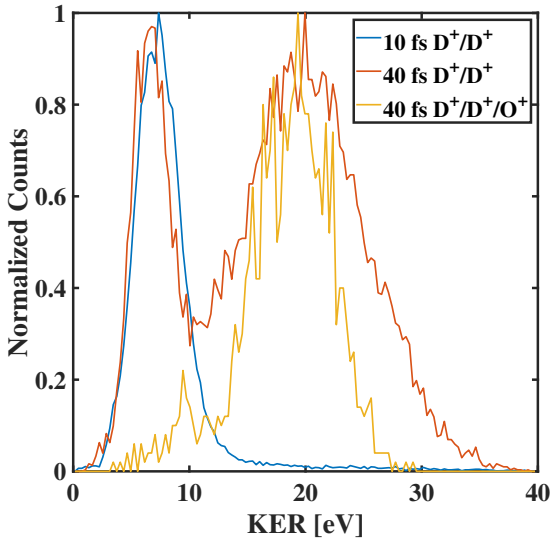


FIG. 13. Kinetic Energy Release (KER) distribution of the $D^+/D^+$ dissociation channel for 10 (blue) and 40 fs pulse durations (red) and $D^+/D^+/O^+$ only for 40 fs pulse (yellow). The two $D^+/D^+$ lineouts correspond to $\beta$-angle-integrated versions of the data shown in Fig.7. The overlap between $D^+/D^+/O^+$ channel and the $D^+/D^+$ in the 40 fs data indicates the high KER region are coming from events missing an $O^+$.

G. Meijer, D. Dimitrovski, M. Abu-Samha, *et al.*, Photoelectron angular distributions from strong-field ionization of oriented molecules, Nat. Phys. **6**, 428 (2010).

[18] F. Schell, A. E. Boguslavskiy, C. P. Schulz, S. Patchkovskii, M. J. Vrakking, A. Stolow, and J. Mikosch, Sequential and direct ionic excitation in the strong-field ionization of 1-butene molecules, Phys. Chem. Chem. Phys. **20**, 14708 (2018).

[19] P. Sándor, V. Tagliamonti, A. Zhao, T. Rozgonyi, M. Ruckenbauer, P. Marquetand, and T. Weinacht, Strong field molecular ionization in the impulsive limit: Freezing vibrations with short pulses, Phys. Rev. Lett. **116**, 063002 (2016).

[20] A. S. Coolidge, H. M. James, and R. D. Present, A study of the Franck-Condon principle, J. Chem. Phys. **4**, 193 (1936).

[21] X. Urbain, B. Fabre, E. M. Staicu-Casagrande, N. de Ruette, V. M. Andrianarijaona, J. Jureta, J. H. Posthumus, A. Saenz, E. Baldit, and C. Cornaggia, Intense-laser-field ionization of molecular hydrogen in the tunneling regime and its effect on the vibrational excitation of $H_2^+$, Phys. Rev. Lett. **92**, 163004 (2004).

[22] L. Fang and G. Gibson, Strong-field induced vibrational coherence in the ground electronic state of hot $I_2$, Phys. Rev. Lett. **100**, 103003 (2008).

[23] P. M. Kraus, S. B. Zhang, A. Gijsbertsen, R. Lucchese, N. Rohringer, and H. J. Wörner, High-harmonic probing of electronic coherence in dynamically aligned molecules, Phys. Rev. Lett. **111**, 243005 (2013).

[24] Z. Liu, J. Yao, J. Chen, B. Xu, W. Chu, and Y. Cheng, Near-resonant Raman amplification in the rotational quantum wave packets of nitrogen molecular ions generated by strong field ionization, Phys. Rev. Lett. **120**, 083205 (2018).

[25] Z. L. Streeter, F. L. Yip, R. R. Lucchese, B. Gervais, T. N. Rescigno, and C. W. McCurdy, Dissociation dynamics of the water dication following one-photon double ionization. I. theory, Phys. Rev. A **98**, 053429 (2018).

[26] D. Reedy, J. Williams, B. Gaire, A. Gatton, M. Weller, A. Menssen, T. Bauer, K. Henrichs, P. Burzynski, B. Berry, *et al.*, Dissociation dynamics of the water dication following one-photon double ionization. II. experiment, Phys. Rev. A **98**, 053430 (2018).

[27] S. L. Horton, Y. Liu, P. Chakraborty, P. Marquetand, T. Rozgonyi, S. Matsika, and T. Weinacht, Strong-field-versus weak-field-ionization pump-probe spectroscopy, Phys. Rev. A **98**, 053416 (2018).

[28] R. Forbes, A. E. Boguslavskiy, I. Wilkinson, J. G. Underwood, and A. Stolow, Excited state wavepacket dynamics in $NO_2$ probed by strong-field ionization, J. Chem. Phys. **147**, 054305 (2017).

[29] X. Ding, R. Forbes, M. Kübel, K. F. Lee, M. Spanner, A. Y. Naumov, D. M. Villeneuve, A. Stolow, P. B. Corkum, and A. Staudte, Threshold photodissociation dynamics of $NO_2$ studied by time-resolved cold target recoil ion momentum spectroscopy, J. Chem. Phys. **151**, 174301 (2019).

[30] C. Petersen, E. Peronne, J. Thøgersen, H. Stapelfeldt, and M. Machholm, Control and imaging of interfering wave packets in dissociating $I_2$ molecules, Phys. Rev. A **70**, 033404 (2004).

[31] F. Légaré, K. F. Lee, I. Litvinyuk, P. Dooley, S. Wesolowski, P. Bunker, P. Dombi, F. Krausz, A. Bandrauk, D. Villeneuve, *et al.*, Laser coulomb-explosion imaging of small molecules, Phys. Rev. A **71**, 013415 (2005).

[32] L. Hong, L. Min, X. Xi-Guo, W. Cong, D. Yong-Kai, W. Cheng-Yin, G. Qi-Huang, and L. Yun-Quan, Charge resonance enhanced multiple ionization of $H_2O$ molecules in intense laser fields, Chin. Phys. Lett. **32**, 063301 (2015).

[33] G. A. McCracken and P. H. Bucksbaum, Ionization induced dynamic alignment of water, J. Chem. Phys. **152**, 134308 (2020).

[34] S. Koh, K. Yamazaki, M. Kanno, H. Kono, and K. Yamanouchi, Ionization and dissociation dynamics of $H_2O$ in ultrashort intense near-IR laser fields by the time-dependent adiabatic state method and the time-dependent configuration interaction method, Chem. Phys. Lett. **742**, 137165 (2020).

[35] A. Howard, C. Cheng, R. Forbes, G. McCracken, W. Mills, V. Makhija, M. Spanner, T. Weinacht, and P. Bucksbaum, Strong-field ionization of water: Nuclear dynamics revealed by varying the pulse duration, Phys. Rev. A **103**, 043120 (2021).

[36] C. Cheng, R. Forbes, A. J. Howard, M. Spanner, P. H. Bucksbaum, and T. Weinacht, Momentum-resolved above-threshold ionization of deuterated water, Phys. Rev. A **102**, 052813 (2020).

[37] J. Benda, J. Gorfinkiel, Z. Mašín, G. Armstrong, A. Brown, D. Clarke, H. van der Hart, and J. Wragg, Perturbative and nonperturbative photoionization of $H_2$ and $H_2O$ using the molecular R-matrix-with-time method, Phys. Rev. A **102**, 052826 (2020).

[38] M. Richter, M. Lytova, F. Morales, S. Haessler, O. Smirnova, M. Spanner, and M. Ivanov, Rotational quantum beat lasing without inversion, Optica **7**, 586 (2020).

[39] M. Lytova, M. Richter, F. Morales, O. Smirnova, M. Ivanov, and M. Spanner, $N_2^+$ lasing: Gain and absorption in the presence of rotational coherence, Phys. Rev. A **102**, 013111 (2020).

[40] Q. Zhang, H. Xie, G. Li, X. Wang, H. Lei, J. Zhao, Z. Chen, J. Yao, Y. Cheng, and Z. Zhao, Sub-cycle coherent control of ionic dynamics via transient ionization injection, Commun. Phys. **3**, 1 (2020).

[41] A. Zhao, M. van Beuzekom, B. Bouwens, D. Byelov, I. Chakaberia, C. Cheng, E. Maddox, A. Nomerot-

ski, P. Svihra, J. Visser, *et al.*, Coincidence velocity map imaging using Tpx3Cam, a time stamping optical camera with 1.5 ns timing resolution, Rev. Sci. Instrum. **88**, 113104 (2017).
[42] C. Cheng, P. Vindel-Zandbergen, S. Matsika, and T. Weinacht, Electron correlation in channel-resolved strong-field molecular double ionization, Phys. Rev. A **100**, 053405 (2019).
[43] M. A. Dugan, J. X. Tull, and W. S. Warren, High-resolution acousto-optic shaping of unamplified and amplified femtosecond laser pulses, J. Opt. Soc. Am. B **14**, 2348 (1997).
[44] P. B. Corkum, Plasma perspective on strong field multiphoton ionization, Phys. Rev. Lett. **71**, 1994 (1993).
[45] W. Bryan, S. Stebbings, J. McKenna, E. English, M. Suresh, J. Wood, B. Srigengan, I. Turcu, J. Smith, E. Divall, *et al.*, Atomic excitation during recollision-free ultrafast multi-electron tunnel ionization, Nat. Phys. **2**, 379 (2006).
[46] O. Jagutzki, A. Cerezo, A. Czasch, R. Dorner, M. Hattas, Min Huang, V. Mergel, U. Spillmann, K. Ullmann-Pfleger, T. Weber, H. Schmidt-Bocking, and G. D. W. Smith, Multiple hit readout of a microchannel plate detector with a three-layer delay-line anode, IEEE Trans. Nucl. Sci. **49**, 2477 (2002).
[47] H. Pedersen, C. Domesle, L. Lammich, S. Dziarzhytski, N. Guerassimova, R. Treusch, L. Harbo, O. Heber, B. Jordon-Thaden, T. Arion, *et al.*, Photolysis of water-radical ions $H_2O^+$ in the XUV: Fragmentation through dicationic states, Phys. Rev. A **87**, 013402 (2013).
[48] S. Zhao, B. Jochim, P. Feizollah, J. Rajput, F. Ziaee, B. Kaderiya, K. Borne, Y. Malakar, B. Berry, J. Harrington, *et al.*, Strong-field-induced bond rearrangement in triatomic molecules, Phys. Rev. A **99**, 053412 (2019).
[49] B. Gervais, E. Giglio, L. Adoui, A. Cassimi, D. Duflot, and M. Galassi, The $H_2O^{2+}$ potential energy surfaces dissociating into $H^+/OH^+$: Theoretical analysis of the isotopic effect, J. Chem. Phys. **131**, 024302 (2009).
[50] H.-J. Werner, P. J. Knowles, G. Knizia, F. R. Manby, and M. Schütz, MOLPRO: a general-purpose quantum chemistry program package, WIREs Comput. Mol. Sci. **2**, 242 (2012).
[51] H.-J. Werner, P. J. Knowles, G. Knizia, F. R. Manby, M. Schütz, *et al.*, MOLPRO, version 2015.1, a package of *ab initio* programs, 2015 (2012), see http://www.molpro.net.
[52] J. Ullrich, R. Moshammer, R. Dörner, O. Jagutzki, V. Mergel, H. Schmidt-Böcking, and L. Spielberger, Recoil-ion momentum spectroscopy, J. Phys. B: At. Mol. Opt. Phys. **30**, 2917 (1997).
[53] R. Dörner, V. Mergel, O. Jagutzki, L. Spielberger, J. Ullrich, R. Moshammer, and H. Schmidt-Böcking, Cold target recoil ion momentum spectroscopy: a 'momentum microscope' to view atomic collision dynamics, Phys. Rep. **330**, 95 (2000).
[54] J. Ullrich, R. Moshammer, A. Dorn, R. Dörner, L. P. H. Schmidt, and H. Schmidt-Böcking, Recoil-ion and electron momentum spectroscopy: reaction-microscopes, Rep. Prog. Phys. **66**, 1463 (2003).
[55] X.-M. Tong, Z. Zhao, and C.-D. Lin, Theory of molecular tunneling ionization, Phys. Rev. A **66**, 033402 (2002).
[56] L. Keldysh *et al.*, Ionization in the field of a strong electromagnetic wave, Sov. Phys. JETP **20**, 1307 (1965).
[57] A. Perelomov, V. Popov, and M. Terent'ev, Ionization of atoms in an alternating electric field, Sov. Phys. JETP **23**, 924 (1966).
[58] A. Saenz, Hydrogen molecules in a strong static electric field, in *AIP Conference Proceedings*, Vol. 525 (American Institute of Physics, 2000) pp. 494–501.
[59] M. Feit, J. Fleck, and A. Steiger, Solution of the Schrödinger equation by a spectral method, J. Comput. Phys. **47**, 412 (1982).
[60] P. H. Bucksbaum, A. Zavriyev, H. G. Muller, and D. W. Schumacher, Softening of the $H_2^+$ molecular bond in intense laser fields, Phys. Rev. Lett. **64**, 1883 (1990).
[61] J. H. Sanderson, A. El-Zein, W. A. Bryan, W. R. Newell, A. J. Langley, and P. F. Taday, Geometry modifications and alignment of $H_2O$ in an intense femtosecond laser pulse, Phys. Rev. A **59**, R2567 (1999).
[62] J. Rajput, T. Severt, B. Berry, B. Jochim, P. Feizollah, B. Kaderiya, M. Zohrabi, U. Ablikim, F. Ziaee, K. Raju P., D. Rolles, A. Rudenko, K. D. Carnes, B. D. Esry, and I. Ben-Itzhak, Native frames: Disentangling sequential from concerted three-body fragmentation, Phys. Rev. Lett. **120**, 103001 (2018).

# Bibliography


[1] S. A. Abdel-Naby, M. S. Pindzola, and J. Colgan, *Differential cross section for the double photoionization of mg*, J. Phys. B Atom. Molec. Phys., 48 (2014), p. 025204.

[2] U. Ablikim, C. Bomme, T. Osipov, H. Xiong, R. Obaid, R. C. Bilodeau, N. G. Kling, I. Dumitriu, S. Augustin, S. Pathak, K. Schnorr, D. Kilcoyne, N. Berrah, and D. Rolles, *A coincidence velocity map imaging spectrometer for ions and high-energy electrons to study inner-shell photoionization of gas-phase molecules (article)*, Review of Scientific Instruments, 90 (2019), p. 055103.

[3] U. Ablikim, C. Bomme, E. Savelyev, H. Xiong, R. Kushawaha, R. Boll, K. Amini, T. Osipov, D. Kilcoyne, A. Rudenko, N. Berrah, and D. Rolles, *Isomer-dependent fragmentation dynamics of inner-shell photoionized difluoroiodobenzene*, Phys. Chem. Chem. Phys., 19 (2017), pp. 13419–13431.

[4] H. Adaniya, B. Rudek, T. Osipov, D. J. Haxton, T. Weber, T. N. Rescigno, C. W. McCurdy, and A. Belkacem, *Imaging the molecular dynamics of dissociative electron attachment to water*, Phys. Rev. Lett., 103 (2009), p. 233201.

[5] K. Alcantara, A. Gomes, L. Sigaud, W. Wolf, and A. Santos, *Outer-shell double photoionization of $CH_4$ and $CH_2Cl_2$ molecules*, Physics Procedia, 66 (2015), pp. 2–9. The 23rd International Conference on the Application of Accelerators in Research and Industry - CAARI 2014.

[6] K. Banaszek, C. Radzewicz, K. Wódkiewicz, and J. S. Krasiński, *Direct measurement of the wigner function by photon counting*, Phys. Rev. A, 60 (1999), pp. 674–677.

[7] M. Ben-Nun and T. J. Martínez, *Nonadiabatic molecular dynamics: Validation of the multiple spawining method for a multidimensional problem*, J. Chem. Phys., 108 (1988), p. 7244.

[8] M. Ben-Nun, J. Quenneville, and T. J. Martínez, *Ab initio multiple spawning: Photochemistry from first principles quantum molecular dynamics*, J. Chem. A, 104 (2000), pp. 5161–5175.

[9] J. Benda, J. D. Gorfinkiel, Z. Mašín, G. S. J. Armstrong, A. C. Brown, D. D. A. Clarke, H. W. van der Hart, and J. Wragg, *Perturbative and nonperturbative photoionization of* $h_2$ *and* $h_2O$ *using the molecular r-matrix-with-time method*, Phys. Rev. A, 102 (2020), p. 052826.

[10] M. P. Bircher, E. Liberatore, N. J. Browning, S. Brickel, C. Hofmann, A. Patoz, O. T. Unke, T. Zimmermann, M. Chergui, P. Hamm, U. Keller, M. Meuwly, H.-J. Woerner, J. Vaníček, and U. Rothlisberger, *Nonadiabatic effects in electronic and nuclear dynamics*, Structural Dynamics, 4 (2017), p. 061510.

[11] M. Born and K. Huang, *Dynamical Theory of Crystal Lattices*, Oxford University Press, November 1998.

[12] R. C. Brown and E. J. Heller, *Classical trajectory approach to photodissociation: The wigner method*, The Journal of Chemical Physics, 75 (1981), pp. 186–188.

[13] W. A. Bryan, S. L. Stebbings, J. McKenna, E. M. L. English, M. Suresh, J. Wood, B. Srigengan, I. C. E. Turcu, J. M. Smith, E. J. Divall, C. J. Hooker, A. J. Langley, J. L. Collier, I. D. Williams, and W. R. Newell, *Atomic excitation during recollision-free ultrafast multi-electron tunnel ionization*, Nature Physics, 2 (2006), pp. 379–383.

[14] P. H. Bucksbaum, A. Zavriyev, H. G. Muller, and D. W. Schumacher, *Softening of the* $H_2^+$ *molecular bond in intense laser fields*, Phys. Rev. Lett., 64 (1990), pp. 1883–1886.

[15] W. B. Case, *Wigner functions and weyl transforms for pedestrians*, Am. J. Phys., 76 (2008), pp. 937–946.

[16] P. Celani and H.-J. Werner, *Analytical energy gradients for internally contracted second-order multireference perturbation theory*, J. Chem. Phys., 119 (2003), p. 5044.

[17] C. Cheng, R. Forbes, A. J. Howard, M. Spanner, P. H. Bucksbaum, and T. Weinacht, *Momentum-resolved above-threshold ionization of deuterated water*, Phys. Rev. A, 102 (2020), p. 052813.

[18] C. Cheng, Z. L. Streeter, A. J. Howard, M. Spanner, R. R. Lucchese, C. W. McCurdy, T. Weinacht, P. H. Bucksbaum, and R. Forbes, *Strong field ionization of water ii: Electronic and nuclear dynamics en route to double ionization*, Phys. Rev. A., (submitted).

[19] C. Cheng, P. Vindel-Zandbergen, S. Matsika, and T. Weinacht, *Electron correlation in channel-resolved strong-field molecular double ionization*, Phys. Rev. A, 100 (2019), p. 053405.

[20] M. S. Child, *Molecular Collision Theory*, Dover Books on Chemistry, 2010.

[21] L. Clarke, I. Glendinning, and R. Hempel, *The MPI Message Passing Interface Standard*, Birkhäuser, Basel, Nov 1994.

[22] J. Colgan, M. Foster, M. S. Pindzola, and F. Robicheaux, *The evolution of the triple differential cross sections for the double photoionization of he and h2*, J. Phys. B Atom. Molec. Phys., 40 (2007), p. 4391.

[23] J. Colgan and M. S. Pindzola, *Double photoionization of beryllium*, Phys. Rev. A, 65 (2002), p. 022709.

[24] J. Colgan, M. S. Pindzola, and F. Robicheaux, *Triple differential cross sections for the double photoionization of* $h_2$, Phys. Rev. Lett., 98 (2007), p. 153001.

[25] A. S. Coolidge, H. M. James, and R. D. Present, *A study of the frank-condon principle*, J. Chem. Phys., 4 (1936), p. 193.

[26] M. J. Davis, *Unimolecular reactions and phase space bottlenecks*, J. Chem. Phys., 84 (1986), p. 5389.

[27] R. de Vivie, C. M. Marian, and S. D. Peyerimhoff, *Spin-forbidden transtions in the presence of an intersystem crossing: application to the* $b^1\sigma^+$ *state in* $oh^+$, J. Chem. Phys., 112 (1987), pp. 349–361.

[28] J. B. Delos and W. R. Thorson, *Semiclassical theory of inelastic collisions. ii. momentum-space formulation*, Phys. Rev. A, 6 (1972), pp. 720–727.

[29] X. Ding, R. Forbes, M. Kübel, K. F. Lee, M. Spanner, A. Y. Naumov, D. M. Villeneuve, A. Stolow, P. B. Corkum, and A. Staudte, *Threshold photodissociation dynamics of $NO_2$ studied by time-resolved cold target recoil ion momentum spectroscopy*, J. Chem. Phys., 151 (2019), p. 174301.

[30] X. Ding, M. Haertelt, S. Schlauderer, M. S. Schuurman, A. Y. Naumov, D. M. Villeneuve, A. R. W. McKellar, P. B. Corkum, and A. Staudte, *Ultrafast dissociation of metastable $CO^{2+}$ in a dimer*, Phys. Rev. Lett., 118 (2017), p. 153001.

[31] T. J. Dunn, I. A. Walmsley, and S. Mukamel, *Experimental determination of the quantum-mechanical state of a molecular vibrational mode using fluorescence tomography*, Phys. Rev. Lett., 74 (1995), pp. 884–887.

[32] R. Dörner, V. Mergel, O. Jagutzki, L. Spielberger, J. Ullrich, R. Moshammer, and H. Schmidt-Böcking, *Cold target recoil ion momentum spectroscopy: a 'momentum microscope' to view atomic collision dynamics*, Physics Reports, 330 (2000), pp. 95–192.

[33] J. H. Eland, *Double photoionisation spectra of methane, ammonia and water*, Chemical Physics, 323 (2006), pp. 391–396.

[34] M. Feit, J. Fleck, and A. Steiger, *Solution of the Schrödinger equation by a spectral method*, J. Comput. Phys., 47 (1982), p. 412.

[35] R. Forbes, A. E. Boguslavskiy, I. Wilkinson, J. G. Underwood, and A. Stolow, *Excited state wavepacket dynamics in $NO_2$ probed by strong-field ionization*, J. Chem. Phys., 147 (2017), p. 054305.

[36] K. P. F.R.S., *Liii. on lines and planes of closest fit to systems of points in space*, The London, Edinburgh, and Dublin Philosophical Magazine and Journal of Science, 2 (1901), pp. 559–572.

[37] J. Gallagher and C. Moore, *Tables of spectra of hydrogen, carbon, nitrogen, and oxygen atoms and ions*, CRC Press, Nov 1993.

[38] B. Gervais, E. Giglio, L. Adoui, A. Cassimi, D. Duflot, and M. E. Galassi, *The $h_2o^{2+}$ potential energy surfaces dissociation into $h^+/oh^+$: Theoretical analysis of the isotopic effect*, J. Chem. Phys., 131 (2009), p. 024302.

[39] M. Gisselbrecht, M. Lavollée, A. Huetz, P. Bolognesi, L. Avaldi, D. P. Seccombe, and T. J. Reddish, *Photodouble ionization dynamics for fixed-in-space* $h_2$, Phys. Rev. Lett., 96 (2006), p. 153002.

[40] S. Goursaud, M. Sizun, and F. Fiquet-Fayard, *Energy partitioning and isotope effects in the fragmentation of triatomic negative ions: Monte carlo scheme for a clasical trajectory study*, J. Chem. Phys., 65 (1976), p. 5453.

[41] D. Griffin, M. S. Pindzola, C. P. Ballance, and J. Colgan, *Double photoionization of be and mg atoms using the r-matrix-with-pseudostates method*, Phys. Rev. A, 79 (2009), p. 023413.

[42] R. Guillemin, P. Decleva, M. Stener, C. Bomme, T. Marin, L. Journel, T. Marchenko, R. Kushawaha, K. Jänkälä, N. Trcera, K. Bowen, D. Lindle, M. Piancastelli, and M. Simon,

*Selecting core-hole localization or delocalization in $CS_2$ by photofragmentation dynamics*, Nat. Comm., 6 (2015), p. 6166.

[43] W. Hastings, *Monte carlo sampling methods using markov chains and their applications*, Biometrika, 57 (1970), pp. 97–109.

[44] E. J. Heller, *Time-dependent approach to semiclassical dynamcis*, J. Chem. Phys., 62 (1975), p. 1544.

[45] ———, *Wavepacket path integral formulation of semiclassical dynamics*, J. Chem. Phys., 32 (1975), pp. 321–325.

[46] ———, *Wigner phase space method: Analysis for semiclassical applications*, J. Chem. Phys., 65 (1976), pp. 1289–1298.

[47] ———, *Quantum corrections to classical photodissociation models*, J. Chem. Phys., 68 (1978), pp. 2066–2075.

[48] ———, *Frozen gaussians: A very simple semiclassical approximation*, J. Chem. Phys., 75 (1981), p. 2923.

[49] ———, *The semiclassical way to molecular spectroscopy*, Acc. Chem. Res., 14 (1981), pp. 368–375.

[50] M. Hillery, R. O'Connell, M. Scully, and E. Wigner, *Distribution functions in physics: Fundamentals*, Phys. Rep., 106 (1984), pp. 121–167.

[51] A. Hishikawa, H. Hasegawa, and K. Yamanouchi, *Sequential three-body Coulomb explosion of $CS_2$ in intense laser fields appearing in momentum correlation map*, Chemical Physics Letters, 361 (2002), pp. 245 – 250.

[52] L. Holmegaard, J. L. Hansen, L. Kalhøj, S. Louise Kragh, H. Stapelfeldt, F. Filsinger, J. Küpper, G. Meijer, D. Dimitrovski, M. Abu-samha, C. P. J. Martiny, and L. Bojer Madsen, *Photoelectron angular distributions from strong-field ionization of oriented molecules*, Nature Physics, 6 (2010), pp. 428–432.

[53] D. A. Horner, S. Miyabe, T. N. Rescigno, C. W. McCurdy, and F. Martín, *Classical two-slit interference effects in double photoionization of molecular hydrogen at high energies*, Phys. Rev. Lett., 101 (2008), p. 183002.

[54] D. A. Horner, W. Vanroose, T. N. Rescigno, F. Martín, and C. W. McCurdy, *Role of nuclear motion in double ionization of molecular hydrogen by a single photon*, Phys. Rev. Lett., 98 (2007), p. 073001.

[55] S. L. Horton, Y. Liu, P. Chakraborty, P. Marquetand, T. Rozgonyi, S. Matsika, and T. Weinacht, *Strong-field-versus weak-field-ionization pump-probe spectroscopy*, Phys. Rev. A, 98 (2018), p. 053416.

[56] R. L. Hudson, *When is the wigner quasi-probability density non-negative*, Rep. Math. Phys., 6 (1974), pp. 249–252.

[57] T. Jahnke, T. Weber, T. Osipov, A. Landers, O. Jagutzki, L. Schmidt, C. Cocke, M. Prior, H. Schmidt-Böcking, and R. Dörner, *Multicoincidence studies of photo and auger electrons from fixed-in-space molecules using the coltrims technique*, Journal of Electron Spectroscopy and Related Phenomena, 141 (2004), pp. 229–238. Frontiers of Coincidence Experiments.

[58] T. H. D. Jr., *Gaussian basis sets for use in correlated molecular calculations. i. the atoms boron through neon and hydrogen*, Rev. Mod. Phys., 90 (1989), p. 100.

[59] L. Keldysh et al., *Ionization in the field of a strong electromagnetic wave*, Sov. Phys. JETP, 20 (1965), pp. 1307–1314.

[60] A. Kenfack and K. Życzkowski, *Negativity of the wigner function as an indicator of non-classicality*, J. Opt. B: Quantum Semiclass. Opt, 6 (2004), pp. 396–404.

[61] S. Kube, C. Lasser, and M. Weber, *Monte carlo sampling of wigner functions and surface hopping quantum dynamcs*, J. of Comp. Phys., 228 (2009), pp. 1947–1962.

[62] C. Kurtsiefer, T. Pfau, and J. Mlynek, *Measurement of the wigner function of an ensemble of helium atoms*, Nature, 386 (1997), pp. 150–153.

[63] M. Kutta, *Beitrag zur näherungsweisen integration totaler differentialgleichungen*, Zeitschrift für Mathematik und Physik, 46 (1901), pp. 435–453.

[64] K. A. Larsen, T. N. Rescigno, T. Severt, Z. L. Streeter, W. Iskandar, S. Heck, A. Gatton, E. G. Champenois, R. Strom, B. Jochim, D. Reedy, D. Call, R. Moshammer, R. Dörner, A. L. Landers, J. B. Williams, C. W. McCurdy, R. R. Lucchese, I. Ben-Itzhak, D. S. Slaughter, and T. Weber, *Photoelectron and fragmentation dynamics of the* $H^+ + H^+$ *dissociative channel in* $NH_3$ *following direct single-photon double ionization*, Phys. Rev. Research, 2 (2020), p. 043056.

[65] X. Li, J. C. Tully, H. B. Schlegel, and M. J. Frisch, *Ab initio ehrenfest dynamics*, J. Chem. Phys., 123 (2005), p. 084106.

[66] H. C. Longuet-Higgins, *The intersection of potential energy surfaces in polyatomic molecules*, Proc. R. Seoc. Long. A., 344 (1975), pp. 147–156.

[67] A. I. Lvovsky, H. Hansen, T. Aichele, O. Benson, J. Mlynek, and S. Schiller, *Quantum state reconstruction of the single-photon fock state*, Phys. Rev. Lett., 87 (2001), p. 050402.

[68] N. Metropolis, A. W. Rosenbluth, M. N. Rosenbluth, A. H. Teller, and E. Teller, *Equation of state calculations by fast computing machines*, J. Chem. Phys., 21 (1953), p. 1087.

[69] T. Mori and T. J. Martínez, *Exploring the conical intersections seam: The seam space nudged elastic band method*, J. Chem. Theory Comput., 9 (2012), pp. 1155–1163.

[70] R. S. Mulliken, *Electronic population analysis on lcao-mo molecular wave functions. i*, J. of Chem. Phys., 23 (1955), pp. 1833–1840.

[71] J. V. Neumann, *Proof of the quasi-ergodic hypothesis*, PNAS, 18 (1932), pp. 70–82.

[72] N. Neumann, D. Hant, L. P. H. Schmidt, J. Titze, T. Jahnke, A. Czasch, M. S. Schöffler, K. Kreidi, O. Jagutzki, H. Schmidt-Böcking, and R. Dörner, *Fragmentation dynamics of* $CO_2^{3+}$ *investigated by multiple electron capture in collisions with slow highly charged ions*, Phys. Rev. Lett., 104 (2010), p. 103201.

[73] G. Nogues, A. Rauschenbeutel, S. Osnaghi, P. Bertet, M. Brune, J. M. Raimond, S. Haroche, L. G. Lutterbach, and L. Davidovich, *Measurement of a negative value for the wigner function of radiation*, Phys. Rev. A, 62 (2000), p. 054101.

[74] G. Olaso-González, M. Merchán, and L. Serrano-Andrés, *Ultrafast electron transfer in photosynthesis: Reduced pheophytin and quinone interaction mediated by conical intersections*, J. Phys. Chem. B, 110 (2006), pp. 24734–24739.

[75] A. Perelomov, V. Popov, and M. Terent'ev, *Ionization of atoms in an alternating electric field*, Sov. Phys. JETP, 23 (1966), pp. 924–934.

[76] C. Petersen, E. Peronne, J. Thøgersen, H. Stapelfeldt, and M. Machholm, *Control and imaging of interfering wave packets in dissociating $I_2$ molecules*, Phys. Rev. A, 70 (2004), p. 033404.

[77] J. Rajput, T. Severt, B. Berry, B. Jochim, P. Feizollah, B. Kaderiya, M. Zohrabi, U. Ablikim, F. Ziaee, K. Raju P., D. Rolles, A. Rudenko, K. D. Carnes, B. D. Esry, and I. Ben-Itzhak, *Native frames: Disentangling sequential from concerted three-body fragmentation*, Phys. Rev. Lett., 120 (2018), p. 103001.

[78] ———, *Native frames: Disentangling sequential from concerted three-body fragmentation*, Phys. Rev. Lett., 120 (2018), p. 103001.

[79] T. J. Reddish, J. Colgan, P. Bolognesi, L. Avaldi, M. Gisselbrecht, M. Lavollée, M. S. Pindzola, and A. Huetz, *Physical interpretation of the "kinetic energy release" effect in the double photoionization of* $h_2$, Phys. Rev. Lett., 100 (2008), p. 193001.

[80] D. Reedy, J. B. Williams, B. Gaire, A. Gatton, M. Weller, A. Menssen, T. Bauer, K. Henrichs, P. Burzynski, B. Berry, Z. L. Streeter, J. Sartor, I. Ben-Itzhak, T. Jahnke, R. Dörner, T. Weber, and A. L. Landers, *Dissociation dynamics of the water dication following one-photon double ionization. ii. experiment*, Phys. Rev. A, 98 (2018), p. 053430.

[81] M. Rosenbluth, *Genesis of the monte carlo algorithm for statistical mechanics*, Conference Proceedings, 690 (2003), p. 22.

[82] C. D. T. Runge, *Über die numerische auflösung von differentialgleichungen*, Mathematische Annalen, 46 (1895), pp. 167–178.

[83] A. Saenz, *Hydrogen molecules in a strong static electric field*, in AIP Conference Proceedings, vol. 525, American Institute of Physics, 2000, pp. 494–501.

[84] J. H. Sanderson, A. El-Zein, W. A. Bryan, W. R. Newell, A. J. Langley, and P. F. Taday, *Geometry modifications and alignment of* $H_2O$ *in an intense femtosecond laser pulse*, Phys. Rev. A, 59 (1999), pp. R2567–R2570.

[85] P. Sándor, V. Tagliamonti, A. Zhao, T. Rozgonyi, M. Ruckenbauer, P. Marquetand, and T. Weinacht, *Strong field molecular ionization in the impulsive limit: Freezing vibrations with short pulses*, Phys. Rev. Lett., 116 (2016), p. 063002.

[86] H. Sann, T. Jahnke, T. Havermeier, K. Kreidi, C. Stuck, M. Meckel, M. S. Schöffler, N. Neumann, R. Wallauer, S. Voss, A. Czasch, O. Jagutzki, T. Weber, H. Schmidt-Böcking, S. Miyabe, D. J.

Haxton, A. E. Orel, T. N. Rescigno, and R. Dörner, *Electron diffraction self-imaging of molecular fragmentation in two-step double ionization of water*, Phys. Rev. Lett., 106 (2011), p. 133001.

[87] J. D. Savee, V. A. Mozhayskiy, J. E. Mann, A. I. Krylov, and R. E. Continetti, *The role of excited-state topology in three-body dissociation of sym-triazine*, Science, 321 (2008), pp. 826–830.

[88] F. Schell, A. E. Boguslavskiy, C. P. Schulz, S. Patchkovskii, M. J. J. Vrakking, A. Stolow, and J. Mikosch, *Sequential and direct ionic excitation in the strong-field ionization of 1-butene molecules*, Phys. Chem., 20 (2018), pp. 14708–14717.

[89] M. S. Schuurman and A. Stolow, *Dynamics at conical intersections*, Annual Review of Physical Chemistry, 69 (2018), pp. 427–450. PMID: 29490199.

[90] J. M. Sellier, M. Nedjalkov, and I. Dimov, *An introduction to applied quantum mechanics in the wigner monte carlo formalism*, Phys. Rep., 577 (2015), pp. 1–34.

[91] L. Serrano-Andrés and M. Merchán, *Are the five natural dna/rna base monomers a good choice from natural selection?: A photochemical perspective*, Journal of Photochemistry and Photobiology C: Photochemistry Reviews, 10 (2009), pp. 21–32.

[92] T. Severt, J. Rajput, B. Berry, B. Jochim, P. Feizollah, B. Kaderiya, M. Zohrabi, U. Ablikim, F. Ziaee, K. Raju P., D. Rolles, A. Rudenko, K. D. Carnes, B. D. Esry, and I. Ben-Itzhak, *Native frames: A new approach for separating sequential and concerted three-body fragmentation*, Phys. Rev. A. In preparation.

[93] T. Severt, Z. L. Streeter, W. Iskandar, K. A. Larsen, A. Gatton, D. Trabert, B. Jochim, B. Griffin, E. G. Champenois, M. M. Brister, D. Reedy, D. Call, R. Strom, A. L. Landers, R. Dörner, J. B. Williams, D. S. Slaughter, R. R. Lucchese, T. Weber, C. W. McCurdy, and I. Ben-Itzhak, *Step-by-stpe, state-selective tracking of sequential fragmentation dynamics of water dications by momentum imaging*, Proceedings of the National Academy of Sciences, (submitted).

[94] Z. Shen, E. Wang, M. Gong, X. Shan, and X. Chen, *Fragmentation dynamics of carbonyl sulfide in collision with 500 ev electron*, The Journal of Chemical Physics, 145 (2016), p. 234303.

[95] T. Shimanouchi, H. Matsuura, Y. Ogawa, and I. Harada, *Tables of molecular vibrational frequencies*, Journal of Physical and Chemical Reference Data, 7 (1978), pp. 1323–1444.

[96] T. Shiozaki and H.-J. Werner, *Explicitly correlated multireference configuration interaction with multiple reference functions: Avoided crossings and conical intersections*, J. Chem. Phys., 134 (2011), p. 184104.

[97] D. T. Smithey, M. Beck, M. G. Raymer, and A. Faridani, *Measurement of the wigner distribution and the density matrix of a light mode using optical homodyne tomography: Application to squeezed states and the vacuum*, Phys. Rev. Lett., 70 (1993), pp. 1244–1247.

[98] E. Sokell, P. Bolognesi, A. Kheifets, I. Bray, S. Safgren, and L. Avaldi, *Photo-double ionization of mg studied by electron-electron coincidence experiments*, Phys. Rev. A, 89 (2014), p. 013413.

[99] Z. L. Streeter, F. L. Yip, R. R. Lucchese, B. Gervais, T. N. Rescigno, and C. W. McCurdy, *Dissociation dynamics of the water dication following one-photon double ionization. i. theory*, Phys. Rev. A, 98 (2018), p. 053429.

[100] L. Tao, C. W. McCurdy, and T. N. Rescigno, *Grid-based methods for diatomic quantum scattering problems. iii. double photoionization of molecular hydrogen in prolate spheroidal coordinates*, Phys. Rev. A, 82 (2010), p. 023423.

[101] X.-M. Tong, Z. Zhao, and C.-D. Lin, *Theory of molecular tunneling ionization*, Phys. Rev. A, 66 (2002), p. 033402.

[102] J. C. Tully, *Perspective: Nonadiabatic dynamics theory*, J. Chem. Phys., 137 (2012), p. 22A301.

[103] J. C. Tully and R. K. Preston, *Trajectory surface hopping approach to nonadiabatic molecular collisions: The reaction of $h^+$ with $d_2$*, J. Chem. Phys., 55 (1971), p. 562.

[104] J. Ullrich, R. Moshammer, A. Dorn, R. Dörner, L. P. H. Schmidt, and H. Schmidt-Böcking, *Recoil-ion and electron momentum spectroscopy: reaction-microscopes*, Reports on Progress in Physics, 66 (2003), p. 1463.

[105] X. Urbain, B. Fabre, E. M. Staicu-Casagrande, N. de Ruette, V. M. Andrianarijaona, J. Jureta, J. H. Posthumus, A. Saenz, E. Baldit, and C. Cornaggia, *Intense-laser-field ionization of molecular hydrogen in the tunneling regime and its effect on the vibrational excitation of* $H_2^+$, Phys. Rev. Lett., 92 (2004), p. 163004.

[106] W. Vanroose, D. A. Horner, F. Martín, T. N. Rescigno, and C. W. McCurdy, *Double photoionization of aligned molecular hydrogen*, Phys. Rev. A, 74 (2006), p. 052702.

[107] J. von Neumann and E. P. Wigner, *Über merkwürdige diskrete Eigenwerte*, Springer Berlin Heidelberg, Berlin, Heidelberg, 1993, pp. 291–293.

[108] M. Waitz, D. Metz, J. Lower, C. Schober, M. Keiling, M. Pitzer, K. Mertens, M. Martins, J. Viefhaus, S. Klumpp, T. Weber, H. Schmidt-Böcking, L. P. H. Schmidt, F. Morales, S. Miyabe, T. N. Rescigno, C. W. McCurdy, F. Martín, J. B. Williams, M. S. Schöffler, T. Jahnke, and R. Dörner, *Two-particle interference of electron pairs on a molecular level*, Phys. Rev. Lett., 117 (2016), p. 083002.

[109] B. Wales, È. Bisson, R. Karimi, S. Beaulieu, A. Ramadhan, M. Giguère, Z. Long, W.-K. Liu, J.-C. Kieffer, F. Légaré, and J. Sanderson, *Coulomb imaging of the concerted and stepwise break up processes of OCS ions in intense femtosecond laser radiation*, J. Elect. Spectr. Rel. Phenom., 195 (2014), p. 332.

[110] T. Weber, A. Czasch, O. Jagutzki, A. Müller, V. Mergel, A. Kheifets, J. Feagin, E. Rotenberg, G. Meigs, M. H. Prior, S. Daveau, A. L. Landers, C. L. Cocke, T. Osipov, H. Schmidt-Böcking, and R. Dörner, *Fully differential cross sections for photo-double-ionization of $D_2$*, Phys. Rev. Lett., 92 (2004), p. 163001.

[111] T. Weber, A. O. Czasch, O. Jagutzki, V. M. AK Müller, A. Kheifets, E. Rotenberg, M. H. P. George Meigs, S. Daveau, A. Landers, T. O. CL Cocke, R. D. Muino, H. Schmidt-Böcking, and R. Dörner, *Complete photo-fragmentation of the deuterium molecule*, Nature, 431 (2004), pp. 437–440.

[112] ——, *Erratum: Complete photo-fragmentation of the deuterium molecule*, Nature, 443 (2006).

[113] J. Weinbub and D. K. Ferry, *Recent advances in wigner function approaches*, Applied Physics Reviews, 5 (2018), p. 041104.

[114] D. J. Wells and H. M. Quiney, *Wigner function analysis of high harmonic generation in atoms*, J. Phys. Commun., 4 (2020), p. 125007.

[115] H.-J. Werner, P. J. Knowles, G. Knizia, F. R. Manby, and M. Schütz, *Molpro: a gerernal-purpose quantum chemistry program package*, WIREs Comput. Mol. Sci., 2 (2012), p. 242.

[116] ——, *Molpro, version 2015.1, a package of ab initio programs*, 2015.

[117] H.-J. Werner and E.-A. Reinsch, *The self-consistent electron pairs method for multiconfiguration reference state functions*, J. Chem. Phys., 76 (1982), p. 3144.

[118] E. Wigner, *On the quantum correction for thermodynamic equilibrium*, Phys. Rev., 40 (1932), p. 749.

[119] R. M. Wood, Q. Zheng, A. K. Edwards, and M. A. Mangan, *Limitations of the axial recoil approximation in measurements of molecular dissociation*, Review of Scientific Intruments, 68 (1997), p. 1382.

[120] C. Wu, C. Wu, D. Song, H. Su, Y. Yang, Z. Wu, X. Liu, H. Liu, M. Li, Y. Deng, Y. Liu, L.-Y. Peng, H. Jiang, and Q. Gong, *Nonsequential and sequential fragmentation of $CO_2^{3+}$ in intense laser fields*, Phys. Rev. Lett., 110 (2013), p. 103601.

[121] D. R. Yarkony, *Diabolical conical intersections*, Rev. Mod. Phys., 68 (1996), p. 985.

[122] F. L. Yip, F. Martín, C. W. McCurdy, and T. N. Rescigno, *Double k-shell photoionization of atomic beryllium*, Phys. Rev. A, 84 (2011), p. 053417.

[123] F. L. Yip, C. W. McCurdy, and T. N. Rescigno, *Double photoionization of excited lithium and beryllium*, Phys. Rev. A, 81 (2010), p. 063419.

[124] F. L. Yip, T. N. Rescigno, and C. W. McCurdy, *Fully differential single-photon double photoionization of atomic magnesium*, Phys. Rev. A, 94 (2016), p. 063414.

[125] F. L. Yip, T. N. Rescigno, C. W. McCurdy, and F. Martín, *Fully differential single-photon double ionization of neon and argon*, Phys. Rev. Lett., 110 (2013), p. 173001.

[126] R. N. Zare, *Photoejection dynamics*, Mol. Photochem., 4 (1972), pp. 1–37.

[127] A. Zhao, M. van Beuzekom, B. Bouwens, D. Byelov, I. Chakaberia, C. Cheng, E. Maddox, A. Nomerotski, P. Svihra, J. Visser, V. Vrba, and T. Weinacht, *Coincidence velocity map imaging using tpx3cam, a time stamping optical camera with 1.5 ns timing resolution*, Review of Scientific Instruments, 88 (2017), p. 113104.